University of Nottingham

UK | CHINA | MALAYSIA

Phosphate-based glass microspheres for bone repair and localised chemotherapy and radiotherapy treatment of bone cancers

Ben Milborne

Thesis submitted to the University of Nottingham for the degree of Doctor of Philosophy

August 2022

Acknowledgements

I would firstly like to thank my primary supervisor Dr Ifty Ahmed whose support and guidance made this work possible. His ability to motivate and inspire myself and all members of the research group during challenging times has been remarkable. Thank you for the endless conversations and time spent reviewing work, I am truly grateful. I would also like to thank Professor Robert Layfield and Dr Alexander Thompson for their supervision and assistance throughout the duration of my project.

Thank you to the members of Dr Ifty Ahmeds' research group and to fellow colleagues within the Advanced Materials Research Group; Dr Towhidul Islam, Dr Abul Arafat, Dr Sabrin Abdus Samad, Dr Reda Felfel, Dr Matthew Wadge, Dr Laura Macrì Pellizzeri, Jesus Molinar Diaz, Henry Forbes, Andi Arjuna, Luke Woodcliffe, Lauren Murrell, and Farah Nigar to name a few. The continued help and support shown throughout my studies is greatly appreciated and the conversations and knowledge gained was invaluable to my work.

I would also like to acknowledge all the technical staff of the ITRC, Wolfson Building and NMRC for their technical assistance and help during my PhD. I would especially like to thank, Dr Hannah Constantin, Dr Nigel Neate, John Kirk, Kieran Orange, Dr Martin Roe, Craig Stoppiello, Dr Graham Rance, Dr Chris Parmenter and Dr Elisabeth Steer. Thank you to Dr Jeremy J. Titman of the Department of Chemistry and to Ian Cardillo-Zallo and Alison McLellan for their assistance with the NMR studies. I would also like to thank Dr Colin Scotchford for access to the cell culture labs within the Wolfson building and to Louise Briggs for all her help for the duration of the cell work.

Thank you to the Engineering and Physical Sciences Research Council (EPSRC) who supported and funded my Centre for Doctoral Training in Bioinstructive Materials for Healthcare Applications.

A final thanks to my family and friends for their constant reassurance throughout, especially to Polly for her unwavering and unconditional support.

Abstract

Phosphate-based glasses (PBGs) are hugely promising materials for bone repair and regeneration as they can be formulated to be compositionally similar to the inorganic component of bone. Alterations to PBG formulations can be made to tailor their degradation rates and subsequent release of biotherapeutic ions to induce cellular responses, such as osteogenesis. In this work, novel invert-PBGs in the series $xP_2O_5 \cdot (56\text{-}x)CaO \cdot 24MgO \cdot 20Na_2O$ (mol%), where x is 40, 35, 32.5 and 30, were formulated to contain pyro (Q^1) and orthophosphate (Q^0) species. These PBGs were then processed into highly porous microspheres (PMS) via a flame spheroidisation process developed within the research group. Compositional and structural analysis using EDX and ^{31}P-MAS NMR analysis revealed significant depolymerisation had occurred with reducing phosphate content, which increased further when PBGs were processed into PMS. A decrease from 50% to 0% of Q^2 species and increase from 6% to 35% of Q^0 species was observed for the PMS when the phosphate content decreased from 40 to 30 mol%. Ion release studies also revealed up to a 4-fold decrease in cations and an 8-fold decrease in phosphate anions released with decreasing phosphate content. *In vitro* bioactivity studies revealed that the orthophosphate rich PMS had favourable bioactivity responses after 28 days of immersion in SBF. Indirect and direct cell culture studies confirmed that the PMS were cytocompatible and supported cell growth and proliferation over 7 days of culture. The P30 PMS with ~65% pyro and ~35% ortho phosphate content revealed the most favourable properties and was proposed to be highly suitable for bone repair and regeneration, especially for orthobiologic applications owing to their highly porous morphology.

Doxorubicin (DOX) was used as a model drug to assess its loading and release kinetics from porous phosphate-based glass microspheres to ascertain their suitability for localised drug delivery for the treatment of bone cancers. P40 PMS revealed a DOX loading efficiency of 55%, which was significantly greater than P30 PMS at 29.1%. Both P40 and P30 PMS released more DOX in phosphate buffered saline (PBS) at pH 5 as compared to release at pH 7.4. P40 PMS released 57% of DOX at pH 5 over a 48-hour period, whereas P30 PMS only released 15% of DOX. A pH-responsive DOX release in a more acidic environment suggests that the chemotherapeutic delivery and efficacy properties may lead to increased drug release within tumour tissues.

Internal radiotherapy has been shown to be an effective treatment modality to destroy cancerous tissues and is usually achieved by the placement of radioactive sources at the tumour site. In this work, a novel processing method was established to combine yttrium oxide

(Y_2O_3) with P40 phosphate glass particles to form uniform, solid microspheres containing very high yttrium levels via our flame spheroidisation process. The 30Y (~15 mol% Y_2O_3) and 50Y microspheres (~39 mol% Y_2O_3) had equivalent and superior yttrium content in comparison to clinically available microspheres used for internal radiotherapy (i.e., Therasphere®). The yttrium-containing microspheres formed were shown to be glass-ceramics, with crystalline phases present but with all elements homogenously distributed throughout the microspheres. Increasing yttrium addition resulted in increased durability of the microspheres, with 50Y microspheres revealing a 10-fold decrease in the release rate of some ions compared to P40 solid microspheres. Indirect and direct cell culture studies confirmed that the 30Y and 50Y microspheres were cytocompatible and supported cell growth and proliferation over 7 days of culture. No significant difference was observed in the metabolic and ALP activity for MG63s for both 30Y and 50Y microspheres from both indirect and direct cell culture studies. Yttrium was incorporated into the phosphate-based microspheres at a level that had not previously been achieved or observed from the literature studies and were shown to support bone cell attachment and growth. A high yttrium content could enable more radiation to be delivered per dose of microspheres, resulting in shorter neutron activation times which could prove beneficial for logistical issues associated with transportation of the biomaterials following nuclear activation.

The radionuclide holmium-166 (^{166}Ho) which is comparable to yttrium-90 (^{90}Y) in that it emits β-radiation with a similar tissue penetration range and a significantly reduced half-life of 26.8 hours, was also investigated. The beneficial paramagnetic properties and density of ^{166}Ho indicates that ^{166}Ho-doped materials could be visualised through clinical imaging techniques, whilst simultaneously delivering a therapeutic dose of radiation. In this work, solid holmium-containing microspheres were similarly produced via the flame spheroidisation process using holmium oxide (Ho_2O_3) and P40 phosphate glass particles. The glass-ceramic microspheres produced had equivalent (30H: ~17mol% Ho_2O_3) and superior (50H: ~30mol% Ho_2O_3) holmium content in comparison to clinically used yttrium-doped microspheres (i.e. Therasphere®). Analogous to yttrium containing microspheres, elevated holmium content resulted in topographically unique features on the surface of some 50H microspheres. This increased holmium content resulted in significantly reduced ion release rates for all the ions and the holmium-microspheres did not show evidence of bioactivity. However, *in vitro* indirect and direct cell culture studies demonstrated their cytocompatibility. No significant difference was observed in the metabolic and ALP activity of MG63 cells for 30H and 50H microspheres in both the indirect and direct cell culture methods. This study appears to be the first to demonstrate microspheres containing high levels of holmium content that can also facilitate direct cell growth and proliferation of human osteoblast-like cells.

The microspheres developed are therefore hugely promising biomaterials for both drug delivery and internal radiotherapy applications, as well as for promoting bone repair and regeneration at damaged sites. High holmium content could also result in higher specific activity per microsphere to increase radiotherapy delivery whilst also promoting higher visibility via imaging modalities.

List of publications

1. **Ben Milborne**, Abul Arafat, Rob Layfield, Alex Thompson, Ifty Ahmed (2020). "*The use of biomaterials in Radiation therapy*". Recent Progress in Materials (ISSN 2689-5846).

2. Jesús Molinar Díaz, John Luke Woodliffe, **Ben Milborne**, Lauren Murrell, Md Towhidul Islam, Elisabeth Steer, Nicola Weston, Nicola Morley, Paul D Brown, Ifty Ahmed (2022). "*Manufacture of cytocompatible, ferromagnetic, phosphate-glass-ceramic, porous microspheres via a flame spheroidisation process*". Bioengineering (Basel). 2022 Oct 25;9(11):611. doi: 10.3390/bioengineering9110611.

3. **Ben Milborne**, Lauren Murrell, Ian Cardillo-Zallo, Jeremy Titman, Louise Briggs, Colin Scotchford, Alexander Thompson, Rob Layfield and Ifty Ahmed (2022). **"***Developing Porous Ortho and Pyrophosphate Containing Glass Microspheres; Structural and Cytocompatibility Characterisation*". *Adv. Mater. Interfaces* 2023, 2202089. https://doi.org/10.1002/admi.202202089

Table of Contents

Abbreviations

ACP	Amorphous calcium phosphate
ADP	Adenosine diphosphate
ALP	Alkaline phosphatase
ATP	Adenosine triphosphate
BG	Bioactive glass
BM	Bone metastases
BMP	Bone morphogenetic protein
BO	Bridging oxygen
BP	Bisphosphonate
CT	Computer tomography
DCPD	Dicalcium phosphate dihydrate
DI	Deionised
DMSO	Dimethyl sulfoxide
DOX	Doxorubicin
DSC	Differential scanning calorimetry
EBRT	External beam radiotherapy
ECM	Extracellular matrix
EDX	Energy dispersive X-ray spectroscopy
ESEM	Environmental scanning electron microscopy
FEG-SEM	Field emission gun scanning electron microscopy
FIB-SEM	Focused ion beam scanning electron microscopy
FTIR	Fourier transform infrared spectroscopy
HA	Hydroxyapatite
HCA	Hydroxycarbonate apatite
HEMA	2-hydroxyethyl methacrylate
ICDD	International centre for diffraction data
ICP-MS	Inductively coupled plasma mass spectrometry
IMS	Industrial methylated spirit
ISO	International organisation for standardisation
LC	Liquid chromatography
MAS	Magic angle spinning
MRI	Magnetic resonance imaging
MS	Microspheres
MSC	Mesenchymal stem cells
NBO	Non-bridging oxygen
NMR	Nuclear magnetic resonance
PBG	Phosphate-based glasses
PBS	Phosphate buffered saline
PLLA	Poly(L-lactic acid)
PMMA	Polymethyl methacrylate
PMS	Porous microspheres
PPi	Inorganic pyrophosphate
ROS	Reactive oxygen species
RT	Radiotherapy
SBF	Simulated body fluid
SEM	Scanning electron microscopy
SIRT	Selective internal radiotherapy

SM	Standard media
SMS	Solid microspheres
SPECT	single-photon emission computer tomography
SRE	Skeletal related events
TCP	Tissue culture plastic
UV	Ultraviolet
XPS	X-ray photoelectron spectroscopy
XRD	Powder X-ray diffraction

Table of Figures

Table of Tables

1 Introduction

1.1 Overview

Bone cancers are devastating diseases that cause disruption to bone structure and function. Although primary bone cancers are rare and have an incidence rate of only 2.6 per 1,000,000 people in the UK, bone is the third most common organ where metastases occur [17]. The incidence of advanced malignant tumours with bone metastasis is 30–75%, depending on the primary tumour type, with high incidence especially common in patients with advanced prostate and breast cancer. Cancers of the bone can cause patients to experience severe pain, result in pathological fractures and can lead to impaired mobility. Surgical resection is the primary treatment method to remove cancerous cells and prevent further metastases [18]. This can result in critical-sized defects that may not heal spontaneously. Although the current gold standard remains autologous bone grafts, the additional morbidity involved for the patients and the risk of the tissue being rejected, in the case of allografts, due to immune responses highlights the need for new and improved treatments. An alternative solution is the use of synthetic bone graft substitute biomaterials that aim to replace native bone and to guide and stimulate bone repair and regeneration [19].

Calcium phosphate-based biomaterials are seen as ideal candidates for bone repair and regeneration and as a result have attracted much attention leading to the continuation of their rapid development [20]. This family of biomaterials are compounds formed through the interaction of calcium and phosphate ions resulting in their unique resemblance to the chemical and structural components of native bone tissue [21]. The calcium phosphate-based biomaterials developed contain a variety of properties that are beneficial when used as a bone-graft substitute or to promote new bone growth, such as; osteoconductivity, osteoinductivity, the ability to fully degrade *in vivo* and the capability to withstand stress at the defect site. In addition to these properties, many techniques have been developed to process the calcium phosphate-based biomaterials into a variety of practical geometries and tissue scaffolds [22].

The ability to formulate phosphate-based glasses and glass-ceramics to be compositionally similarity to the inorganic component of bone has led to their exploration as biomaterials to facilitate bone repair. These materials can act as osteoconductive surfaces that support cell growth, whilst simultaneously releasing therapeutic ions that can stimulate increased tissue repair [23]. Alterations to phosphate-based glass formulations can dramatically affect many of the glass properties, such as the melting temperature, chemical durability, and ion release rates [24]. These glasses therefore have the potential to be tailored to encompass the

chemical and mechanical properties as well as induce the biological functions required to meet the specific requirements for bone regeneration.

During surgical resection, complete removal of all malignant bone tissue is challenging. Consequently, often a multi-modal treatment strategy involving chemotherapy and radiotherapy is employed prior to and following surgical resection to both reduce bone tumour mass and to eliminate residual cancerous cells [25]. The systemic administration of many prominent chemotherapy drugs results in unwanted off-target side-effects that cause the detrimental adverse effects suffered by many cancer patients. Techniques continue to be developed that allow for localised chemotherapy delivery that can increase efficacy at the target site whilst simultaneously result in a reduction of off-target effects [26].

External beam radiation therapy (EBRT) for bone metastasis is commonly employed as a palliative therapy with 60-89% patients having a partial response and 25-30% having a complete response to treatment [27]. Despite this, the deep lying nature of bone tissue limits the ability to perform EBRT on a large proportion of bone cancer patients. In other cancers where EBRT is not possible, such as in unresectable liver carcinomas, internal radiotherapy is delivered using radionuclide-doped glass microspheres. The glass microspheres contain the element yttrium, which upon neutron activation form the β-emitting ^{90}Y radionuclide. The microspheres are therefore able to deliver site specific internal radiotherapy to malignant cancer cells which has been shown to improve patient prognosis [28].

The beneficial properties of glass microspheres, such as their improved flow properties compared to irregular shaped particles and their ability to be administered via minimally invasive injection techniques, has led to their use beyond internal radiotherapy applications. Porous microspheres can act as a substrate for cell growth and proliferation and have enhanced gas and nutrient flow which has facilitated their use in a wide range of tissue engineering applications [29]. Furthermore, porosity can be exploited to enable the loading of these microspheres with therapeutic cargo for localised delivery to overcome issues associated with the systemic administration of drugs, growth factors and other biological and non-biological compounds [30].

1.2 Aims and Objectives

In this work, phosphate-based microspheres were investigated as suitable biomaterials to address the above problems associated with current bone cancer treatment strategies. The primary aim of this project was to manufacture and characterise phosphate-based microspheres that can be tailored to form part of a treatment strategy for bone repair and

regeneration following bone cancer and its associated treatments. Phosphate-based glass formulations were processed to produce solid and porous microspheres that can release therapeutic ions upon degradation to stimulate cells and guide bone regeneration at sites following bone devastation due to cancer or surgical resection. The microspheres were designed to simultaneously act as osteoconductive surfaces that could promote bone cell attachment and growth. This project also aimed to encapsulate a chemotherapeutic drug (Doxorubicin) within the porous structure of the microspheres for potential application in localised drug delivery for the treatment of bone cancer. These multifaceted microspheres were intended to deliver localised chemotherapeutics to sites of bone cancer, thereby negating the adverse effects of systemic administration, whilst facilitating the controlled delivery of therapeutic ions to promote bone repair and regeneration.

Extensive work was also undertaken to process novel high content yttrium and holmium containing phosphate-based microspheres that could be used for localised bone cancer radiotherapy. The development of a processing methodology that can achieve high levels of both yttrium and holmium content could increase the specific activity per microsphere and increase the radiotherapy efficacy delivered, whilst decreasing the number of microspheres required for treatment.

The studies conducted included the following specific objectives:

- Processing phosphate-based glasses into solid and highly porous microspheres and performing elemental, structural and cytocompatabilty characterisation.

- Investigate the loading and release of doxorubicin from porous microspheres and assess their potential as localised drug delivery vehicles.

- Develop a processing methodology to produce high yttrium content phosphate-based microspheres and perform elemental, structural and cytocompatabilty characterisation.

- Develop a processing methodology to produce high holmium content phosphate-based microspheres and perform elemental, structural and cytocompatabilty characterisation.

2 Literature review

2.1 Bone anatomy and structure

Bone is a specialised type of connective tissue that plays an essential role in many biological processes that include locomotion, protection and support of soft tissues, mineral homeostasis and haematopoiesis [31]. Its cellular and extracellular composition give rise to a highly organised architecture which is responsible for bones unique physical and biomechanical properties. Four types of cells are found within bone: osteoblasts, osteoclasts, bone lining cells and osteocytes, with each type playing distinct roles in bone homeostasis [32]. Most of the volume of bone is made up of its extracellular matrix that is comprised of an organic and inorganic component. The organic component is formed from proteins, such as collagen, glycoproteins and proteoglycans, which surround the bone cells [33]. Calcium and phosphate ions that form to create hydroxyapatite crystals are the main constituent of the inorganic component but other ions such as magnesium are also found within the extracellular matrix of bone (see Figure 2.1). [34].

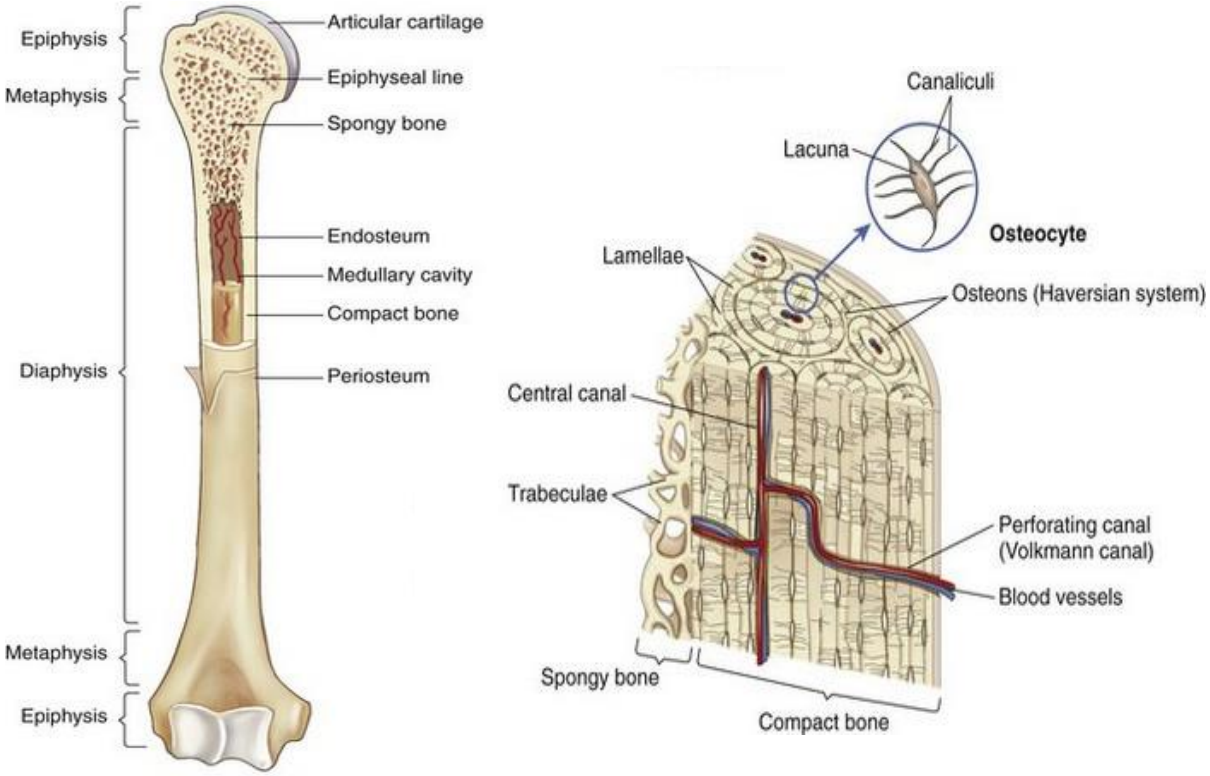

Figure 2.1 The structure of cortical (compact) and cancellous (spongy) bone. [12]

2.2 Remodelling of bone

Bone is metabolically active and is a highly dynamic tissue that is constantly undergoing adaptive remodelling in response to mechanical and chemical stimuli. Bone remodelling is a highly complex process and involves the constant cycle of old bone being resorbed and new bone replacing it [35]. This process is regulated through the coordinated action and interaction of the osteoblasts, osteoclasts, osteocytes and bone lining cells (see Figure 2.2). Bone resorption occurs following activation of osteoclasts whilst osteoblasts are responsible for forming new bone at the remodelling site. Bone remodelling is influenced and controlled by multiple local and systemic factors such as hormones, cytokines, prostaglandins, ions and mechanical loading [31]. A greater understanding of the dynamic nature of bone tissue and the remodelling process continues to aid in the development of new therapeutic approaches to bone diseases.

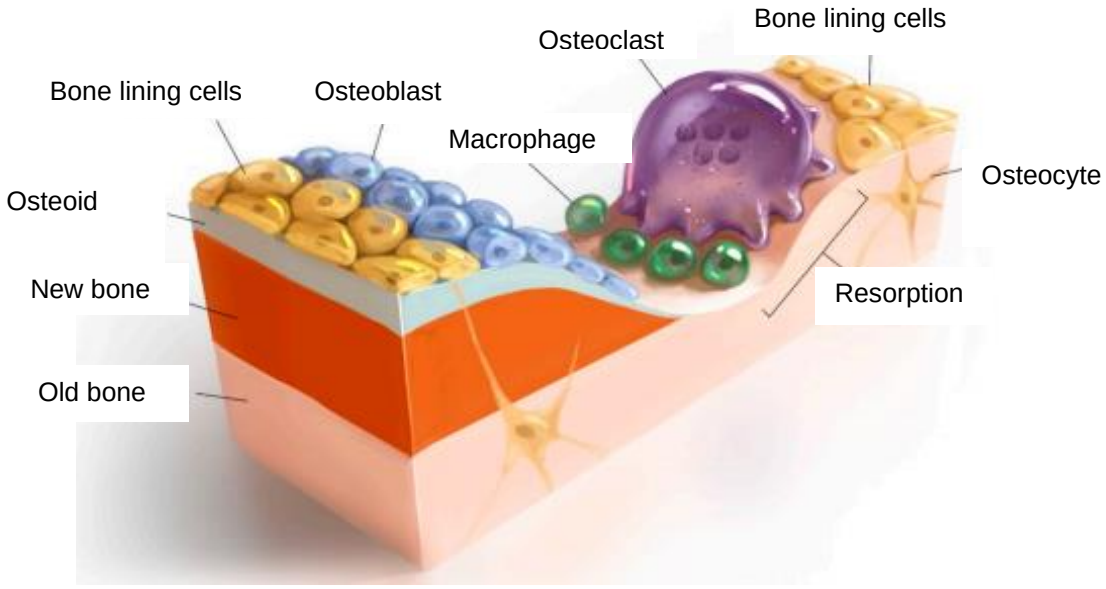

Figure 2.2 Schematic of the structure of bone and the locations of bone cells. [5]

2.3 Primary bone cancer

Osteosarcomas are the most common form of primary malignant tumours of the bone [36]. Osteosarcomas are characterised by the production of osteoid and local tissue invasion by the malignant cells and are most commonly, but not exclusively, found in children and young adults. Osteosarcomas usually develop in the long bones at the metaphysis, due to this region experiencing the most rapid growth, and frequently present in the distal femur, proximal tibia

and proximal humerus (see Figure 2.3) [37]. Histological examination is performed to grade osteosarcomas on the likelihood that these malignant cells will continue to grow and spread to other parts of the body. There are several types of highly aggressive osteosarcomas, such as osteoblastic, fibroblastic and chondroblastic, dependent on which matrix-producing cells dominate and less aggressive forms such as parosteal osteosarcomas [38].

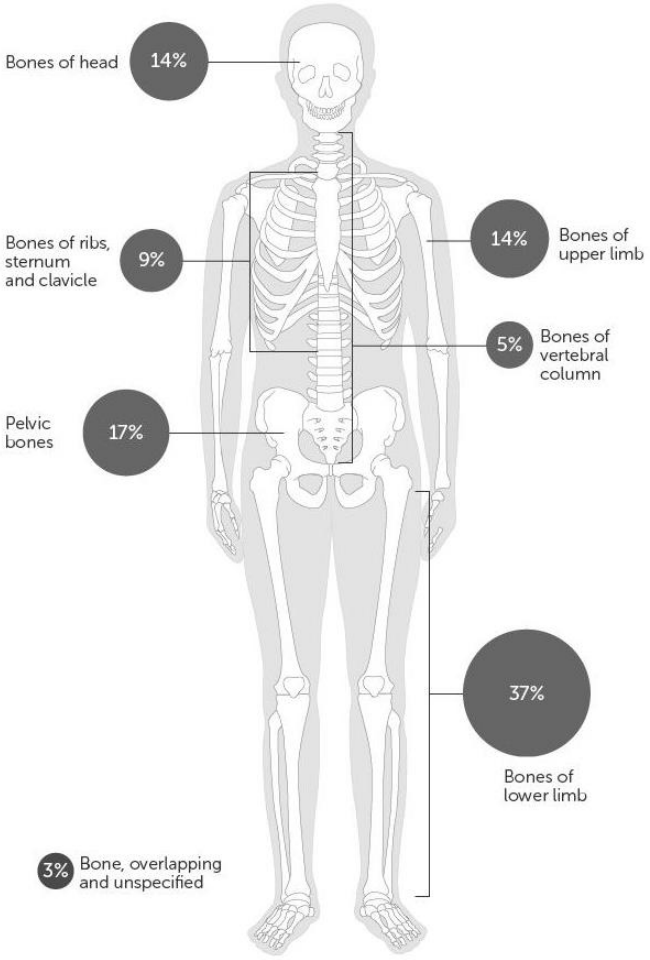

Figure 2.3 Percentage distribution of bone sarcoma cases by anatomical site. [3]

Ewing sarcoma is the second most diagnosed form of primary bone cancer and like osteosarcomas is most often seen in children and young adults. This highly malignant form of tumour is found in flat bones, such as the pelvis and ribs, as well as throughout long bones [39]. Other forms of primary bone cancer include chondrosarcoma, chordoma and angiosarcoma [38].

2.4 Secondary bone cancers

Bone is a common site of metastases and ranks third amongst all organ metastases, behind hepatic and pulmonary metastases respectively, and is more frequently observed than primary bone tumours [40]. The increase in prevalence of bone metastases has been attributed to the prolonged survival of cancer patients, due to advances in treatment, in addition to more sophisticated diagnostic techniques [41]. The type and incidence of bone metastases is dependent upon the primary tumour site. Primary breast and prostate cancer are accountable for most bone metastases, with the incidence as high as 65-75% in patients with advanced stage breast or prostate cancer. The median-survival from diagnosis of bone metastases in breast and prostate cancer ranges from 12-53 months but is as low as 6-7 months in advanced stage lung cancer patients, where the incidence is 30-40% [42]. Secondary bone cancers have a significant clinical impact and are a major cause for morbidity. Skeletal related events (SREs) that arise as a result of metastases in the bone are characterised by severe pain, pathological fractures, impaired mobility, spinal cord compression and hypercalcemia [43].

For a metastasis to transpire, a complex cascade of events occurs starting with the cancer cells detaching from the primary tumour, intravasation into blood and lymphatic vessels and then extravasation into the tissue of a distant organ. This ‘seed and soil’ hypothesis has provided the basis for research into the molecular mechanisms that orchestrate the frequency of bone metastases in many cancer patients (see Figure 2.4) [44]. Initially, primary cancer cells undergo epithelial-to-mesenchymal transition, a process in which epithelial type cancer cells experience a phenotypic transformation to cells presenting mesenchymal characteristics. The cancer cells lose cell surface intracellular adhesion proteins and epithelial polarisation and secrete factors that enable them to migrate to surrounding tissue and into systemic circulation [45]. The site of the primary tumour and anatomy of the surrounding vessels influences the likely location of the bone metastases once the tumour cells are in systemic circulation. For instance, prostate cancer metastasis is most commonly seen in the axial skeleton in the sacrum, lumbar spine and pelvis as a result of the venous drainage of the prostate through the pelvic plexus [18].

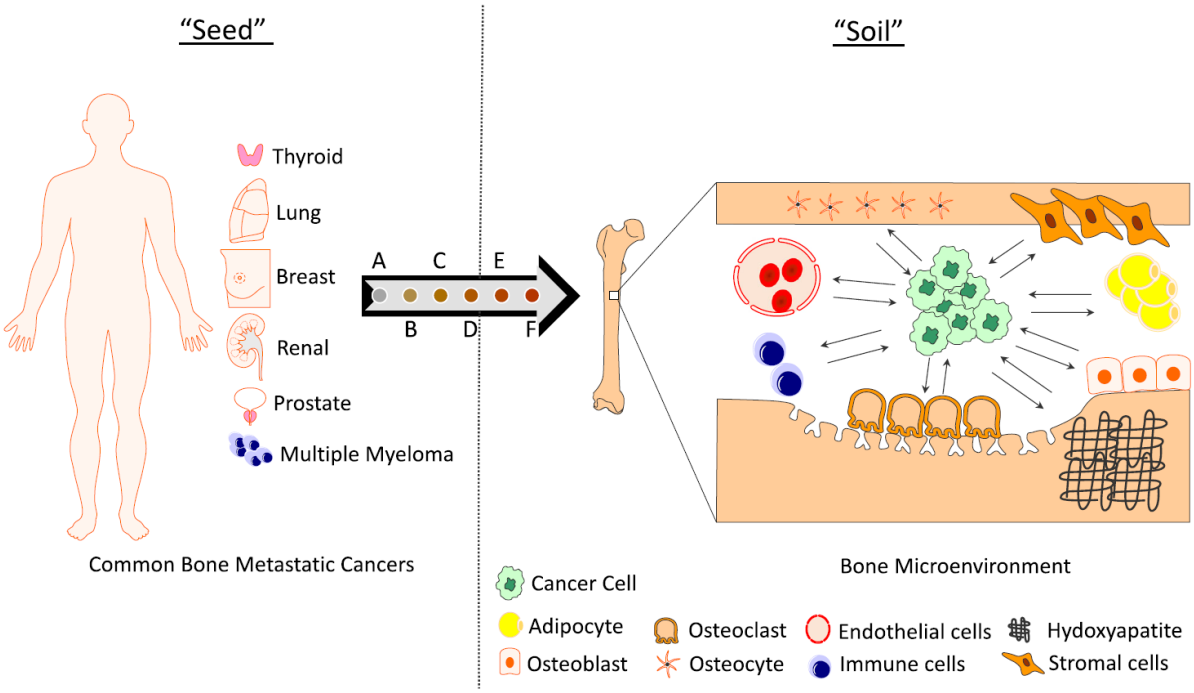

Figure 2.4 Schematic representation of the "seed" and "soil" hypothesis for bone metastases. (A) Site of primary tumour, (B) Local invasion, (C) Intravasation, (D) Dissemination via blood and lymphatic vessels, (E) Extravasation, (F) Colonisation at site of bone metastases. [15]

The circulating tumour cells often end up residing in bone due to multiple mechanisms that are initiated by the tumour cells. The primary tumour cells release specific growth factors and cytokines that can recruit bone marrow derived cells (BMDCs), which in turn cause an increase in extracellular matrix remodelling, promote vascular permeability, and can suppress some levels of immune function. This creates an environment favourable for tumour cell attachment and subsequent growth known as the pre-metastatic niche [46]. The circulating tumour cells have been shown to over-express specific chemokine receptors, namely C-X-C motif chemokine receptor 4 (CXCR-4), of which the specific ligand CXCL-12 is produced by various stromal cells found in bone marrow (mesenchymal stem cells, endothelial cells and osteoblasts). This chemo-attractive mechanism facilitates osteotropism and causes the cancer cells to hone to and colonise the pre-metastatic bone niche [47]. The cancer cells then enter a state of quiescence, enabling the cells to evade the actions of the immune system and rendering them resistant to treatment. A combination of local and systemic factors then initiate the development of the bone metastasis with different mechanisms responsible as to whether the bone metastases is osteoblastic, osteolytic or a combination of both [48].

Osteolytic bone metastases most commonly arise from breast cancer and multiple myeloma [49]. The tumour cells that are residing in the pre-metastatic niche interact with the bone microenvironment and establish a self-propagating vicious cycle that disrupts normal bone homeostasis and structure [50]. The tumour cells secrete various cytokines that, either directly or indirectly via osteoblast, promote osteoclast differentiation and activity. The result of this is an increase in bone resorption which is accompanied by the subsequent release of matrix-embedded growth factors, such as platelet-derived growth factor (PDGF) and insulin-like growth factor. These growth factors stimulate tumour growth and proliferation, whilst inhibiting osteoblast activity, thereby perpetuating the vicious cycle and leading to further bone devastation [43]. The destruction of the normal bone architecture means that this type of bone metastases has the highest rate of fracture. Patients with multiple myeloma have been found to have the highest fracture incidence of 43% with the fracture incidence as high as 35% in breast cancer patients. A study showed that patients who developed a pathologic fracture had a significant increased risk of death (32% multiple myeloma, 20% breast cancer) relative to patients without a fracture [51]. The mechanisms that cause the formation of osteoblastic lesions are less well understood but are most common with metastases from prostate cancer. Growth factors, such as TGF- β, bone morphogenetic protein (BMP) and Wnt, are secreted from the tumour cells which in turn stimulate the differentiation of mesenchymal progenitors into osteoblasts. This results in an imbalance in bone turnover and increased bone formation through osteogenesis [52]. Osteoblastic lesions also result in pathological fractures but to a lesser extent than seen in osteolytic lesions. A study of 640 prostate cancer patients with bone metastases found that there was a fracture incidence of 19% [51]. An increased understanding of the multifaceted and complex nature of bone metastases has revealed numerous cellular and molecular targets for treatment within the metastatic cascade, which include osteoblasts, osteoclasts, endothelial cells, immune cells, circulating tumour cells and the extracellular matrix of the bone microenvironment [50].

2.5 Treatment for primary bone cancer

Surgery remains the principal treatment option for most primary bone cancer cases. A wide-excision is performed in which the whole tumour is resected as well as some of the healthy tissue around it to ensure that all the cancerous cells are removed. For the majority of patients, limb-sparing surgery is possible but in a number of cases amputation of limbs is necessary in order for an effective wide-excision to be performed and the successful removal of all cancer cells [53]. Advances in surgical and imaging techniques has meant that the extent of bone and surrounding tissue resected during surgery has decreased but remains a very invasive and drastic course of action. This in conjunction with more sophisticated and innovative

reconstructive procedures has improved not only the survival rates for patients but also the functional outcomes following such operations [54]. A curettage method can be used in some cases to scrape out and remove cancerous cells in certain regions of long bones and in the skull and spine. This can reduce the critical size of bone resected but still leaves regions of bone that need regenerating or to be reconstructed (see Figure 2.5) [55]. Pre- and post-operative chemotherapy is traditionally used in adjunct to surgical intervention, particular with patients suffering with osteosarcoma and Ewing sarcoma, to induce tumour necrosis and prevent any residual tumour cells from surviving and continuing to proliferate. Intraoperative cryoablation and percutaneous bone cement injections (cementoplasty) are additional adjuvant procedures that are sometimes performed during open bone tumour surgery to improve the clinical outcome [56]. In some instances, radiation therapy can also be used to shrink the overall size of the tumour prior to surgical intervention although no consensus has been reached about the optimal dose whether the radiotherapy should be delivered in a single dose or in multiple treatments. The location, severity and condition of the patient will dictate the treatment regimen. Following the removal of the tumour, an endoprosthetic or biological reconstruction of the defected site may be required but is dependent upon numerous patient and tumour-related factors [57].

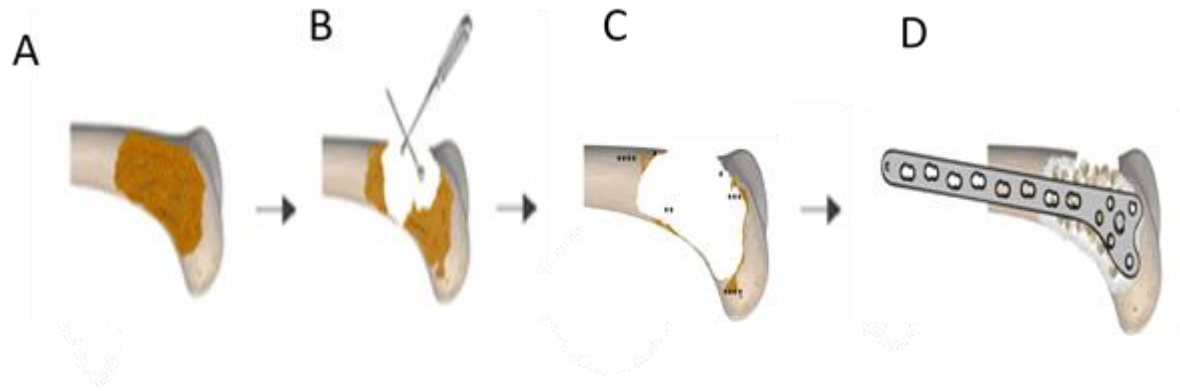

Figure 2.5 Schematic representation of the surgical curettage technique used for the removal of a bone tumour. (A) Bone tumour identified in the distal femur. (B) Curettage and high-speed burring are performed to remove the tumour. (C) Residual tumour cells may still be present following excision of the tumour. Cyroablation and chemotherapy can be used to remove residual tumour cells. (D) Reconstruction of the defected bone region via internal fixation or the use of bone grafts and biomaterial substitutes can be performed. [58]

Multiple clinical trials have shown that the standard treatment strategy for primary bone cancer of neoadjuvant chemotherapy, surgical resection followed by adjuvant post-operative chemotherapy improves prognosis for patients. Some variability exists in the precise combination chemotherapy regime a patient receives but in most cases some of the most well-established chemotherapeutics, such as methotrexate, doxorubicin, adriamycin, cisplatin and ifosfamide are administered [25]. The tumour necrosis response to neoadjuvant chemotherapy has been found to be a strong indicator of the overall response to treatment. A study of 97 osteosarcoma patients by O'Kane *et al.* revealed that patients with 90% tumour necrosis or more exhibited an 82% five-year survival rate, whereas patients with less than 90% tumour necrosis only had a 68% five-year survival rate [59]. Patients usually remain on the same chemotherapy regime post-operative unless poor responders pre-operatively or if experiencing extreme adverse events. The chemotherapy drugs used in the management of primary bone cancer are a systemic treatment and following administration circulate in their bloodstream to reach and destroy cancer cells located throughout the body. The toxic nature and systemic administration of these chemotherapeutics results in the well documented and inadvertent side effects of chemotherapy (see Figure 2.6). Ifosfamide has been shown to cause hemorrhagic cystitis, peripheral neuropathy can arise due to cisplatin treatment and adriamycin-induced cardiomyopathy can be a life-long effect of treatment [60].

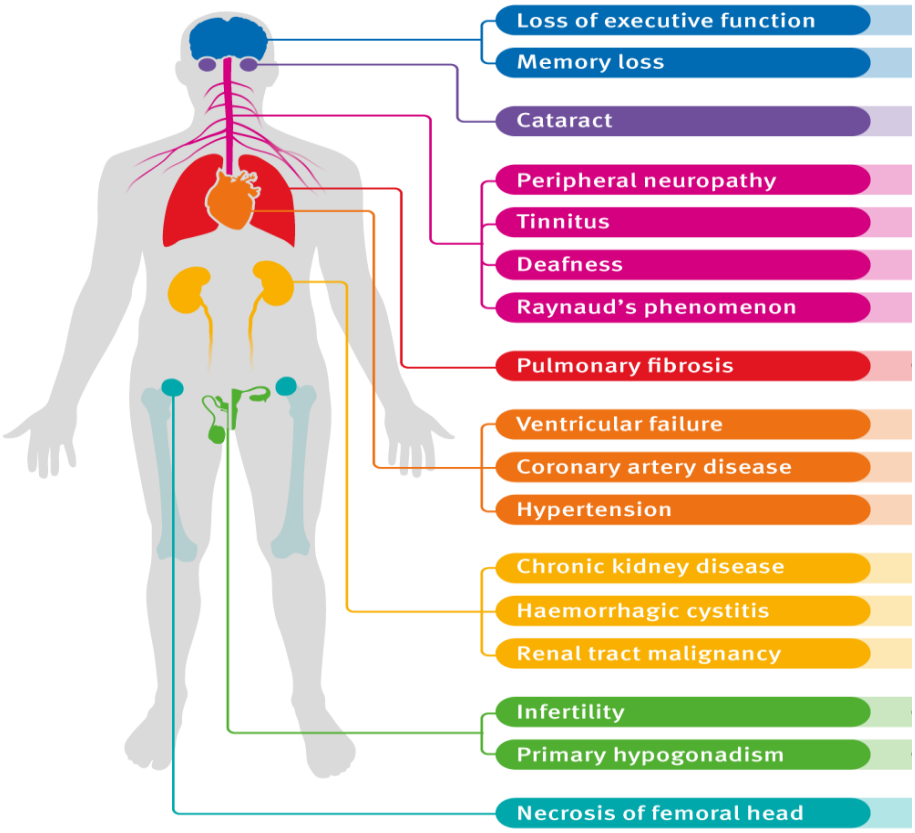

Figure 2.6 Common long-term adverse effects associated with the systemic administration of many non-specific chemotherapeutics. [2]

2.6 Treatment for secondary bone cancer

In bone metastases, surgical intervention is usually a palliative treatment option performed to alleviate pain and to restore function and mobility to affected areas. As with primary bone cancer, surgical intervention may be curative in certain instances when a solitary resectable metastasis is present. Typically bone metastases involves multiple sites and while resection of multiple bony defects followed by complex endoprosthetic reconstructive surgery is occasionally performed, the complex nature of such procedures and the spread of an individual's metastases do not always facilitate such practice [61]. Surgery can be performed for prophylactic fixation of impending fractures and to stabilise pathological fractures that occur at sites of metastases. A multi-modal treatment strategy is therefore required to improve the outcome of treatment for the patient with a typical regime comprised of a combination of chemotherapy, hormone therapy, radiotherapy and surgical intervention in some regards [62]. Numerous patient and cancer-related factors, such as the type of primary cancer, the site of

metastases, the presence of multiple metastases as well patients age, physical condition and prognosis will dictate the course of treatment [63].

The site of primary cancer will ultimately dictate the chemotherapy regime that a patient with bone metastases will undergo. The frontline treatment is systemic chemotherapy that is effective against the primary tumour type. Additional therapeutics that specifically target the bone and the site of metastasis are also used to alleviate pain as well as prevent skeletal morbidity and hypercalcemia. Bisphosphonates (BPs) are seen as the gold standard in bone-targeted therapeutics for the treatment of osteolytic bone metastases and other bone diseases characterised by abnormally high bone resorption [64]. Bisphosphonates are a class of drug that are stable analogues of pyrophosphate, where a P-C-P bond is present in place of the P-O-P bond of pyrophosphate, making them resistant to chemical and enzymatic hydrolysis. The P-C-P backbone presents two phosphonate groups that can bind to chelating calcium ions on hydroxyapatite surface causing bisphosphonates to have a high binding affinity to bone. The molecular structure of the two covalent side chains, R_1 and R_2, affect the binding affinity and the pharmacological activity of the various BPs [65]. Bisphosphonates are classified as nitrogen BPs or non-nitrogen BPs depending on the presence or absence of a nitrogen atom in their R_2 side chain.

Nitrogen BPs or non-nitrogen BPs have different mechanisms of action but both inhibit osteoclast-mediated bone resorption by supressing osteoclast activity [66]. Non-nitrogen BPs are metabolised into cytotoxic analogues of adenosine triphosphate (ATP) and the subsequent accumulation of the resulting metabolites within osteoclasts induces apoptosis. Nitrogen BPs effect the cholesterol synthesis by inhibiting diphosphate synthase in the mevalonate pathway. The downstream effect of this is disruption to the morphology, cytoskeletal arrangement, membrane ruffling and ultimately the osteoclasts ability to function and resorb bone [11] (see Figure 2.7).

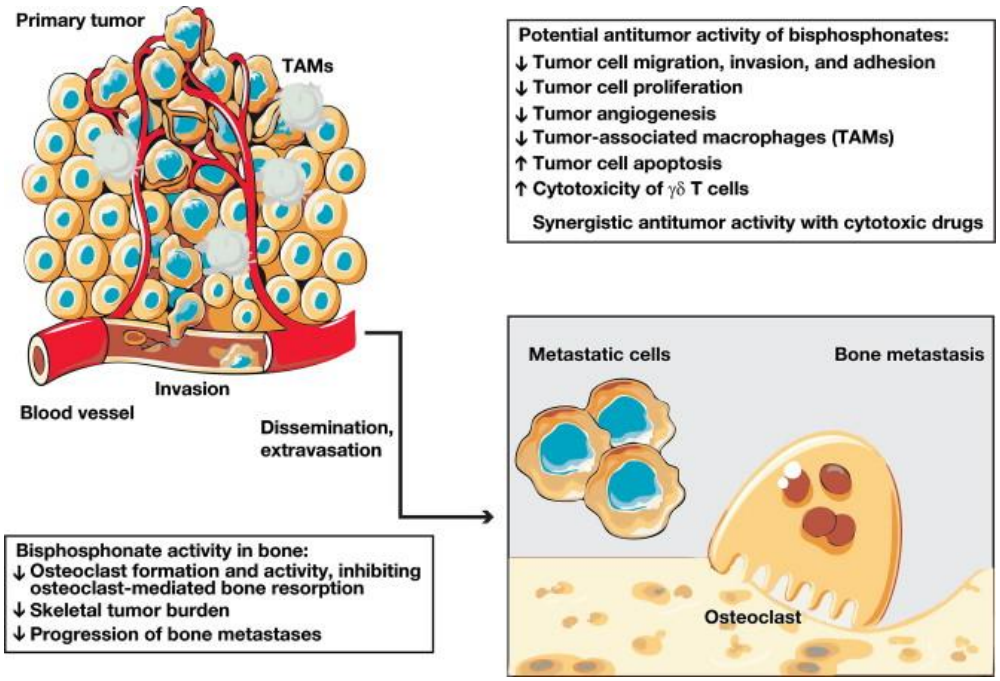

Figure 2.7 The proposed mechanisms of action of bisphosphonates that result in their antitumor activity. [11]

As is the case for all cancers, novel ways in which drug therapies can be administered in a targeted, site-specific manner for the localised delivery of a high concentration of antitumor agents are being developed and investigated for the treatment of bone cancers. Ozben *et al.* loaded polymethyl methacrylate (PMMA), which is used for intraoperative cementoplasty during orthopaedic surgery, with cisplatin and investigated the cytotoxicity on primary osteosarcoma Saos-2 cells. The mechanical properties of PMMA remained unaltered by cisplatin addition but cisplatin did cause a significant reduction in the viability of Soas-2 cells following incubation. They proposed that cisplatin loaded PMMA may be used to fill the area following resection of a bone tumour to prevent tumour growth [67]. Antitumour agents such as doxorubicin and gemcitabine have been conjugated with BPs to improve their targeted delivery to bone metastases [68]. Studies continue to be undertaken to find ways in which to improve the therapeutic efficacy of treatment and reduce adverse effects associated with systemic delivery of non-targeted drugs [69].

2.7 Radiation therapy and treatment for bone cancer

Radiotherapy has become one of the most common and vital modalities for effective cancer treatment and care and is used either alone or in combination with surgery, chemotherapy and

immunotherapy in approximately half of all cancer cases worldwide [70]. Ionising radiation is utilised for the treatment of cancer due to its ability to deposit energy that damages the genetic material of cells, resulting in their inability to survive and proliferate further. The unregulated manner in which cancer cells rapidly proliferate means that they are more susceptible to radiation-induced DNA damage than normal healthy cells [71]. Irradiation can also damage the DNA double helix structure by inducing DNA single and double-strand breaks, which in turn induces cellular events such as apoptosis, necrosis and abnormal mitosis [72]. DNA can also be damaged indirectly by reactive oxygen species (ROS) and through free radicals generated in cells by radiation (see Figure 2.8) [73]. The genomic instability of cancer cells means that they are inefficient or lack the ability to effectively repair DNA damage induced by radiation in comparison to normal cells. This mechanism underpins radiotherapy's selectivity for inducing cancer cell death [74]. Unfortunately, radiation inadvertently also causes damage to healthy cells adjacent to cancerous cells, or those in the radiation path. As such, advancements in this field need to consider maximising the dose of radiotherapy to aberrant cancer cells whilst minimising exposure to normal healthy cells.

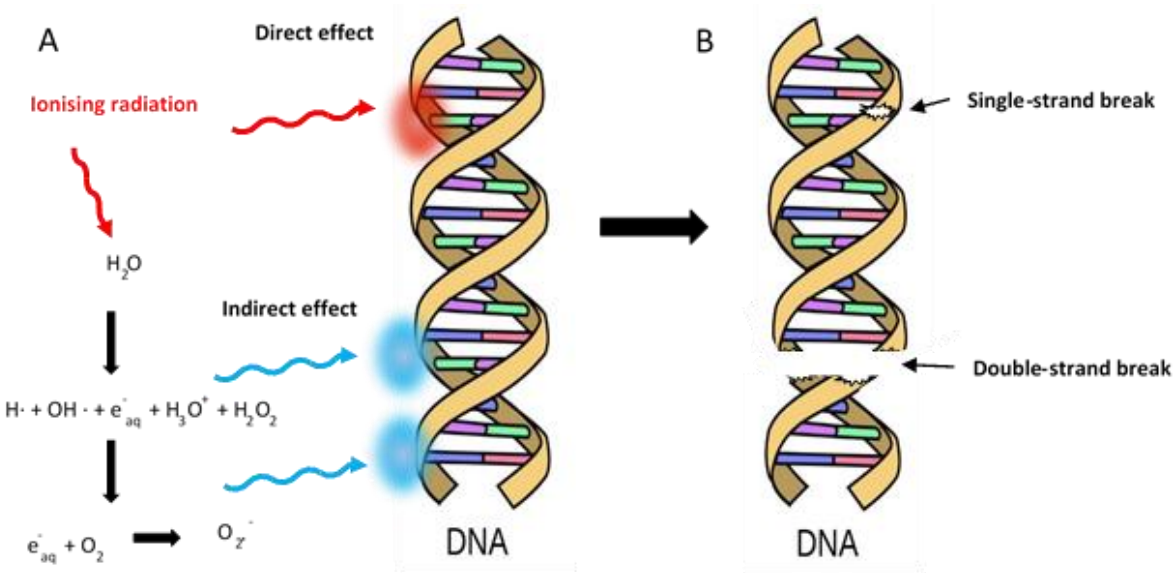

Figure 2.8 (a) Schematic of how ionising radiation utilised for radiotherapy can damage DNA. Radiation can directly damage DNA or indirectly damage it through the generation of reactive oxygen species (ROS). (b) DNA damage can occur because of single-strand breaks (SSB), double-strand breaks (DSB) or other interactions with DNA and proteins.

Depending on the type of cancer, radiotherapy can be used to cure localised cancer, as palliative treatment to reduce symptoms, or to limit progression of the disease in incurable cases [75]. Radiotherapy can be delivered at different stages of a patient's treatment regime. Neoadjuvant radiotherapy is performed pre-operatively with the aim of reducing the size of a tumour prior to surgical resection. Radiotherapy can also be used as an adjuvant therapy intra-operatively and post-operatively to help eliminate any residual tumour cells [76].

The radiation itself can be delivered to cancerous targets in two opposing ways, externally or internally. External Beam radiation is the most prevalent form of radiotherapy used in the clinical setting and involves aiming high-energy rays, in the form of photons (X-rays or gamma rays), protons or particle radiation, from outside of the body to the specific tumour site. Conversely, Internal Radiation occurs as a result of placing radioactive sources within the body, usually adjacent to or directly into the tumour itself [77]. Technological advances are continuing to drive progression in both external and internal radiotherapy to improve its therapeutic efficacy and reduce adverse effects.

Radiation therapy plays an important role in the palliative treatment of bone metastases. It is administered to patient's primarily to relieve pain and to improve their quality of life by ameliorating skeletal function, preventing pathological fractures or spinal cord compressions and therefore reducing analgesic requirements [78]. The tumour cells present in the bone microenvironment disrupt the physiological equilibrium between osteoblasts and osteoclasts causing structural damage and fractures. Invading tumour cells can directly compress surrounding nerve cells at the site of metastases and the increased expression of chemical mediators further stimulates nerve fibres and results in local pain. Ionising radiation can reduce osteoclast activation, kill tumour cells at the site of bone metastases and thereby increase ossification. The reduction in tumour volume that can be achieved using radiation therapy is capable of providing symptomatic relief by reducing the stimulation to adjacent nerve cells and by reducing the inflammatory response at the bone metastases site [79].

External beam radiotherapy (EBRT) is most commonly used and between 50% and 80% of patients have been found to respond to at least partial pain relief following treatment and up to one-third experiencing complete relief [80]. Technological advances in imaging techniques and the ability to deliver the radiotherapy has meant that highly conformal therapies, such as stereotactic body radiation (SBRT) and three-dimensional conformal radiation therapy (3-DCRT), are routinely employed. These techniques can accurately target specific bone metastases and deliver a maximum ionising radiation to the target, whilst minimising the dose to surrounding healthy tissue. The modality, total dose and fraction of the radiotherapy schedule are considered on an individual basis and are dependent on both the condition of

the patient and the cancer [81]. Clinical considerations such as location of the tumour and its subsequent proximity to surrounding critical structures and radiosensitive tissue can mean it may not always be possible to utilise EBRT in the treatment of cancers of the bone [82].

Injectable radiopharmaceuticals have also been used for the treatment of secondary bone cancer, particularly when the cancer has metastasised to multiple bone sites [83]. Currently, there are four commercially available radiopharmaceuticals for bone cancer treatment: $^{89}SrCl_2$ (Metastron®), $^{223}RaCl_2$ (Xofigo®) ^{153}Sm-EDTMP (Quadramet®), and ^{186}Re-HEDP (186Re-etidronate®) [84]. Both Radium and Strontium are alkaline earth metals and follow very similar metabolic pathways *in vivo* to calcium and therefore have a natural tropism for bone. Samarium and rhenium are conjugated to phosphonates (EDTMP, ethylenediaminetetramethylene phosphonate and HEDP, hydroxyethylidene diphosphonate), which are molecules that have a very strong affinity toward calcium present in the actively growing bone. The radiotherapeutic agents therefore localise in bone mineral to act as bone-targeting therapies. The uptake of these agents occurs preferentially at sites of active osteogenesis meaning that a greater concentration of these agents can occur at osteoblastic lesions and multiple metastatic sites simultaneously [85]. The ionising radiation emitted from the radiopharmaceutics has low tissue penetration and consequently can target the bone metastases with minimal irradiation of adjacent soft tissue. Myelosuppresion is the most serious of adverse side effects that is occasionally seen in addition to the common adverse effects of radiation therapy [86]. The systemic administration of radiopharmaceuticals is limited to certain patients since the majority of cancers require the ablative radiation dose to be targeted and to occur directly at the cancerous tissue over a short time period, with a rapid fall-off in dose to ensure minimal irradiation of healthy tissues [87].

Radiation therapy is a very important treatment strategy for most cancers and although well-established within treatment regimens there is ongoing efforts to design new treatment modalities and ways of delivering radiation. Selective internal radiation therapy (SIRT) is a method that has been employed to treat unresectable hepatocellular carcinoma to great effect. This process involves administering ^{90}Y-doped SiO_2-Al_2O_3 radioactive insoluble glass microspheres that become trapped in hepatic vasculature supplying the tumour. The result of this is the localised delivery of a high dose of radiation directly to the tumour, whilst reducing the exposure to surrounding healthy tissue (see Figure 2.9) [88]. Further work has investigated utilising bioactive glasses as radioisotope vectors for the potential treatment of other types of cancer and for an array of additional therapeutic applications [89]. Ions such as yttrium and strontium can be incorporated into bioactive glasses and exposure to neutron bombardment prior to injection can activate radioactive isotopes such as ^{90}Y and ^{89}Sr. Careful

formulation development is required as neutron activation may cause other elements present within the glass to activate into undesirable radionuclides. The size, shape and bioactivity of bioactive glasses microspheres facilitates their transport and delivery to specific locations and can provide *in situ* radiotherapy.

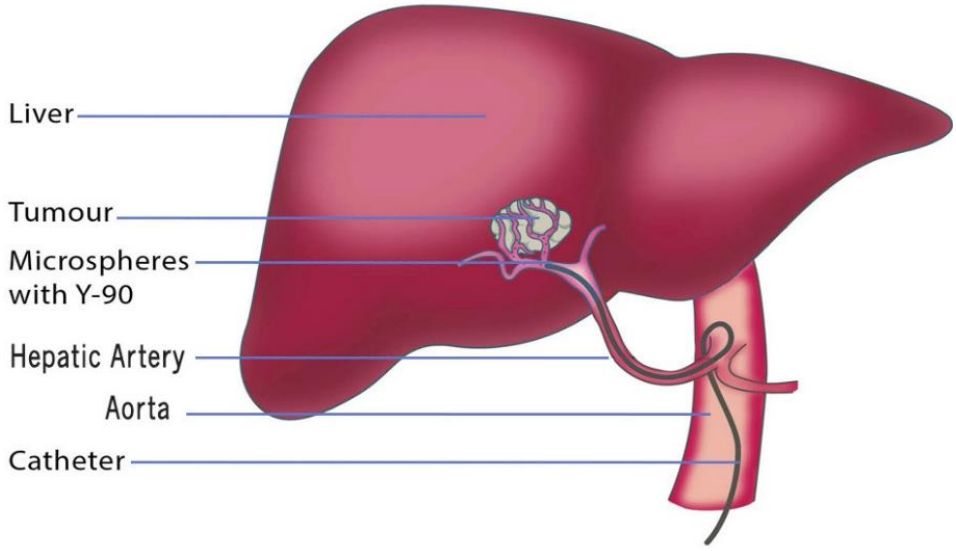

Figure 2.9 Schematic of SIRT and the use of Y-doped microspheres for the treatment of liver cancer. Microspheres are administered via a catheter into the hepatic vasculature. Microspheres emit beta radiation to the kill tumour cells whilst having an embolic effect to further induce tumour apoptosis. [7]

2.8 Bioactive glasses

Since their discovery in 1969 by Hench *et al.* bioactive glasses have been extensively used as the bulk material for producing medical devices for orthopaedic and dental applications and more recently for both hard and soft tissue engineering [90, 91]. The original 45S5 Bioglass® (46.1% SiO_2, 24.4% NaO, 26.9% CaO and 2.6% P_2O_5, in mol%) was found to form strong chemical bonds with host bone tissue without triggering fibrosis. The bioactivity of 45S5 Bioglass® and its ability to bond to bone occurs through a sequence of chemical reactions and the formation of a hydrocarbonate apatite (HCA) layer on the glass surface. The similarity between HCA and bone mineral means that collagen fibrils bond to the HCA and integrate the glass with the bone [92]. This discovery led to a whole field of research into the use of glasses, glass-ceramics and ceramics as bioactive materials in the biomedical field. There are now three main types of bioactive glasses based on their network former: silicate, borate and phosphate-based glasses. The ability to tailor the glass properties by altering the composition of the glass with network modifiers and modifying oxides means that these biomaterials offer a wide range of potential therapeutic applications. Alterations in the glass formulation affect

the glasses physico-chemical and mechanical properties, bioactivity and dissolution rate. New glass formulations have been developed to improve the properties and to enhance the clinical translatability of bioactive glasses in order for them to address specific medical needs and elicit therapeutic responses [93].

In contrast to crystalline solids, glasses have no periodic atomic arrangement and long-range order and are instead organised in a short-range order (see Figure 2.10). This short-range order depends on the glass composition and the addition of network modifying oxides alters the structure of the glass and therefore many of its properties. Glasses are considered amorphous, disordered materials and this gives rise to the unique glass transformation behaviour that all glasses must exhibit [94]. This means that glasses have greater compositional flexibility than crystalline solids, due to the lack of constant and well-defined stoichiometry, meaning that precise compositions can be formulated to produce glasses with specific properties. It is possible to dope glasses with ions by the addition of modifier oxides to the glass composition. Since the structure of the glass directly affects its density, stability, solubility and ion release in an aqueous environment, doping the glass composition with certain oxides allows for the controlled release of ionic species. This is possible to a greater extent when using phosphate-based glasses as opposed to silicate-based glasses. The ability to dope glass formulations with specific ions has been central to the development of bioactive glasses, as their release has the potential to stimulate an array biological processes and therapeutic actions [95].

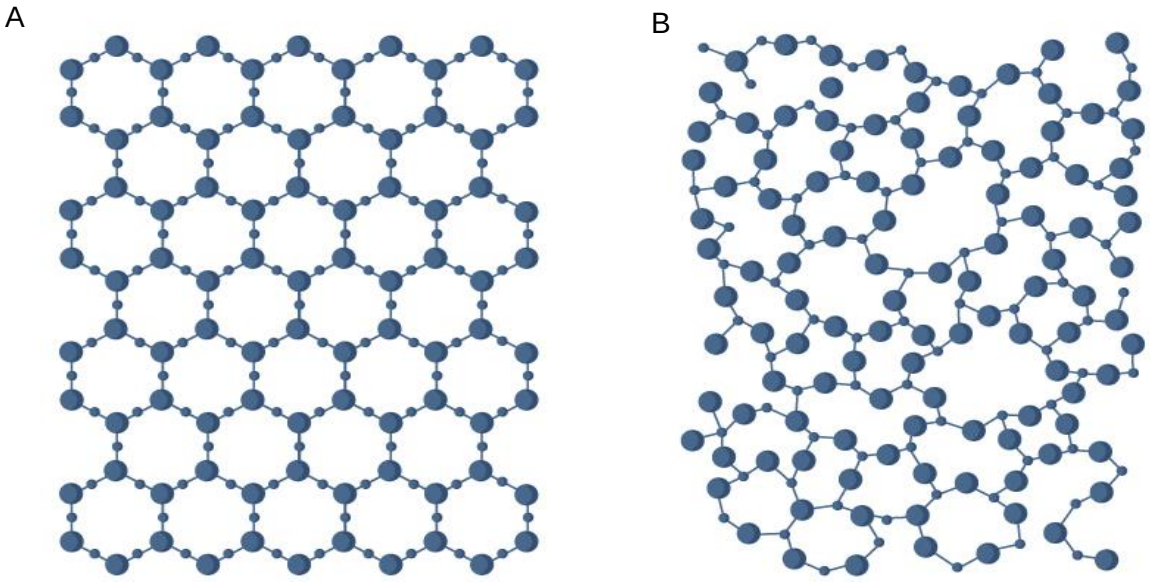

Figure 2.10 Schematic structure of (A) a crystalline solid with periodic atomic arrangement and (B) an amorphous glass with no long-range periodicity. [9]

A major advantage of delivering metallic ions to elicit a cellular response is that they do not suffer from the instability and decomposition issues to the same extent as organic molecules. Ions are known to be essential cofactors of enzymes and can alter cellular functions due to their interactions with other ions, nucleic acids, by directly interacting with ion channels or acting as second messenger molecules [96]. Extraphysiological levels of certain ions can result in toxicity and have detrimental effects on vital homeostatic mechanisms and therefore limits their ability to be administered systemically. The controlled, localised delivery of metallic ions at specific concentrations will improve their selectivity and ability to interact with the desired molecular targets. Bioactive glasses can allow for continuous ion release thereby providing a sustained therapeutic effect throughout the glass degradation.

2.9 Phosphate-based glasses for bone repair and regeneration

Phosphate-based glasses (PBGs) can be formulated to be compositionally similar to the inorganic component of bone and their biocompatibility and the ability to control their degradation profile makes them encouraging materials for hard tissue engineering applications [97]. The primary network former of pure phosphate glass is P_2O_5 but due to its hygroscopic nature, modifying oxides are added to improve the stability and properties of PBGs [94]. The PO_4^{3-} tetrahedral groups are the structural unit of PBGs, where the phosphorous atom is covalently bonded to three oxygens via single bonds and to a terminal oxygen via a double bond. The presence of a terminal oxygen reduces the connectivity of PBGs relative to silicate-based glasses [98]. The P-O-P bonds that form between adjacent tetrahedral are known as bridging oxygens (BOs) and the structure of PBG is related to the number of BO's [98]. Q^n terminology is used to describe the species present within PBGs, where n signifies the number of BO's per PO_4^{3-} tetrahedron [99]. A range of phosphate glass anionic Q^n species can be produced from Q^3, Q^2, Q^1 and Q^0 species which are referred to as ultra-, meta-, pyro- and orthophosphates, respectively (see Figure 2.11) [99].

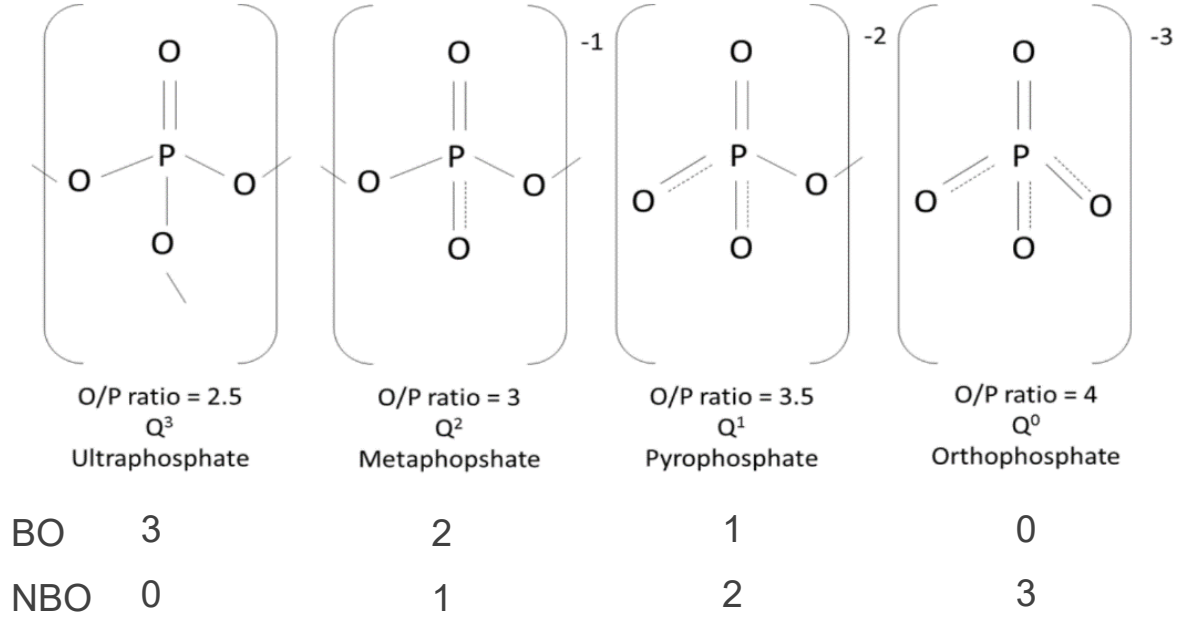

Figure 2.11 The structure of different phosphate Qn species.

PBGs generally degrade faster than silicate-based glasses and altering the glass composition can vary the rates of dissolution by several orders of magnitude [5]. The network connectivity and the arrangement of modifier cations within the glass structure can dictate the dissolution rates of PBGs. The addition of alkali (MeO) and alkaline earth (Me_2O) oxides reduces the network connectivity of the PBGs by decreasing the number of BO's between the PO_4^{3-} tetrahedrons. The modifier oxides reside in the spaces between the PO_4^{3-} tetrahedrons and the ionic strength of the modifiers determines the strength of the bond between them and the network former. The strength of these interactions can have a profound effect on the physical properties of the glass, such as their transparency and heat resistance, as well asthe dissolution rate [100]. The addition of MeO and Me_2O can be used to introduce a controlled amount of therapeutic ions into the phosphate glass composition during the standard manufacturing process. These therapeutic ions are subsequently released upon glass degradation *in vivo* [101]. Careful formulation development can therefore be used to tailor the specific ions as well as the rate in which they are released from PBGs.

The relative ease at which ions of various concentrations with physiological activity and therapeutic properties can be incorporated into PBGs has led to numerous novel formulations being developed and investigated. Single inorganic ions such as calcium (Ca), phosphorous (P) and magnesium (Mg) are vital for bone metabolism and for the growth and mineralisation of bone tissue [19]. Calcium ions are known to promote osteoblast proliferation and

differentiation and activate Ca-sensing receptors on osteoblasts to increase the expression of growth factors, such as IGF-I and IGF-II [102]. Magnesium is essential for the formation of the alkaline phosphatase (ALP) enzyme, which has a vital regulatory role in bone mineralisation. Furthermore, magnesium deficiency has been shown to impede bone growth and increase bone resorption [103]. Additional ions such as strontium (Sr) have also been incorporated into PBGs since Sr has been shown to increase ALP, metabolic activity and differentiation of osteoblasts whilst also inhibiting osteoclast differentiation [104].

The release rate is as equally important as the specific ions that are released during a glasses dissolution *in vivo*. Excessive ion release can lead to local toxicity and increase the likelihood of unwanted off-target effects. This is particularly important when using glasses to deliver radiotherapy in a site-specific manner since leaching of radionuclides can cause irradiation of nearby healthy tissue [89]. The biocompatibility, controllable resorption profiles and the ability to incorporate specific therapeutic ions in PBGs has led to extensive studies into their use as part of treatment strategies for bone repair and regeneration (see Figure 2.12) [105].

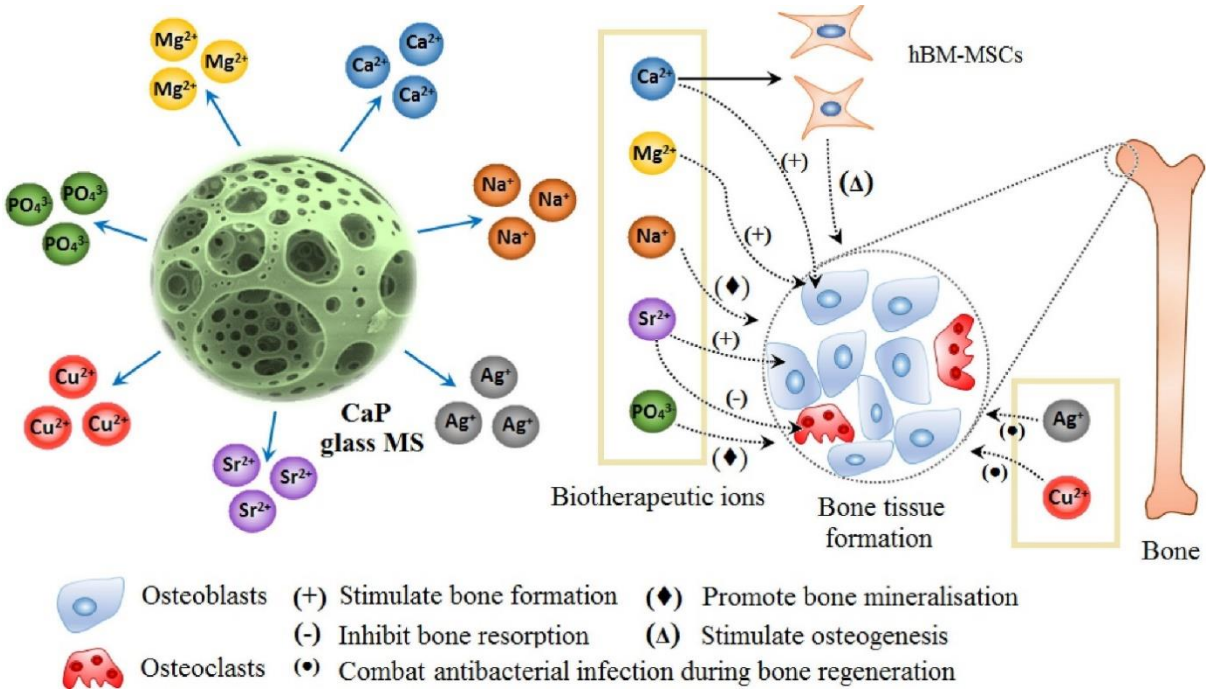

Figure 2.12 The various therapeutic ions that can be doped in phosphate-based glasses and their role in bone tissue formation. [13]

MeO and Me_2O modifying oxide addition subsequently causes a reduction in the structural connectivity and can be used to tailor the phosphate species present with PBGs. Invert

phosphate glasses, that typically contain less than 40 mol% P_2O_5, are primarily composed of pyro- and orthophosphate species and have been shown to have slower degradation rates than ultraphosphate PBGs [106]. Pyro- and orthophosphates are present within the body and are integral to the natural cycle of bone resorption and formation [107]. Although inorganic pyrophosphate (PPi) can inhibit mineralisation by preventing attachment and crystal growth of hydroxyapatite (HA), it has also been demonstrated to promote ALP activity and gene expression [108]. ALP, which is secreted by active osteoblasts, can hydrolyse PPi into orthophosphates causing a loss of PPi inhibition on HA formation whilst simultaneously resulting in the local saturation of orthophosphates that induce mineralisation [109]. As such, development of PBGs that contain these anionic phosphate species could hold significant potential for bone repair due to their intrinsic role in bone mineralisation.

2.10 Microspheres for clinical applications

Bioactive glasses can be synthesised by either melt quenching or sol-gel methods but can be further processed by an array of techniques, such as fibre drawing, additive manufacturing and flame-spheroidisation, into a variety of geometries [110-112]. The different processing techniques allows for bioactive glasses to be fabricated into numerous different practical morphologies. Glass fibres, rods and monoliths, 3D tissue scaffolds and microspheres have all been created using bioactive glasses with the desired morphology relating to the intended clinical application [113].

Microspheres have been extensively investigated for biomedical applications due to their beneficial functional characteristics. Spheres exhibit a greater uniformity in size and shape than irregular-shaped particles and enhanced flow properties. Bioactive glasses microspheres therefore have a more controlled and predictable rate of degradation and subsequent release of incorporated therapeutic ions, as opposed to irregular shaped particles [1]. In addition to this, microspheres have improved delivery properties and the ability to be administered by minimally invasive surgical injections.

Microspheres can be manufactured to be solid, porous and hollow depending on their intended purpose. Porosity further increases surface area which allows for greater cell attachment, encapsulation of bioactive compounds and the flow of nutrients and gases [114]. As a result of this, porous microspheres made from polymers, glasses and glass-ceramics have been developed for cell culture and tissue engineering applications as well as for vehicles for the delivery of therapeutic cargo [115].

Different manufacturing processes can be utilised to create porous microspheres. For polymer based porous microspheres, emulsion-solvent evaporation, phase separation and spray drying have been the most commonly utilised techniques [116]. Various manufacturing processes, such as sol-gel and polymer foam replication, have been used to manufacture porous glass and glass-ceramic microspheres [20]. Many of these techniques are time-consuming and labour intensive due to their multi-step nature and the need to remove residual contaminants. Recent studies have shown that a novel single-stage flame spheroidisation method can be used to produce highly porous calcium phosphate glass microspheres [21].

The flame spheroidisation method involves feeding irregular-shaped particles of ground glass into a flame, where the high temperatures cause the glass to melt. The surface tension as the particles travel through the air results in spheroidisation and the microspheres can be collected following solidification upon cooling (see Figure 2.13) [1]. Numerous parameters and factors in the manufacturing process have been found to influence the microspheres size, surface morphology and chemical composition. The initial particle size, flame temperature, oxygen and fuel flow rates, the residence time of particles in the flame and the porogen used can all be altered to tailor the final microsphere product [117].

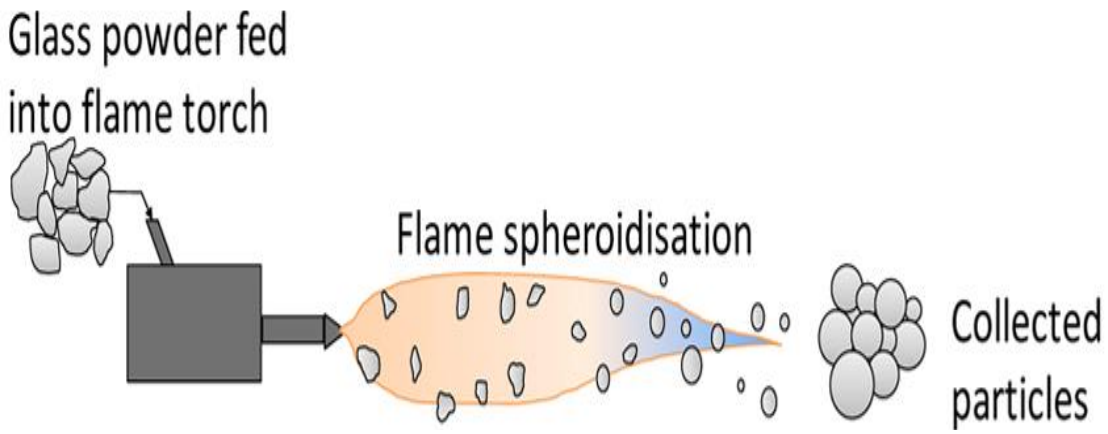

Figure 2.13 Schematic of the flame spheroidisation process used to manufacture phosphate-based glass microspheres. [1]

3 Materials and methodology

3.1 Glass fabrication

The phosphate glasses were prepared using the following precursors: sodium dihydrogen phosphate (NaH_2PO_4), calcium hydrogen phosphate ($CaHPO_4$), calcium carbonate ($CaCO_3$) and magnesium hydrogen phosphate trihydrate ($MgHPO_4 \cdot 3H_2O$) (Sigma Aldrich, UK). The glass compositions and their corresponding codes are presented in Table 4.1. The precursors were weighed according to the composition and mixed thoroughly before being heated in a 5% Au/Pt crucible at 350°C for 30 minutes. This initial heating phase was performed to dehydrate the samples and remove CO_2 and was then followed by melting at 1150°C at a heating rate of 10°C/min and held at this temperature for 90 minutes. The molten glass was then quenched between two stainless plates at room temperature or on plates that had been kept at -20°C for 4 hours prior to casting. Once the glass had cooled it was broken up and ground using a Retsch PM100 milling machine and the ground glass samples sieved to obtain particles in the range of 63 - 125 µm.

3.2 Phosphate-glass microsphere manufacture

Microspheres were processed using a flame spheroidisation method that utilised a thermal spray gun (MK74, Metallisation Ltd, UK). For solid microspheres, ground glass particles in a size range between 63-125 µm were fed through a funnel feeder, containing a 200 µm mesh, into an oxy-acetylene flame at a gas ratio of 3:3. A DC vibratory motor was connected to the funnel feeder to obtain a sufficient flow of particles into the flame and was used for both solid and porous microsphere manufacture. Calcium carbonate ($CaCO_3$) was used as the porogen for porous microsphere manufacture. $CaCO_3$ was sieved into a size range of 45-63 µm and mixed homogenously with the ground glass particles using a bench top vortex mixer in a 1 part glass:3 parts $CaCO_3$ ratio. The glass and porogen was then fed into the flame and collected in the same manner as solid microspheres. Post manufacture, the microspheres were cooled and collected before being sized at 63 µm. The microspheres were then submerged in 5M acetic acid for 120 seconds and then further washed in 1 litre of deionised water for 5 minutes. The solution was then filtered using a funnel and filter paper and dried overnight at 50 °C.

3.3 Yttrium and holmium-containing microsphere manufacture

The P40 phosphate glass was ground using a Retsch PM100 milling machine and sieved into a size range of 45-63 µm. The glass was then mixed with the corresponding ratio of yttrium (III) oxide (ACROS Organics, UK) or holmium oxide (Alfa Aesar, UK) using a benchtop vortex to achieve homogenous mixing of the two components. The glass to yttrium/holmium oxide mixture were processed into microspheres using the flame spheroidisation method that utilised a thermal spray gun (MK74, Metallisation Ltd, UK). The particles were fed into an oxy-acetylene flame at a gas ratio of 3:3. A DC vibratory motor was connected to the funnel feeder to obtain a sufficient flow of particles into the flame. The microspheres were washed with deionised water and left to dry in a 50°C oven overnight. The microspheres were then sieved into a size range of 45 – 125 µm.

Modifications to the materials processing technique were made in attempts to prepare yttrium and/or holmium-containing porous microspheres. These are discussed in more detail in sections 5.2.18 and 6.2.17.

3.4 Characterisation methods

3.4.1 Scanning electron microscopy (SEM)

Morphological analysis of microspheres manufactured from phosphate glass was performed using a JSM-6490LV (JEOL, USA). Representative samples of the microspheres were mounted on carbon tabs attached to aluminium stubs and sputter coated with ~15 nm of platinum under an argon atmosphere.

To examine the internal structures of the microspheres, a sample of microspheres was embedded in cold set epoxy resin. The resin blocks were polished using SiC paper followed by a polishing cloth embedded with diamond paste down to 1µm whilst using Industrial methylated spirit (IMS) (Sigma Aldrich, UK) as a lubricating medium. The resin block was placed in an ultrasonic bath of IMS for 5 minutes and left to dry. The samples were then splutter coated using a Quorum Q150V (Quorum, UK) with 15 nm carbon or sputter coated with ~15 nm of platinum under an argon atmosphere.

3.4.2 Size analysis

Image J was used on the acquired SEM images to analyse microsphere size. A threshold was applied to the SEM images to remove background and to select microspheres based on their

sphericity. Particles at the border of the images and any that overlapped were not selected for quantification.

3.4.3 Field-Emission Gun Scanning Electron Microscopy

Image acquisitions for higher resolution scans were conducted on a Field-Emission Gun Scanning Electron Microscope (FEG-SEM) using a JEOL 7100 FEG-SEM (JEOL, USA). Samples were prepared the same as section 3.4.1.

3.4.4 Focused-Ion Beam Scanning Electron Microscopy

Focused-Ion Beam Scanning Electron Microscopy (FIB-SEM) was performed on a Zeiss Crossbeam 550, imaging was performed at a range of accelerating voltages from 2kV to 5 kV. Gallium ion beam milling was performed at an accelerating voltage of 30kV and currents from 300pA to 3nA. Elemental analysis (EDX) was performed using an Oxford Instruments X-Max 170 detector running Aztec 5 software. Samples were mounted on carbon tabs attached to aluminium stubs and sputter coated with ~15nm of carbon using a Quorum Q150V (Quorum, UK).

3.4.5 Energy dispersive X-ray spectroscopy (EDX)

Compositional analysis was performed on ground glass samples and on solid and porous microspheres. Samples were mounted on carbon tabs attached to aluminium stubs and sputter coated with carbon using Q150T Turbo-Pumped Sputter Carbon Coater (Quorum, UK). An Oxford Instruments INCA EDX system fitted with a Si-Li crystal detector was attached to the JSM-6490LV SEM and operated with an accelerating voltage of 15kV and a working distance of 10mm for EDX analysis.

3.4.6 Powder X-ray diffraction (XRD)

A Bruker D8 Advanced X-ray diffractometer (Bruker-AXS, Karlsruhe, Germany) was used to determine the amorphous/crystalline nature of the ground phosphate glass samples and both solid and porous microspheres at room temperature using a Ni-filtered Cu-Kα radiation source. Data points were obtained every 0.02° from 10-70° over a 10 minute period. The resulting data was analysed using DIFFRAC.EVA software (DIFFRAC-plus suite, Bruker-AXS) to identify phases through a database of known peaks from the International Centre for Diffraction Data (ICDD) database 2015.

3.4.7 Differential thermal analysis (DTA)

Approximately 40 mg of each glass composition were heated in platinum pans within a simultaneous thermal analysis (SDT, TA Instruments SDT Q600, New Castle, DE, USA) instrument from 40°C to 1000°C at a ramp rate of 10°C min^{-1} and a flow rate of 100ml min^{-1} nitrogen gas. An empty pan measurement was performed before a glass sample was run to obtain a baseline which was then subtracted from the thermal traces obtained using TA universal analysis 2000 software. The glass transition temperature (Tg), crystallisation temperature (Tc), melting temperature (Tm) and processing window (Tc onset - Tg onset) of each glass sample was determined using the thermal traces.

3.4.8 Density

The density of each sample was measured using Micromeritics AccuPyc 1340 pycnometer, with helium as the displacement gas. For each measurement, a series of repeat readings were taken until a series of five results agreed within an error of ± 0.02 g cm^{-3}.

3.4.9 NMR experiments

Quantitative 1D ^{31}P spectra were recorded at room temperature on a Varian Chemagnetics Infinityplus spectrometer at a Larmor frequency of 121.47 MHz, using a 4 mm zirconia MAS probe spinning at approximately 10 kHz. The ^{31}P 90° pulse duration was 3.5 µs, the spectral width was 100 kHz and the acquisition time was 10.24 ms. Chemical shifts are quoted relative to 85% H_3PO_4 in H_2O, using $Na_4P_2O_7{\cdot}10H_2O$ as a secondary reference. The resulting spectra were deconvoluted into a series of Gaussian lineshapes, which were integrated to quantify the relative proportions of the Q^n sites. Deconvolution and fitting were achieved using a routine written in MATLAB and included 1st and 2nd order sidebands.

^{31}P 2D exchange spectra were recorded at room temperature on a Varian Chemagnetics Infinityplus spectrometer at a Lamor frequency of 121.47 MHz, using a zirconia 4 mm MAS probe spinning at approximately 10 kHz. The dipolar coupling was recoupled by irradiation of rotor-synchronised 180° pulses during the mixing time, which was varied between 0 and 18 ms. The mixing time was an integral number of rotor periods, t_R, where t_R = (spinning frequency)$^{-1}$, which was typically ~ 100 µs. t_1 was incremented from 0 to 96 µs, with 8 scans per increment. The acquisition time was 40.96 ms, and the pulse lengths were 3.88 µs for 90° pulses and 7.75 µs for 180° pulses. To make the 2D experiment feasible, a saturation recovery was performed at the beginning of the pulse sequence, to ensure the reproducibility of the

magnetisation for each experiment. The saturation pulses were 20 ms long, and the recovery delay was 85 s.

3.4.10 Fourier transform infrared spectroscopy (FTIR) analysis

Infrared spectroscopy of the glass particles was performed using a Brüker Tensor 27 Fourier transform infrared spectrometer (Brüker Optics,Germany) which was operated in absorbance mode. Glass samples were ground to a fine powder using a Retsch PM100 milling machine and glass microspheres using a mineral pestle and mortar. Spectra were measured in the region of 400 to 6000 cm^{-1} utilising a Standard Pike ATR cell (Pike Technologies, Inc.,UK). OPUS software version 5.5 was used for the analysis.

3.4.11 Raman analysis

Confocal Raman microscopy was performed using a HORIBA LabRAM HR Raman microscope. Spectra were acquired using either a 532 or 660 nm laser (at ~20 mW power), a 100x objective and a 200 µm confocal pinhole. To simultaneously scan a range of Raman shifts, either a 600 or 300 lines mm^{-1} rotatable diffraction grating along a path length of 800 mm was employed. Spectra were detected using a Synapse CCD detector (1024 pixels) thermoelectrically cooled to −60 °C. Before spectra collection, the instrument was calibrated using the zero order line and a standard Si(100) reference band at 520.7 cm^{-1}. The spectral resolution is better than 1.5 cm^{-1} (532 nm laser, 600 lines mm^{-1} grating) and 2.4 cm^{-1} (660 nm laser, 300 lines mm^{-1} grating) in the respective configurations.

For each glass formulation, point spectra were acquired over the range 200-1700 cm^{-1} with 15-60 s integration time and four accumulations to automatically remove the spikes due to cosmic rays and improve the signal to noise ratio. Where multiple spectra were obtained, these were then averaged to give a mean.

For the yttrium and holmium-containing microspheres, multiple spectra were collected (0.01^{-2} s integration time, 1 accumulation, 200-1700 cm^{-1}) in 1 µm steps from within a 20x20 µm area (441 spectra). The spatial resolution (xyz) is ~1x1x5 µm in this configuration. Surface topography was corrected using AutoFocus and ViewSharpTM functionalities. Spectra were manually despiked to remove artefacts. At least three maps were collected from each sample with both 660 and 532 nm lasers to evaluate the microsphere-to-microsphere homogeneity.

Images were generated by plotting the intensity ratio (as peak area) of peaks associated with the cubic phase of Y_2O_3 (377 cm^{-1}, 345-410 cm^{-1}, Raman-active Ag mode) relative to the phosphate glass (965 cm^{-1}, 910-1020 cm^{-1}, Raman-active PO_2 symmetric stretching mode of

non-bridging oxygens in Q^0 units). The images were scaled to the minimum and maximum values and false coloured using the hot colour palette.

3.4.12 X-ray Photoelectron Spectroscopy

X-ray photoelectron spectroscopy (XPS): Samples were analysed using the Kratos AXIS ULTRA with a mono-chromated Al kα X-ray source (1,486.6 eV) operated at 10 mA emission current and 12 kV anode potential (120 W.) Spectra were acquired with the Kratos VISION II software. A charge neutralizer filament was used to prevent surface charging. Hybrid slot mode was used measuring a sample area of approximately 300 µm × 700 µm. The analysis chamber pressure was better than 5×10^{-9} mbar. Three areas per sample were analysed. A wide scan was performed at low resolution (Binding energy range 1,400 to −5 eV, with pass energy 80 eV, step 0.5 eV, and sweep time 20 min). High resolution spectra at pass energy of 20 eV, step of 0.1 eV, and sweep time of 10 min each were also acquired for photoelectron peaks from the detected elements and these were used to model the chemical composition. The spectra were charge corrected to the C 1s peak set to 284.5 eV.

3.4.13 Ion release studies

Ion release profiles of the microspheres were determined by immersing 400 mg of microspheres in 40 mL of ultrapure (Milli-Q) water at 37°C. The dissolution medium at each time point (3, 7, 14, 21, and 28 days) was extracted via filtration and replaced. The concentration of sodium, phosphate, calcium, magnesium, yttrium and holmium ion release was analysed using inductively coupled plasma mass spectrometry (ICP-MS, Thermo-Fisher iCAP-Q model). The pH of the solutions was measured at each time point using a pH electrode InLab Pure Pro-ISM (Mettler Toledo, UK).

3.4.14 Bioactivity studies

Simulated body fluid (SBF) was prepared according to ISO 23317:2014. The apatite forming-ability of the bioactive glass particles within this study was performed using the TCO4 method. 75 mg of phosphate-based glass microspheres and particles of 45S5 Bioglass were immersed in 50 mL SBF within Falcon tubes. The tubes were placed on an orbital shaker and agitated at 120 rpm whilst in a 37°C incubator. The samples were incubated for different time points: 3, 7, 14, 21 and 28 days. At the end of each time point, the sample was removed from the solution by filtration using 20 µm filter paper. The particles were washed with DI water and the subject to post-immersion characterisation testing involving and SEM, XRD and EDX.

A Bruker D8 Advanced X-ray diffractometer (Bruker-AXS, Karlsruhe, Germany) was used to determine the amorphous nature of the ground phosphate glass samples at room temperature using a Ni-filtered Cu-Kα radiation source. Data points were obtained every 0.01° from 5-70° over a 4 hour period with a step size of 2.2 seconds. The resulting data was analysed using DIFFRAC.EVA software (DIFFRAC-plus suite, Bruker-AXS) to identify phases through a database of known peaks from the International Centre for Diffraction Data (ICDD) database 2005.

3.4.15 Microspheres sterilisation and preparation of conditioned media

Sterilisation of microspheres was performed using two washes of 10 minutes with 100% ethanol followed by complete evaporation at room temperature overnight in sterile conditions. For the preparation of conditioned medium containing microsphere ion extracts for MG63 cells, 100 mg/ml of sterile microspheres were incubated in standard cell culture medium (SM) (DMEM supplemented with 10% foetal calf serum, 1% penicillin and streptomycin, 1% L-Glutamine, 1% of non-essential amino acids, 1.5% ascorbic acid, Thermofisher, UK) at 37 °C and 5% CO_2. The conditioned media containing microsphere ion extracts were collected and replaced with equal volume of fresh medium every 48 hours. Before being administrated to the cells, the solutions were filtered through 0.22 µm syringe filters to remove any debris or precipitate.

3.5 *In vitro* cell culture studies

3.5.1 Indirect cell culture studies

For the indirect culture method with microsphere-conditioned media, the human osteoblast-derived cell line MG63 (obtained from European collection of cell cultures - ECACC) were seeded at a density of 10,000 cells/cm^2 in 300 µl of standard cell culture medium in 48-well plates. 48 hours after seeding, cells were washed with PBS and 300 µl of the appropriate conditioned media was added. Cells cultured with either unconditioned standard medium (+ve), or standard cell culture medium supplemented 5% DMSO (-ve) were used as controls. All media was refreshed every 48 hours. Two independent biological replicates were performed with 3 experimental replicates for each condition.

3.5.2 Direct cell culture studies

For direct seeding of cells onto the porous PBG microspheres, MG63 cells were seeded at a density of 10,000 cells/cm^2 onto 10 mg sterilised microspheres from each formulation into low-adherent 48-well plates previously coated with 1% (w/v) solution of poly(2-hydroxyethyl methacrylate) (poly-HEMA, Sigma-Aldrich, UK) and ethanol 95% in 300 µl of standard cell culture medium. Cells were cultured for 7 days at 37 °C and 5% CO_2. The media was refreshed every 48 hours.

3.5.3 Cell metabolic activity

Cell metabolic activity of MG63 cells was evaluated at days 2 and 7 using Alamar Blue assay. Three hundred µL of Alamar Blue solution (1:9 Alamar blue:Hanks Balanced Salt Solution) was added to each well and incubated for 90 min at 37°C and 5% CO_2 followed by further 10 min on a shaker at 150 rpm. For each condition, three aliquots of 100 µl were transferred to a 96-well plate. FLx800 fluorescence microplate reader (BioTek Instruments Inc.) was used to measure fluorescence at 530 nm excitation and 590 nm emission wavelengths.

3.5.4 Alkaline phosphatase (ALP) activity

At day 7, cells were washed three times with warm (37ºC) PBS and immersed in 1 ml of deionised water. Samples were freeze-thawed three times to lyse the cells and release nuclear content. The Granutest 25 ALP assay (Randox, UK) was used to measure ALP activity in MG63 cells. Three aliquots of 50 µl of cell lysate were transferred to a 96-well plate and topped with 50 µl of ALP substrate (p-nitrophenyl phosphate 10 mM in diethanolamine buffer 1 mM at pH 9.8, with $MgCl_2$ 0.5 mM). Plates were shaken gently for 5 min on a plate shaker, and absorbance was measured at wavelength of 405 nm using an FLx800 microplate colorimeter (BioTek Instruments), every 5 minutes for 45 minutes until the readings became constant. The same process was used for cells grown in both in indirect and direct culture.

3.5.5 DNA content assay

Lysed cell samples used to measure ALP activity were thoroughly mixed using a vortex for 30-60 seconds and 100 µl of each sample was aliquoted into a 96-well plate. Hoechst 33258 stain was prepared (1 mg of BisBenzimide stain dissolved in 1 ml of double distilled water and diluted to 1:50 in TNE buffer) and DNA standards were prepared using calf thymus DNA (Sigma, UK) and TNE buffer (10 mM Tris, 2M NaCl, and 1mM EDTA in deionised water, adjusted to pH 7.4) as a diluent, to generate a standard curve for DNA concentrations. One

hundred µl of Hoechst 33258 stain was added to each well and mixed on plate shaker for 5 minutes at 150 rpm. FLx800 plate reader (BioTek Instruments) was used to read the plate at excitation 360 nm, emission 460 nm.

3.5.6 Statistical analysis

Two independent experiments were performed, and results are shown as mean ± standard error of mean (unless otherwise stated). Statistical analysis was performed using Prism software package (version 9.2.0, GraphPad Software, San Diego, CA, www.graphpad.com). Two-way analysis of variance was calculated followed by a Tukey's multiple comparison test. The mean difference was considered to be significant at 0.05 and 95% confidence interval.

3.5.7 Cell imaging

In the indirect study, bright-field images of living cells were taken on day 2 using an EclipseT2 Nikon microscope coupled with a D3300 Nikon camera.

For imaging of cell attachment to microspheres, at day 7 the MG63s were washed three times with warm (37°C) PBS and fixed with 4% paraformaldehyde for 10 minutes. Fixative was then removed, and the sample washed twice deionised water. For Environmental Scanning Electron Microscopy (ESEM), post fixed cells were analysed using a FEI Quanta 650 ESEM microscope.

3.5.8 Proteomic profiling by LC-MS/MS

The indirect culture method with either P40, 30Y or 30H solid microsphere-conditioned media was performed using MG63 cells seeded at a density of 10,000 cells/cm^2 in 3 ml of standard cell culture medium in a 6-well plates. Forty eight hours after seeding, cells were washed with PBS and 3 ml of the appropriate conditioned media was added. All media was refreshed every 48 hours. After 7 days of culture in conditioned media, media was removed, and cells were washed three times with PBS prior to being pelleted at 1200 rpm for 4 minutes. Cell pellets were washed a further three times with PBS before removal of any supernatant and storage at -20 °C.

Cell pellets were solubilised in sodium dodecyl-sulfate polyacrylamide gel electrophoresis (SDS PAGE) loading buffer and subjected to tryptic digestion using sequencing-grade trypsin. 20 ug aliquots of the whole proteome in Coomassie-stained polyacrylamide gel slices were

separated by tandem mass spectrometry (MS/MS) on an LTQ-Orbitrap-Velos spectrometer (ThermoScientific, Wilmington, USA) with nano-flow liquid chromatography (Dionex Ltd, Camberley, UK). Proteome Discoverer (version1.4.0.288, ThermoScientific, Wilmington, USA) was used to process the raw data file obtained from the LC-MS/MS acquisition. The file was then searched using Mascot (version2.2.04, MatrixScienceLtd, Marylebone, London,UK) against the UniProt Human_2018_03 database. Peptides were identified in data-dependent mode combining Mascot and X! Tandem search engines to validate MS/MS assigned spectra from Proteome Discoverer. The peptide and MS/MS tolerance were set to 10 ppm and 0.02 Da, respectively. Fixed modifications were set as alkylation of cysteine, and variable modifications set as deamidation of Asn and Gln, and oxidation of Met and Pro residues. Peptides were identified at greater than 95% probability, with a minimum of two peptides required for protein identification.

3.6 Doxorubicin loading and release

3.6.1 Drug encapsulation process

Fifty µg/ml of Doxorubicin (DOX) drug was dissolved in phosphate buffered saline (PBS). 50 mg of 125 - 200 µm P40 and P30 porous microspheres were added to DOX-PBS solution and placed on an orbital shaker at 300 rpm for 24 hours at room temperature. After 24 hours, the supernatant was removed using a pipette and the DOX-loaded microspheres dried in a 37°C oven for 24 hours. The supernatant was scanned at different wavelength within the range of 200–800 nm by UV–vis spectroscopy, and the maximum absorption wavelength of DOX in PBS was found at 475 nm, which correlated well with the literature [118]. As a result, the standard curve was drawn in the range of 0-100 µg/ml and determined the DOX concentration using a wavelength of 475 nm. The standard curve showed a linear (R^2 = 0.999) relationship between absorbance and concentration of DOX. The relationship in the standard cure was as follows:

$$Abs = 0.017C + 0.016$$

where Abs is the absorbance of DOX, C is concentration of DOX.

The concentration of unloaded DOX was determined by measuring the absorbance of the supernatant after centrifugation.

3.6.2 Encapsulation efficiency

The encapsulation efficiency was determined by comparing the difference in concentration of DOX-PBS solution before and after loading. The encapsulation efficiency of DOX in porous microspheres was calculated according to the following equation.

$E= (M_i-M_r)/M_i \times 100\%$

Where M_i represents the initial amount of DOX and M_r is the residual amount of DOX after drug loading.

3.6.3 Drug release profiles

The DOX-loaded microspheres were immersed in 4 ml PBS solution (pH 7.5) at 37°C and placed on an orbital shaker at 200rpm. At each predetermined time point (1, 2, 4, 8, 24 and 48 hours), 2 ml of DOX-PBS solution was removed from the test sample to analyse the concentration of DOX and replenished with 2 mL of fresh PBS. The supernatant was centrifuged and the concentration of released drug in the collected solutions were determined via UV-vis spectroscopy (λ = 475nm). Finally, cumulative concentration of DOX released from porous microspheres was calculated based on the following equation.

$$Ctcumu = Ct + \frac{v}{V}\sum_{0}^{t-1} Ct$$

Where Ct_{cumu} is the cumulative concentration of DOX, C_t is the actual concentration at time t, v is volume of being collected at time t, and V is the total volume of PBS medium.

3.6.4 Drug release kinetic models

Several mathematical kinetics models were used to describe the drug release kinetics to analyse *in vitro* drug release data. The model dependent approaches included zero order, first order, Higuchi and Korsmeyer-Peppas.

3.6.5 Zero order model

Zero order kinetics can be described the system where the rate of drug release is independent of its concentration. The release of the drug which followed first order kinetics can be expressed by the equation.

$\log C = \log C_0 – K_1t / 2.303$

where C_0 is the initial concentration of drug and K_1 indicates first order rate constant.

3.6.6 Higuchi model

The Higuchi model is considered one of the most widely used drug release equations to understand drug release mechanisms, such as dissolution or diffusion. The Higuchi equation can be represented in the simplified form:

$$Q=K_H \times t^{1/2}$$

where Q is the cumulative drug release at time t and K_H is the Higuchi dissolution constant.

3.6.7 Korsmeyer-Peppas model

After determining that the primary mechanism of drug release (diffusion or dissolution) from the Higuchi plot, the next step is to determine the sort of diffusion the drug follows. The empirical equation provided by Korsmeyer and Peppas was used to fit the release data. The equation is as follows:

$$M_t/M\infty = K_{kp}t^n$$

where Mt/M∞ is a fraction of drug released at time t, K_{kp} is Korsmeyer-Peppas constant and n is release exponent.

3.6.8 Cryosectioning

DOX-loaded porous microspheres were placed into cryosectioning molds, covered with OCT embedding medium (Thermo Scientific) and frozen. 50µm sections were cut using an Accu-Edge low-profile blade (Sakura) within a Cryostat CM 3050S (Leica) and collected on slides to allow for confocal laser microscopy.

3.6.9 Confocal Laser Scanning Microscopy

A Zeiss ELYRA PS.1 Laser Scanning Confocal Imaging System (LSM 780), equipped with a 405 nm laser, was used to observe the distribution of drug within the microspheres. EC Plan-Neofluar 10x/0.30 M27 objective was used. Dichroic was 488/561, and emission range was detected between 569-633nm. The software used for the Confocal Laser Scanning Microscopy imaging and analysis was Zeiss Zen Black 2012 SP5.

4 Developing porous ortho and pyrophosphate microspheres

4.1 Introduction

Early biomaterials used for hard tissue engineering applications were commonly designed to be bioinert and were created with the primary intention of being able to endure the physiological stress of having cells cultured on or within them and their implantation into the body [119]. These materials were not designed to stimulate any specific cellular response and have had limited clinical success. As a greater understanding of the cellular microenvironment has developed and appreciation of the role that its constituent parts play in cell behaviour, so has the function of biomaterials. Nowadays, biomaterials to facilitate bone repair and regeneration are developed by rational design to provoke specific, desired, biological responses [120]. The incorporation of additional therapeutic cargo within or onto the biomaterial can further dictate their ability to manipulate and influence cell behaviour and tissue formation.

For bone regeneration specifically designed, highly porous biomaterials have been shown to facilitate the growth and proliferation of osteoprogenitor cells and the incorporation of bioactive molecules can promote further differentiation and proliferation. The materials are designed to stimulate the formation of new and functional bone tissue [121]. The role of these materials is to facilitate the restoration of the tissue structure and function therefore allowing an overall improvement in the state of the affected tissue [122]. Certain biodegradable materials are of particular interest since their breakdown *in vivo* can stimulate the body to repair and regenerate by its own intrinsic mechanisms and circumvents issues around surgical retrieval of permanent implants. These materials can promote specific biological processes, such as osteoinduction and angiogenesis, which are essential for new tissue growth at sites of trauma and disease [123].

Phosphate-based glasses (PBGs) can be formulated to be compositionally similar to the inorganic component of bone and their biocompatibility and the ability to control their degradation profile makes them encouraging materials for hard tissue engineering applications [97]. In order for PBG microspheres to become an effective material for bone repair and regeneration, a detailed understanding of the physio-chemical and structural properties, their interactions with cells, as well as the degradation and their long-term effects in the body are required [124]. This chapter explores in detail the characterisation of different

PBG formulations as candidates for bone repair and regeneration. A novel processing technique has been employed to produce solid and porous microspheres from the PBG and the structural and physiochemical properties of the microspheres has been explored. The cellular response of osteoblast-like cells using an indirect and direct cell culture was used to investigate the cytocompatibilty and osteogenic potential of the porous microspheres. Processing the PBG into porous microspheres offers the potential to load the microspheres with therapeutic cargo that can be locally delivered at sites damaged by bone cancer and its subsequent treatment. Studies involving the loading and release of Doxorubicin (DOX) from porous microspheres were performed to ascertain their suitability of vehicles capable of delivering localised chemotherapy.

4.2 Results

4.3 Glass characterisation

4.3.1 EDX Analysis

Quaternary phosphate glasses in the series $xP_2O_5{\cdot}(56\text{-}x)CaO{\cdot}24MgO{\cdot}20Na_2O$ (mol%), where *x* is 40, 35, 32.5 or 30, were produced using a traditional melt-quenching process. The MgO and Na_2O content remained constant throughout the glass compositions, whereas the P_2O_5 content was decreased with a subsequent increase in CaO (mol %) (see Table 4.1 for formulations produced and corresponding glass codes used through the chapter and thesis).

EDX was used to confirm the amount of each of the elements present within the glasses made and to compare them to their expected theoretical value. This analysis confirmed that the glass formulations produced were within ±1.5% of the target mol%.

Table 4.1 Compositions of the phosphate-based glass formulations investigated using EDX analysis alongside their corresponding glass codes used.

Glass codes	P_2O_5 (Expected/Actual value) (mol%)	CaO (Expected/Actual value) (mol%)	MgO (Expected/Actual value) (mol%)	Na_2O (Expected/Actual value) (mol%)
P40	40 / 38.7 ± 1.3	16 / 16.3 ± 1.1	24 / 24.9 ± 1.5	20 / 20.1 ± 1.2
P35	35 / 33.7 ± 0.4	21 / 20.0 ± 0.5	24 / 26.1 ± 0.1	20 / 20.3 ± 0.2
P32.5	32.5 / 30.1 ± 0.1	23.5 / 22.5 ± 0.2	24 / 27.6 ± 0.2	20 / 19.7 ± 0.2
P30	30 / 28.8 ± 0.1	26 / 24.7 ± 0.2	24 / 26.3 ± 0.3	20 / 20.3 ± 0.1

4.3.2 XRD Analysis

The XRD spectra for P40, P35, P32.5 and P30 glass compositions are shown in Figure 4.1. A single broad halo peak at 2θ values of ~30-32° was observed and the absence of any detectable crystalline peaks confirmed the amorphous nature for each of the glass compositions produced.

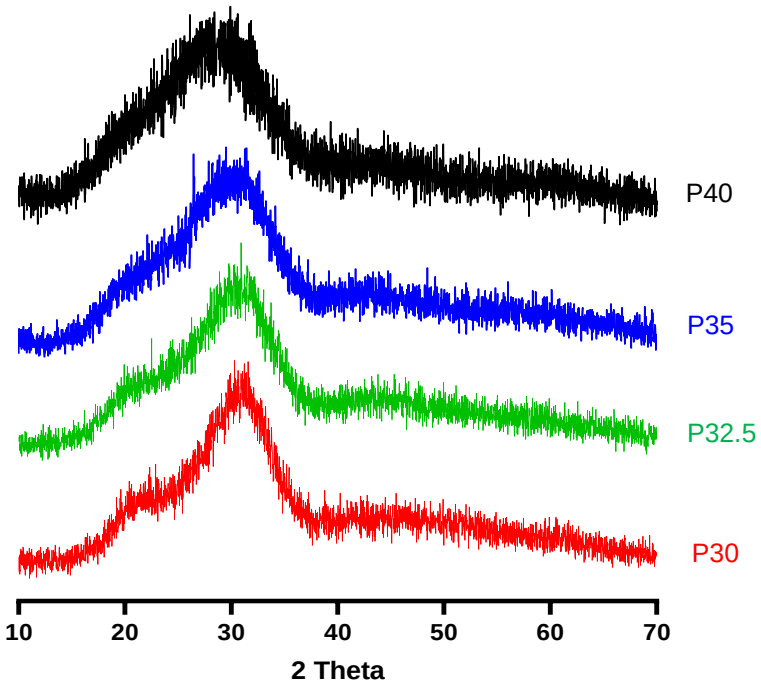

Figure 4.1 Powder XRD patterns of the four phosphate glass compositions. P40 (black), P35 (blue), P32.5 (green) and P30 (red).

4.3.3 Thermal Analysis

The Differential scanning calorimetry (DSC) traces of the starting glasses explored are shown in Figure 4.2 below along with their corresponding glass transition (T_g), crystallisation (T_c), melting temperature (T_m) and the calculated thermal processing window (i.e. T_c onset – T_g).

An increase in the T_g temperature from 434 °C to 472 °C to 486 °C was observed from P40 to P35 to P32.5, after which a slight reduction to 482°C was seen for the P30 glass. The increase in T_g may arise from structural cross-linking between the shorter phosphate chains in the lower phosphate content glasses that contain a greater amount of CaO. No apparent trend was

observed for the T_c values which were seen to decrease from 573°C in P40 glass to 526°C for P35 but then increased to 586°C for P32.5°C, with a subsequent decrease to 566°C for P30 glass. Multiple T_c peaks in P32.5 and P30 glass suggested the presence of several phases. The melting peaks for P40 and P35 were less well-defined and reduced in area compared to the other two glass compositions. Moreover, P32.5 exhibited a sharp singular peak at 831°C, whereas P30 displayed two melting peaks at 789°C and 822°C.

The P30 glass formulation had the greatest tendency to crystallise during glass manufacture and as a result had to be splat quenched onto steel plates that had been refrigerated at 4°C during the melting process. This caused the glass to cool more rapidly and prevent it from surface crystallisation. Despite P35 having a smaller thermal processing window than P32.5 (see Figure 4.2), P32.5 had a greater tendency to crystallise than P35 and was therefore also splat quenched between the two steel casting plates.

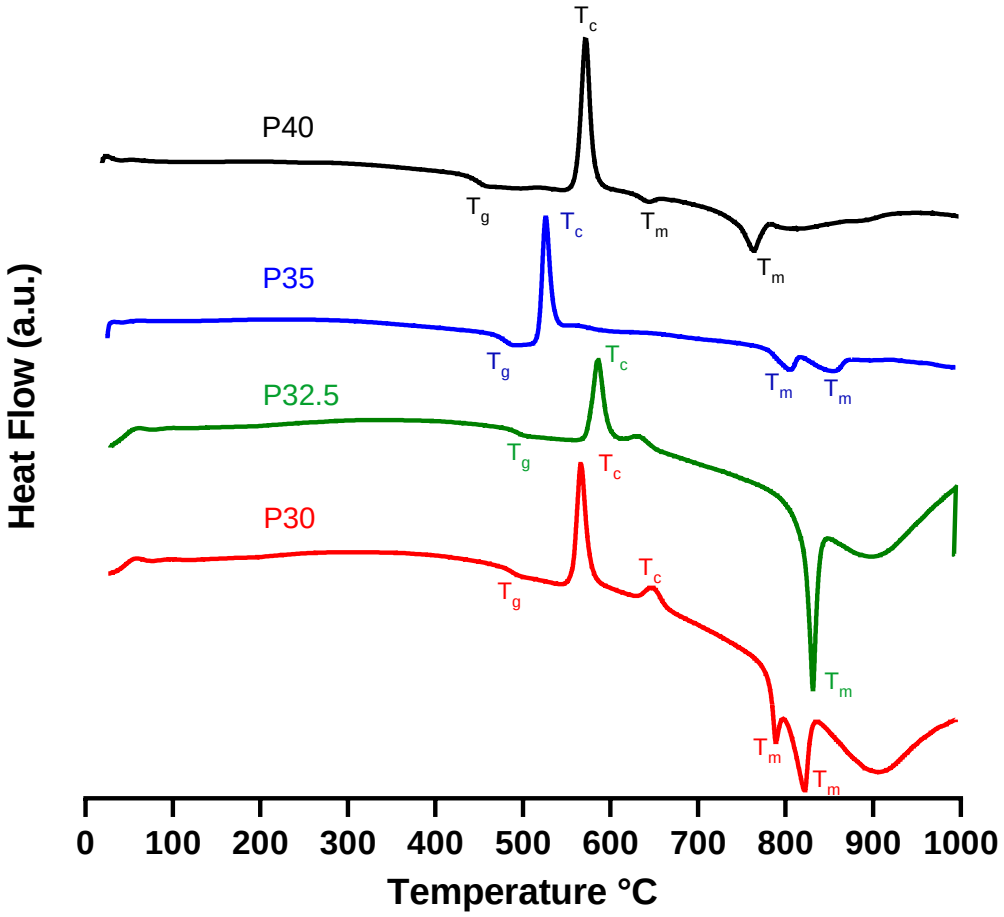

Sample	T_g		T_c		Processing window	T_m	
	Onset	Mid	1	2	(T_c onset – T_g onset)	1	2
P40	434	463	573		139	645	765
P35	472	486	526	564	54	804	854
P32.5	486	498	586	633	100	831	
P30	482	495	566	649	84	789	822

Figure 4.2 DSC thermal analysis profiles of P40, P35, P32.5 and P30 glass. Table below highlights Tg, Glass transition temperature, Tc, Crystallisation temperature, Tm, melting temperature as well as the processing window values for each formulation.

4.3.4 Density

Density of ground glass particles and $CaCO_3$ (which was used as the porogen) were obtained via helium pycnometry. P40 glass had the highest density at 2.71 g/cm^3. The density then decreased as the phosphate content of the glass decreased within the series from P40 to P30. The density of P32.5 and P30 was identical to each other and to $CaCO_3$ (see Table 4.2). Acquisition of glass density was performed to identify whether discrepancies in density between formulations may have resulted in different outcomes following spheroidisation.

Table 4.2 Density measurements of ground glass particles and $CaCO_3$ acquired using a helium pycnometer.

Material	Density (g/cm^3)
P40	2.71 ± 0.0018
P35	2.31 ± 0.0018
P32.5	2.12 ± 0.0035
P30	2.12 ± 0.0008
$CaCO_3$	2.12 ± 0.0014

4.4 Microsphere characterisation

4.4.1 Morphology confirmation of the microspheres produced

SEM analysis was performed to confirm the morphology of the microspheres following spheroidisation. To obtain solid microspheres, particles of ground glass in the size range of 63-125 µm were fed into the hottest region of the oxy-acetylene flame. Cross-sectional SEM images of resin embedded microspheres confirmed that the microspheres were solid and lacking porosity throughout (see Figure 4.3E – H).

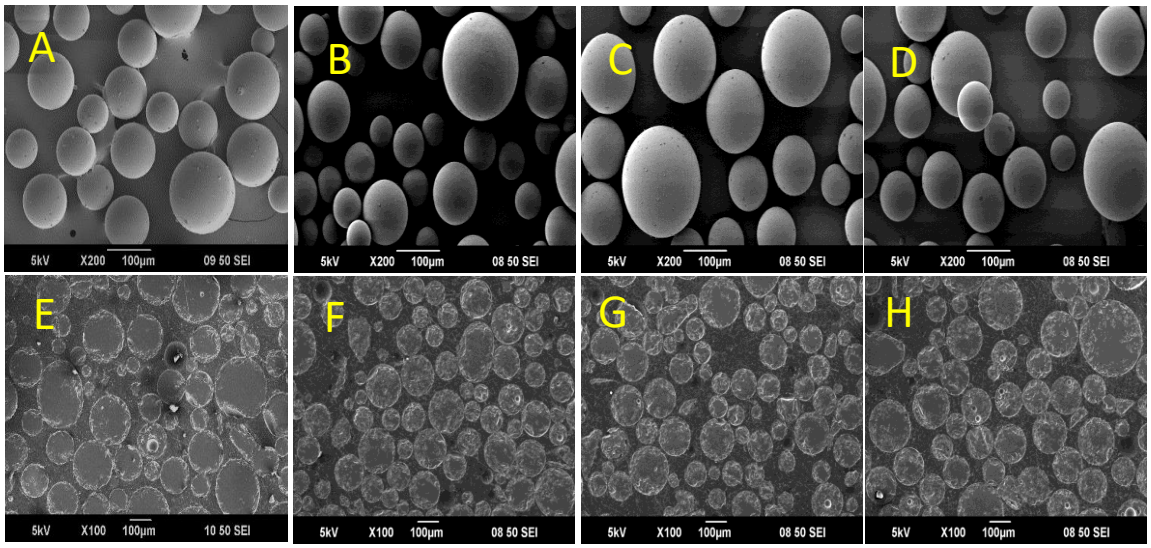

Figure 4.3 SEM images of the morphology of the solid microspheres and their cross section. (A & E) P40, (B & F) P35, (C & G) P32.5 and (D & H) P30.

Calcium carbonate ($CaCO_3$), in the range of 45-63 µm, was used as the porogen material and was homogenously mixed with the ground glass particles prior to entry into the flame to produce porous microspheres. As seen from the SEM images in Figure 4.4 below, $CaCO_3$ proved to be an effective porogen for producing a high yield of highly porous microspheres from each of the four glass compositions investigated (Figure 4.4). Cross-sectional SEM images of resin embedded porous microspheres, of each formulation, revealed that the pores were not limited to the surface of the microspheres but also exhibited inner porosity with interconnected pores (see Figure 4.4E to H).

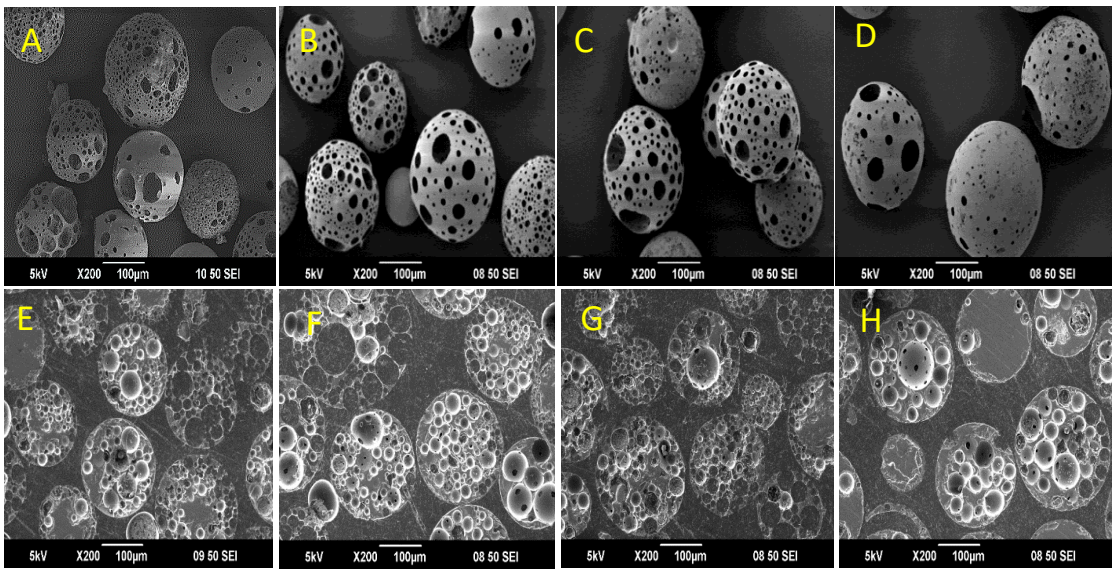

Figure 4.4 SEM images of the morphology of the porous microspheres and their cross section. (A & E) P40, (B & F) P35, (C & G) P32.5 and (D & H) P30.

Both solid and porous microspheres produced varied in size for all glass compositions. The addition of $CaCO_3$ resulted in the formation of larger porous microspheres in comparison to the solid microspheres formed from particles of the same size range and from each glass composition investigated. Porous microspheres formed from each composition had a higher D50 and D90 value than their solid microsphere counterparts, demonstrating that a greater proportion of microspheres with a larger diameter were produced. The D10, D50 and D90 values indicate the size below which 10%, 50% or 90% of all particles were found. For P32.5 and P30 porous microspheres this was accompanied by a decrease in the D10 value suggesting that a lower percentage of microspheres in the smaller size range were produced (see Figure 4.5).

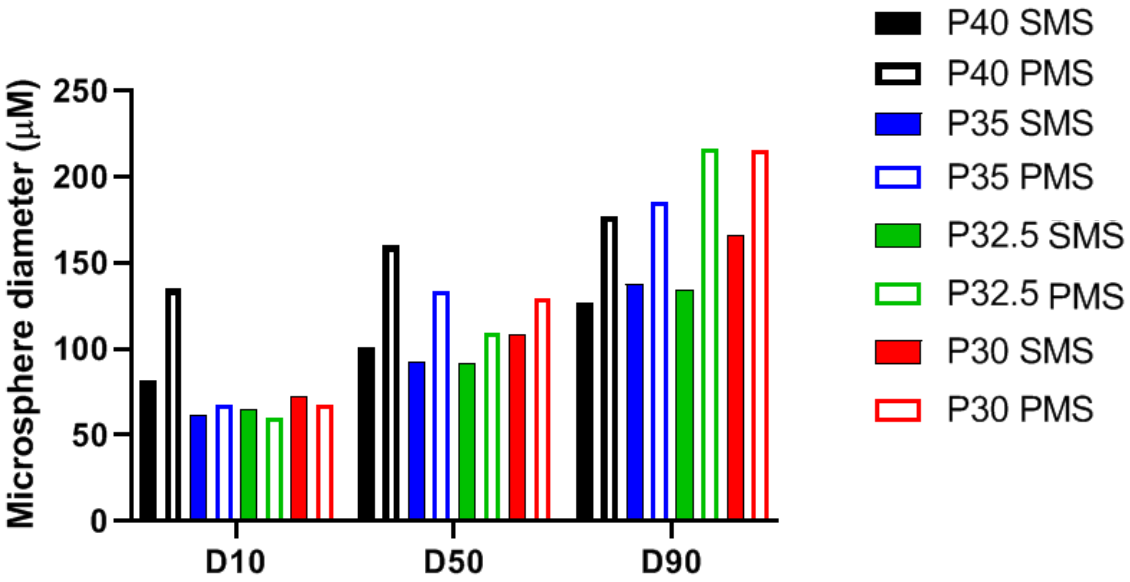

Figure 4.5 Size distribution of solid and porous microspheres produced from P35, P32.5 and P30 glass. D10, D50 and D90 correspond to the percentages 10%, 50% and 90% of particles under the reported particle size.

Porous microspheres were sieved into two groups, 0 - 125 µm and 125 - 200 µm and viewed using SEM analysis. This confirmed that a lower yield of porous microspheres (<50%) were present in the smaller size group for all four glass compositions with a large proportion not having visible porosity (Figure 4.6). Due to the low yield of microspheres with the desired morphology in the <125 µm range, microspheres of 125 – 200 µm diameter were subsequently used for the rest of the study.

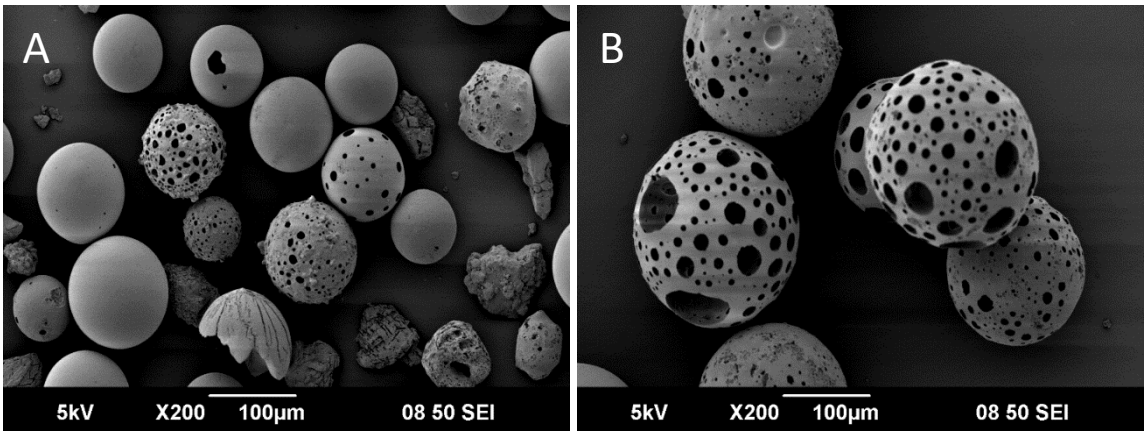

Figure 4.6 SEM images of (a) P32.5 porous microspheres 0 – 125 µm size range and (b) P32.5 porous microspheres greater than 125 µm produced from the same batch.

4.4.2 XRD Analysis

XRD analysis on solid microspheres showed that for each of the glass formulations, with the exception for P30, processing via flame spheroidisation resulted in the formation of spherical glass particles which remained amorphous, as depicted by the lack of any sharp crystalline peaks in Figure 4.7. Although the P30 solid microspheres had the same characteristic broad peak at 2θ values of ~–30-32° as the other formulations, several small crystalline peaks at 24°, 32° and 35° were also observed. These peaks corresponded to sodium calcium phosphate (ICDD 00-003-0751) and sodium phosphate (ICDD 00-030-1232).

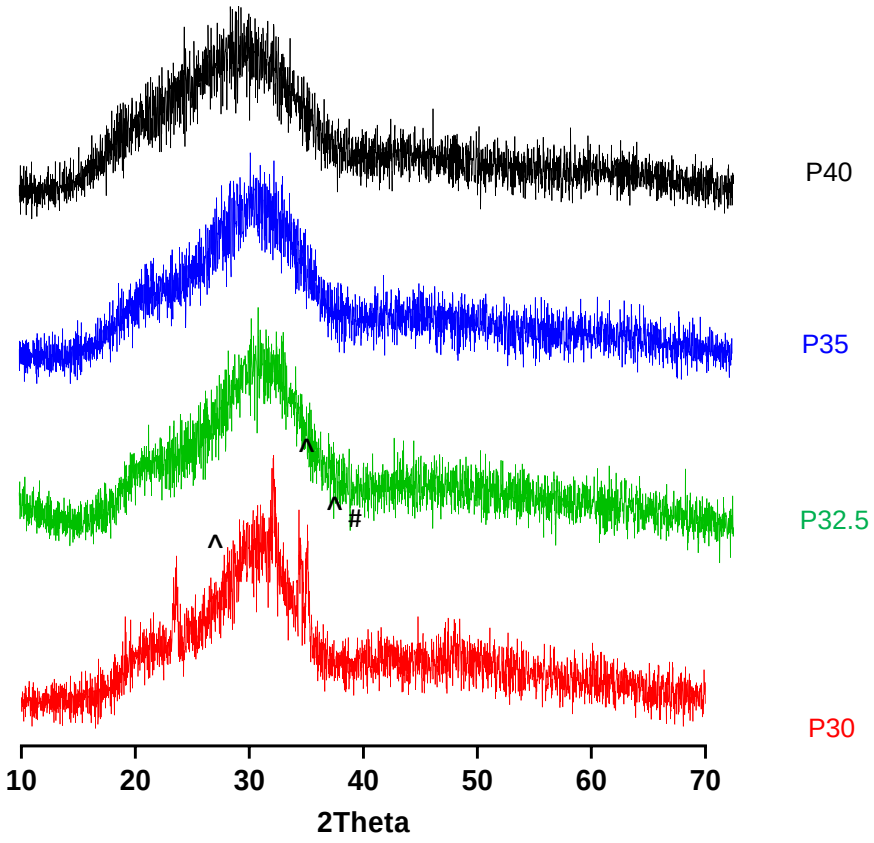

Figure 4.7 XRD profiles of P40 (black), P35 (blue), P32.5 (green) and P30 (red) solid microspheres. The crystalline peaks matched for sodium calcium phosphate (^) (ICDD 00-003-0751) and sodium phosphate (#) (ICDD 00-030-1232).

XRD of the porous microspheres of each formulation revealed the presence of sharp peaks at ~ 29° 2θ and at 36°, 39° and 43° 2θ values. These peaks were matched to $CaCO_3$ according to powder diffraction file 01-072-1937 (ICDD database). The same sodium calcium phosphate (ICDD 00-003-0751) and sodium phosphate (ICDD 00-030-1232) peaks that were present in the P30 solid microspheres were also evident in the P30 porous microspheres (see Figure 4.8).

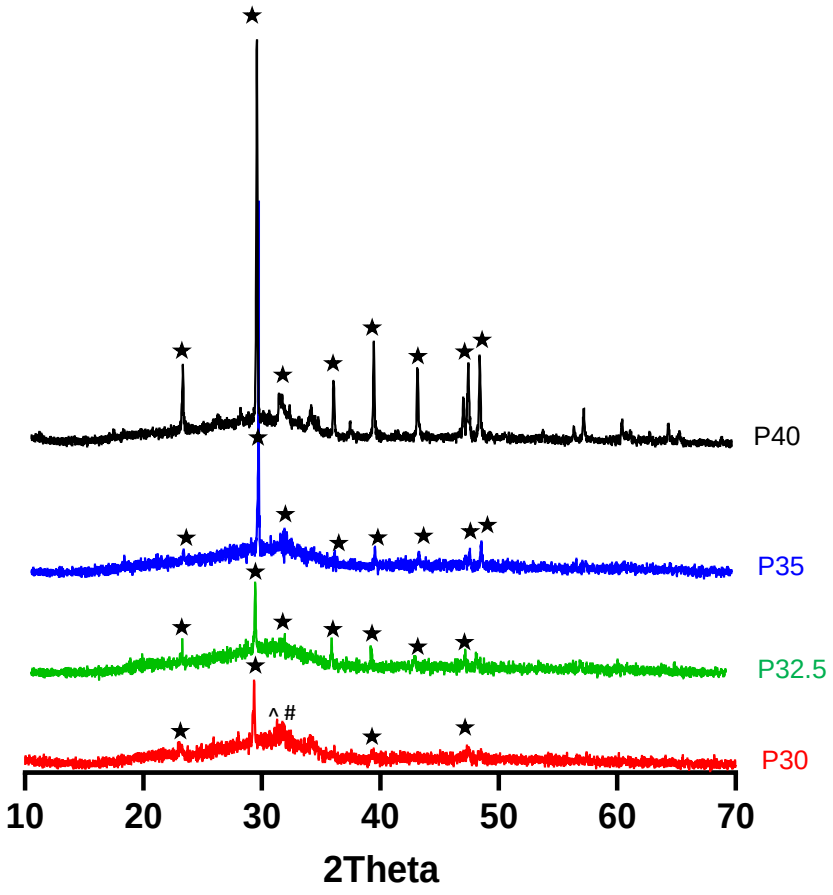

Figure 4.8 XRD profiles of P40 (black), P35 (blue), P32.5 PMs (green) and P30 (red) porous microspheres with the crystalline peak matched for $CaCO_3$ (★) (ICDD 01-072-1937), sodium calcium phosphate (^) (ICDD 00-003-0751) and sodium phosphate (#) (ICDD 00-030-123).

4.4.3 EDX Analysis

Elemental values for the starting glass, solid and porous microspheres were obtained using EDX analysis and compared with the target composition to evaluate whether processing altered their chemical composition. Processing into solid microspheres resulted in relatively

small changes in the particles composition compared to the starting glass. Processing P32.5 and P30 glass into solid microspheres resulted in an increase of 1.7 and 0.4 mol % of P_2O_5 from the glass particles. Both P32.5 and P30 solid microspheres displayed 1.8% and 2.2% elevated levels of CaO in comparison to their unprocessed glass particles. P40 and P35 solid microspheres had a slight reduction of 0.2 and 0.6 mol% in P_2O_5 respectively and only a very slight increase in CaO, less than 0.2% in both cases. P32.5 and P30 solid microspheres also exhibited a decrease in the MgO, with this being most prominent in the P32.5 microspheres, and decreased Na_2O values. P35 solid microspheres displayed a stable MgO mol% with a slightly elevated Na_2O above that of the P35 glass particles (see Figure 4.9).

Processing each of the formulations into porous microspheres resulted in far more significant changes in chemical composition. Porous microspheres from all four compositions exhibited elevated CaO content of ~ 2.9 – 7.1%. This change was most prominent in the porous P40 microspheres, followed by P32.5 and then by P35 and P30. As a result of this CaO increase, all compositions of porous microspheres had a lower MgO and Na_2O values compared to the starting glass. An apparent trend visible in Figure 4.9 is that the greater the increase in CaO, the greater the decrease in MgO. A decrease in P_2O_5 content between ~ 0.5 – 3.9% lower than the starting glass composition was observed (see Figure 4.9). The largest decrease in P_2O_5 content was seen in P40 PMS and this correlated with the much larger increase in CaO content that was observed.

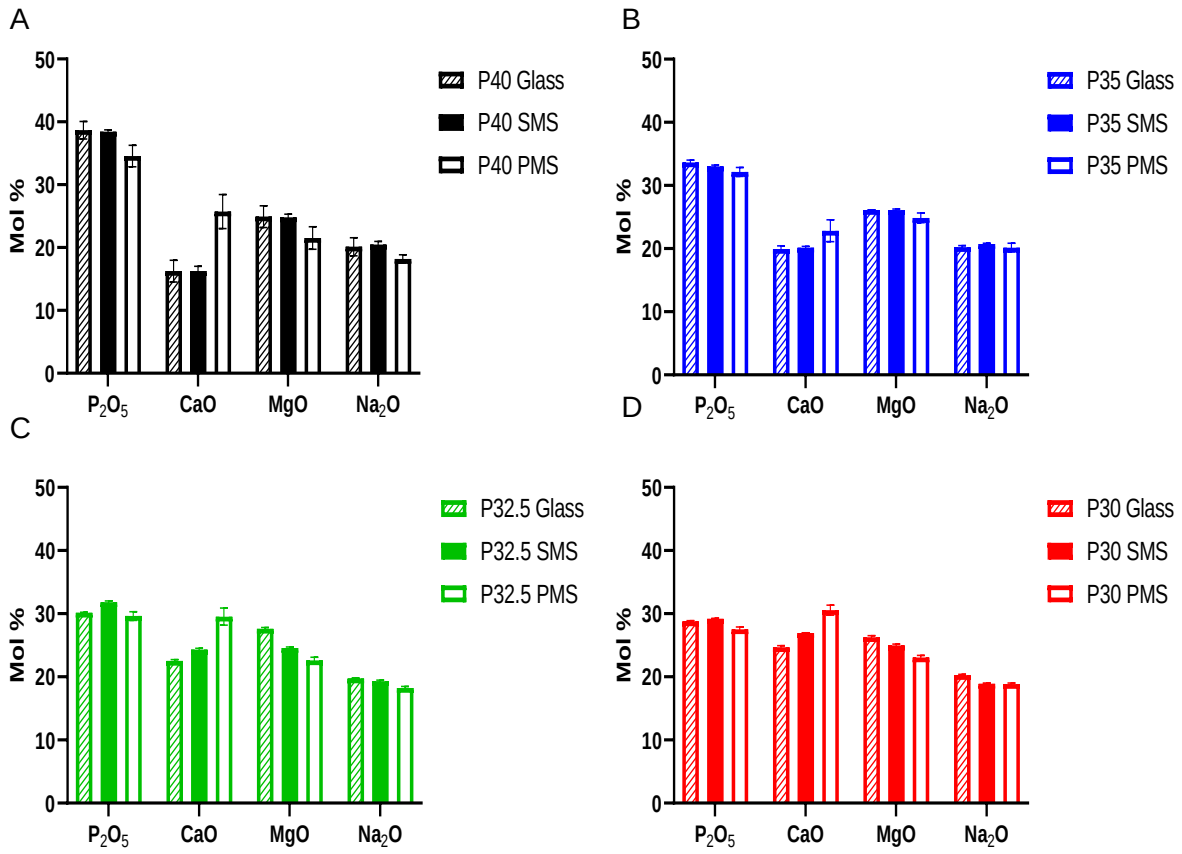

Figure 4.9 Chemical composition of the starting glass, solid and porous microspheres ascertained via EDX analysis. (A) P40, (B) P35, (C) P32.5 and (D) P30.

4.4.4 EDX mapping

EDX analysis was also performed to map the distribution of the elements within the microsphere structure. In all glass compositions and for both the solid (see Figure 4.10) and porous (see Figure 4.11) microspheres all elements were found to be homogenously distributed throughout the microspheres.

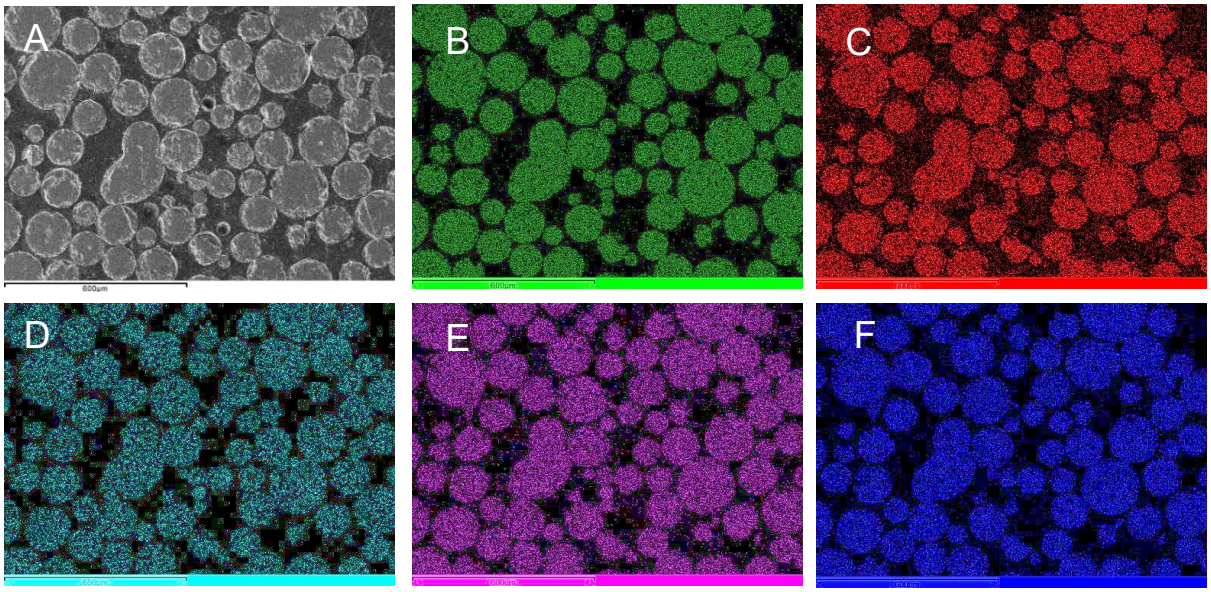

Figure 4.10 EDX mapping of P30 solid microspheres. (a) SEM image, (b) phosphorous (green), (c) oxygen (red), (d) calcium (cyan), (e) magnesium (purple) and (f) sodium (blue).

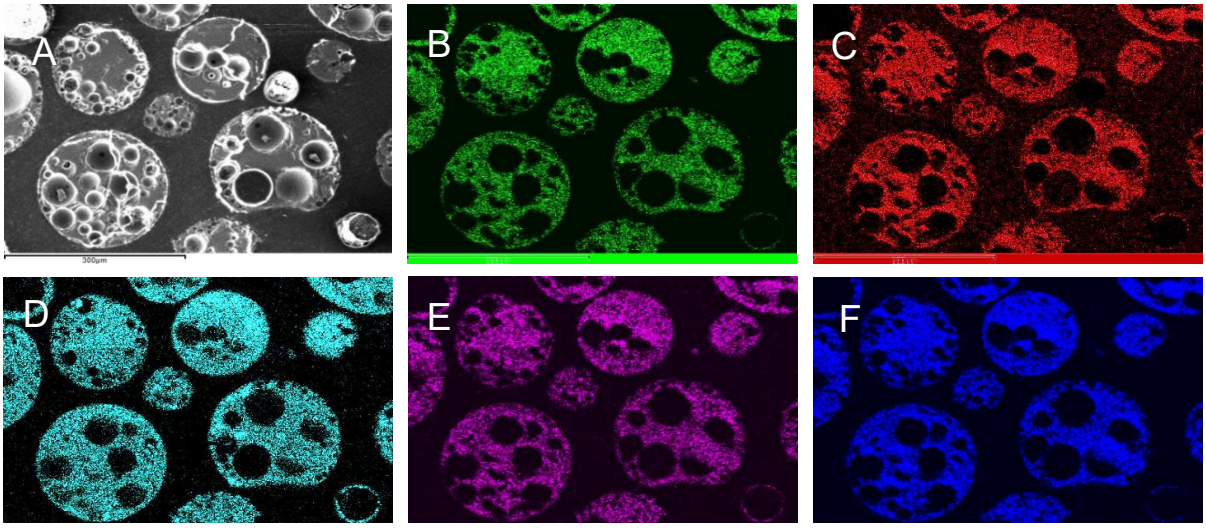

Figure 4.11 EDX mapping of P30 porous microspheres. (a) SEM image, (b) phosphorous (green), (c) oxygen (red), (d) calcium (cyan), (e) magnesium (purple) and (f) sodium (blue).

4.4.5 Quantitative 1D ^{31}P MAS NMR and 2D NMR

Quantitative 1D ^{31}P magic angle spinning (MAS) solid state nuclear magnetic resonance (NMR) spectroscopy was used to determine the distribution of the Q_n species of the phosphate glasses and their microspheres. From the spectra obtained it was possible to determine the isotropic shifts and the relative abundance of Q^2, Q^1 and Q^0 species for each glass composition and to explore whether any changes had occurred due to processing into alternate geometries (see Table 4.3).

Table 4.3 Relative abundance of Q^2, Q^1 and Q^0 species for P40, P35, P32.5 and P30 glass, solid and porous microspheres obtained using 1D 31P MAS-NMR.

		Q^2 (%)	Q^1 (%)	Q^0 (%)
P40	Glass	50	50	0
	SMS	38	61	1
	PMS	31	62	6
P35	Glass	19	81	0
	SMS	16	81	3
	PMS	13	80	7
P32.5	Glass	7	75	18
	SMS	6	74	20
	PMS	4	70	26
P30	Glass	0	68	32
	SMS	0	65	35
	PMS	0	65	35

As seen in Figure 4.12, as the phosphate composition decreased going from P40 to P30 in the phosphate glass there was a gradual decrease in structural connectivity and increased average number of non-bridging oxygen atoms (NBOs). The proportion of Q^2 species decreased from 50% to 18% to 7% in P40, P35 and P32.5 glass respectively and were not detected at all for the P30 glass. The P40 glass was found to be composed of 50% Q^2 and 50% Q^1 species. However, for the other glasses in the series a decrease in the proportion of Q^1 species from 81% to 75% and 68% for P35, P32.5 and P30 glass, respectively, was also observed. Conversely, the proportion of Q^0 species observed for the P35 glass was less than 1%, which increased to 18% in P32.5 glass and significantly increased to 32% for the P30 glass composition.

When the phosphate glass particles were processed into both solid and porous microspheres further depolymerisation of the glass network occurred, although this trend was less pronounced than the effect observed from decreasing phosphate content (see Figure 4.12). For the P40 glass, an increase in Q^1 species to 61%, at the expense of Q^2 was observed, which reduced to 35% and 1% Q^0 were detected when they were formed into solid microspheres. Interestingly, the formation of porous microspheres resulted in a further reduction of Q^2 species, to 31%, and increase in Q^0 to 6% was also observed. Similar depolymerisation of the glass network occurred when the P35, P32.5 and P30 glasses were processed into solid and porous microspheres, albeit to a lesser extent. Processing the starting glass materials into porous microspheres resulted in the most significant glass network depolymerisation in comparison to solid microspheres.

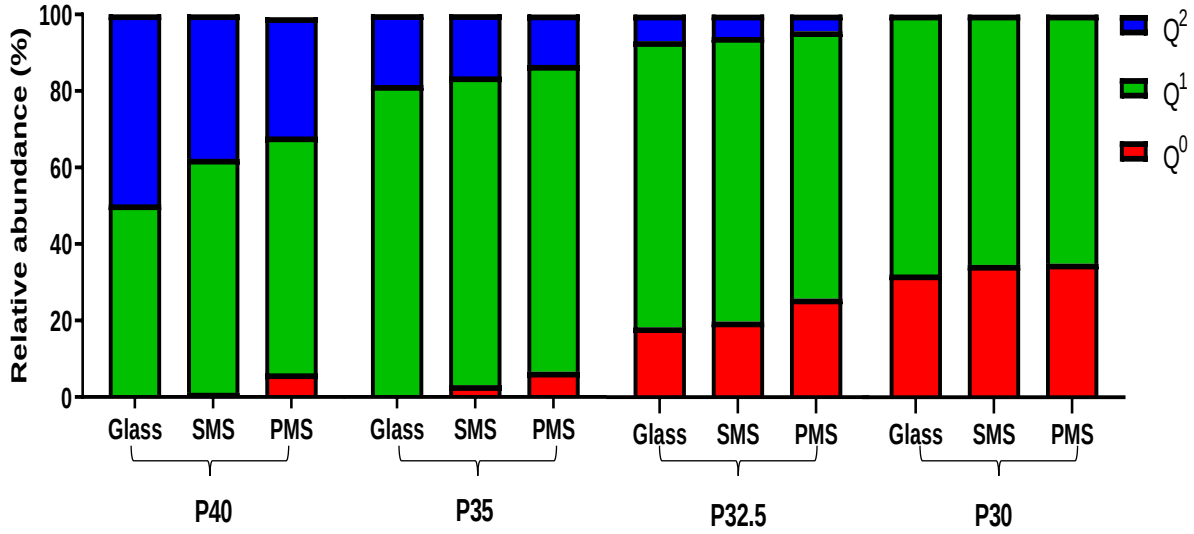

Figure 4.12 Relative abundance of Q^2, Q^1 and Q^0 species for glasses of the P40, P35, P32.5 and P30 composition obtained using 1D 31P MAS-NMR. Samples of glass particles, solid microspheres (SMS) and porous microspheres (PMS) morphology are displayed.

Previous studies have reported that cyclic metaphosphate species are found within glasses containing equal to and greater than 50% phosphate content [125]. Based on this assumption and the highest phosphate content within a formulation being 40 mol%, the average chain length (n_{av}) within the glass structures could also be theoretically modelled based on the phosphate content (i.e P30, x = 0.3), by using Equation 4.1:

$$n_{av} = 2x/(1-2x) \qquad \textit{Equation 4.1}$$

As seen in Table 4.4, there is a significant decrease in chain length as the phosphate composition decreases within the glasses.

Table 4.4 Theoretical calculation of average chain length (n_{av}) within P40, P35, P32.5 and P30 glass formulations.

Formulation	n_{av}
P40	4.00
P35	2.33
P32.5	1.86
P30	1.50

2D exchange spectrum for P35 solid microspheres (SMS) exhibited a narrow Q^2 auto peak despite prolonged mixing times. The auto-correlation peaks were calculated over the duration of the experiment and had the same chemical shift in both frequency dimensions. The mixing time determined the degree to which magnetisation could be transferred between ^{31}P nuclei. The intensities of signals in the 2D exchange spectrum are proportional to the strength of the magnetisation transfer. A narrow Q^2 auto peak demonstrated that there was no significant exchange between Q^2 species and therefore suggestive that the units were not in close proximity. This would indicate that there were no metaphosphate species that contain more than one Q^2 unit and were therefore composed of a maximum of three phosphate tetrahedra (Q^1-Q^2-Q^1 chains). This correlated with the theoretical calculations relating to average chain length seen in Table 4.5. Therefore, the largest Q^2 containing structures found within P35 and P32.5 glass and microspheres would be composed of Q^1-Q^2-Q^1 chains. For P30 samples, where there was an absence of Q^2 species, Q^1 species were present in the Q^1-Q^1 dimeric form as pyrophosphates, whilst Q^0 orthophosphate species are isolated from any other phosphate tetrahedra [126]. In the absence of 2D exchange spectrum for P40 particles, it was possible to calculate the structural chains forming the glass network based on the 1D P-NMR data and chain length calculations. For there to be a 50:50 split of Q^2 and Q^1 species, the chains within the network must be Q^1-Q^2-Q^2-Q^1 for the proportion of the species to be the same and gives the same chain length of 4 as the theoretically calculated value.

From the acquired quantitative 1D spectra's, it was apparent that two very narrow peaks were present in both the P30 solid and porous microspheres that were not seen in any of the other samples (see Figure 4.13B and C). These narrow peaks at 2.89 ppm and 0.41 ppm and at 2.98 ppm and 0.13 ppm were indicative of areas of crystallinity within the microspheres structure. The narrow width of the peaks relates to the very limited range of bonding

geometries present. The isotropic shift of values for these peaks suggested that crystalline Q^0 species were likely responsible for their formation, with two separate peaks with different shifts possibly the result of two distinct crystal structures.

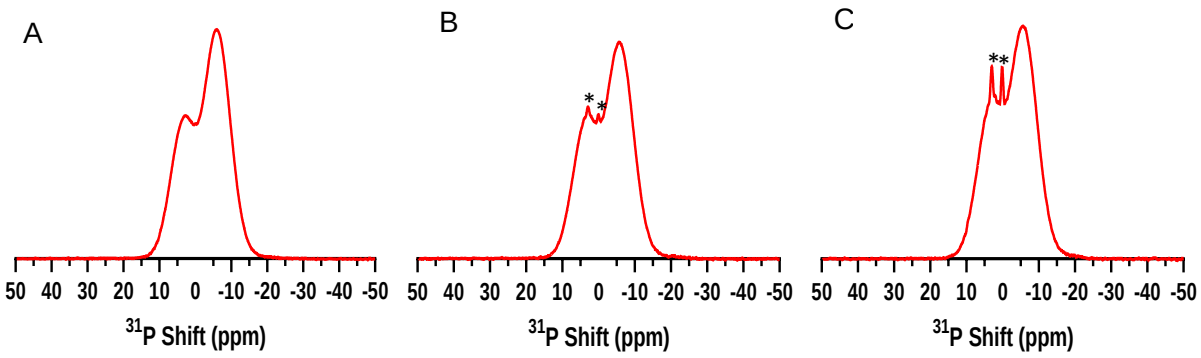

*Figure 4.13 Quantitative 1D ^{31}P NMR spectra for (A) P30 glass particles, (B) P30 solid microspheres and (C) P30 porous microspheres. Crystalline peaks are identified with a *.*

4.4.6 Theoretical calculation of Q species and BO to NBO ratio

The expected percentage of Q^n species and bridging oxygen (BO) to non-bridging oxygen (NBO) ratio from each of the four glass compositions could be calculated based on the oxygen to phosphorous ratio (O/P). As seen in Table 4.5, the O/P ratios for P40 and P35 glass were considered to be within the metaphosphate region ($3 \leq O/P \leq 3.5$), whereas P32.5 and P30 were considered within the pyrophosphate region ($3.5 \leq O/P \leq 4$) [127]. According to the glass composition regions, the fraction of Q^2 and Q^1 can be theoretically calculated for the metaphosphate glasses using Equation 4.2 [128]:

$$\text{For } 3 \leq O/P \leq 3.5 \quad f(Q^2) = \frac{3.5 - (O/P)}{0.5} \times 100 \qquad \textit{Equation 4.2}$$
$$f(Q^1) = 100 - f(Q^2)$$

For the pyrophosphate glasses P32.5 and P30, the fraction of Q^1 and Q^0 can be theoretically calculated using Equation 4.3:

$$\text{For } 3.5 \leq O/P \leq 4 \quad f(Q^1) = \frac{4 - (O/P)}{0.5} \times 100 \qquad \textit{Equation 4.3}$$
$$f(Q^0) = 100 - f(Q^1)$$

As seen in Table 4.5, the theoretical percentages of Q species correlated very well with the experimental NMR results obtained for the P40, P35 and P30 glass and were near identical in the case of P40 and P30. The theoretical values for P32.5 did not correlate to the experimental NMR due to the fact the equations used predict the distribution of phosphate species as a binary model, where only two types of Q^n tetrahedra (^{n} and $^{n+1}$) exist for any one phosphate composition. The results from the NMR revealed that three phosphate species were present within P32.5 glass therefore the equations used to predict Q^n speciation for the other glasses could not be applied to this composition.

The O/P ratio could additionally be used to evaluate the number of BO (Equation 4.4) and NBO (Equation 4.5) in the phosphate tetrahedral units of each of the glasses by using the following equations:

$$N_{BO} = 8 - 2 \times (O/P) \qquad \textit{Equation 4.4}$$

$$N_{NBO} = 4 - N_{BO} \qquad \textit{Equation 4.5}$$

Table 4.5: Theoretical calculation of O/P, Q species and BO to NBO ratio for P40, P35, P32.5 and P30 glass formulations

Formulation	O/P	Q^2	Q^1	Q^0	N_{BO}	N_{NBO}	BO/NBO
P40	3.25	50	50	0	1.5	2.5	0.6
P35	3.43	14	86	0	1.14	2.86	0.40
P32.5	3.53	0	94	6	0.94	3.06	0.31
P30	3.66	0	68	32	0.68	3.32	0.20

4.4.7 FTIR analysis

The FTIR spectra of each of the four glass compositions are shown in Figure 4.14. All compositions display bands around 720 – 740 cm^{-1} and 890-900 cm^{-1} which were assigned to symmetric (v_s) and asymmetric (v_{as}) stretching of P-O-P linkages respectively [129]. Bands at both ~990 and ~1100 cm^{-1} were also seen in all glass compositions and were assigned to the symmetric and asymmetric stretching modes of the chain terminating Q^1 groups [130]. A band at ~1040 cm^{-1} is visible in P35, P32.5 and P30 glass which is assigned to symmetric stretching modes of PO_4^{3-} tetrahedral in Q^0 calcium orthophosphates [131]. The intensity of this band increased from P35 to P30 and this correlates with the increase in Q^0 species from the ^{31}P NMR studies (see Figure 4.13). This band was not visible in P40, where no orthophosphate

groups were measured using ^{31}P NMR. A band at ~1245 cm^{-1} was seen in the P40 glass and is assigned to asymmetric (ν_{as}) stretching modes of the two non-bridging oxygens bonded to phosphorous atom in Q^2 species [132]. The variations in the FTIR spectra were expected as the phosphate network structure altered between glass compositions, as seen by the changing O/P ratio and by complementary experimental data obtained via ^{31}P MAS-NMR.

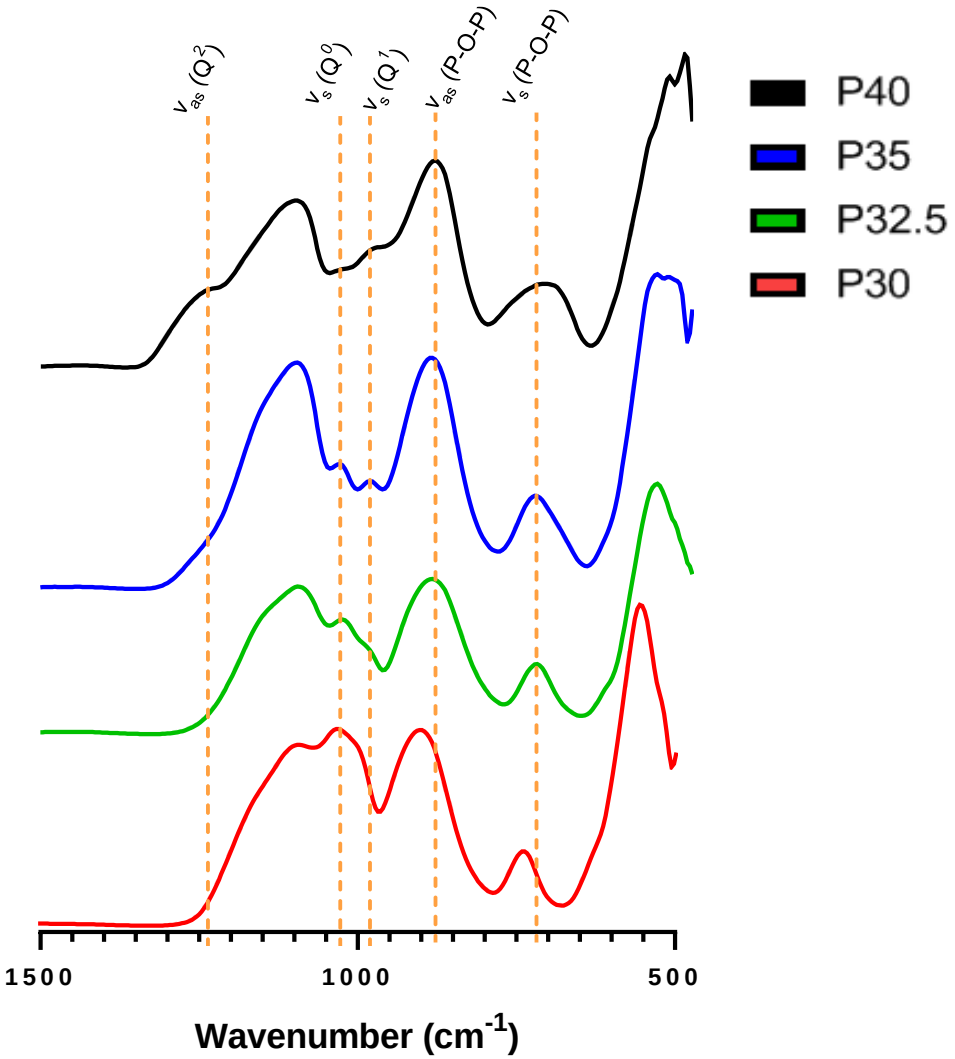

Figure 4.14 FTIR spectra obtained for the four phosphate glasses. P40 [14], P35 (blue), P32.5 PMs (green) and P30 (red). The dotted lines indicate prominent bands in the spectra.

4.4.8 Raman Analysis

Figure 4.15 displays the Raman spectra for each phosphate glass with each spectrum being averaged and baseline corrected. The assignment of peaks is based on the PO_2 symmetric stretching mode of non-bridging oxygens in Q^n units [133]. The band at ~ 965 cm^{-1} is assigned to Raman-active PO_2 symmetric stretching mode of non-bridging oxygens in Q^0 units, whereas

the band at 1050 cm^{-1} was associated with Q^1 units and 1110 – 1160 cm^{-1} associated with PO_2 symmetric stretching of non-bridging oxygen in Q^2 units.

The Raman spectra acquired at both 660 and 532 nm excitation showed the same general trend and were broadly consistent with the ^{31}P NMR experiments that were performed to determine the distribution of the Q_n species. As seen in Figure 4.15, P30 appears to comprise exclusively of Q^0 and Q^1 species, whereas P32.5 comprises predominantly Q^1, but some Q^0 and Q^2. P40 is comprised exclusively of Q^1 and Q^2 species with no Q^0 species being detected, which correlated with the results seen using ^{31}P NMR and FTIR.

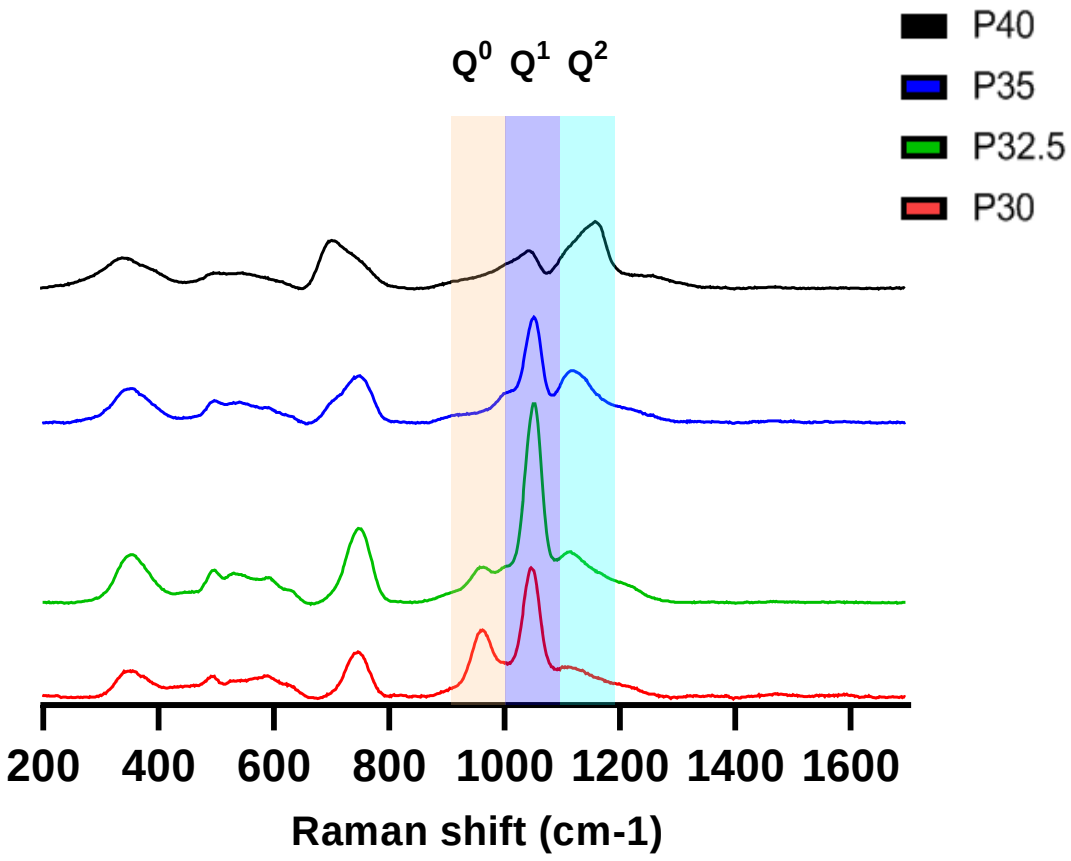

Figure 4.15 Raman spectra obtained for the four phosphate glasses. P40 (black), P35 (blue), P32.5 PMs (green) and P30 (red). Shaded regions represent the likely Q species that a prominent band relates to.

4.4.9 Ion Release Studies

Figure 4.16 shows the cumulative ion release profiles, calculated from measurements obtained via Inductively Coupled Plasma (ICP) analysis, for the porous microspheres over 28 days and the calculated ion release rates. For each of the four porous microsphere formulations, the ions appeared to exhibit linear ion release over the time measured (Figure 4.16A – D). A clear trend in the release rate of each ion was seen across the microsphere series. P40 microspheres released all the glass forming ions at a statistically significant higher rate in comparison to the other formulations (Na and P: $p < 0.0001$; Mg: $p < 0.00$; *Ca: vs P32.5 and P30* $p < 0.01$*)* (see Figure 4.16E). As the phosphate content in the microspheres decreased, so did the release rate for all ions. Porous P40 microsphere had the highest release rate for all the ions and P30 the lowest. P40 porous microspheres released P at a rate of 10.2 ppm/day and this was at a rate over 4 times greater than P35, 6 times greater than P32.5 and 7 times greater than P30 porous microspheres.

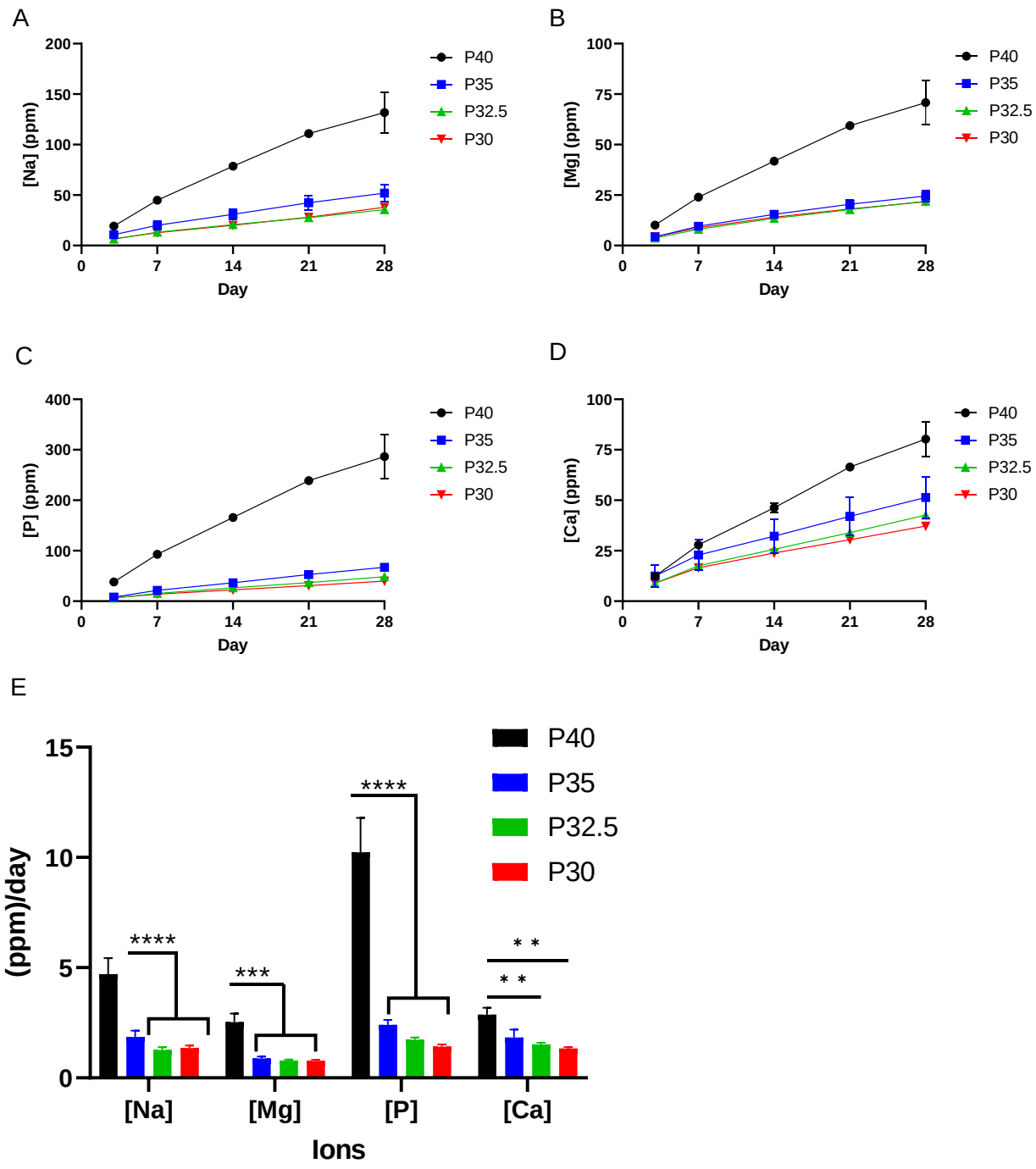

Figure 4.16 Cumulative ion release profile of (A) [Na], (B) [Mg], (C) [P] and (D) [Ca] measured via ICP-MS PMS of phosphate glasses investigated in milli-Q water during 28 days of immersion period. (E) Ion release rates (ppm per day) of P40, P35, P32.5 and P30 porous microspheres calculated from the linear cumulative ion release profiles (observed in A – D) (Error bars are also included in the data above).

The pH of the milli-Q water used to immerse the porous microspheres over the 28-day period is displayed in Figure 4.17A. For the solution containing P40 porous microspheres, there was a small decrease in pH from ~7.8 at day 3 to ~7.0 by day 28. The pH of the solution at day 3 was higher for the other 3 glass formulations at a pH of 8.8 – 9.2. For all formulations, the pH gradually decreased from day 7 onwards. A trend was apparent in that the lower the phosphate content of the microsphere, the higher the pH of the milli-Q water.

The slightly alkaline pH of the microsphere containing milli-Q water was attributed to any residual porogen retained on or within the microspheres. As seen in Figure 4.8, the XRD traces revealed the presence of $CaCO_3$ within porous microsphere but not for the solid microspheres post-processing. As seen in Figure 4.17A, lower pH values were observed for the higher phosphate containing microspheres, which was likely due to the release and breakdown of phosphate chains leading to more PO_4 groups and a subsequent increase of PO_4^{3-} ions into solution [134]. To confirm the role that residual $CaCO_3$ within porous microspheres was having on the pH of the solution, solid microspheres of the same formulation and size were also immersed in milli-Q water for 28 days. The pH of the solutions containing the solid microsphere followed the same trend but were at a slightly lower, more neutral pH (Figure 4.17B). This was most evident between day 3 and 7.

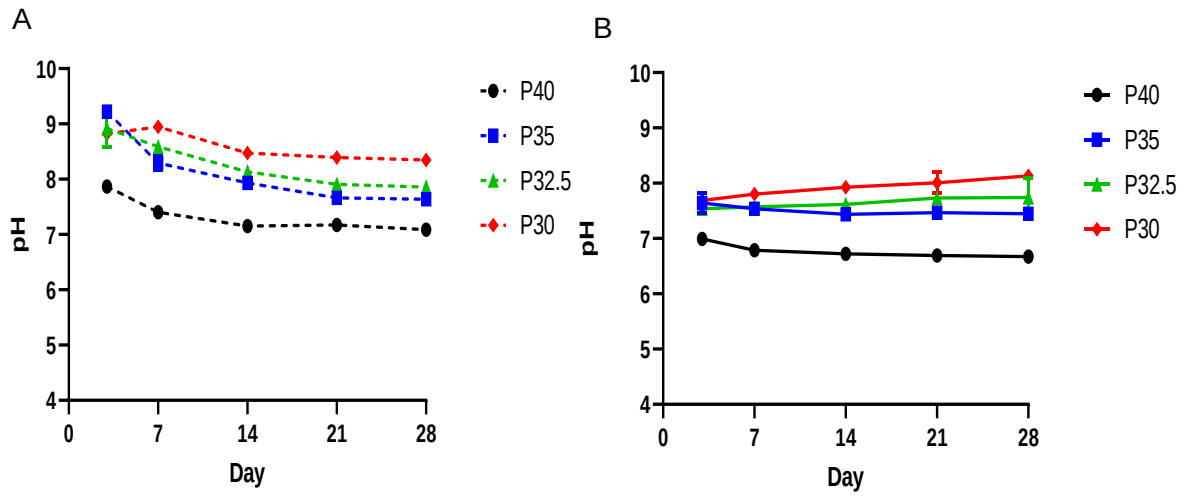

Figure 4.17 pH of milli-Q water during 28 days of (a) porous microspheres and (b) solid microspheres immersion within the solution. (Error bars are also included in the data above).

4.4.10 Degradation analysis

SEM images of the PMS from the four glass formulations following 28 days immersion in milli-Q water were taken to assess any morphological changes that may occur due to microsphere degradation (see Figure 4.18). A large proportion of P40 microspheres displayed evidence of surface integrity deterioration and degradation occurring between adjacent pores. Similar small cracks and morphological changes were seen in P35 microspheres but to a much lesser extent. These changes were not apparent in both P32.5 and P30 microspheres with PMS from both formulations appearing to remain intact following 28 days immersion.

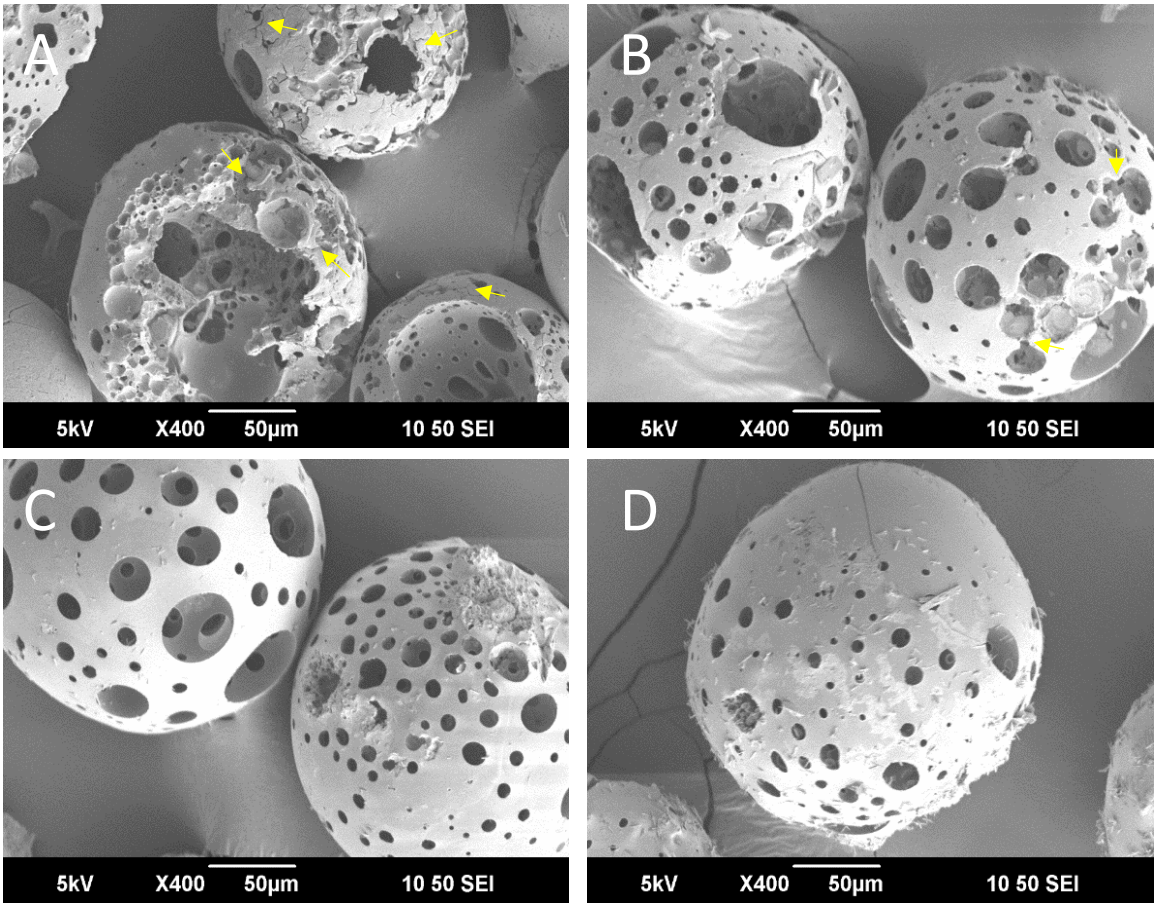

Figure 4.18 SEM images of (A) P40 (B) P35 (C) P32.5 and (D) P30 PMS after 28 days immersion in milli-Q water. Yellow arrows indicate regions of degradation on the microspheres surface.

4.4.11 Bioactivity Studies Using SBF: SEM Images

Since porosity can facilitate enhanced gaseous and nutrient exchange and encapsulation of therapeutic compounds, the bioactivity of porous P40, P35, P32.5 and P30 microspheres was explored to assess their suitability for *in vivo* orthobiological applications. SEM images were acquired at each time point following immersion in SBF of porous microspheres of each of the compositions and compared to particles of 45S5 Bioglass (to confirm media validation). 45S5 was shown to form deposits on its surface characteristic of hydroxycarbonate apatite (HCA) following 24 hours of immersion within SBF (see Figure 4.19). This was consistent with other studies where HCA deposits are also seen within this time [135]. These depositions on the glass surface increased in both size and number as immersion time increased.

The phosphate glass microspheres did not display the characteristic HA-like deposits even after 28 days. Of the 4 glass compositions, P30 porous microspheres appeared to display regions which closely resembled the depositions as seen on the surface of 45S5 (see Figure 4.19). The SEM images also revealed evidence of degradation and that extensive cracking had appeared on the surface of P40 porous microspheres. P35, P32.5 and P30 porous microspheres did not display these features. The formation of cracks between pores and the topographical changes that occurred to the P40 microspheres after SBF immersion appeared to be like those seen in milli-Q water (see Figure 4.18).

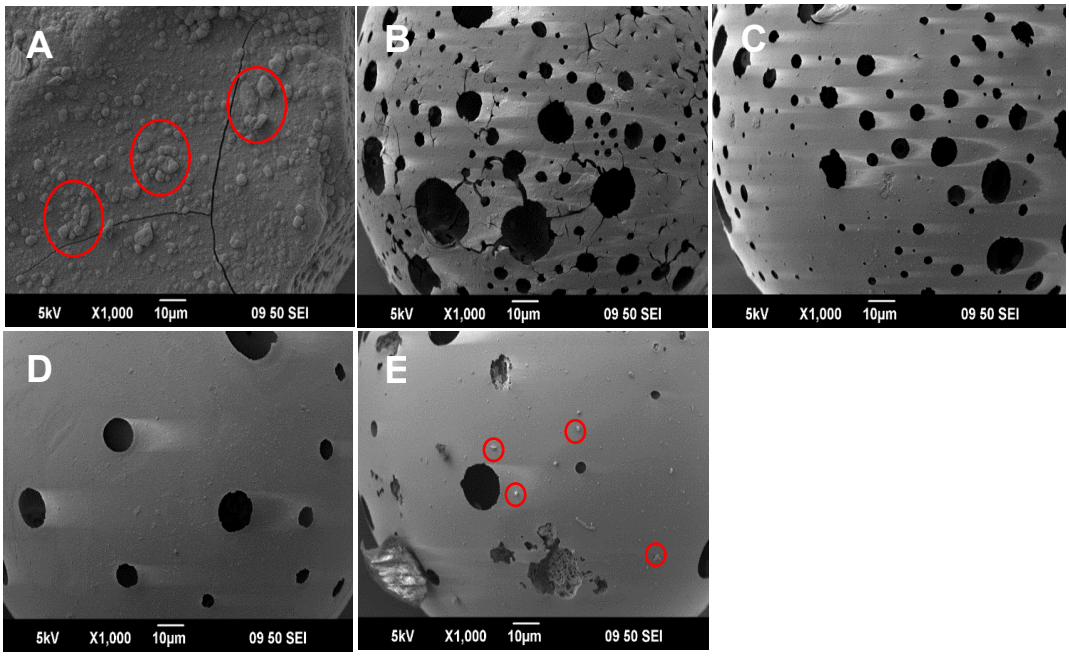

Figure 4.19 SEM images of (a) 45S5 particles, (b) P40, (c) P35, (d) P32.5 and (e) P30 porous microspheres following 28 days immersion in SBF. Depositions visible on the particles surface are circled in red.

4.4.12 Bioacytivity studies using SBF: EDX Analysis

EDX analysis was also performed and used to calculate the Ca:P ratio (wt%) of the porous microspheres prior to and after 28 days immersion in SBF. The porous microspheres from each of the formulations exhibited elevated Ca:P ratios in comparison to their parent glass formulations, which was attributed to the increase in CaO content from use of the $CaCO_3$ as porogen. Following immersion in SBF for 28 days, microspheres from each glass composition exhibited an increase in the Ca:P ratios, which were used to predict any potential phases present on the surface of the microspheres (see Figure 4.20).

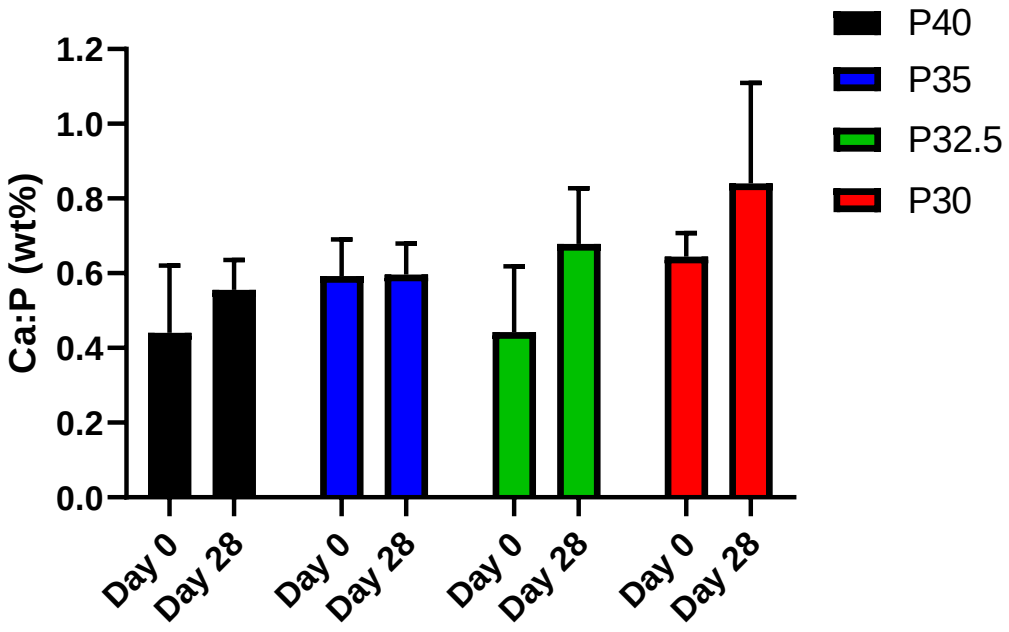

Figure 4.20 Ca:P ratio (wt%), determined by EDX, for porous microspheres from each composition prior to SBF immersion and after 28 days immersion.

The deposits seen on the surface of P30 porous microspheres had a Ca:P ratio of between of 1.2 – 1.3, which was higher than that of the microspheres themselves (Figure 4.21).

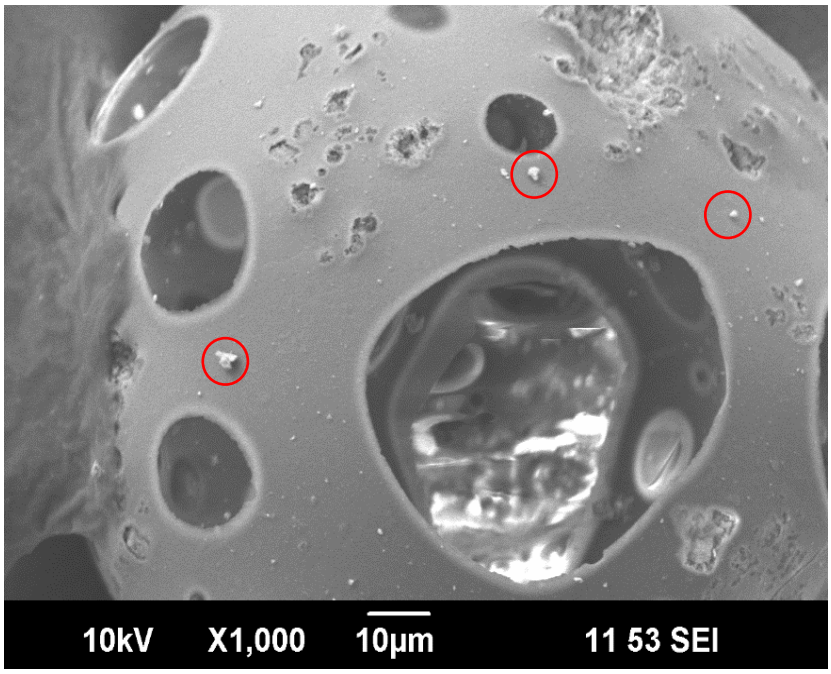

Figure 4.21 SEM image of the depositions on P30 PMs that underwent EDX analysis. Depositions are circled in red.

4.4.13 Bioactivity studies using SBF: XRD Analysis

XRD profiles of the four PBG porous microspheres and 45S5 following 28 days immersion in SBF are shown in Figure 4.22. The XRD spectra for 45S5 were in good agreement with the results seen in other studies, with sharp peaks at 2θ values of 26° and 32° from day 7 onwards revealing HCA (ICSD 01-084-1998) formation [136]. The spectra obtained for P40 and P35 lacked the sharp peaks at 2θ values of 26° and 32° that indicate the formation of HCA on the microsphere surface. A prominent peak at 2θ value of 29° and smaller peaks at 36°, 39°, 47° and 48° correlated with peaks for $CaCO_3$ (ICSD 00-024-0027) that had previously been identified using XRD on porous microspheres, prior to SBF immersion (see Figure 4.7). Peaks at 29°, 36°, 39°, 47° and 48° were present at each time point. P32.5 and P30 spectra displayed peaks for $CaCO_3$ at each time point and by day 28 peaks at 2θ values of 31° and 34° were also visible which corresponded to DCPD (i.e. brushite) (ICSD 00-004-0740) (see Figure 4.22).

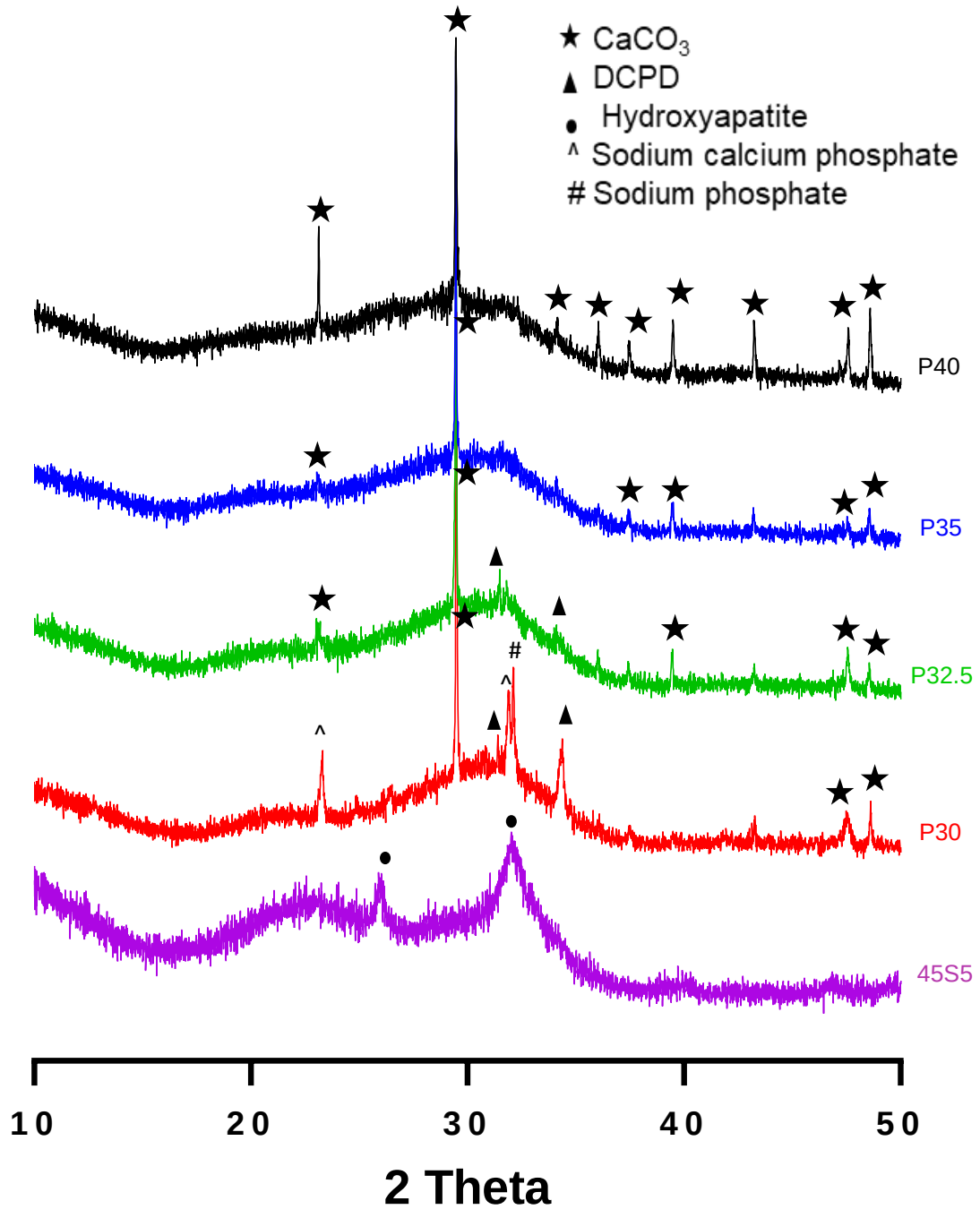

Figure 4.22 Powder XRD patterns for P40 (black), P35 (blue), P32.5 (green), P30 (red) and 45S5 (purple) following 28 days immersion in SBF.

4.4.14 *In vitro* indirect Cell culture Studies

To determine the cytocompatibility of the porous glass microspheres, an indirect cell culture method was performed which involved feeding microsphere-conditioned media to osteoblast-like cells (MG63s) to evaluate their biological response to the dissolution products released by each porous microsphere composition, over time. Standard medium (SM) and SM containing 5% DMSO were included as positive and negative controls, respectively. Analysis of metabolic activity via the Alamar Blue assay showed a significant increase in cell response when each of the four porous microsphere conditioned media was applied between days 2 to day 7. This increase in metabolic activity was also seen for cells treated with SM but cells treated with SM + 5% DMSO did not have an increase in metabolic activity from day 2 to day 7 (D2 vs D7: p <0.0001). No significant difference was detected between all formulations at day 2, apart from comparison to SM +5% DMSO (p <0.0001) (see Figure 4.23A). Although not statistically significant, a trend for increased metabolic activity for the lower phosphate containing microsphere formulations was also observed.

At day 7, the trend towards increasing metabolic activity with decreasing phosphate content in the microspheres became significant. Cells grown in P30 conditioned media had a statistically significant higher metabolic activity response to cells grown in all other conditions except for those in P32.5 conditioned media (vs P40, P35, SM, SM+5% DMSO $p < 0.0001$). Cells grown in P40 media had a significantly lower cell response in comparison to P32.5 ($p < 0.05$) and P30 cells ($p < 0.0001$) but was comparable to cells grown in P35 conditioned media and SM (see Figure 4.23A).

Bright field images taken at day 2 of treated cells confirmed the formation of homogenous cell monolayers that were comparable to the cells grown in the SM control. Cells grown in SM + 5% DMSO were sparsely distributed, and their small and spherical morphology was visibly different to the elongated shape of the MG63's grown in all other conditions (see Figure 4.23B).

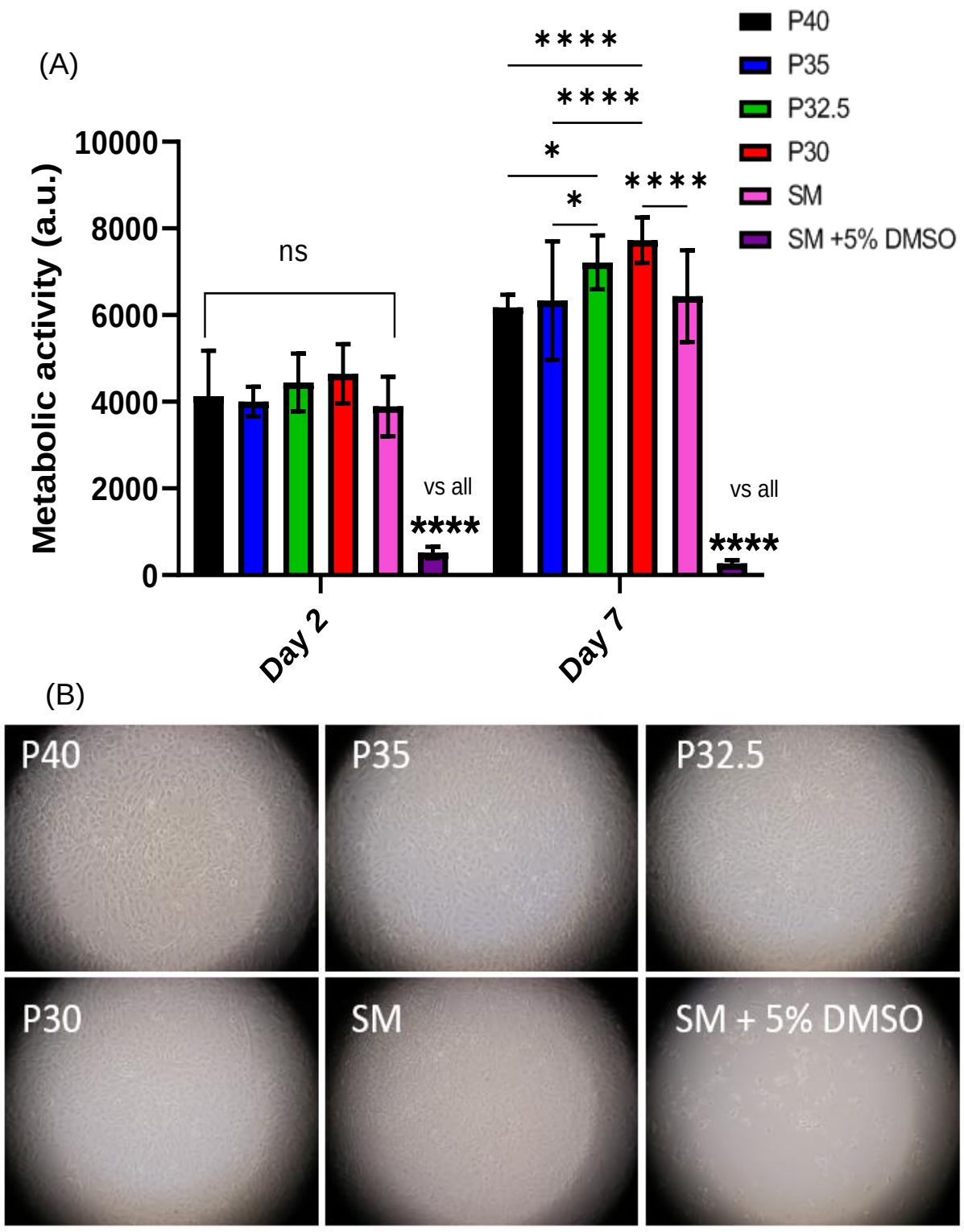

*Figure 4.23 (A) Evaluation of cell metabolic activity in indirect culture of porous microspheres at day 2 and day 7. ****p < 0.0001, *p < 0.05. (B) Cell appearance at day 2 of indirect culture.*

Alkaline phosphatase (ALP) activity was measured as an early marker of osteogenic differentiation in MG63 after 7 days of indirect culture from the four phosphate-glass microsphere formulations. The ALP activity was normalised to the DNA content of the samples investigated. Cells grown in P40 conditioned media had significantly higher ALP activity compared to cells grown in the three other microsphere conditioned media as well as standard media (*vs* P35, P32.5 and P30: $p < 0.001$; *vs* SM: $p < 0.05$). There was no statistically significant difference in ALP activity between cells grown in SM and those grown with P35, P32.5 and P30 conditioned media ($p > 0.05$) (see Figure 4.24).

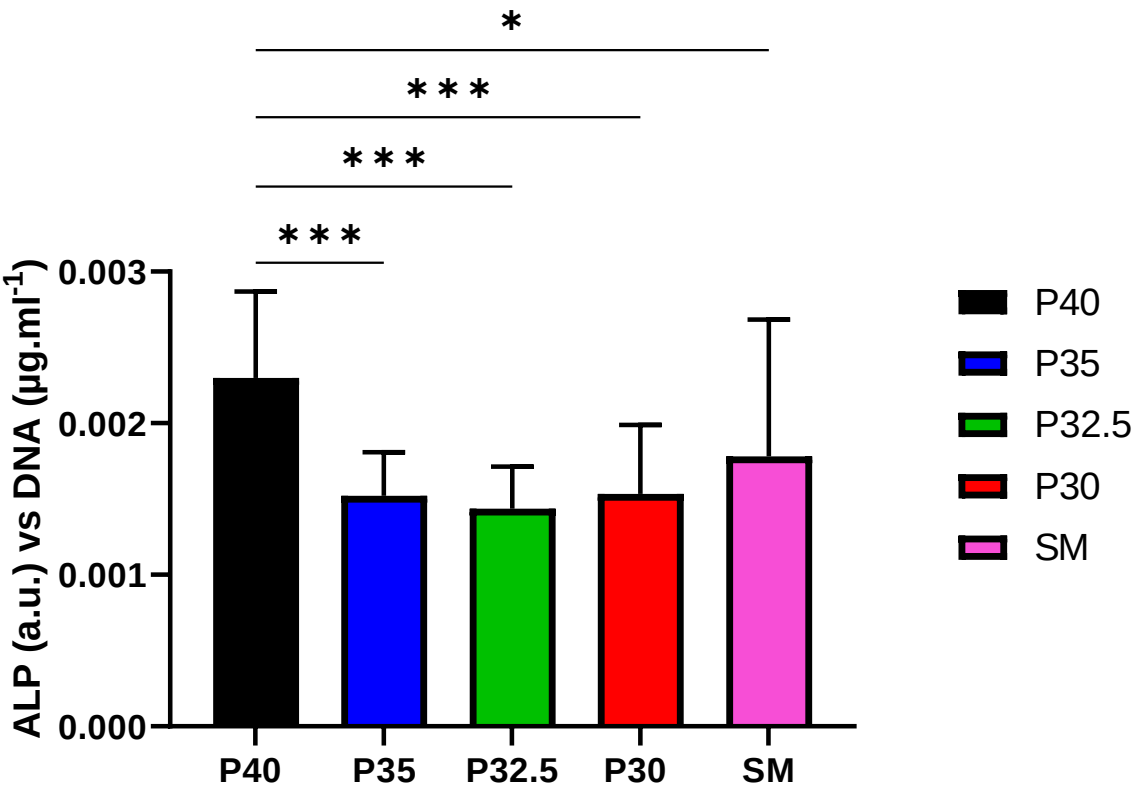

*Figure 4.24 Evaluation of ALP activity in indirect culture with porous microspheres at day 7. ****p < 0.0001.*

4.4.15 *In vitro* direct Cell Culture Studies

Seeding of MG63 cells directly onto the microspheres was performed to evaluate the cellular response to direct contact with the four porous microsphere formulations and assess their suitability as biomaterials for bone repair and regeneration applications. Analysis of metabolic activity of cells in direct physical contact of the microspheres showed that after 2 days of cell culture there was no statistically significant difference in cells grown on the four different microsphere formulations ($p > 0.05$) (see Figure 4.25).

Metabolic activity decreased slightly by day 7, with this response only being significantly lower for P32.5 microspheres. After 7 days of culture there was no statistically significant difference in metabolic activity measured between cells cultured on the four microsphere formulations ($p > 0.05$). The metabolic activity of cells cultured on tissue culture plastic (TCP) as a positive control was significantly lower at day 2, and by day 7 was significantly higher ($p < 0.0001$) (see Figure 4.25).

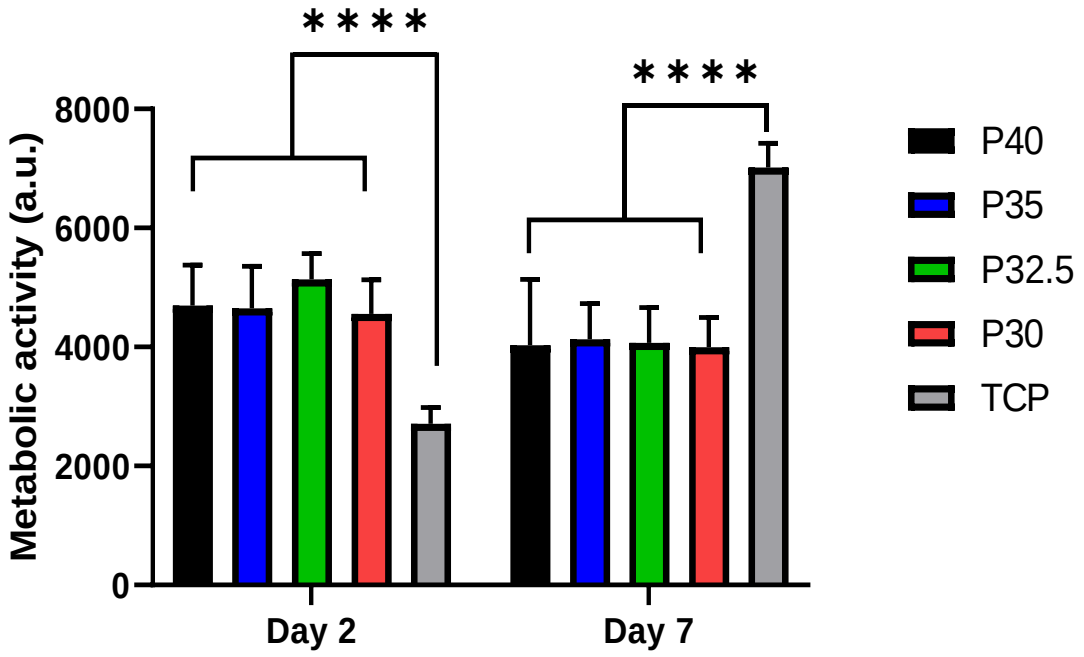

*Figure 4.25 Evaluation of cell metabolic activity in direct culture of porous microspheres at day 2 and day 7. ****p < 0.0001.*

ALP was evaluated after 7 days of direct culture and was normalised to DNA concentrations of each sample. ALP activity can be used as a measure of cell mineralisation as it is an early marker of cell matrix maturation. The ALP activity after 7 days of MG63 cell growth on all four microsphere formulations was significantly higher than those grown on the TCP control ($p < 0.0001$), although no statistically significant difference was detected between the formulations ($p > 0.05$) (see Figure 4.26).

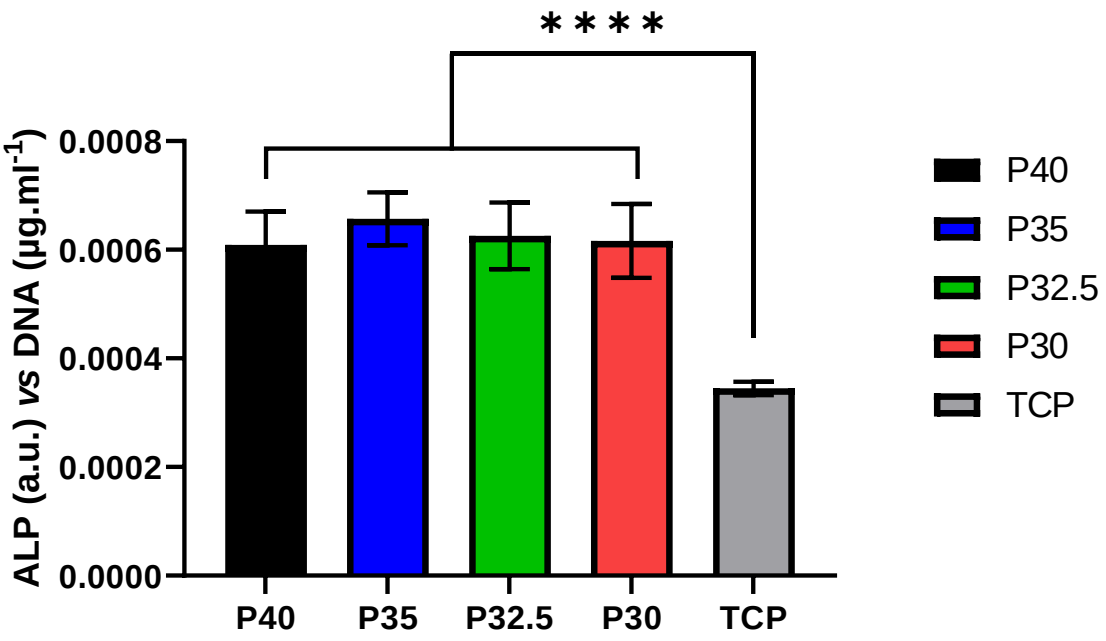

*Figure 4.26 Evaluation of ALP activity in direct culture of porous microspheres at day 7. ****p < 0.0001.*

MG63 cells that were directly cultured on the four microsphere formulations were visualised using ESEM at day 7. Cells were shown to adhere onto the microspheres from each of the four glass formulations (see Figure 4.27).

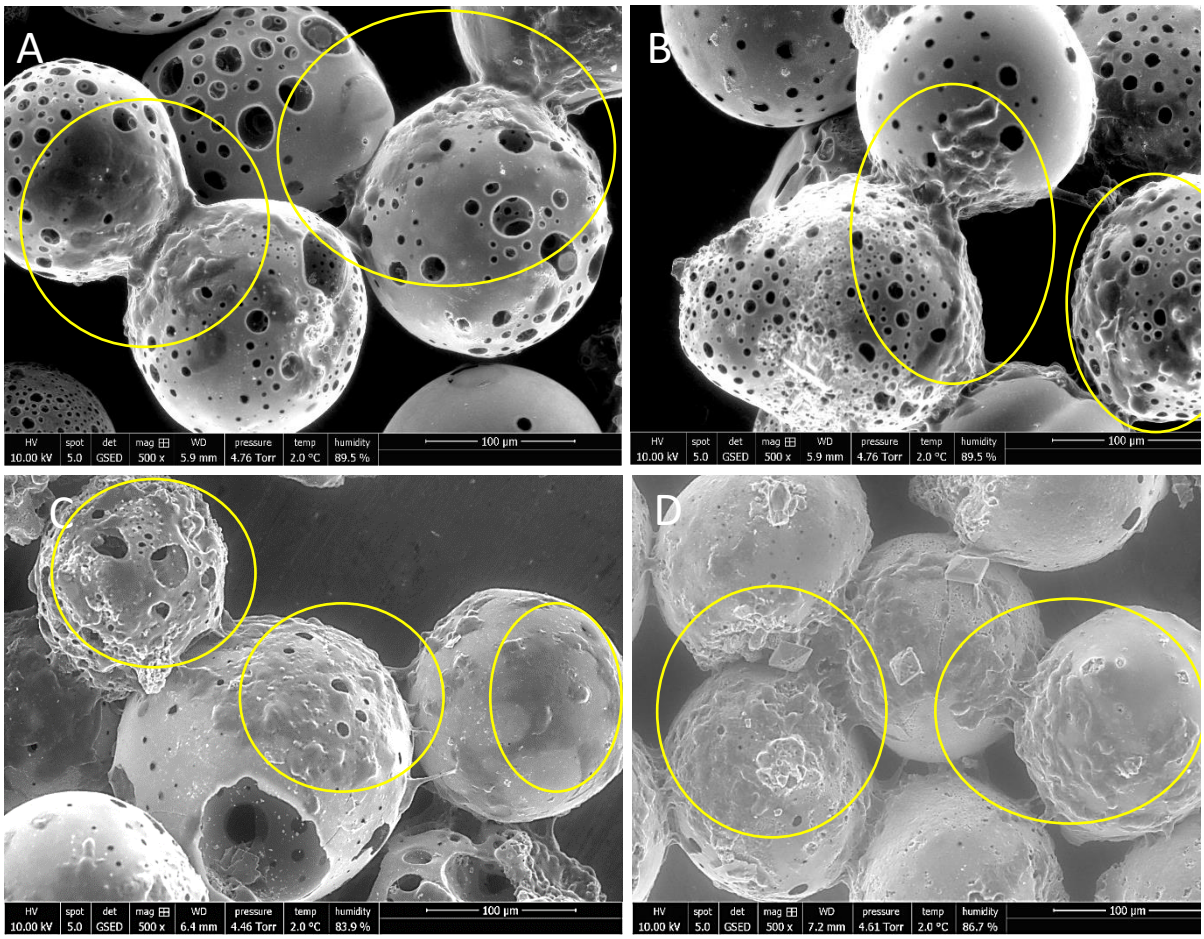

Figure 4.27 ESEM images of (A) P40 (B) P35 (C) P32.5 and (D) P30 PMS after 7 days direct culture with MG63 cells. Yellow circles indicate regions of cells attachment and the formation of colonies on the microspheres surface.

At a higher magnification it was possible to observe that MG63 cells appeared to have spread and colonised pore regions within the microspheres structure (Figure 4.28). It was also evident that cells were spreading and appeared to be displaying lamellipodia and filopodia projections that were bridging adjacent neighbouring microspheres as well as penetrating into the pores (Figure 4.28).

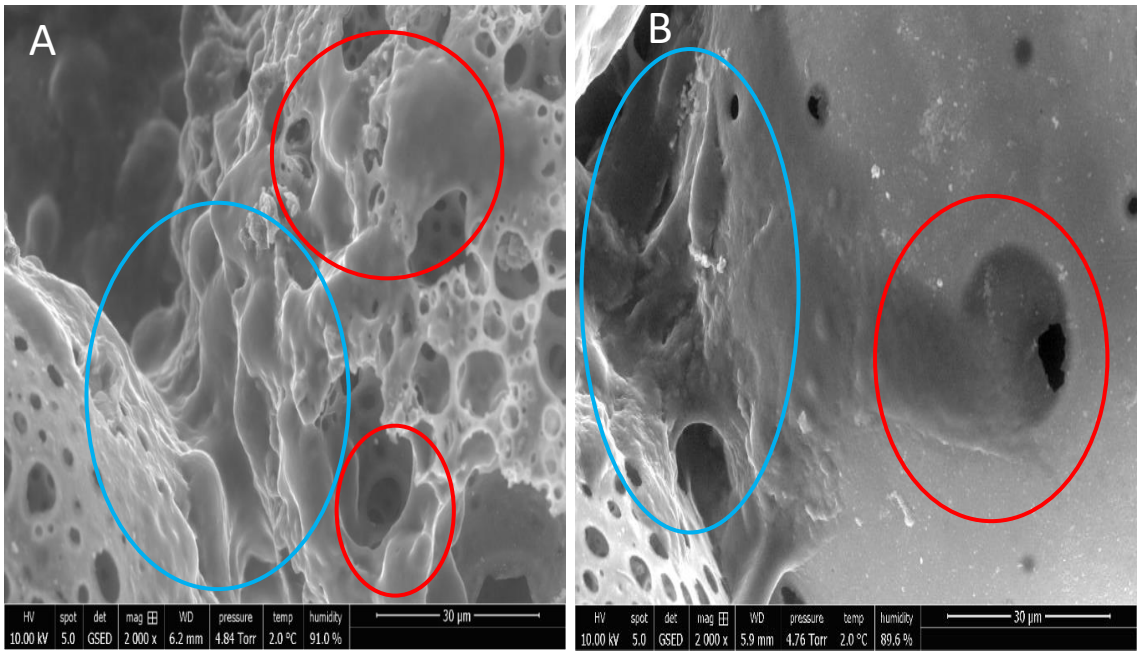

Figure 4.28 ESEM images of MG63 cells cultures on P30 porous microspheres after 7 days. (A) Red circles indicate regions of cells colonisation within pore regions and (B) blue circle indicating where cells have spread and attached to adjacent microspheres.

4.5 Doxorubicin loading and release studies

4.5.1 DOX loading studies

Doxorubicin (DOX) was used as a model drug to assess its loading and release kinetics from porous phosphate-based glass microspheres to ascertain their suitability for localised drug delivery for the treatment of bone cancers. For this study, porous microspheres with the highest phosphate content (P40) and the lowest (P30) were selected to see whether compositional differences affected drug loading and release. DOX encapsulation efficiency was determined by measuring the DOX concentration prior to and following loading within PBS using an orbital shaker (as explained in section 3.6.1). The encapsulation efficiency, as measured via UV–vis spectroscopy (see section 3.6.2), for P40 porous microspheres was 54.8% (± 1.4%, n = 6) and was statistically significantly lower for P30 porous microspheres at 29.1% (± 1.3%, n = 6) ($p < 0.0001$) (see Figure 4.29).

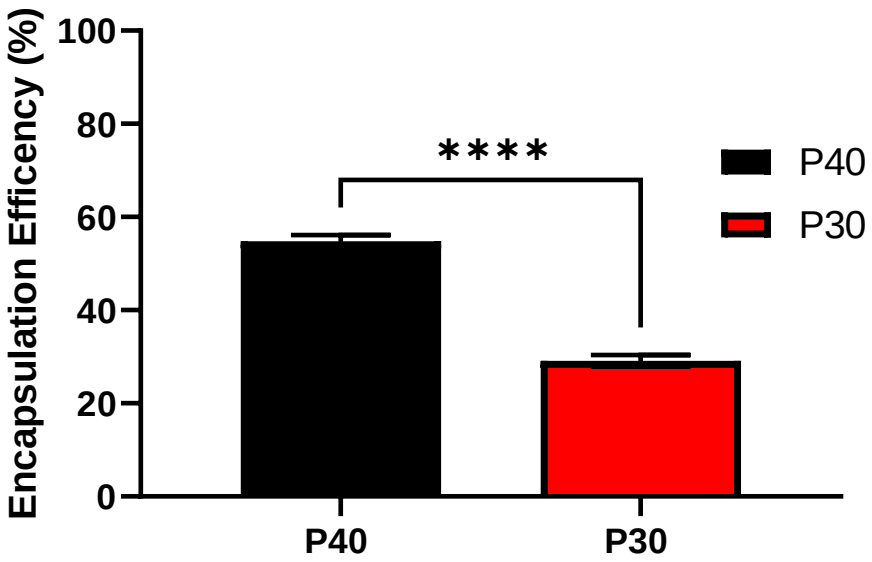

Figure 4.29 The encapsulation efficiency measured via *UV–vis spectroscopy* of DOX into P40 and P30 porous microspheres after 24 hours.

4.5.2 *In vitro* DOX release studies

In vitro DOX release studies were performed for both P40 and P30 microspheres at pH 7.4 and pH 5 over a 48-hour period. As seen in Figure 4.30A, the release rate of DOX from P40 PMS at both pH involved an initial burst release over the first 4 hours, which then plateaued slowly until 48 hours. A significantly greater quantity of DOX was released from microspheres within PBS with a pH of 5 compared to that of 7.4. At 4 hours, P40 microspheres in PBS at pH 5 had released 38.9% of the DOX compared to 27.6% at pH 7.4. By 48 hours the difference between the two had increased as much as 56.6% and 36.8% released in PBS at pH 5 and 7.4, respectively (see Figure 4.30A).

Figure 4.30B shows the same DOX release studies performed with P30 PMS. In addition to having a lower encapsulation efficiency, P30 PMS released a significantly reduced amount of DOX throughout the duration of the study. In a similar manner to P40 PMS, an initial burst release of DOX was seen during the initial 4 hours of immersion in PBS and then a more gradual release was observed until 48 hours. As with P40 PMS, a greater amount of DOX was released at pH 5 in comparison to pH 7.4. Even at pH 5, P30 PMS released 14.7% of DOX after 48 hours and this was only 3.0% at pH 7.4.

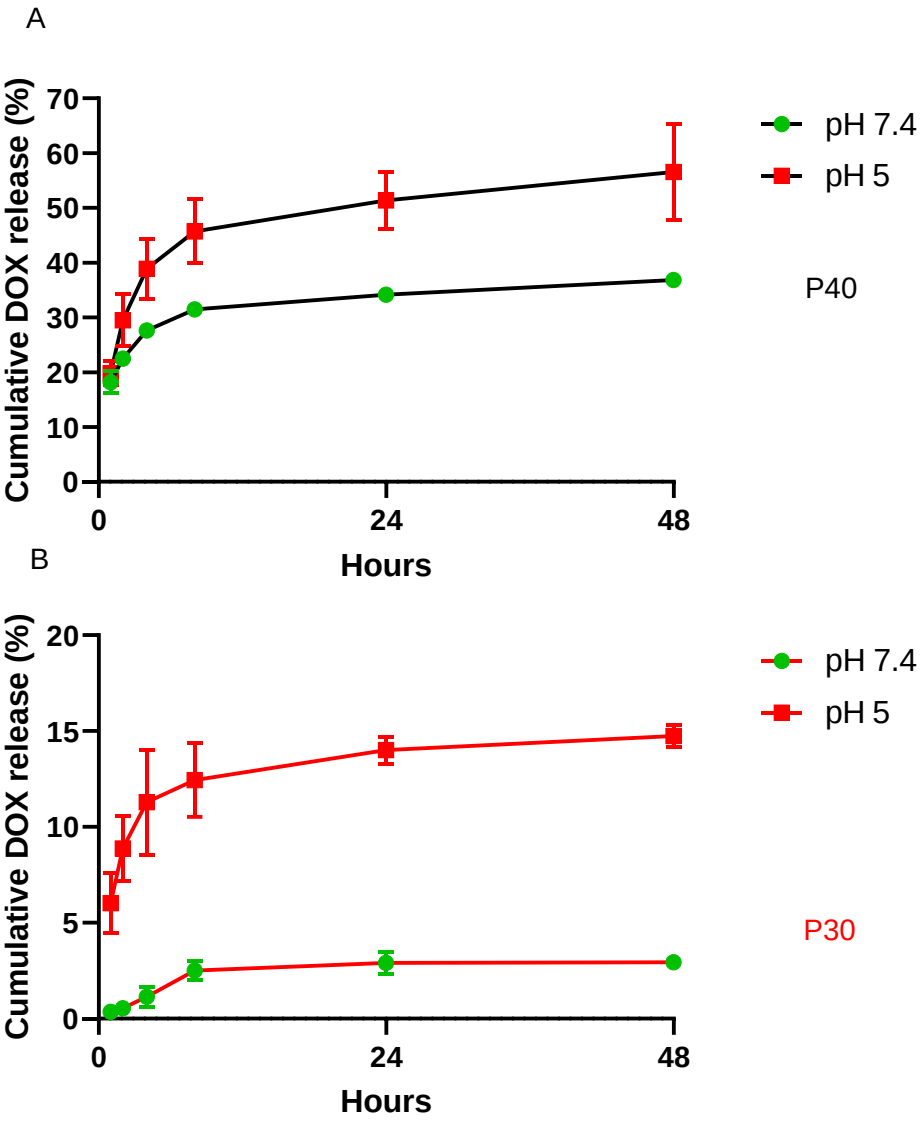

Figure 4.30 The cumulative drug release profiles of DOX from (A) P40 PMS and (B) P30 PMS within PBS at pH 7.4 and 5.0.

4.5.3 DOX release kinetics modelling

To investigate the release kinetics and associated release mechanisms of DOX from the microspheres, various mathematical models were applied, which included Zero order, First order, Higuchi and Korsmeyer–Peppas to understand the experimental release profile of DOX at the two different pHs. The release kinetics and mechanism were determined by fitting the release data to these models. The equations for each model are outlined in section 3.6.4. According to literature studies, the model which showed an R^2 value closest to 1 indicated the best fitting with the release profile data [137].

4.5.4 Zero order kinetics model

For the zero order kinetics model, the correlation coefficient value was calculated by plotting the percentage cumulative drug release against time as represented in Figure 4.31. For P40 PMS, poor linearity was observed at both pH 7.4 (R^2 = 0.655) and at pH 5 (R^2 = 0.586). Similar poor linearity was also seen for the P30 PMS at both pH 7.4 (R^2 = 0.429) and at pH 5 (R^2 = 0.405).

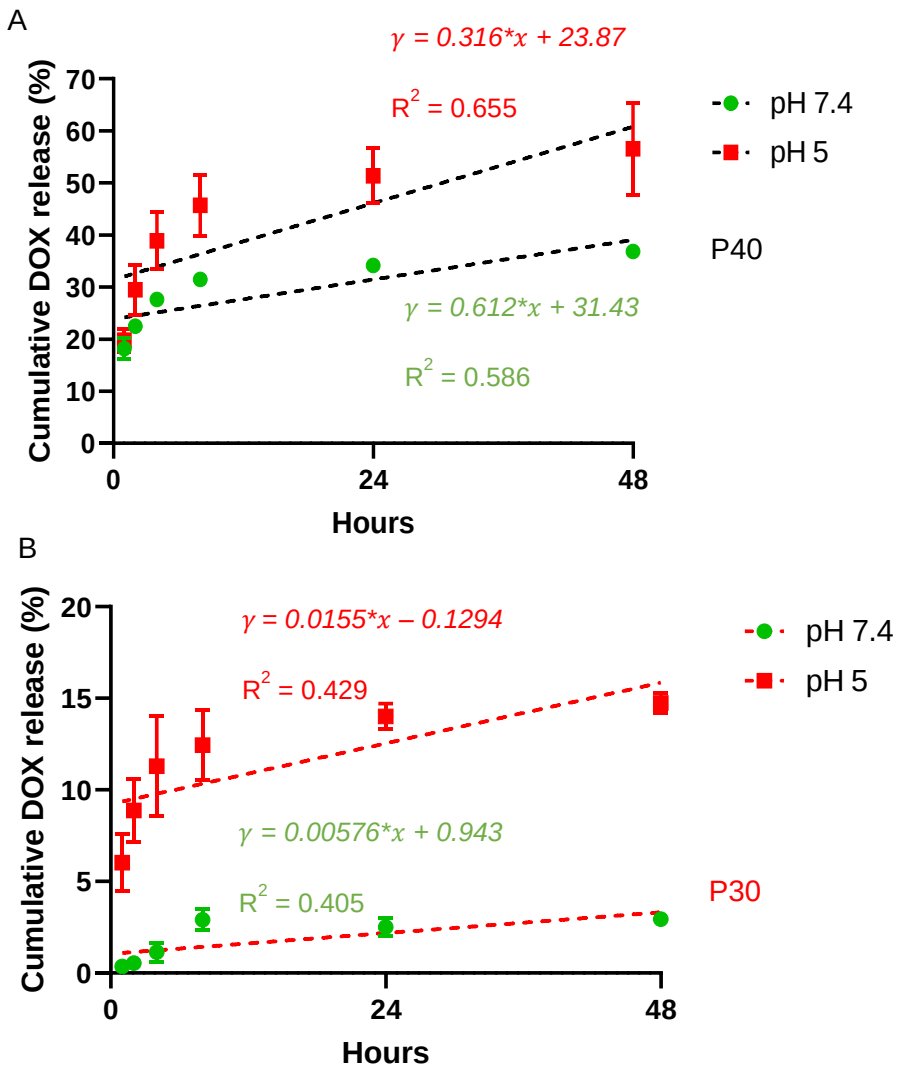

Figure 4.31 Zero order kinetics release model of DOX from (A) P40 PMS and (B) P30 PMS within PBS at pH 7.4 and 5.0.

4.5.5 First order kinetics model

The correlation coefficient value of first order kinetics was obtained by plotting the log cumulative drug release (as a percentage) *vs* time. As with the zero order model, both P40 PMS at pH 7.4 (R^2 = 0.567) and at pH 5 (R^2 = 0.549) as well as P30 PMS at both pH (R^2 = 0.567 for pH 7.4 and R^2 = 0.567 for pH 5) showed poor linearity (see Figure 4.32).

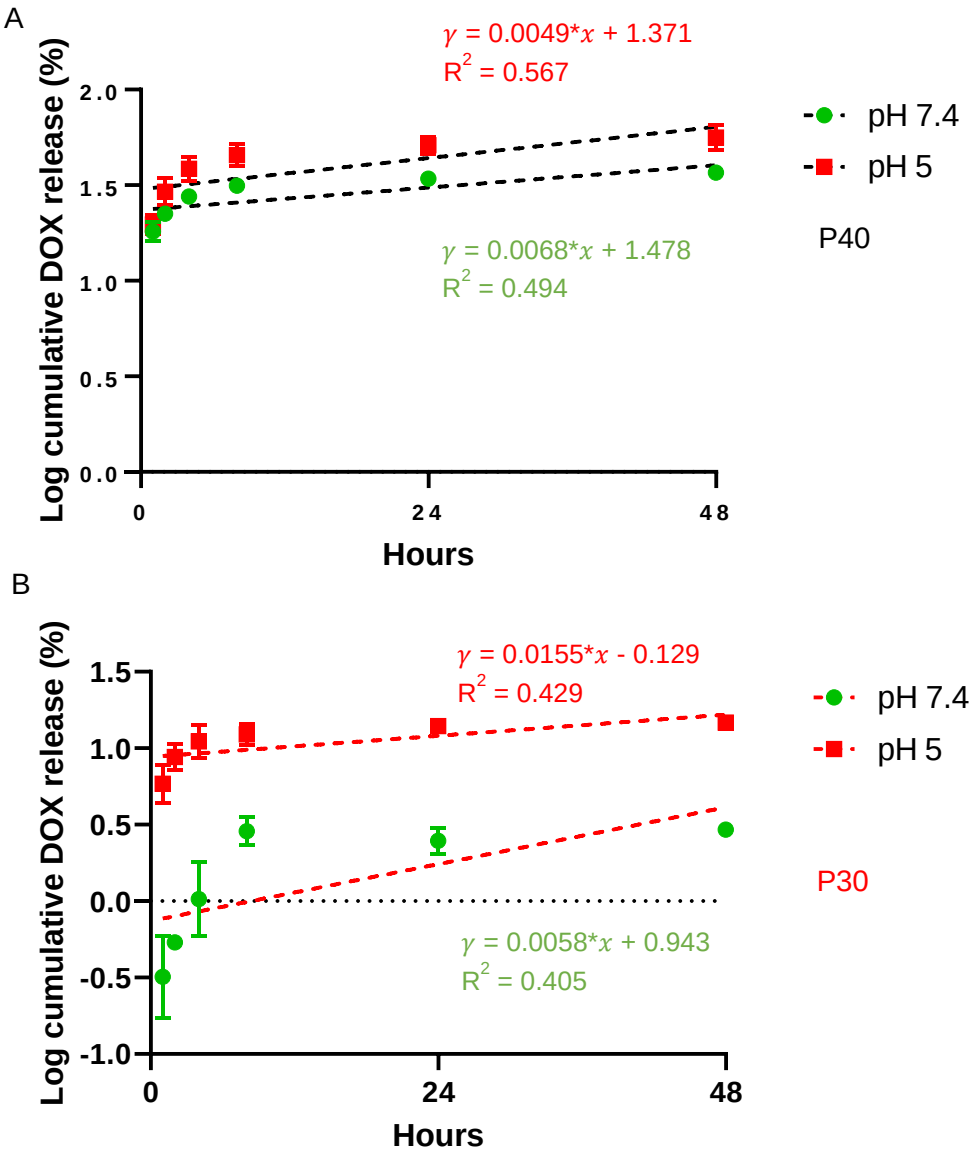

Figure 4.32 First order kinetics release model of DOX from (A) P40 PMS and (B) P30 PMS within PBS at pH 7.4 and 5.0.

4.5.6 Higuchi kinetics model

The Higuchi model was applied to evaluate the kinetics of DOX release from the PMS by evaluating the linear relationship between the amount of DOX released and the square root of time at the two pH values. P40 PMS were shown to best fit to the Higuchi model at pH 7.4 with an R^2 value of 0.909. An R^2 value of 0.803 was determined for P40 PMS at pH 5 with the linearity of P30 PMS being much lower with R^2 values of 0.617 and 0.626 at pH 7.4 and 5, respectively (see Figure 4.33).

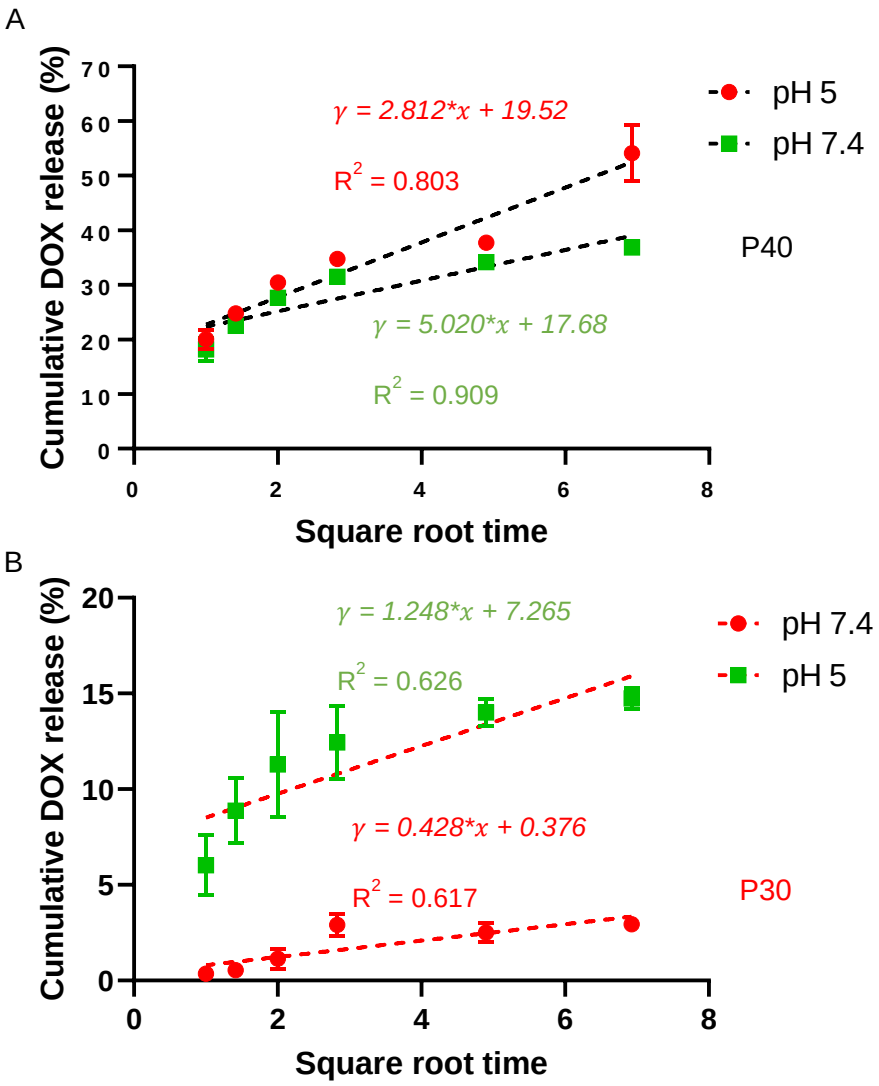

Figure 4.33 Higuchi release model of DOX from (A) P40 PMS and (B) P30 PMS within PBS at pH 7.4 and 5.0.

4.5.7 Korsmeyer-Peppas kinetics model

To further investigate the drug release mechanism, the release data was then fitted to the Korsmeyer-Peppas model. Here, P40 PMS showed better linearity at both pH 7.4 (R^2 = 0.812) and at pH 5 (R^2 = 0.891) in comparison to P30 PMS that had R^2 values of 0.693 and 0.752 at pH 7.4 and 5, respectively (see Figure 4.34). Despite the relatively low linearity, P40 PMS at pH 5 and P30 PMS at both pH 5 and 7.4 best fit to the Korsmeyer-Peppas model. The diffusion exponent or drug release exponent (n) values were calculated to be 0.251 and 0.176 for P40 PMS, which indicated Fickian diffusion as the release mechanism of DOX. For P30 PMS, n values of 0.217 and 0.590 at pH 7.4 and 5 also indicated that Fickian diffusion was the release mechanism at the lower pH but non-Fickian diffusion was indicated as the mechanism at pH 7.4 (see Figure 4.34).

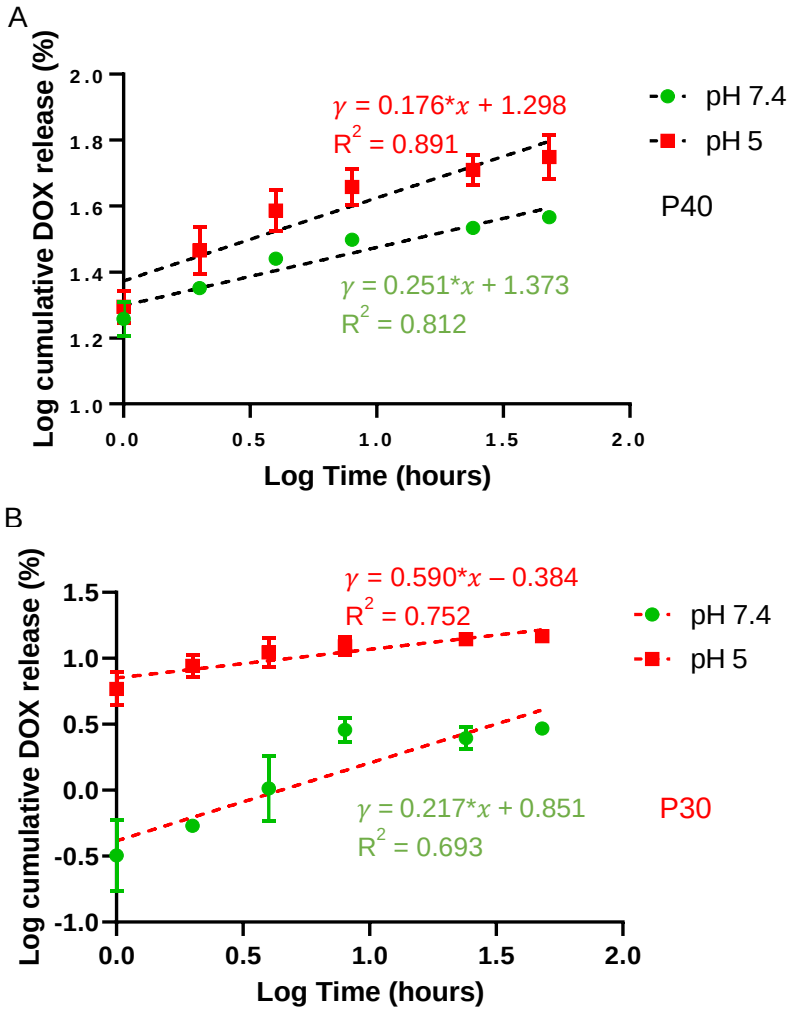

Figure 4.34 DOX release data from (A) P40 PMS and (B) P30 PMS within PBS at pH 7.4 and 5.0 fitted to the Korsmeyer-Peppas kinetics model.

The kinetic parameters such as the zero order rate constant (K_0), first order rate constant (K_1), Higuchi constant (K_H), diffusional exponent (n) and correlation coefficient (R^2) for the different kinetic models are presented in Table 4.6 for P40 PMS and in Table 4.7 for P30 PMS.

Table 4.6 DOX release kinetic parameters from P40 PMS at pH 7.4 and 5.

pH	Zero order		First order		Higuchi		Kormeyer-Peppas	
	K_0	R^2	K_1	R^2	K_H	R^2	n	R^2
7.4	0.316	0.655	0.0049	0.567	2.812	0.803	0.176	0.891
5	0.612	0.586	0.0068	0.494	5.020	0.909	0.252	0.812

Table 4.7 DOX release kinetic parameters from P30 PMS at pH 7.4 and 5.

pH	Zero order		First order		Higuchi		Kormeyer-Peppas	
	K_0	R^2	K_1	R^2	K_H	R^2	n	R^2
7.4	0.0155	0.429	0.0058	0.405	0.428	0.617	0.590	0.752
5	0.0058	0.405	0.0155	0.429	1.248	0.626	0.217	0.693

4.5.8 SEM analysis

SEM images were taken following the 48-hour release study to ascertain whether alterations to the pH of the solution had resulted in changes to the microspheres morphology. As seen in Figure 4.35, both P40 and P30 PMS showed no evidence of any significant degradation or morphological changes after 48 hours. In the pH 5 solution, there was evidence of a breakdown of the surface integrity of the microspheres and signs of degradation. This was more prominent in the P40 PMS in comparison to the P30 PMS.

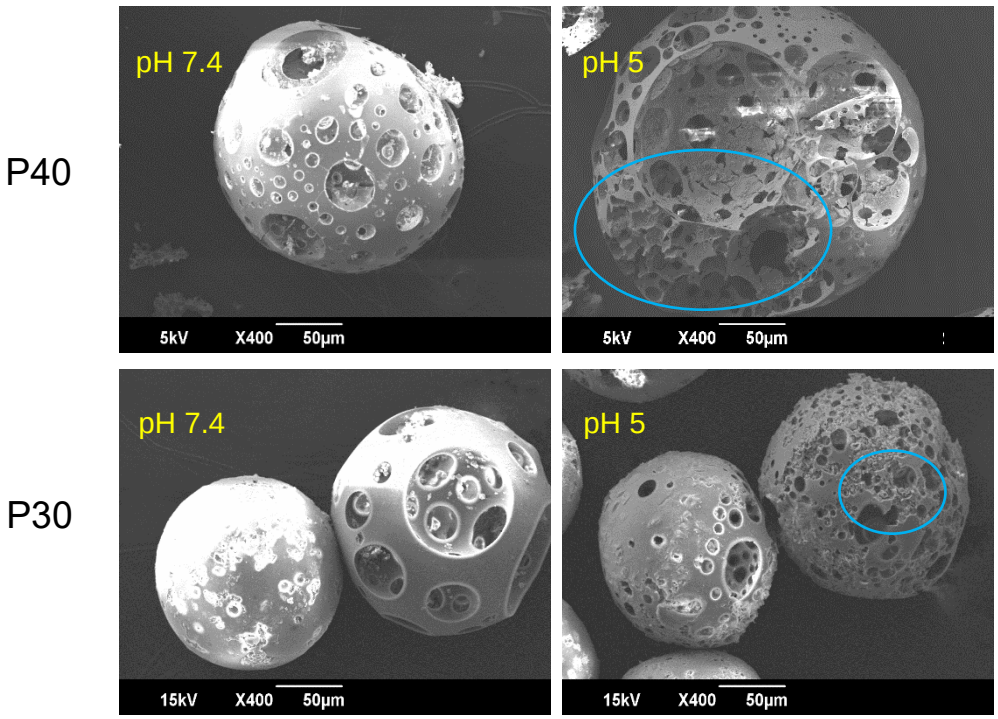

Figure 4.35 SEM images of P40 and P30 porous microspheres following 48-hour release study. Areas of degradation circled in blue.

4.5.9 Confocal laser scanning microscopy

Confocal laser microscopy was employed to confirm the encapsulation and distribution of DOX within porous P40 microspheres. As seen in Figure 4.36, following 24 hours of DOX loading clear red fluorescent regions were visible on and within the cross-sections of the porous P40 microspheres, indicating the presence of DOX. No red fluorescent regions were detected in the P40 samples that had not been loaded with DOX.

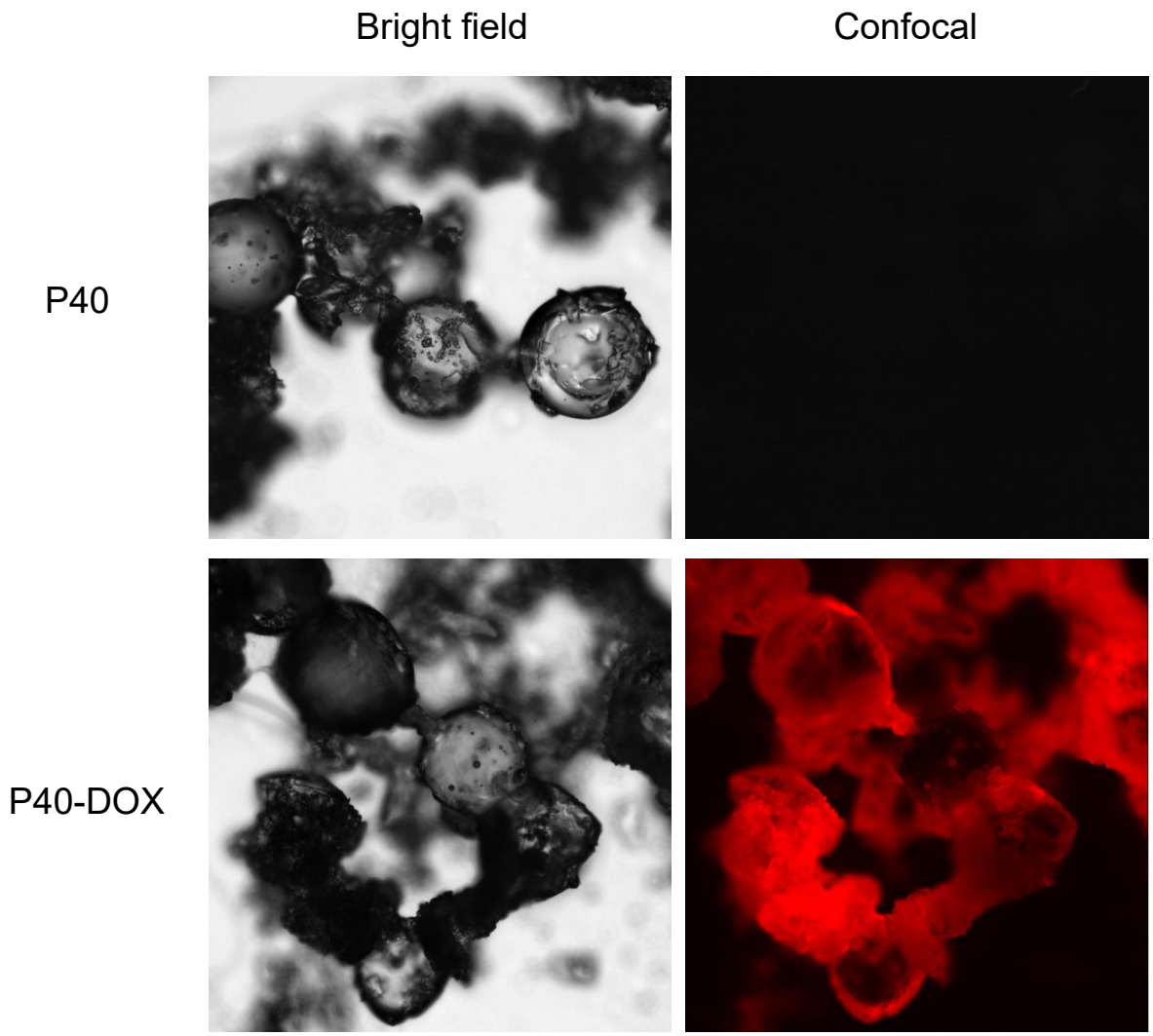

Figure 4.36 Bright field and Confocal laser microscopy images of P40 and DOX-loaded P40 porous microspheres following 24 hours of encapsulation.

4.6 Discussion

Recently, studies have shown that bioactive materials consisting mainly of pyro- and ortho-phosphate species show highly favourable cytocompatibility responses [107, 109]. These phosphate species have been shown to play a vital role in bone mineralisation as well as stimulating osteogenic differentiation, matrix gene expression and ALP activity in osteoblasts [108].

In this work, PBG formulations termed P40, P35, P32.5 and P30 were produced and EDX analysis confirmed that the elemental compositions of the starting glasses produced were within 1.5% error margin of the target values. This is commonly seen in other studies involving phosphate glasses where a 1 – 2 mol% error between the theoretical and empirically obtained values is usually observed [138]. The slight discrepancies between the expected and target values reported in other studies on phosphate-based glasses are often attributed to the hygroscopic nature of phosphate precursor salts used in the glass manufacturing process [139].

A high yield (>90%) of both solid and porous microspheres, in the size range of 125 – 200 µm, were successfully processed from each composition using the flame spheroidisation process developed within the research group. For the porous microspheres at each composition, pores of varying diameters were present throughout the surface and inner body of the microspheres and were shown to be interconnected. Evaluating the elemental composition of the glass formulations and of both solid and porous microspheres revealed that processing into porous microspheres had a more pronounced effect on the composition than processing into solid microspheres. The addition of calcium carbonate as a porogen resulted in in all PMS having elevated CaO content in comparison the starting glass formulation (Figure 4.9). This was seen to the greatest extent in P40 PMS and not only did this correlate with the greatest decrease in P_2O_5 but also the increased porosity observed in this formulation (Figure 4.4).

Cross-sectional SEM images of resin embedded porous microspheres revealed that the pores were not limited to the surface of the microspheres but exhibited inner porosity and interconnected pores (Figure 4.4). The interconnected porosity will have increased the surface area of the microspheres thereby increasing the rate of degradation and subsequent release of therapeutic ions [140]. It is hypothesised that the increased surface area would also facilitate greater potential to load the microspheres with therapeutic cargo (such as chemotherapeutics or growth factors) and subsequent release of cargo from the microspheres. The cross-sectional SEM images also revealed that some of the microspheres from each glass composition had pores on their surface but a solid core. This may have been due to the glass

particles not having resided within the flame during spheroidisation for long enough or at a region hot enough for the whole glass particle to become molten [117]. It is possible that there may not have been sufficient porogen mixed with and in close proximity to those glass particles.

XRD analysis confirmed that processing of the P40, P35 and P32.5 glass formulations into solid microspheres resulted in the retention of their amorphous nature. However, when processing into porous microspheres crystalline peaks were observed which were attributed to residual porogen remnants within the microspheres which had not been fully removed during the wash step. Conversely, crystalline regions were detected in P30 solid and porous microspheres by both XRD and ^{31}P MAS-NMR spectroscopy (Figure 4.7 and Figure 4.13).

Quantitative 1D ^{31}P MAS-NMR spectroscopy was used to explore the distribution of the phosphate glasses Q^n species and for both solid and porous microspheres. The individual Q^n species each have a topologically unique and characteristic role within the glass network structure: Q^0 (isolated), Q^1 (terminating) or Q^2 (bridging) (see Figure 4.37). Structural analyses revealed that as the phosphate content of the glass particles and the microspheres decreased, a gradual decrease in structural connectivity (Q^2 to Q^1 to Q^0) and increased average number of non-bridging oxygen atoms was observed. The ^{31}P MAS-NMR data showed an absence of Q^0 species for P40 glass and a considerable increase from less than 1% for P35 glass up to 18% and 32% for P32.5 and P30 glass, respectively. The increase in Q^0 as phosphate content decreased was accompanied with a subsequent decrease of Q^2 and Q^1 species (Figure 4.12). These changes were attributed to the higher proportion of modifier oxides present in the lower phosphate content glasses, which indicated that more non-bridging oxygens were needed to charge balance the cations. This led to a greater number of oxygen atoms that were therefore unable to covalently bond with adjacent phosphate tetrahedra leading to depolymerisation of the glass network [141].

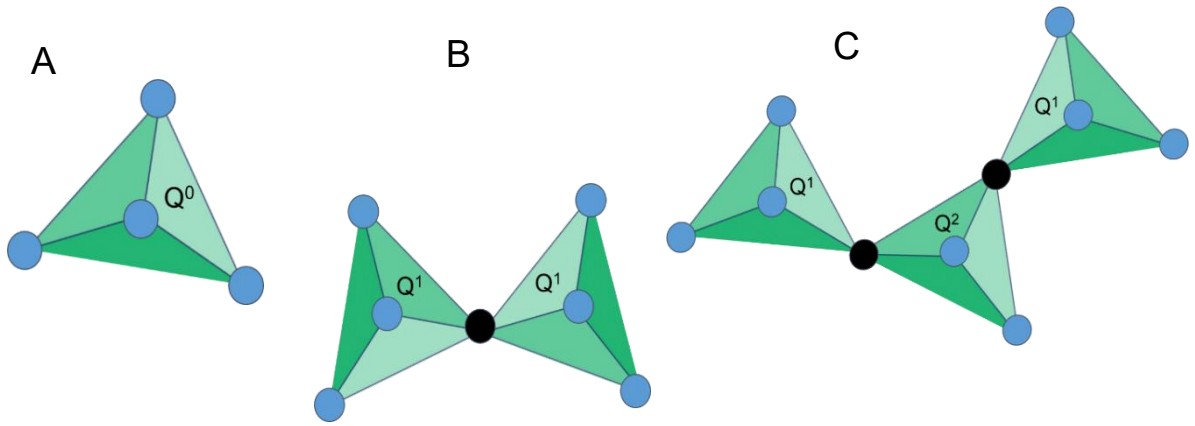

Figure 4.37 The structure of (a) Q^0 orthophosphate, (b) Q^1-Q^1 pyrophosphate and (c) Q^1-Q^2-Q^1 metaphosphate chain displaying the tetrahedral phosphate environments. Bridging oxygen atoms are displayed in black and non-bridging oxygen atoms in blue.

As seen in Figure 4.12, the P30 glass, solid and porous microspheres contained exclusively Q^0 and Q^1 tetrahedra at an approximate 1:2 ratio. The glass compositions used in this study were considered 'invert glasses' as the network modifier ions govern the properties of the glass rather than the anionic network forming ions [100]. Previous studies found that invert phosphate glasses, in the series P_2O_5-CaO–Na_2O–MgO (where P_2O_5 content ranged from 39.4 to 28.7 mol%), were predominantly formed of pyro ($P_2O_7^{4-}$) and orthophosphates (PO_4^{3-}) [142]. Q^0 orthophosphates replace the role of the network modifying cations Ca^{2+}, Na^+ and Mg^{2+} and act to charge balance the cations [141]. In the absence of Q^2 or Q^3 species in P30 samples, Q^1 must be present as Q^1-Q^1 dimers, which subsequently creates inorganic pyrophosphate group ($P_2O_7^{4-}$). As a result of this, it is proposed that P30 samples are therefore not composed of a cross-linked or two-dimensional structure of polymerised phosphate tetrahedra. Instead, they are arranged through a distribution of isolated molecular PO_4^{3-} and $P_2O_7^{4-}$ anions, which electrostatically interact with the surrounding Ca^{2+}, Na^+ and Mg^{2+} ions [126].

Although 1D ^{31}P MAS-NMR provided information on the structure of the glass through quantitative information on the distribution and abundance of Q^n species, it is unable to investigate the connectivities of the tetrahedra and probe the longer-range (~1 nm) structure of the glass [143]. In order to achieve this two-dimensional (2D) NMR experiments can be used to determine the network connectivity of the glass where magnetisation between nuclei can indicate the proximity of nuclei [144].

1D ^{31}P MAS-NMR spectroscopy showed that the higher the phosphate composition of the samples studied, the greater the proportion of covalently bonded phosphate species present. 2D ^{31}P MAS-NMR spectroscopy revealed that the phosphate chain length appeared not to exceed a maximum of three phosphate tetrahedra for P35 and P32.5 samples. Despite P35 glass containing 18% Q^2 species and less than 1% Q^0 species, its structure can still be regarded as a distribution of isolated molecular anions surrounded by Ca^{2+}, Na^+ and Mg^{2+} ions [141].

Processing the phosphate glasses into porous microspheres resulted in a more significant change in the Q^n species than processing into solid microspheres. EDX analysis revealed that the addition of $CaCO_3$ (which was used to induce porosity in the microspheres) resulted in an increase in CaO content compared to the initial glass sample. This increase caused a subsequent decrease in the proportion of P_2O_5, MgO and Na_2O (Figure 4.9). The additional calcium cations incorporated into the glass structure introduced an excess of positive charge that resulted in an increase in the quantity of non-bridging oxygens to neutralise the charge balance. In order to achieve a greater proportion of non-bridging oxygen atoms network depolymerisation must occur and is seen with the increased proportion of Q^0 and a decrease primarily in Q^2 but also Q^1 species [126].

A high proportion of orthophosphate (Q^0) and pyrophosphate (Q^1) species were detected for the P32.5 and P30 glasses, which were likely responsible for the high crystallisation tendency of these glasses during manufacture (especially P30) [106]. The tendency for a glass to crystallise is closely associated to the viscosity of the melt, with lower viscosities facilitating the arrangement of the components into an ordered crystalline structure more easily. The disrupted structure created by the short phosphate units meant that the P30 and P32.5 glasses had a lower viscosity of the melt and therefore higher tendency to crystallise [126]. This was the likely reason that crystalline peaks were observed for P30 SMS and PMS following processing but were not seen in the other formulations. Nevertheless, it should be noted that porous microspheres were still successfully produced from both these formulations. The 1D ^{31}P MAS-NMR spectra identified crystalline regions within the structure of P30 solid and porous microspheres that were likely due to two distinct crystal Q^0 structures (Figure 4.13). It is postulated that these phases are Sodium Calcium Phosphate (α- Na_3CaPO_4) and Sodium Phosphate (β-Na_3PO_4) that were identified via XRD (Figure 4.7).

The glasses used in this study have been formulated to largely be composed of pyrophosphates and in the case of P30 exclusively from pyro and orthophosphates. Pyro and orthophosphate ions play a vital role in bone mineralisation. Pyrophosphates are known to be inhibitors of HA formation and therefore control biomineralisation [145]. Alkaline phosphatase

(ALP) is released by active osteoblasts which hydrolyses pyrophosphate ions into orthophosphates [67]. This results in the loss of inhibition of HA formation and causes super saturation of orthophosphates in the extracellular fluid thereby inducing mineralisation [109]. It is hypothesised that the high pyrophosphate and orthophosphate content within the microspheres may provide enzymatically controlled levels of these ions that are required and beneficial for enhanced mineralisation.

Evaluation of the apatite forming ability of a bioactive glass can provide useful information about its potential bone-bonding ability *in vivo*. In this study the Bioglass Technical Committee 4 (TCO4) of the International Commission on Glass (ICG) method was used for evaluating the apatite-forming ability of bioactive glasses *in vitro* [136]. This was due to the TCO4 method fixing the particle mass per solution volume ratio instead of fixing the surface area to volume ratio when comparing samples. As well as the glass microspheres used throughout this study, 45S5 Bioglass particles of the same size range were used during this set of experiments as positive controls. Immersion of 45S5 within SBF confirmed the apatite-forming ability of the SBF solution (Figure 4.22). Analysis of SEM images revealed that HA-like deposits were present on 45S5 particles after 7 days immersion in SBF. These depositions on 45S5 increased in size and frequency with increased immersion time. Small depositions were first present on P30 porous microspheres after 14 days immersion and increased in prevalence by day 28. The presence of these depositions was not conclusive in confirmation of apatite formation.

XRD analysis was performed to identify and differentiate crystalline phases present on the glass microspheres following immersion in SBF. By day 28, P30 and P32.5 microspheres exhibited peaks that corresponded to dicalcium phosphate dihydrate (DCPD), whilst P40 and P35 porous microspheres only exhibited $CaCO_3$ peaks that were present in all the compositions. The Ca:P ratios (wt%) at day 28 for P32.5 (0.68) and P30 (0.84) porous microspheres were within the range suggested for precipitated amorphous calcium phosphate (ACP) (0.67 – 1.5) [146]. It has been reported that precipitated ACP formed on calcium phosphate biomaterials acts as a precursor phase towards the eventual formation of HA [147]. DCPD and other calcium orthophosphates, such as octacalcium phosphate (OCP), are also known to form prior to precipitation of HA crystals on phosphate based bioactive glasses [148]. The lack of apatite-like depositions on metaphosphate glasses has been reported in other studies. Kasuga *et al.* performed NMR analysis of ternary phosphate glasses in the system xCaO·(90 – x)P_2O_5·10TiO_2 (x = 45 ~ 60) [149]. It was reported that 60CaO·30P_2O_5·10TiO_2 glass contained orthophosphate and pyrophosphate groups, whereas glasses with a higher P_2O_5 content consisted predominantly of metaphosphate groups. Studying the apatite forming

ability of these glasses revealed that a bonelike apatite phase formed on the surface of the $60CaO{\cdot}30P_2O_5{\cdot}10TiO_2$ glass particles following 7 days immersion in SBF. Additionally, it was reported an apatite-like phase did not form on the metaphosphate glasses [150]. However, the P30 and P32.5 glass formulations developed which contained high proportions of orthophosphates and pyrophosphates did exhibit greater bioactivity and cytocompatibility, which would lead to more favourable environments to promote bone repair and regeneration than the other higher phosphate species containing glasses.

Phosphate-based glasses have the potential to aid in bone repair and regeneration by the controlled release of therapeutic ions in a targeted manner. The glass compositions used in this work were tailored to contain a high proportion of calcium, magnesium, and phosphate to be released in a controlled fashion to aid bone regeneration. These ions are not only present in the inorganic component of bone but their release from the microspheres are intended to play an important role in the formation of new bone by stimulating growth and osteogenic differentiation of cells via continuous release of Ca^{2+}, PO_4^{3-} and Mg^{2+} ions. Several studies have reported that up to a concentration of around 5 mM, the addition of PO_4^{3-} and Mg^{2+} ions during stem cell culture can enhance the osteogenic activity of the cells [151]. The microspheres are releasing several ions simultaneously so it may be difficult to ascertain the role those individual ions are having on cell activity. However, biomaterials that can provide a bioactive surface and release specific ions are likely to have a synergistic effect that can cause an increase in the materials ability to promote bone formation [152]. The dissolution of the glass microspheres must not be too rapid as extraphysiological levels of certain ions can result in toxicity and have detrimental effects on vital homeostatic mechanisms [96]. Many therapeutic ions are unable to be administered systemically due to potential off-target effects, which can be mitigated by localised delivery. It is therefore of great advantage to be able to have a predictable release rate of therapeutic ions from a biomaterial and being able to alter or fine tune the release by changes to the physico-chemical composition of the material. Tailoring the morphology of the phosphate-based glass product can also impart further control on degradation and subsequent release of ions.

The porous P40 microspheres released a significantly greater amount at an increased rate of all the ions in comparison to the other three porous microsphere formulations. Microspheres from each of the four porous formulations exhibited linear ion release profiles and as the phosphate composition decreased from P40 to P30 this was accompanied by a subsequent decrease in ion release (Figure 4.16). The quantity and rate of ion release from P40 PMS correlated well with previous studies that investigated ion release from porous microspheres of the same formulation [1]. It is well established that the dissolution behaviour of phosphate

glasses depends on the phosphate anions and the associated metal ions that constitute the glass structure [153]. The P35, P32.5 and P30 formulations are considered as invert glasses as their properties are controlled by the interactions of cations with the phosphate groups rather than the P_2O_5 network and the entanglement of phosphate chains [100]. P32.5 and P30 microspheres released the lowest amount of all the ions and in comparable amounts, including Ca^{2+} which they contained a greater amount of in comparison to the other formulations. Calcium ions within phosphate glasses are known to have strong complexing abilities with linear polyphosphates forming cross-linking interactions which strengthen the glass network [154]. A more compact phosphate glass network, due to the presence of ortho and pyrophosphate groups and increased cross-linking, is responsible for the lower solubility and subsequent ion release profiles due to the inability of water molecules to easily penetrate and hydrate the structure [155]. Although there was variation in the quantities of ions released, all four porous microspheres formulations released calcium, phosphate, magnesium and sodium ions throughout the duration of the study. Continued, localised ion release from the microspheres could deliver therapeutic ions in a site-specific manner, which would not only optimise their therapeutic efficacy but minimise any off-target effects [156]. The role of ions, such as calcium, phosphate and magnesium, within the bone regeneration processes have been established with them primarily acting as enzyme co-factors. They are therefore able to stimulate various signalling pathways and their controlled release can influence stem cell differentiation down specific lineages and be harnessed to increase osteogenesis [157]. The conversion of mesenchymal stem cells (MSCs) down the osteogenic lineage into osteoblasts is a vital process to facilitate bone mineralisation at sites of osseous tissue damage during bone remodelling and repair [158]. ICP analysis was unable to determine the specific phosphate species released by the microspheres. However, it has been reported that some of the phosphate anions released into solution are the same structural units present from the glass. Phosphate chains released from the glass surfaces then dissolve (via hydrolysis) in aqueous conditions to smaller phosphate units [159].

From the indirect cell culture studies performed (using microsphere degradation conditioned media from each of the four formulations) to assess cellular responses, it was demonstrated that the ion release products from the microspheres were cytocompatible. Cells grown in all four microsphere conditioned media had either comparable or significantly increased metabolic activity in comparison to cells grown in SM (Figure 4.23). At day 7, a trend was observed where increasing metabolic activity correlated with decreasing phosphate content in the microspheres. Cells grown in P30 conditioned media revealed a significantly higher metabolic activity response to cells grown in all other conditions except for those in P32.5 conditioned media. Ion release studies (Figure 4.16) revealed that the release rate of all ions

decreased as the phosphate content in the microspheres decreased. As highlighted above, the ^{31}P MAS-NMR revealed that P30 microspheres were formed exclusively from ortho- and pyrophosphate species and that P32.5 were also comprised of a greater proportion of these species in comparison to P35 and P40 microspheres. It is suggested that the concentration of ions and the specific phosphate species released from the microspheres resulted in the increased metabolic activity for the MG63 cell line. As shown in Figure 4.17, the ion release products from the four porous microsphere formulations did not result in radical changes or fluctuations to the pH of solution. Therefore, the profiles observed most likely created a stable and highly favourable microenvironment for cell growth and proliferation.

After 7 days of indirect culture from the four phosphate-glass microsphere formulations, the MG63s grown in P40 conditioned media revealed significantly higher ALP activity in comparison to the three other microsphere formulations (Figure 4.24). As seen in Figure 4.16, the P40 microspheres degraded faster and hence released a greater quantity of ions. In a study by Gupta *et al*., hMSCs exposed to solid microspheres, with the same P40 glass formulation also resulted in higher ALP activity compared to cells cultured in the slower degrading borosilicate ($1.7CaO{\cdot}7.11Na_2O{\cdot}78.6SiO_2{\cdot}9.5B_2O_3{\cdot}3.1Al_2O_3$) and P45 ($45P_2O_5{\cdot}16CaO{\cdot}24MgO{\cdot}11Na_2O{\cdot}4Fe_2O_3$ mol%) microsphere conditioned media [117]. The correlation between increased ALP activity for the faster degrading microsphere formulation, in comparison to the slower degrading formulations, was also seen in the present study. Intracellular Ca^{2+} has been shown to enhance glutamate secretion inside cells, which has been proposed as one mechanism for promoting osteogenic fate of osteoprogenitor cells [160]. The Ca^{2+} and other ions released from the P40 microspheres may have led to a greater osteogenic effect in comparison to the other microsphere formulations investigated. Conversely, Gupta *et al*. showed hMSCs exposed to P40 solid microsphere media also resulted in cells revealing higher metabolic activity in comparison to the slower degrading microsphere formulations, which was not seen in this study. It is vital to assess the effect that degradation products of the microspheres have on cell response as this greatly influences the success of a material for bone repair applications.

The direct cell culture method exposed cells to both the effects of the microsphere dissolution products as well as to the physical environment via contact with the materials themselves. All four porous microsphere formulations showed cell growth over the 7 days of culture tested (Figure 4.25). In contrast to the indirect study, there was no significant difference in the metabolic activity of cells regardless of which microsphere formulation they were grown on. A study by De Melo *et al.* explored how tailoring the phosphate species within phosphate-based glasses effected the adhesion of hMSCs to the glass surface. As the phosphate content

decreased from 40 to 30 mol% in the glass series (40-*x*)P_2O_5·(16+*x*)CaO·24MgO·20Na_2O (*x* = 0,5 and 10 *mol*%) depolymerisation of the glass network resulted in the formation of a greater abundance of ortho- and pyrophosphate species at the expense of metaphosphate species. This decrease in phosphate content in this glass series correlated with an increase in the number of hMSC's that adhered to the polished surface of the flat glass discs and greater metabolic activity of cells after 24 hours. This effect was not seen in the present study, where MG63 cells were used and cultured over a longer time on phosphate glasses but with a different morphology and geometry.

Studies involving longer *in vitro* cell culture are required to establish further how the chemical formulation, geometry and degradation products of the microspheres could affect cell growth. Visible signs of some surface deformation was present in the higher phosphate containing microsphere after 28 days in both milli-Q water and SBF (Figure 4.18 and Figure 4.21). These cracks and delamination may result in decreased cell attachment, loss of extracellular matrix deposition from established cells and reduced proliferation [161]. Deformation and the effects of degradation are likely to be exacerbated in highly porous microspheres, where low-volume areas and small struts that connect adjacent pores are most susceptible to damage. In this work, P40 microspheres exhibited the greatest degree of porosity as well as being the fastest degrading formulations. It may be that increased breakdown of the material surface coupled with the release of fragments or particulates from the microspheres could negatively affect cells in long-term culture [162].

Changes to the surface integrity of biomaterials can affect the ability of cells to adhere to their surface. Figure 4.18 highlights the surface morphology of the microspheres following 28 days immersion in milli-Q water and revealed that the majority of microspheres remained intact at this point and similar images were acquired following 28 day immersion in SBF (Figure 4.21). It is likely that the 7 days over which the cells were cultured on the microspheres, there was not a drastic breakdown to the physical surfaces of the microspheres and would therefore be unlikely to impair the ability of the cells to adhere. Both the physical attachment of the cells as well as the cellular microenvironment will affect the rate of degradation of the microspheres. The stable glass surface and gradual ion release from all glass formulations in this study is likely to be creating favourable environments devoid of drastic pH (Figure 4.17) and osmolarity fluctuations that can be detrimental to the osteogenic response and potential of the cells [163].

Previous studies involving direct cell culture with phosphate-based glass microspheres showed that cells attaching to and proliferating on and between adjacent microspheres alongside colonisation of the inner pore regions [1]. This was also observed in the present study, further indicating the suitability of the porous microspheres as substrates for cell growth

and proliferation (Figure 4.27). Biomaterials that facilitate bone repair and regeneration would ideally be both osteoconductive (provide optimum conditions for bone growth) and osteoinductive (induce stem cell differentiation down the bone lineage). Additional desirable characteristics that significantly enhance the regenerative potential of the material are mechanical stability and porosity [164]. An interconnected, 3D network of pores has been shown to facilitate cell attachment and allow for the infiltration of osteoblastic and vasculature cells that support matrix deposition and the ingrowth of new bone [165]. Microporosity has been attributed to promoting bioactivity and protein interaction, whereas larger pores, ranging from 1 - 100µm, support cell adhesion, proliferation and migration [166].

The essential and synergistic role of phosphate anions in combination with calcium and magnesium cations for the development of new bone tissue is well established [167]. Ortho- and pyrophosphates can directly influence the natural cycle of bone formation and resorption and are utilised to increase the generation of new bone tissue and stimulate HA crystallisation. Orthophosphates are vital for the mineralisation of collagen fibres formed from osteoblasts within the remodelling process [168]. Inorganic pyrophosphates can modulate biomineralisation by acting as both an inhibitor for mineralisation but also as a source of orthophosphates following their hydrolysis by ALP. Furthermore, pryophosphates can stimulate extracellular matrix gene expression, ALP activity and differentiation of osteoprogenitor cells [108].

The phosphate-based glass formulations produced herein have huge potential for hard tissue engineering applications due to their ability to influence biomineralisation through their release of specific ions in a controlled manner [169]. Microspheres that release ortho- and pyrophosphate species may provide enzymatically controlled levels of the inorganic components required for mineralisation [109]. Biomaterials such as these can be tailored to induce specific biological responses as opposed to materials that are designed solely to mimic a component of a biological structure [170]. The P32.5 and P30 porous microspheres used in this study were designed to release ortho- and pyrophosphate anions in addition to calcium, magnesium and sodium cations to create a favourable micro-environment for the migration, proliferation and differentiation of osteoblast and osteoprogenitor cells. They act not only as vehicles to deliver ions but provide a surface structure to improve osteointegration of new bone tissue, whilst limiting inflammatory or fibrotic responses following *in vivo* delivery. The microsphere size and morphology facilitate their delivery via minimally invasive (injection) techniques and allows them to be utilised for orthobiological applications [171]. Ideally, the microspheres would release ions that stimulate osteogenesis, support cell growth upon their surface and degrade at a suitable rate for new bone tissue formation [22].

Surface structures and geometries have been shown to directly influence cellular responses including adhesion, proliferation and osteogenic differentiation [172]. *In vivo* studies have indicated that collagen deposition and new bone formation occurs preferentially at concavities on biomaterial surfaces, further signifying the potential for porous microspheres to influence osteogenic differentiation over extended culture periods [173]. It may be that these concavities resulted in the increased ALP activity of cells grown directly on the microspheres in comparison to those on TCP (Figure 4.26). The increased ALP activity seen for cells cultured on the porous microspheres suggests that the microspheres provided a more favourable surface for influencing osteoblast cell differentiation and mineralisation of bone compared to TCP. A possible upregulation in ALP activity of the cells directly grown on the microspheres may be responsible for the slight reduction in metabolic activity seen at day 7 in comparison to day 2. It has been reported that the upregulation in ALP activity is coupled with a down regulation of cell proliferation, as maturation of the extracellular matrix occurs [174].

Longer *in vitro* direct studies involving osteoprogenitor cells will be required to assess whether the microsphere formulation and morphology have a more profound effect of cell fate and therapeutic potential. Investigating extracellular matrix deposition (ECM), calcium deposition and collagen (a late osteogenic differentiation marker) can provide evidence as to which formulation may be most suitable for bone repair and regeneration. Several mechanisms including chemical factors, such as ions, hormones and growth factors, as well as environmental factors, including mechanical stimuli, material geometry and topography, have been identified as being able to influence osteogenic differentiation [175].

Previous *in vivo* studies involving the implantation of porous P40 microspheres into ovine bone defect model, over a 13-week period, established their biocompatibility and potential as candidates for bone repair and regeneration. Histological analysis comparing cellular response and tissue formation between porous P40 microspheres, and a slower degrading Ti-containing formulation (P40Ti) revealed marked differences [176]. In the defects where P40 microspheres were implanted, reduced trabeculae-like interconnection and higher fatty bone marrow content was observed, whereas P40Ti microspheres promoted dense interconnected tissue. The widely distributed connective tissue coupled with the lack of trabecular organisation led to McLaren *et al.* suggesting that although the slower degrading P40Ti microspheres stimulated greater tissue formation, this may have delayed tissue maturation and remodelling at the bone defect. In the groups treated with P40 microspheres, a greater amount of mineralised tissue was identified in comparison to the P40Ti treated group. The varying degradation rates of the two formulations used affected tissue formation due to both structural effects of the material and instructive cues through ion release. This work highlighted

that long term *in vivo* studies are vital in establishing the potential of the four microsphere formulations used in the present study for bone regeneration applications. The differing degradation rates coupled with the type and relative quantity of ions released have the potential to be used to modulate bone remodelling and regeneration [102]. *In vivo* studies comparing P40 and P30 porous microspheres could be hugely valuable to confirm the potential efficacy of the slower degrading, ortho and pyrophosphate-rich P30 composition. Fully resorbable biomaterials offer the possibility to stimulate bone growth and be progressively substituted by new tissue whilst re-establishing physiological functionality.

The microspheres in the present study are biomaterials that have the potential to influence and instruct beneficial responses to endogenous cells that are present at the site of injury following bone cancer treatment. Bioinstructive materials that do not need exogenous cells grown *in vitro* on or within them remove the logistical and technical issues around the retrieval, proliferation and differentiation of the exogenous cells and implantation into the injured site [177]. Cell-based therapies can suffer from patient-to-patient variability, whereas a material can possess specific, reproducible properties capable of eliciting specific therapeutic responses to restore tissue structure and function at the injured sites [178].

The porous microspheres not only have the potential to facilitate bone repair at regions where tissue has been damaged as a result of bone cancer or its surgical resection, but they can also be loaded with therapeutic cargo to improve bone cancer treatment outcomes. Many chemotherapeutic drugs are toxic to normal cells and often their lack of specificity and selectivity can prevent their use in high dosages [179]. Delivering chemotherapeutics to solid tumours remains challenging due to the complex nature of tumour vasculature and the distinctive microenvironment that they create. Hypoxic and acidic conditions can limit the efficacy and availability of drugs delivered and result in reduced penetration and accumulation within the tumour, particularly within osteosarcomas [180]. Chemotherapy is one of the primary strategies employed to improve bone cancer patient's prognosis by destroying malignant cancer cells and preventing them spreading. It is often utilised throughout the course of treatment adjuvant to other forms of therapy. The synergistic effect of chemotherapy and radiotherapy has the potential to enhance cancer treatment efficacy and a consequential reduction in the treatment time for patients. Chemotherapy is commonly employed as an adjuvant therapy prior to and following radiotherapy to enhance its tumorcidal ability [7]. Chemotherapy is predominantly administered systemically and is often non-selective, which can cause radiosensitivity of healthy tissue and therefore limits drug dosage and potential efficacy [181, 182]. Postoperative chemotherapy is also crucial for destroying any residual cancer cells that remain after treatment and to prevent any cancer recurrence [183]. As such,

producing microspheres that can locally deliver chemotherapeutics simultaneously to and after radiotherapy in a site-specific manner have the potential to improve and enhance the effect of both treatment forms.

Doxorubicin (DOX) is a prominent chemotherapy drug that is commonly used for the treatment of osteosarcomas, as well as several other types of cancer. The use of DOX is often dose-limited due to both acute cardiotoxicity (e.g tachycardia and myopericarditis) and chronic adverse cardiac effects (congestive heart failure), in addition to the other common side effects of myelosuppression and mucositis [184]. Various drug delivery systems have been investigated to deliver DOX in a site-specific manner to reduce the risk of cardiomyopathy, and other systemic adverse events, whilst increasing the dose received at the target [185]. Liu *et al.* fabricated poly(propylene fumarate)-co-poly(L-lactic acid) (PPF-*co*-PLLA) porous microspheres by thermally induced phase separation incorporating DOX and embedding within an oligo(poly[ethylene glycol] fumarate) (OPF) hydrogel. This technique allowed for localised and long-term delivery of DOX and *in vitro* cytotoxic effects up to 30 days in the osteosarcoma 143B cell line [185]. Calcium phosphate-based biomaterials have also been explored for DOX delivery for osteosarcoma treatment. Hess *et al.* produced tricalcium phosphate/alginate beads loaded with DOX or cisplatin and incorporated them within porous hydroxyapatite matrixes obtained by freeze gelation. The co-loaded composites were shown to enhance toxicity towards MG63 cells with the porous matrix structure additionally acting as a scaffold for future bone formation [186]. In the present work, preliminary studies involving P40 and P30 phosphate-based glass porous microspheres were performed to investigate their suitability as drug delivery vehicles by investigating the loading and release of DOX from the microspheres.

At a concentration of 50 µg/ml of DOX, P40 PMS were found to have a far greater encapsulation efficiency, 54.8% (± 1.4%), in comparison to P30 PMS 29.1% (± 1.3%). This was likely due to the increased porosity of the P40 microspheres (observed via SEM, Figure 4.4), with the increase in both size and quantity of the pores invariably resulting in increased surface area as seen in other studies [1]. The increase in loading efficiency may also be due to increased electrostatic interactions between the DOX and the P40 PMS. DOX has a free amino group (see Figure 4.38) that is positively charged at physiological and acidic pH, whereas phosphate-based glasses are hydrophilic materials which can develop negative charges on their surface due to the formation P-OH groups [187]. Increased OH- content within calcium phosphate-based materials has been shown to effect electrostatic interactions, with HA having more OH-groups compared to tricalcium phosphate, which therefore improved its electrostatic interactions with other molecules [188]. To improve drug loading efficiency,

further studies are required in which the concentration of the drug and time used to load DOX is explored. This would allow for the development of an optimal process by which an efficient and clinically relevant amount of DOX could be loaded and subsequently released from the microspheres over time. *In vitro* cellular studies would be required to establish the effectiveness of the porous microspheres to deliver tumoricidal doses of chemotherapeutics.

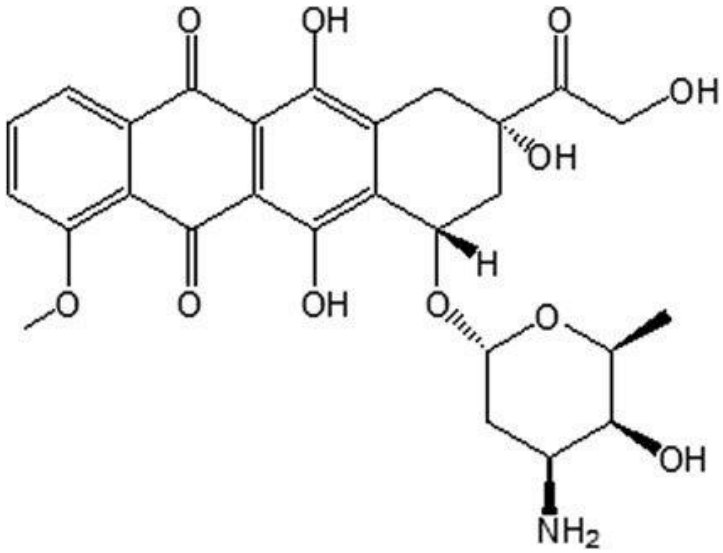

Figure 4.38 The chemical structure of Doxorubicin (DOX). [8]

In addition to being loaded with a significantly lower amount of DOX, P30 PMS also released a significantly reduced amount of DOX at both pH 7.4 and pH 5. Both P30 and P40 microspheres exhibited similar release behaviours in that an initial release of DOX was seen over the first 4 hours, followed by a more gradual release over the subsequent duration of the study. This initial rapid release could be attributed to the increased proportion of DOX located on and near the microsphere surface, as evident from the confocal laser scanning microscopy image in Figure 4.36. For both microsphere formulations, drug release was highest in PBS with a pH of 5 in comparison to 7.4. A pH of 7.4 and 5 were selected to simulate normal physiological and the acidic tumour microenvironment that can develop in bone sarcomas. The source of acidosis in the tumour microenvironment arises mainly due to altered glycolytic metabolism that results in extracellular proton accumulation, which becomes an intrinsic driver of malignancy [189]. This extracellular acidosis increases invasion, angiogenesis, metastasis and can result in resistance to certain types of therapy [190]

Elevated DOX release at pH 5 may be due to increased breakdown of the integrity of the microspheres surfaces and changes in their morphology. The hydrolysis reaction that cleaves the P-O-P and P-O-MeO/$Me_2$0 bonds are accelerated at lower pH where there is additional protons, therefore resulting in a faster rate of hydration and dissolution [191]. Interconnecting regions between pores at the surface are most susceptible to degradation and loss of structural integrity here can lead to exposure of inner pore regions allowing greater drug release. As seen in Figure 4.35, it was evident that P40 PMS underwent a more substantial change to their morphological integrity at pH 5 compared to pH 7.4. Phosphate glasses containing longer phosphate chains (e.g. meta and ultraphosphates) are more prone to hydration and hydrolysis than pyro and orthophosphate species [192]. As seen in Figure 4.16, P40 PMS degraded at a much faster rate and released more ions in comparison to P30 microspheres when immersed within milli-Q water. The increased drug release in the more acidic environment indicates excellent chemotherapeutic delivery properties. A pH-responsive DOX release within tumour tissue could selectively kill cancer cells, whilst reducing DOX delivery to healthy cells within normal physiological pH environments [68]. The sustained localised delivery could therefore not only increase therapeutic efficacy but may also lead to a reduction in adverse unwanted effects to healthy tissues.

P40 PMS at pH 7.4 most closely followed the Higuchi drug release model, which indicated that the drug release profiles were diffusion controlled release [193]. P30 porous microspheres at both pH values as well as P40 PMS at pH 5 were shown to best fit to the Korsmeyer-Peppas model. The diffusion exponent, *n*, derived from the Korsmeyer-Peppas model was determined by plotting of log cumulative percentage drug release versus log time. The diffusion exponent characterises the release mechanism and for P40 microspheres at both pH 5 and 7.4 the *n* value was calculated to be ≤ 0.43, indicating a Fickian diffusion mechanism being responsible for the release [194]. Fickian diffusion was also indicated for P30 PMS at pH 7.4, but at pH 5 the *n* value fell within the range of $0.43 < n < 0.85$ meaning that non-Fickian diffusion was the dominant release mechanism and that a combination of diffusion and erosion based drug release was occurring [195].

Further studies are required to ascertain whether the porous phosphate glass microspheres could deliver other therapeutics that may improve bone cancer treatment or aid in bone repair. Often a combined regimen of multiple therapeutics prior to and following surgical intervention is used when treating bone sarcomas. Clinical and preclinical studies have shown that nitrogen-bisphosphonates (BPs), such as zoledronic acid, can prevent skeletal related events (SRE) in patients suffering from bone metastases and also exhibit antitumour activity that can prevent the spread of bone metastasis in certain cases [196]. BPs are thought to induce

apoptosis of circulating primary tumour cells, reduce tumour and endothelial cell proliferation as well as having an antiangiogenic effect. This causes the bone microenvironment and pre metastatic niche to be a less conducive region for cancer cell survival and may provide a means to prevent cancer recurrence [197].

The skeleton is a rich source of growth factors and during bone resorption, which is upregulated in osteolytic lesions, these matrix-embedded factors are released. Nitrogen-BPs ability to inhibit the action of osteoclasts prevents the release of the bone-derived factors that stimulate tumour growth and proliferation [11]. Several studies have shown that when zoledronic acid is used as a neoadjunvant therapy alongside other chemotherapeutics it has a synergistic beneficial effect [198]. It may be that future studies could look at incorporating BPs within the porous microspheres used in this study and investigate their synergistic effect with other clinically used chemotherapeutics.

5 Yttrium- doped phosphate-based microspheres for internal radiotherapy delivery

5.1 Introduction

Internal radiation therapy is a form of cancer treatment that involves the placement of radioactive sources within the body, usually adjacent to or directly within a cancerous tumour [77]. This treatment can be particularly effective against cancers where the response to chemotherapy is poor or when external beam radiotherapy is not possible due to the location of the cancerous tissue [199]. In order for effective treatment, the delivery of the radiation must maximise the dose of radiotherapy to aberrant cancer cells, whilst minimising exposure to surrounding healthy cells [71]. One strategy that has been successfully used to deliver internal radiotherapy is the use of radionuclide doped microspheres. Direct injection of the microspheres into the tumour cavity, or into the blood vessel supplying a tumour, increases the localised *in situ* delivery of tumoricidal doses of radiotherapy [200].

Various biomaterials have been employed to deliver specific radionuclides that emit alpha, beta or gamma radiation for internal radiation therapy. Beta-emitting (β) radionuclides have been the most comprehensively utilised due to their ability to deliver high doses of radiation with sufficient levels of tissue penetration [201]. The properties of the radionuclide are used to select the best candidate to deliver the desired dose of radiation, over the required distance, to achieve the most efficacious treatment for the specific tissue or organ [202].

Yttrium 90 (^{90}Y) is a radionuclide that has been extensively studied and has been used clinically to deliver internal radiotherapy. Non-radioactive ^{89}Y is activated to the pure β -emitter ^{90}Y by neutron bombardment prior to implantation, with the resulting ^{90}Y having a half-life of 64.2 hours, a tissue penetration depth ranging from 2.5 -11 mm and the capability of delivering therapeutic doses of ionising radiation [203]. Currently two different types of ^{90}Y containing microspheres are commercially available that are used in Selective Internal Radiation Therapy (SIRT) (also known as radioembolisation) for the treatment of unresectable hepatocellular carcinoma [88]. SIR-Spheres (Sirtex Medical, Sydney, Australia) are resin-based microspheres that are comprised of a proprietary biocompatible microsphere that is coated with a cross-linked cation exchange polystyrene resin. Yttrium is integrated into and immobilised within the resin matrix via ion exchange of sodium for yttrium followed by its precipitation as a phosphate salt [7]. TheraSphere (Boston Scientific, United Kingdom) are alumina silicate glass microspheres produced via traditional melt-quenching technique

involving yttrium oxide (Y_2O_3), aluminium oxide and silicon dioxide, followed by flame-spheroidisation [204].

Glass microspheres are attractive materials for the delivery of internal radiotherapy since the non-radioactive isotope is able to be incorporated into the chemical and physical structure of the glass during the manufacturing and processing procedure [113]. Neutron activation is the final step in the manufacturing process, and this therefore provides an inherent safety benefit during their fabrication. Once irradiated, the glass microspheres need to possess high chemical durability in order to prevent leaching of the radionuclide and irradiating the patient away from the target site. [205]. The time from neutron activation of the microspheres to their delivery in the clinic is also used to ensure a specific dose is administered. Despite this, significant decay of the microspheres radioactivity occurs before treatment has started due to the relatively short half-life of ^{90}Y [206]. Therefore, production of microspheres that are not only chemically durable/stable but also contain a high yttrium content are greatly desirable.

Several studies in the literature have reported on the use of bioactive glasses as vectors for internal radiotherapy delivery [207]. Bioactive glasses undergo a series of surface reactions *in vivo* or when exposed to physiological fluids that allow them to bond with native host tissue and their dissolution products can stimulate cellular responses, such as osteoconduction and angiogenesis [208]. Modifications in the glass formulation affect the glasses physico-chemical and mechanical properties, bioactivity and dissolution rate. This allows for the ability to tailor the properties of the glass for the desired application. Bioactive glasses that are fully resorbable or capable of delivering multiple therapeutic responses are of great interest in medical research. The amount of Y_2O_3 that can be incorporated into the glass structure is currently limited to around 18 mol% in silicate based glasses and requires a high temperature melting process, due to Y_2O_3 melting temperature of 2,425°C [209]. A study by Arafat *et al.* investing the crystallisation behaviour of glasses within the system $45P_2O_5$– (30 − x) Na_2O–$25CaO–xY_2O_3$—(where x = 0 to 10) found that the addition of Y_2O_3 was limited to 5 mol%, as further addition resulted in crystallisation of the glass [210]. This demonstrates the difficulties often encountered when trying to incorporate high quantities of Y_2O_3 within a phosphate-based glass although Martin *et al.* incorporated approximately 31 mol% Y_2O_3 within yttrium alumino-phosphate glasses [211]. The low concentration of yttrium incorporated into glass microspheres reduces the maximum dose of radiation, therefore limiting efficacy of treatment and results in an increased time required to activate the radionuclide through neutron bombardment [212].

Alternative biomaterials, such as ceramics, have also been used to fabricate microspheres containing yttrium for internal radiotherapy delivery. Ceramics are an attractive material of

choice since certain bioceramics, particularly calcium phosphate based ceramics, have been shown to be cytocompatible and have the ability to both bond to bone and enhance new bone tissue formation [213]. Ceramic materials typically have high chemical durability making them suitable for radiotherapy and hard tissue engineering applications [214]. The formation of YPO_4 and Y-doped calcium phosphate microspheres via hydrated ion exchange for internal radiotherapy delivery has been explored by Zhou *et al.* [215]. Beta-tricalcium phosphate (β-TCP) based composites have also been formed by classical ceramic sintering route of chemically synthesised and calcined β-TCP with up to 50 wt% yttrium phosphate powders [216]. Microspheres formed solely from Y_2O_3 and YPO_4 powder have been fabricated using a high-frequency induction thermal plasma melting technique to increase the yttrium content per microsphere. This would increase the amount of radiation that could be delivered per microsphere and at levels greater than are currently achieved using conventional yttrium-doped glass microspheres [217]. Microspheres that are comprised of yttrium and phosphorous are of increased interest due to ^{31}P, which is found at a natural abundance of 100%, yielding radioactive ^{32}P, which is a β-emitter with a half-life of 14.3 days following neutron bombardment [206]. A biomaterial containing ^{32}P within its structure could deliver localised radiotherapy simultaneously with another radionuclide, such as ^{90}Y, and over an increased duration potentially enhancing their radiotherapeutic effect [218].

Microspheres formed from a biomaterial that has intrinsic bioactive properties, whilst also simultaneously being able to deliver radiation therapy via neutron activated radionuclide would be highly advantageous over clinically available options. Once the ionising radiation has decayed, the dissolution of the microspheres into harmless products and resorption in the body could circumvent issues associated with permanent implantation and surgical retrieval of devices that occurs in other forms of internal radiotherapy, such as brachytherapy. The degradation of some bioactive materials have the capability of promoting new and rapid growth of healthy tissue that would aid in the regeneration and repair of tissue damaged by cancer and its accompanying treatment [212]. Fabricating such a microsphere that could achieve the properties is challenging since bioactivity only occurs due to specific surface reactions, whilst a sufficiently low release rate of any radionuclides is required during their period of radioactivity.

Glass-ceramics are polycrystalline materials composed of one or more glass and crystal phases that are produced when glasses are subjected to heat treatment and undergo crystallisation to a lower energy state [219]. This is generally a highly controlled process as both the starting glass composition and the temperatures used have been empirically shown to have a direct effect on the final properties of the glass-ceramics and the phases present

[220]. Glass-ceramics are not fully-crystalline in nature with typically 30-70% volume of the microstructure being crystalline and residual glass accounting for the rest [221]. The composition of the crystalline phase or phases produced as a result of heating, as well as residual glass, are different to that of the original parent glass [222]. The crystallisation process is usually performed to produce a material that has enhanced properties over the parent glass. When employed as biomaterials, the properties that are most desirable for glass-ceramics is high physical and chemical durability combined with biocompatibility [223]. Certain calcium phosphate glasses have demonstrated biocompatibility, bioactivity, bioresorbability and osteoconductivity and have therefore been investigated as potential parent glasses for glass-ceramic fabrication [224].

This chapter discusses processing and structural characterisation of yttrium-containing phosphate-based microspheres that could be used to deliver internal radiotherapy for the treatment of bone cancers. *In vitro* bioactivity and cytocompatibility studies have been performed to assess the microspheres' ability to support cell growth and proliferation and to facilitate bone repair and regeneration to damage tissue following devastation due to bone cancer and it associated treatments.

5.2 Results

5.2.1 Morphological and elemental analysis

SEM analysis confirmed that following processing and sieving a high yield of spherical microspheres were produced via the flame spheroidisation method. As seen in Figure 5.1, a lack of aggregation and a narrow size distribution was achieved using this manufacturing process. This was apparent at each yttrium oxide to glass ratio that was used prior to spheroidisation. Initial SEM analysis revealed that the microspheres topography was not homogenous with different surface features visible on microspheres produced at the various compositions.

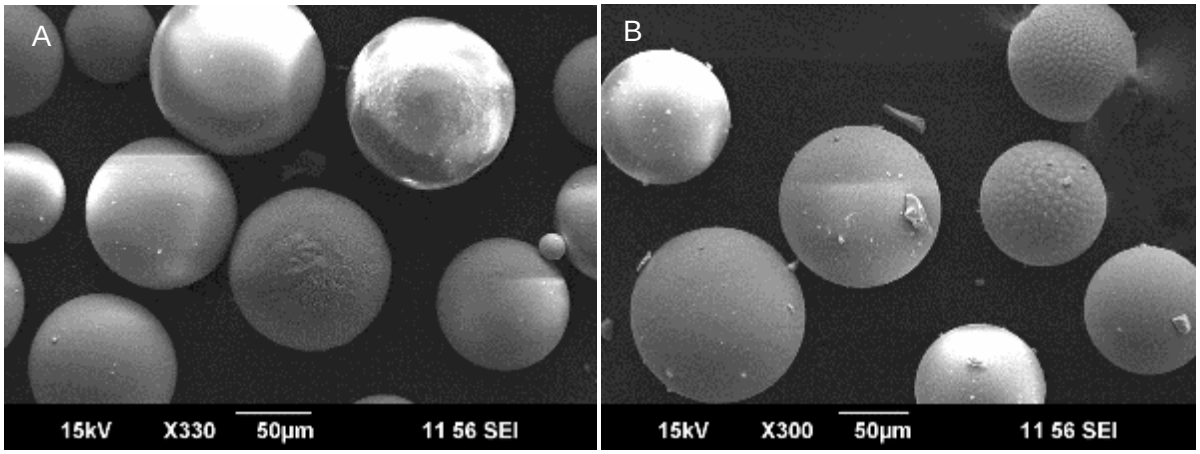

Figure 5.1 SEM images of the morphology of the yttrium-containing microspheres produced. (A) Microspheres processed using a 30:70 yttrium oxide to P40 glass ratio (30Y) and (B) microspheres processed using a 50:50 yttrium oxide to P40 glass ratio (50Y).

*E*DX analysis was performed to confirm the composition on the microspheres manufactured at each yttrium oxide to glass ratio. As the amount of yttrium oxide that was mixed with the glass increased, there was a proportional decrease in all the other glass elements within the microspheres (see Figure 5.2).

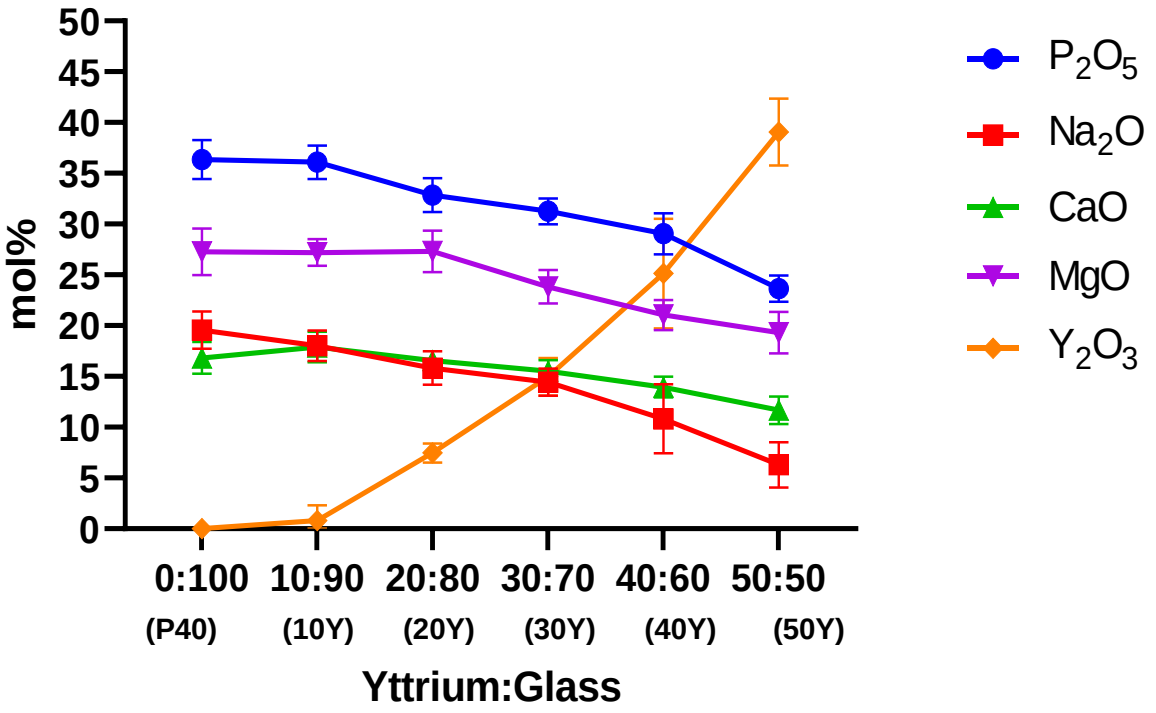

Figure 5.2 Elemental composition determined EDX of the yttrium microspheres produced via flame spheroidisation.

Throughout this work, the following naming convention was used to refer to the samples i.e 30Y, where 30 refers to the ratio of yttrium oxide mixed with P40 glass prior to spheroidisation and Y the radionuclide of interest. 30Y microspheres were chosen for further characterisation and study due to their yttrium content (15.0 mol% ±1.8) being comparable to that of Therasphere™ and containing a P_2O_5 content of ~30 mol%. 50Y microsphere were also used as these had the highest yttrium content (39.1 mol% ±3.3) and revealed some rather intriguing surface morphologies.

5.2.2 30Y Surface topography and elemental analysis

For the 30Y composition, microspheres appeared to present with two topographically different surface features (see Figure 5.33A). Most microspheres had a smooth surface with almost no distinguishable features visible. A second distinct group of microspheres presented with grain-like structures over some or all the microspheres' surfaces. Field Emission Gun (FEG)-SEM was used to further investigate the surface of these yttrium-containing microspheres (see Figure 5.33B and C).

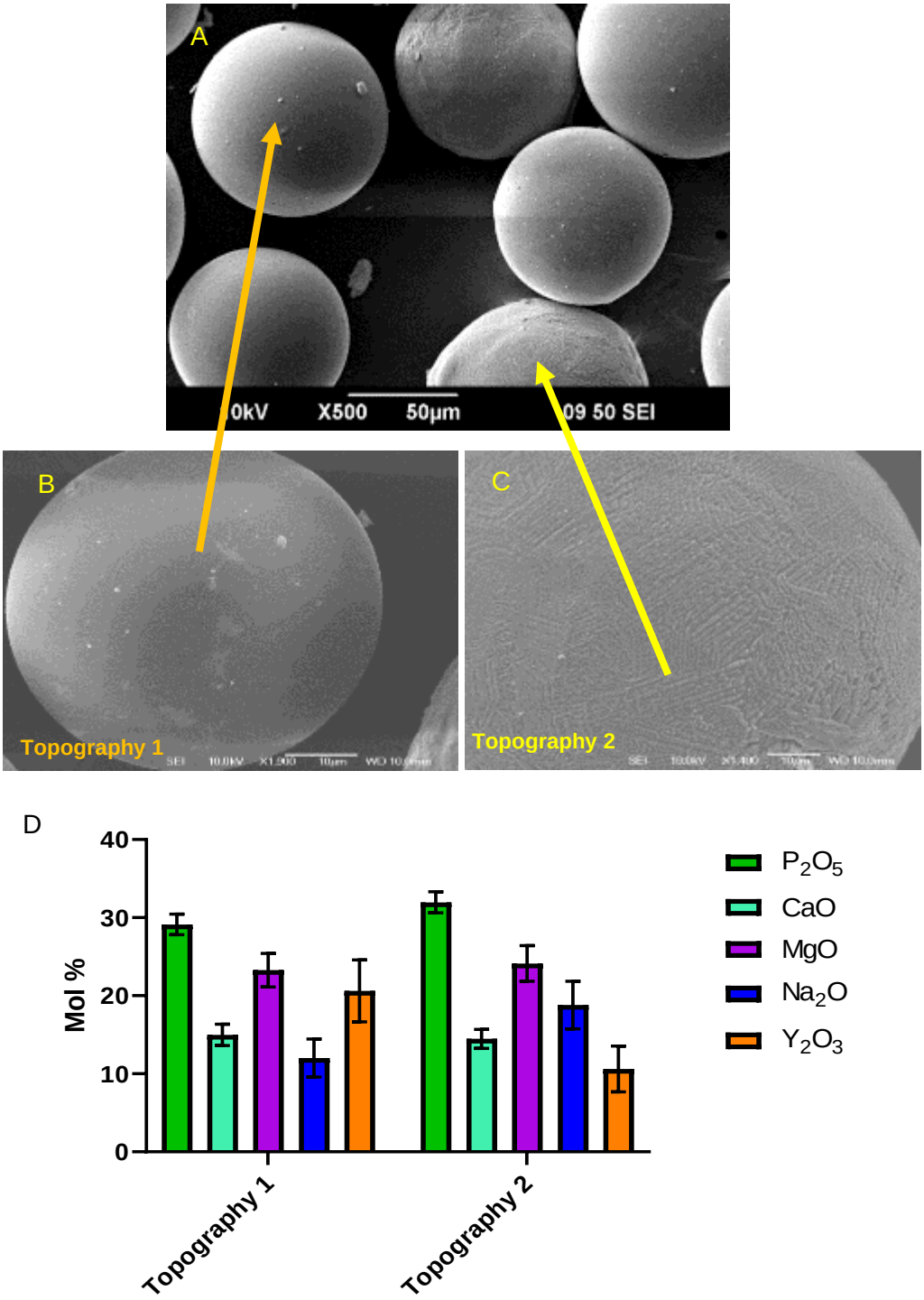

Figure 5.3 (A) SEM image of multiple 30Y microspheres (B) FEG-SEM image showing example 30Y microsphere with a smooth topography. (C) FEG-SEM image showing example 30Y microsphere with a rough topography and grain-like structures on its surface. (D) Elemental composition determined EDX of 30Y microspheres with the two different

EDX analysis of the two subsets of microspheres revealed that their topography appeared indicative of the yttrium content. Microspheres with a smooth surface topography had a higher yttrium content, 20.6 mol% (± 3.9), compared to those with the grain-like structures on their surface, revealing ~10.6 mol% (± 2.9). The elevated yttrium content in the smooth microspheres meant there was a proportional decrease in the other elements in comparison to microspheres with the rougher surface morphology (see Figure 5.33D above).

EDX mapping of resin embedded microspheres was performed to establish whether any of the elements were concentrated at regions within the microspheres. The mapping showed that yttrium was homogenously distributed throughout the whole of the 30Y microspheres and did not appear to be concentrated at the surface. This was also apparent for the other elements that were present from the P40 glass (see Figure 5.4). The intensity of the yttrium correlated with the quantitative EDX values obtained in that there was variability in the yttrium content between microspheres.

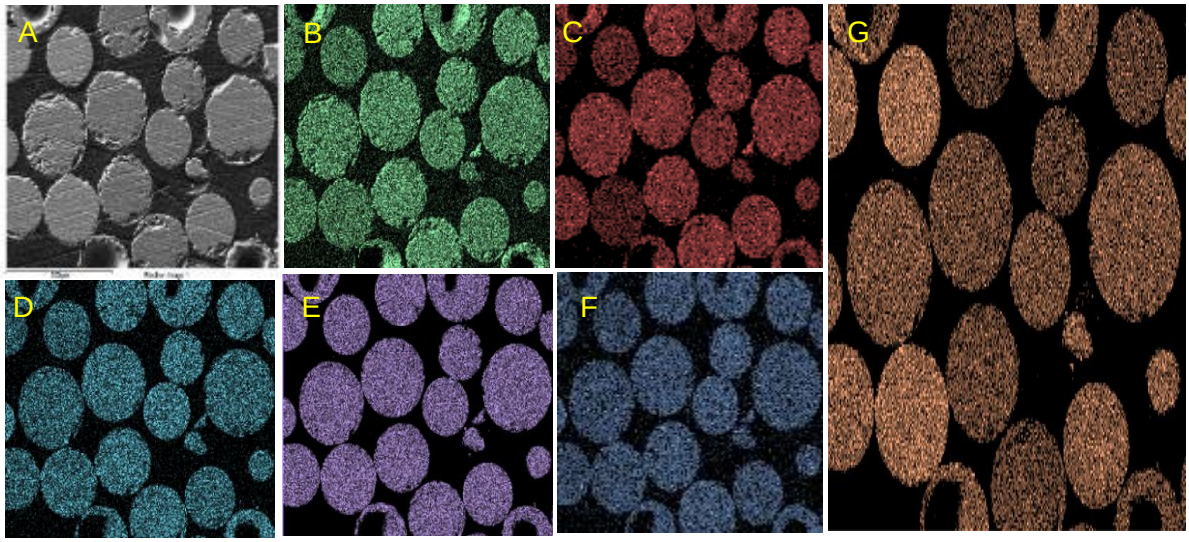

Figure 5.4 EDX mapping of resin embedded 30Y microspheres showing the homogenous distribution of all the elements throughout the microspheres produced

5.2.3 50Y Surface topography analysis and elemental analysis

From the SEM images obtained, it was apparent that a greater proportion of the 50Y microspheres had topographically distinct features in comparison to 30Y microspheres (see Figure 5A). Using FEG-SEM analysis, at an increased magnification it became evident that three topographically distinct microspheres were present within 50Y samples produced from the same batch. All the microspheres within the 45 – 125 µm size range displayed a spherical shape but some had a rough topography with repeating units of irregular shape on their surface (see Figure 5.5A and B). These structures were highly ordered, with each structure appearing discrete from one another. The units on the microsphere surfaces ranged in size, with the largest visible approximately 10 µm in diameter (topography 1). Other microspheres appeared to have a smooth surface topography, like those seen in the 30Y samples, when viewed using the SEM but closer inspection using FEG-SEM revealed the presence of submicron units on the surface of some microspheres (see Figure 5.5C; topography 2). Using the SEM, it was difficult to distinguish these units even at a high magnification. A third group of microspheres displaying a rough surface that contained grain-like structures randomly orientated on a proportion or the whole of a microspheres surface were also identified (see Figure 5.5A and D; topography 3).

EDX analysis of 50Y microspheres revealed that the distinctive, highly ordered structures on the microspheres surface were indicative of yttrium content. Microspheres that displayed the highly ordered structures on their surface had the largest yttrium content of 41.4 mol% (± 4.9). Within this subset of microspheres, the larger, more prominent these features, the greater the yttrium content. Microspheres that appeared almost completely smooth or that had much smaller features on their surface at increased magnification, had a slightly lower yttrium content, 34.9 mol% (± 2.9). Microspheres that displayed the rough surface and grain like structures had the lowest yttrium content, 16.3 mol% (± 3.9), in comparison to the other two topographically different microspheres (see Figure 5.5E).

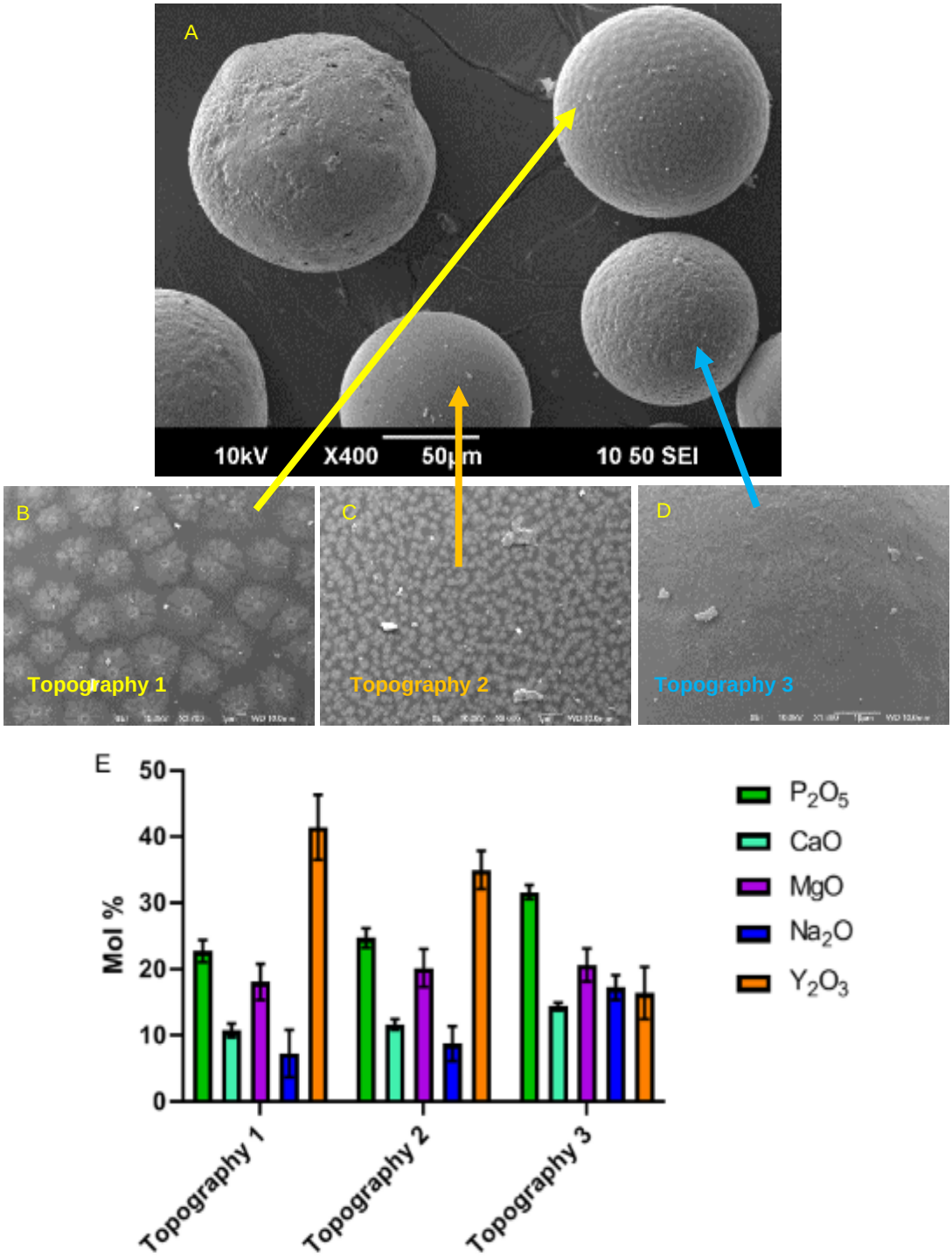

Figure 5.5 (A) SEM image of multiple 50Y microspheres (B) FEG-SEM image showing example 50Y microsphere with a unique ordered structures on the microspheres surface. (C) FEG-SEM image showing example 50Y microsphere with a smooth topography. (D) FEG-SEM image showing example 50Y microsphere grain-like structures on its surface. (E) Elemental composition determined EDX of 50Y microspheres with the two different topographies (n=10).

EDX analysis of the surface features on the 50Y microspheres was able to determine that the individual units displayed localised regions of yttrium content. The centre of the structure was shown to contain the highest yttrium content, with a slightly reduced level of yttrium found in the surrounding unit. The spaces between each unit contained around two thirds the amount of yttrium in comparison to the centre and elevated levels of the glass elements (see Figure 5.6A and B). EDX mapping of these small regions confirmed the localised concentration of yttrium at the centre of each unit and the higher proportion of the glass elements around each unit (see Figure 5.6C).

A

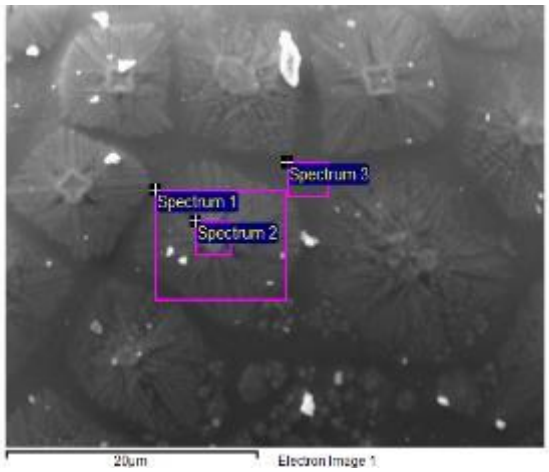

B

	Spectrum 1	Spectrum 2	Spectrum 3
P_2O_5	20.0	18.4	21.8
CaO	11.1	10.3	13.6
MgO	19.1	17.1	23.6
Na_2O	10.8	9.4	12.4
Y_2O_3	39.1	44.7	28.6

C

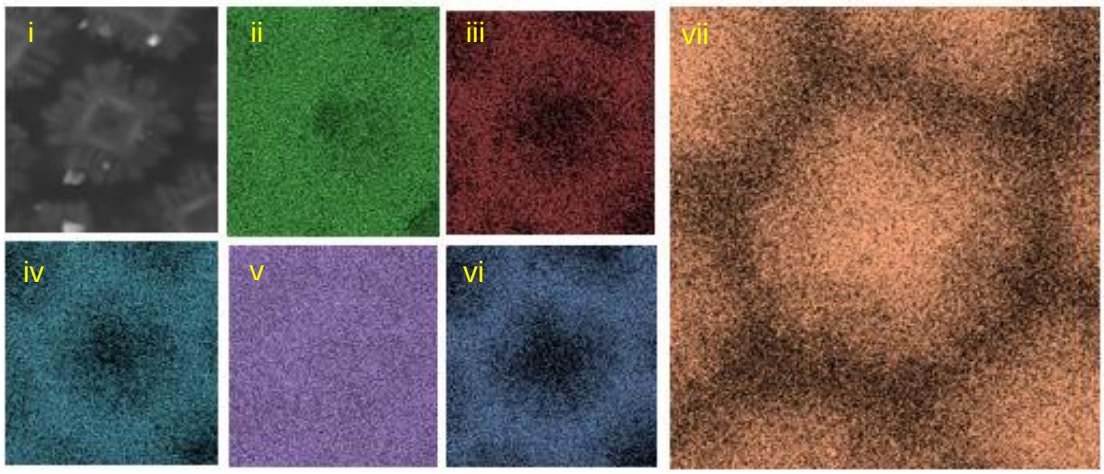

Figure 5.6 (A) SEM image of the 50Y microsphere surface and regions analysed. (B) Elemental values obtained via EDX of the different regions on the surface (C) EDX mapping of the surface of a 50Y microspheres showing localised yttrium content. (i) SEM image (ii) Oxygen (iii) Sodium (iv) Magnesium (v) Phosphorous (vi) Calcium (vii) Yttrium

Despite the presence of localised regions of yttrium content, EDX mapping of resin embedded 50Y microspheres showed that all the elements were distributed throughout the microspheres. Yttrium was detected and appeared homogenously distributed throughout the whole body of the microspheres (see Figure 5.7).

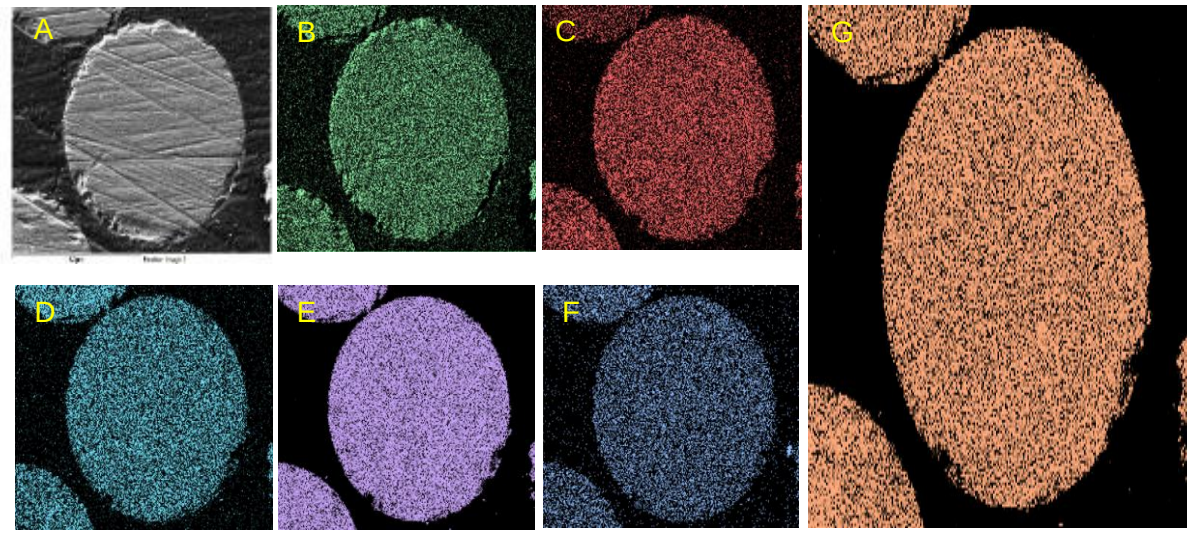

Figure 5.7 EDX mapping of resin embedded 50P40Y microspheres showing the homogenous distribution of all the elements throughout the microspheres produced via flame spheroidisation. (a) SEM image (b) Oxygen (c) Sodium (d) Magnesium (e) Phosphorous (f) Calcium (g) Yttrium

5.2.4 FIB-SEM

Focused Ion Beam Scanning Electron Microscopy (FIB-SEM) was subsequently utilised to ablate away a section of the microspheres to perform high resolution observational and elemental analysis to investigate below the microsphere surface. As seen in Figure 5.5, a significant quantity of 50Y microspheres displayed altered surface morphology because of localised regions of high yttrium content (Figure 5.5; topography 1). Ablation of a surface section from a topographically unique microsphere revealed that it possessed distinctive and heterogeneously organised structures beneath the microsphere surface. Figure 5.8 shows that the lighter and darker regions present in the body of the microsphere were clearly distinguishable from one another. The lighter regions appeared to be concentrated directly below the raised features that caused these microspheres to have the distinctive topography, highlighted below in Figure 5.8.

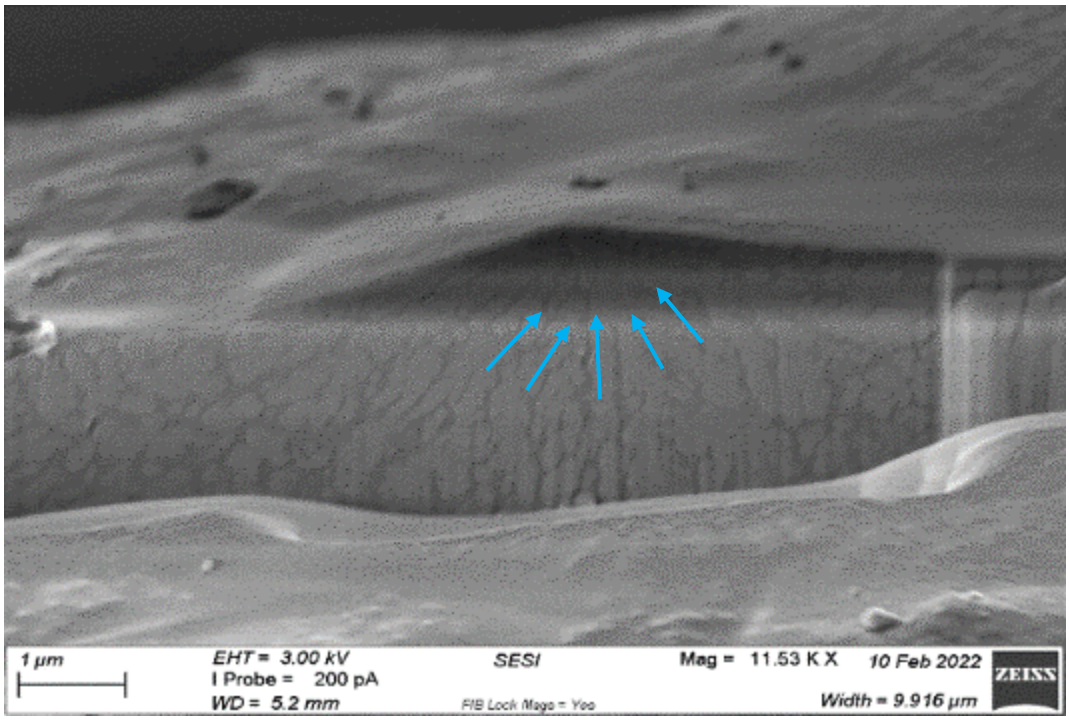

Figure 5.8 An image acquired using FIB-SEM in which a focused ion beam was used to mill through the surface of a 50Y microsphere to expose its inner structure. Blue arrows indicate the concentration of lighter regions below a raised surface feature.

EDX analysis was performed to determine whether the two distinctive regions were also elementally discrete from one another. Figure 5.9 shows where an EDX line scan was performed that started within a darker region of a 50Y microsphere and moved through, from left to right, into a lighter region. Yttrium was present in the darker regions but when the scan reached the lighter region, a greater amount of yttrium was detected. This contrasted with phosphorous, where much more was detected in the darker region and almost no detection visible in the lighter region. The glass forming elements, Na and Mg, which were able to be detected at the accelerating voltage used, and O remained constant throughout the duration of the scan from dark to light region (see Figure 5.9).

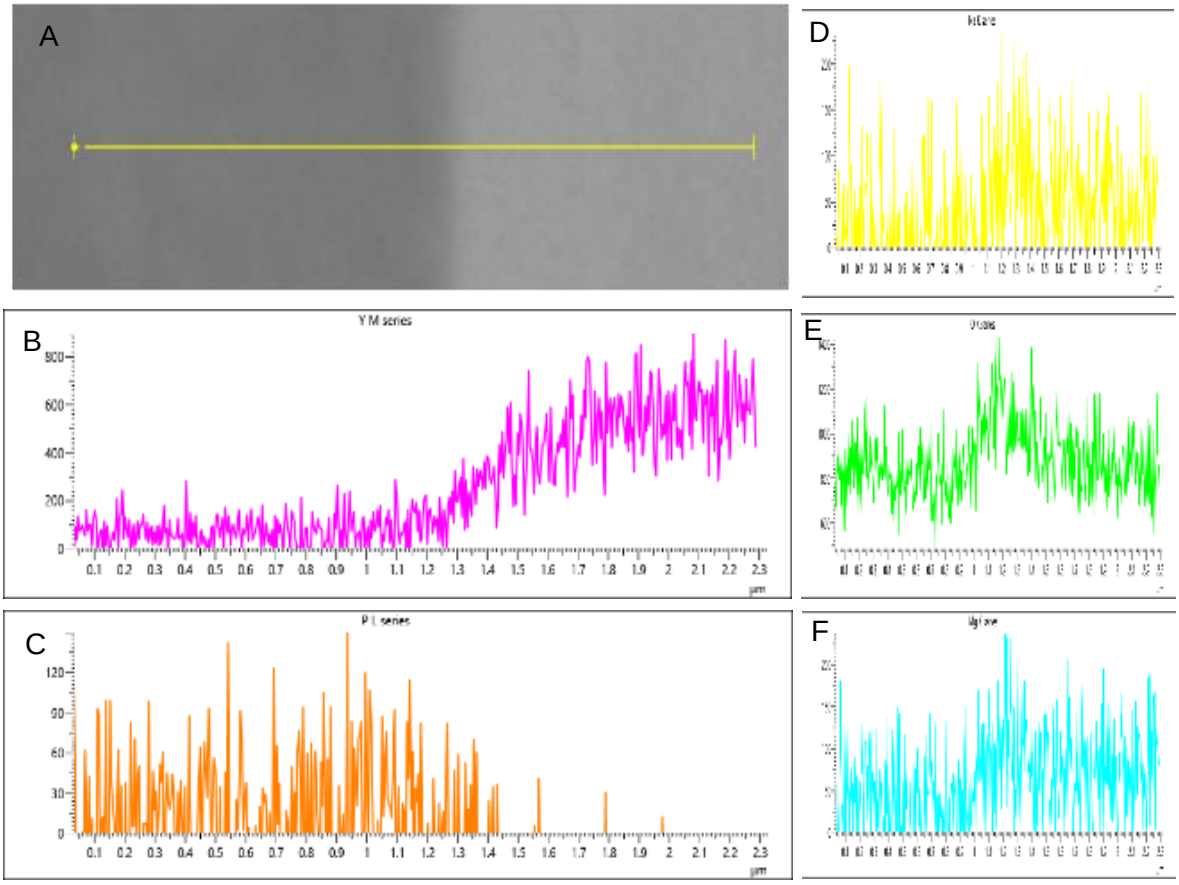

Figure 5.9 (A) An EDX line scan taken between two distinct regions with the inner structure of a 50Y microsphere acquired using FIB-SEM. (B) EDX analysis of yttrium as the scan moved from left to right. (C) EDX analysis of phosphorous (D) EDX analysis of sodium (E) EDX analysis of oxygen (F) EDX analysis of magnesium.

The surface of a 50Y microsphere that displayed a smooth surface topography (Figure 5.5A; topography 2) was also ablated using focused ion beam. This revealed that underneath the microsphere surface there was no homogenous core but the presence of a large quantity of distinct and spherical features (see Figure 5.10A). EDX analysis was performed on these structures and on the darker regions around them. From the spectra obtained, it was not possible to determine whether there was any significant difference in the elemental composition despite the differences in appearance (see Figure 5.10B, C and D).

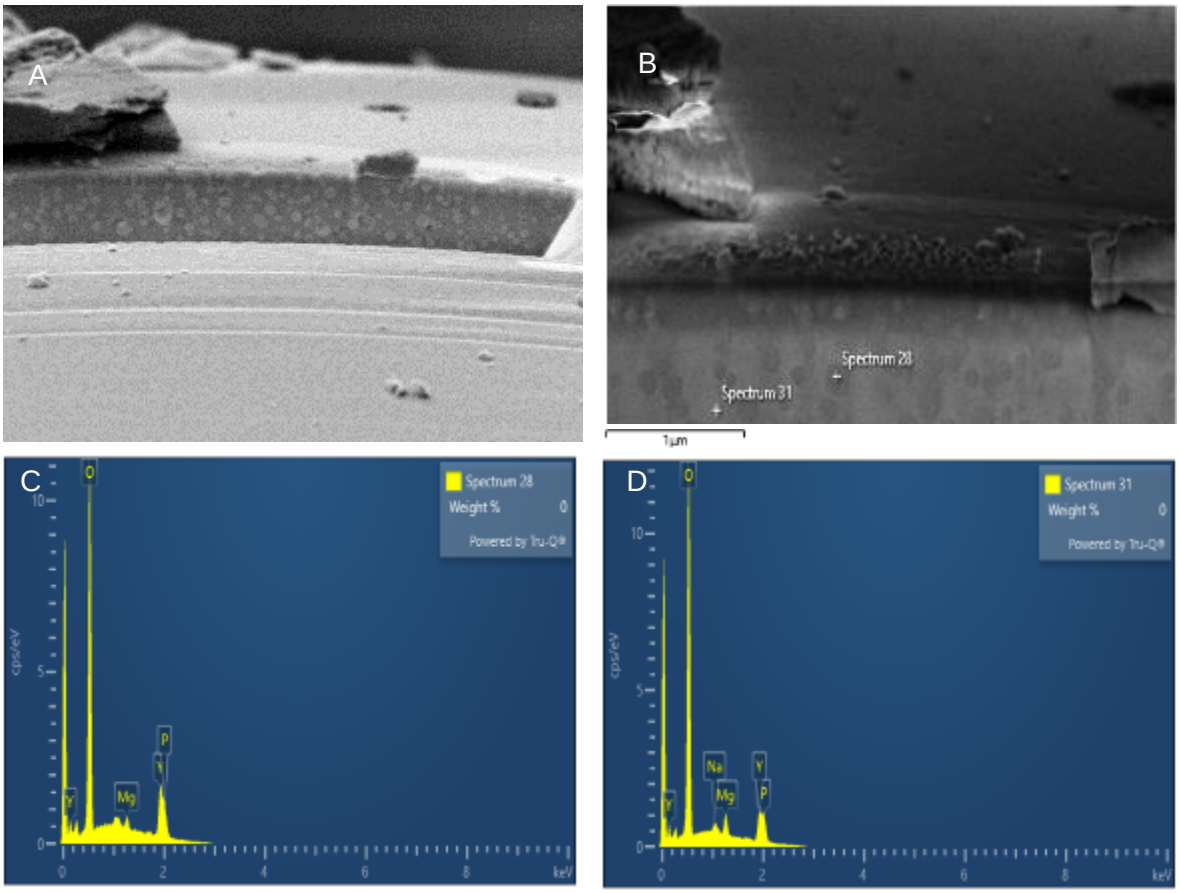

Figure 5.10 (A) FIB-SEM image of 50Y microsphere with an apparent smooth topography and its inner structure (B) Areas where EDX analysis was performed. (C) EDX spectra for position 28 (D) EDX spectra for position 31.

As seen in Figure 5.11, a different 50Y microsphere that exhibited the rough surface topography also contained contrasting light and dark regions within the microsphere following ablation of the surface (Figure 5.5; topography 3). The size, shape and orientation of the lighter regions was not uniform and appeared to be concentrated below the raised protrusions observed on the microsphere surfaces. A larger dark area was present in the valley region between the areas with a high number of light sections observed (see Figure 5.11A).

To further investigate the differences between the light and dark regions, single point EDX spectra were obtained from each of the two distinct regions. As seen in Figure 5.11C and D, Spectrum 39 represents an area within a light region and Spectrum 40 in a dark region. The spectra seen here correlates with Figure 5.9, in that a yttrium peak with a greater intensity was seen in light region (spectrum 39), indicating that this region was yttrium rich, in comparison to the dark region represented by spectra 40. Spectrum 40 exhibited peaks with greater

intensity for Na and Mg revealing the darker regions contained a greater proportion of the glass forming elements (see Figure 5.11C and D).

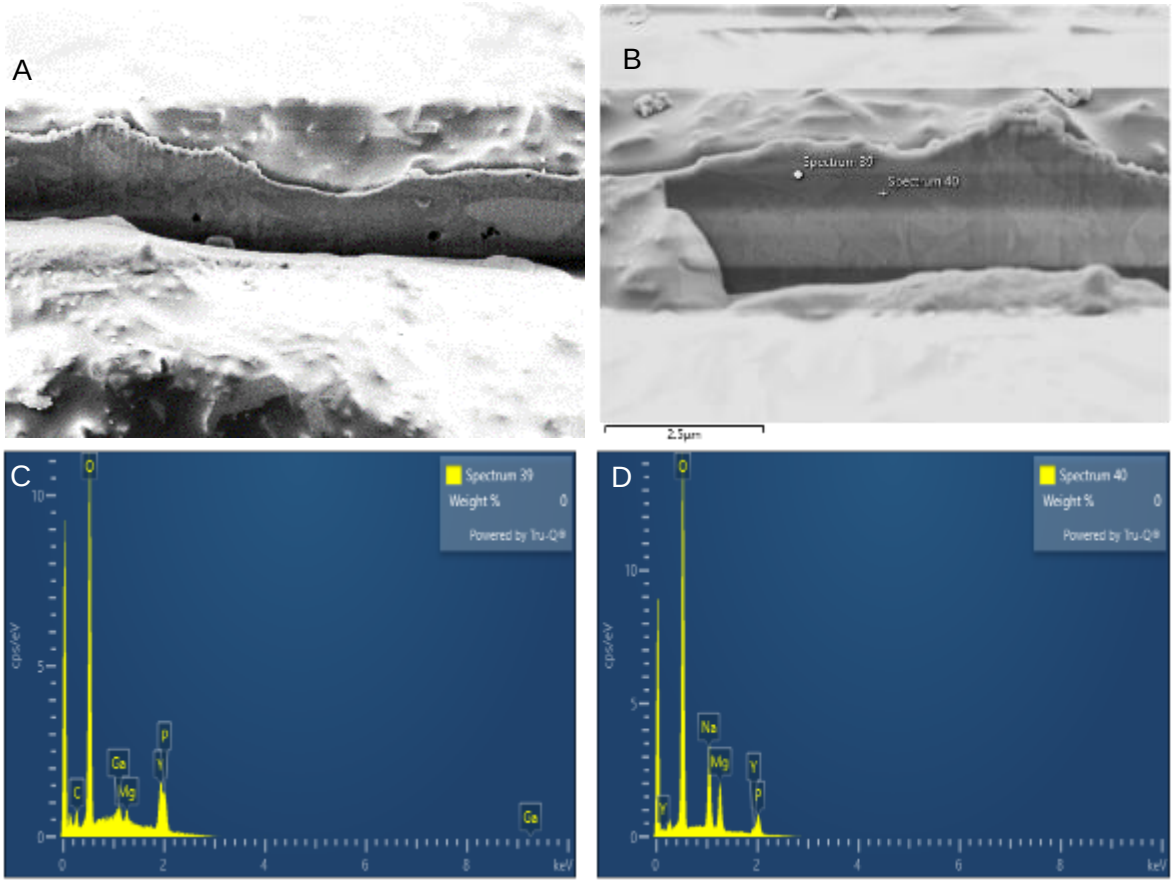

Figure 5.11 (A) FIB-SEM image of 50Y microsphere with a rough topography and its inner structure (B) Areas where EDX analysis was performed. (C) EDX spectra for position 39 (D) EDX spectra for position 40.

5.2.5 XRD

Figure 5.12 shows the XRD profiles for the solid microspheres made from P40 parent glass and both 30Y and 50Y microspheres. A single broad halo peak at 2θ values of ~20-40° was observed for the P40 solid microspheres and the absence of any detectable crystalline peaks confirmed the amorphous nature of the glass microspheres. In the spectra for 30Y microspheres, following processing the presence of crystalline peaks indicated that the microspheres produced were glass-ceramics and not purely amorphous samples. Sharp peaks at ~ 29°, 34°, 49°, 58° and 61° 2θ values were observed, which were matched to cubic Y_2O_3 according to powder diffraction file 01-079-1257 (ICDD database) (see Figure 5.12). Additional peaks were also seen at ~30° and 32° which were matched to hexagonal Y_2O_3 according to powder diffraction file 01-076-7397 (ICDD database). Peaks at ~26° and 35° were also seen and corresponded to $Y(PO_4)$ (ICDD 01-084-0335). In the 50Y microspheres spectra, only peaks at ~ 29°, 34°, 49°, 58° and 61° 2θ values which corresponded to cubic Y_2O_3 were observed (01-079-1257 ICDD database).

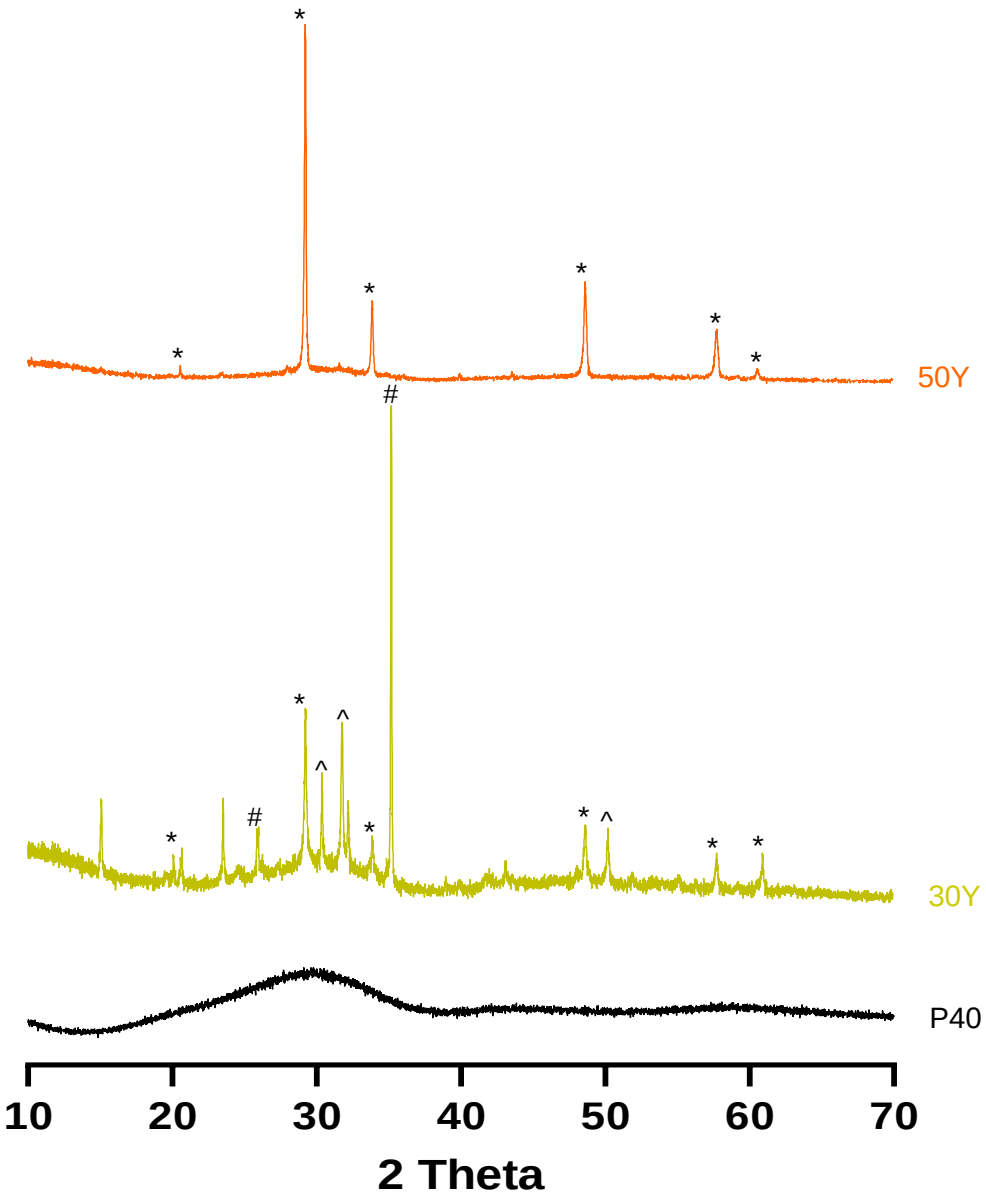

Figure 5.12 XRD spectra of P40 SMS (black), 30Y (gold) and 50Y (orange) solid microspheres. The crystalline peaks matched for cubic Y_2O_3 (*) (01-079-1257), hexagonal Y_2O_3 (^) (01-076-7397) and $Y(PO_4)$ (#)(01-084-0335).

5.2.6 1D ^{31}P MAS-NMR

Quantitative 1D ^{31}P MAS-NMR spectroscopy was used to determine the Q^n distribution of the phosphate species present in the microspheres. The yttrium-containing microspheres were compared to microspheres of the same size made from the parent P40 glass formulation. As seen in Figure 5.13A, for P40 solid microspheres there were two clearly defined peaks at -8ppm and -22 ppm, which corresponded to Q^1 and Q^2, respectively. Fitting the spectra into a series of Gaussian line shapes indicated there were also a small proportion of Q^0 species present at ~ 2ppm.

For both the 30Y and 50Y microspheres, the 1D ^{31}P MAS-NMR spectra only had one defined ^{31}P peak centred approximately at -1 ppm. Due to the presence of only one line to fit, it was not possible to obtain the relative proportions of Q^0, Q^1 or Q^2. Signals in the 30Y microspheres indicated the presence of undefined crystalline region/s that had ^{31}P resonance (see Figure 5.13B and C).

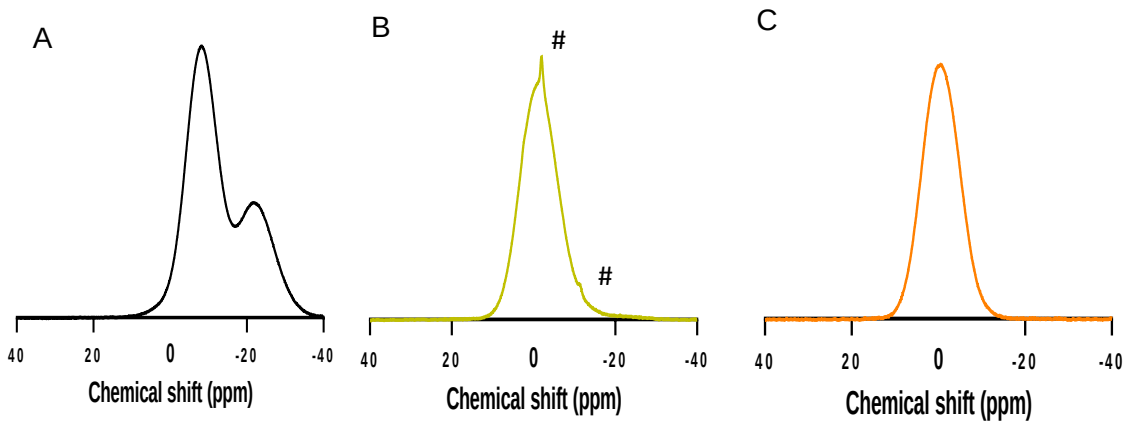

Figure 5.13 Quantitative 1D ^{31}P NMR spectra for (A) P40 solid microspheres, (B) 30Y solid microspheres and (C) 50Y porous microspheres. Crystalline peaks are identified with a #.

5.2.7 Thermal analysis

The Differential scanning calorimetry (DSC) trace of the parent P40 glass showed the presence of a solitary crystallisation temperature of 573 °C. The initial crystallisation temperature increased for both the yttrium-containing microsphere samples. In 30Y microspheres, an initial crystallisation temperature (T_c) of 610 °C was recorded and was higher still for the 50Y sample at 680 °C. 30Y microspheres exhibited additional T_c at 661 °C, 694 °C and 956 °C, whilst 50Y had additional T_c at 741 °C and 921 °C. These peaks were broader and less defined than those seen in P40 sample. P40 displayed two melting temperature peaks at 645 °C and 765 °C. In the 30Y microspheres the melting temperature peaks were higher at 648 °C and 826 °C and these increased further in the 50Y microspheres to 718 °C and 804 °C (see Figure 5.14).

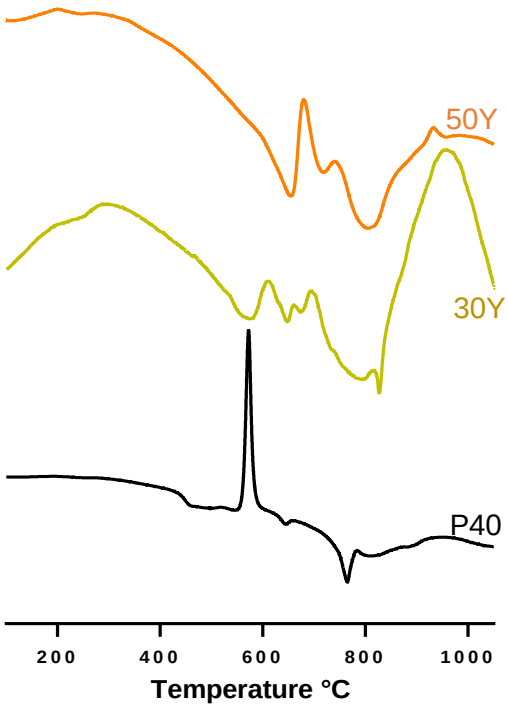

Sample	T_g		T_c			T_m	
	Onset	Mid	1	2	3	1	2
P40	434	463	573			645	765
30Y		580	610	661	694	648	826
50Y		656	681	742	921	718	804

Figure 5.14 DSC thermal analysis profiles and corresponding Tg, Tm and Tc values for P40, 30Y and 50Y solid microspheres.

5.2.8 High temperature XRD

Thermal analysis via DSC suggested the presence of multiple crystallisation phases within the 30Y and 50Y microspheres. XRD was then performed on samples which had been heat treated to specific temperatures within the XRD instrument, via a temperature stage, and scanned to try and ascertain whether certain phases were present or formed at specific temperatures.

For 30Y microspheres, the crystallisation temperatures were 610 °C, 661 °C and 694 °C, the scans were performed at 630 °C, 681 °C and 714 °C to ensure each crystallisation temperature was achieved. As seen in Figure 5.15, no discernible change was observed in the XRD pattern at each of the three temperatures scanned. All three spectra showed sharp peaks at 29, 34, 49 and 58° 2θ, which were matched to Y_2O_3 according to powder diffraction file 01-079-1257 (ICDD database). Peaks at ~30°and 32° which were matched to hexagonal Y_2O_3 according to powder diffraction file 01-076-7397 (ICDD database) and at 35° were also seen to correspond with $Y(PO_4)$ (ICDD 01-084-0335) as was seen in the XRD scans at room temperature. A singular peak at 23° 2θ grew in intensity as the temperature increased but could not be matched using ICDD database 2021.

For 50Y microspheres, the crystallisation temperatures were 681 °C, 742 °C and 921 °C, the scans were performed at 701 °C, 762 °C and 941 °C to ensure each crystallisation temperature was achieved. As seen in Figure 5.16A, no detectable change was observed in the XRD pattern at each of the three temperatures scanned. All three spectra showed sharp peaks at 29, 34, 49 and 58 2θ, which were matched to Y_2O_3 according to powder diffraction file 01-079-1257 (ICDD database) and had previously been identified as the only phase present in 50Y microspheres at room temperature.

Following high temperature XRD, the 30Y and 50Y microspheres were imaged using SEM to see whether any structural or topographical changes had occurred due to heat treatment. As seen in Figure 5.15B and Figure 5.16B, all the microspheres retained their spherical morphology. There did not appear to be a difference in the proportion or appearance of the microspheres displaying the different morphologies at the 30Y and 50Y compositions post heat treatment.

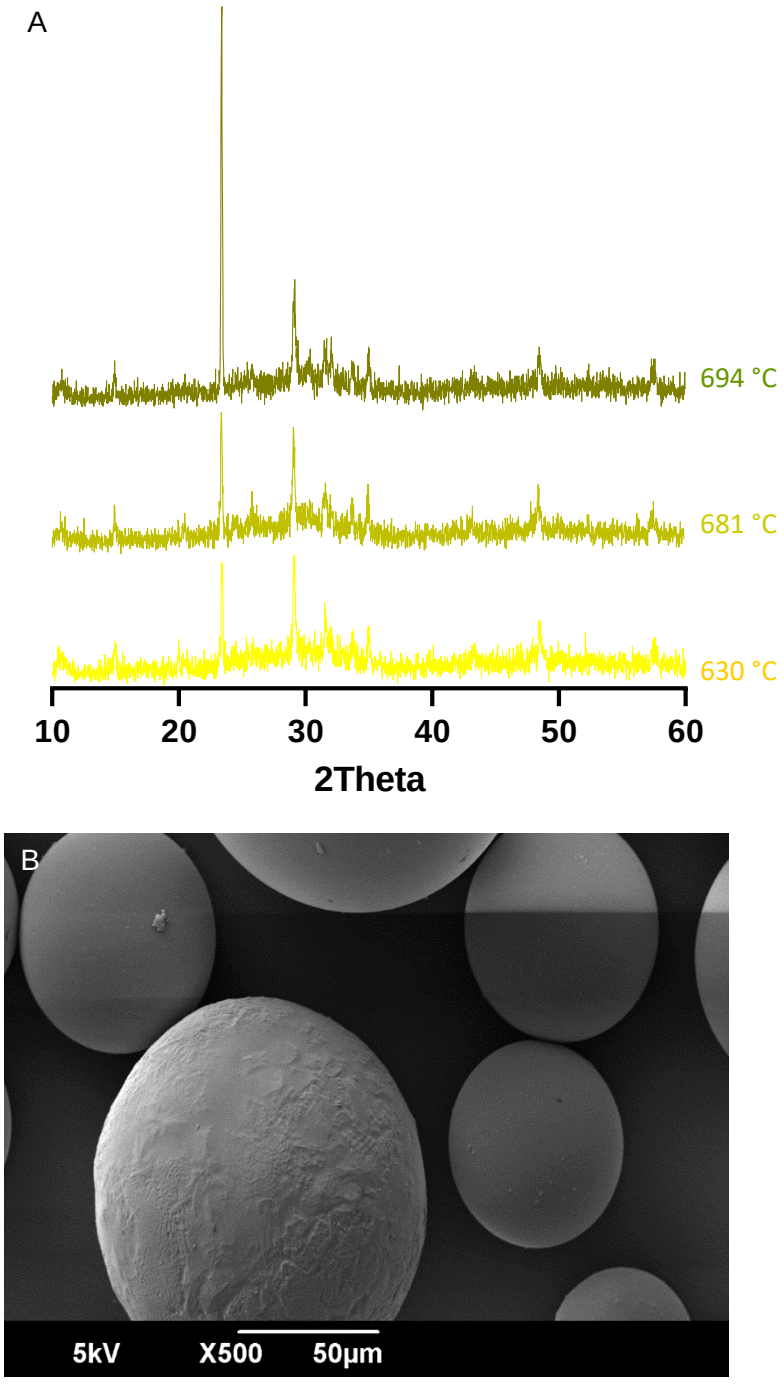

Figure 5.15 (A) XRD traces for 30Y microspheres at different temperatures. (B) SEM image of 30Y microspheres after heat treatment for XRD experiment.

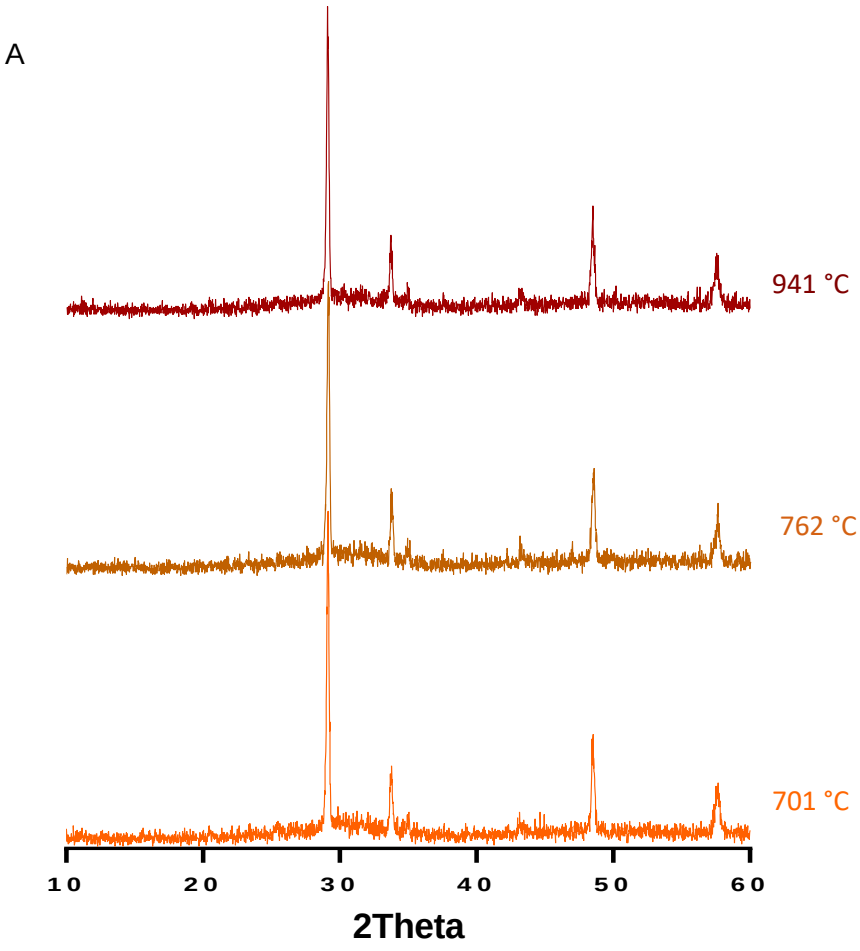

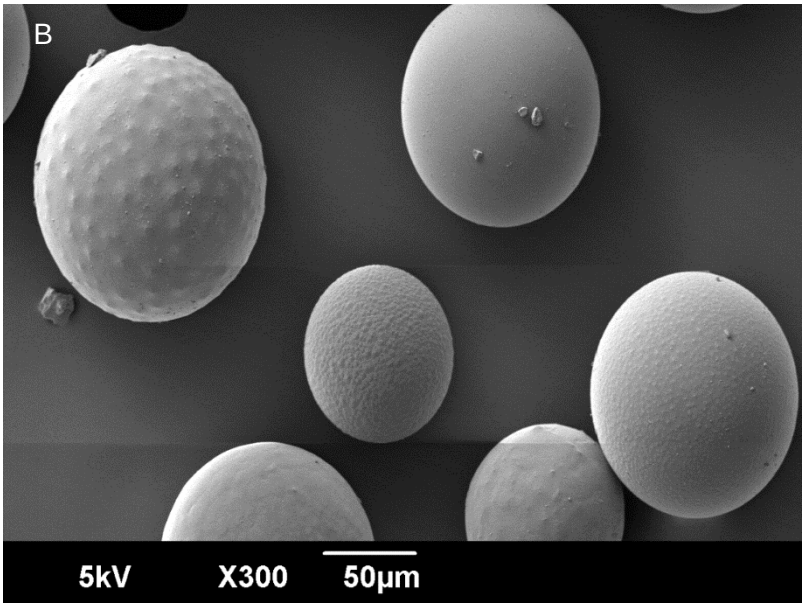

Figure 5.16 (A) XRD traces for 50Y microspheres at different temperatures. (B) SEM image of 50Y microspheres after heat treatment for XRD experiment.

5.2.9 Raman Spectroscopy

For Raman analysis, a hot colour palette was used to generate images which plotted the intensity ratio (as area) of peaks associated with the cubic phase of Y_2O_3 (377 cm^{-1}, 345-410 cm^{-1}, Raman-active A_g mode) relative to the Raman-active PO_2 symmetric stretching mode of non-bridging oxygen's in Q^0 units within phosphate glass (965 cm^{-1}, 910-1020 cm^{-1}) [133]. For reference, the intensity ratio I_{377}:I_{965} is ~560 and ~0 in the cubic-Y_2O_3 reference and the parent P40 glass, respectively, i.e., a high intensity ratio means high cubic-Y_2O_3 content, and a low intensity ratio means high glass content.

As seen in Figure 5.17, which represents analysis of a 50Y microsphere, the brighter regions of the image are associated with cubic-Y_2O_3 rich spectrum, ~377 cm^{-1}, whereas the spectrum related to the darker region are glass-rich with a more prominent peak seen at ~965 cm^{-1}.

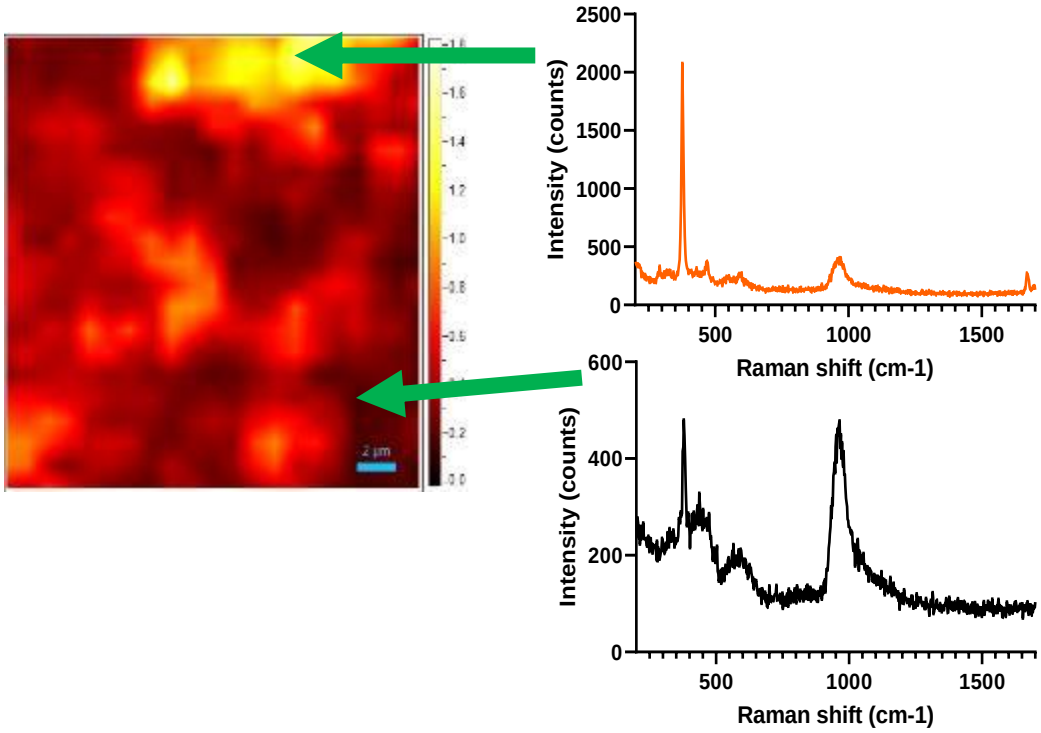

Figure 5.17 Raman mapping experiment in which hot colour palette image created by using intensity ratio I_{377}:I_{965} with corresponding spectra for c-Y_2O_3-rich spectrum (orange) and glass-rich spectra (black).

The hot palette images and the mean spectrum extracted from each mapping experiment from three different 50Y microspheres, using a 660 nm laser, are shown in Figure 5.18A, B and C. There was significant similarity between the spectra from each of the microspheres, indicating that on average, the composition of the microspheres is relatively uniform and that Y_2O_3 is abundant. As seen in Figure 5.18A, B and C, although Y_2O_3 was abundant, it was variable in absolute quantity as a function of spatial location.

The spectra represent an approximate superposition of cubic-Y_2O_3 and phosphate glass. Q^0 were the most abundant phosphate species present within the microspheres, although there was a tail on the right-hand side of the main peak at ~965 cm^{-1} indicating that some Q^1 or Q^2 may also have been present (see Figure 5.18D).

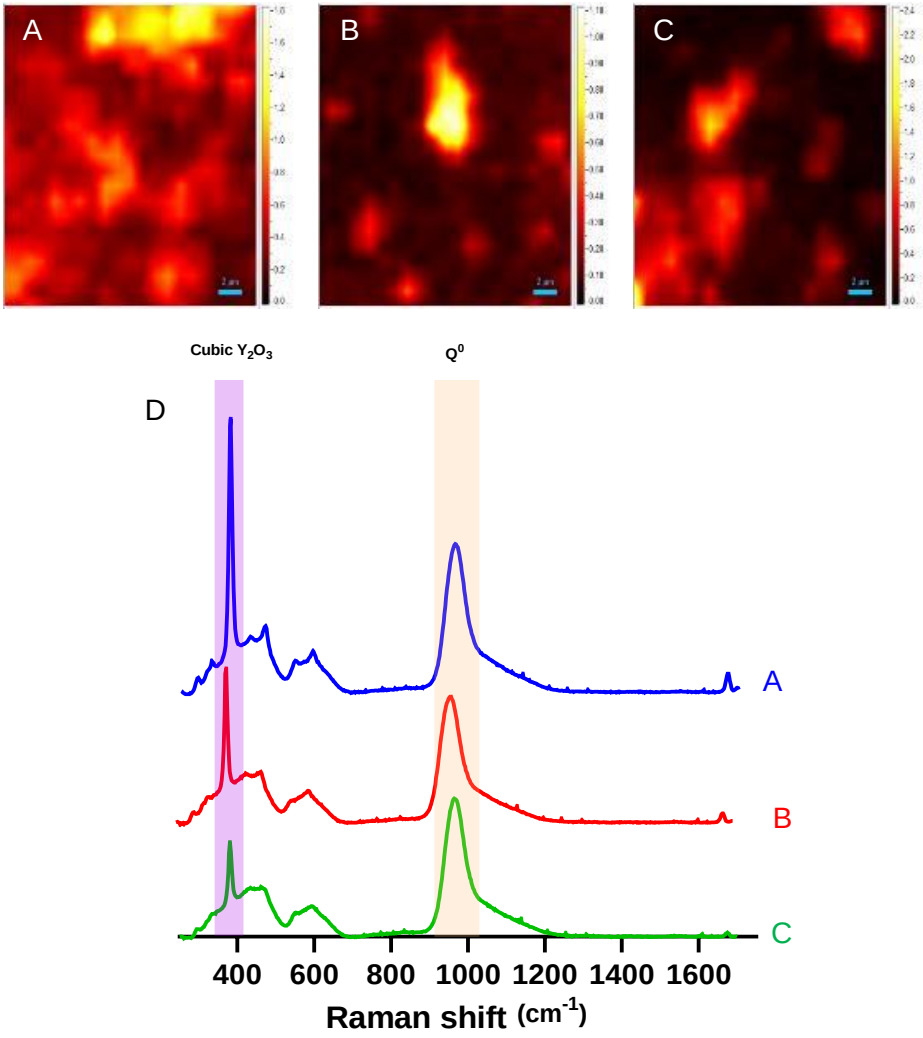

Figure 5.18 Raman mapping experiment using 660 nm laser in which hot colour palette image created by using intensity ratio I_{377}:I_{965} for three separate 50Y microspheres (A), (B) and (C). (D) The Raman spectra for 50Y microsphere (A) blue, microsphere (B) red and microsphere (C) green.

The same experimental process was performed on 30Y microspheres and the mean spectrum extracted from each mapping experiment at 660nm is shown in Figure 5.19A. There was little to no direct evidence of cubic-Y_2O_3 present, with the spectra for microspheres 2 (green) and 3 (red) appearing to be glass-only. Additional Raman peaks at ~1100 – 1200 cm^{-1} in the spectra collected from microsphere 1 (blue) were present (Figure 5.19A). The main peak at ~965 cm^{-1} in the spectra of all three microspheres indicated that Q^0 were the most abundant phosphate species, though there may have been some Q^1 and Q^2 present due to the tail on the right-hand side of the main peak at ~965 cm^{-1}. In comparison to 50Y, there was significant difference between mean microsphere spectra for the 30Y microspheres, suggesting that the composition was more heterogeneous at the lower yttrium content.

As seen in Figure 5.19B, when using a 532nm laser, again no direct evidence of cubic-Y_2O_3 was found in the three 30Y microspheres. Microsphere 2 appeared to be glass-only but additional Raman peaks at ~1100 – 1200 cm^{-1} for microspheres 1 and 3 were present like the spectra from the 660 nm experiment. The mean spectrum from microsphere 2 showed no evidence for cubic Y_2O_3 and only exhibited peaks associated with phosphate glass. The prominent main peak at ~970 cm^{-1} indicated that the primary species was Q^0, although the slight tail on the peak suggest some Q^1 and Q^2 were potentially present.

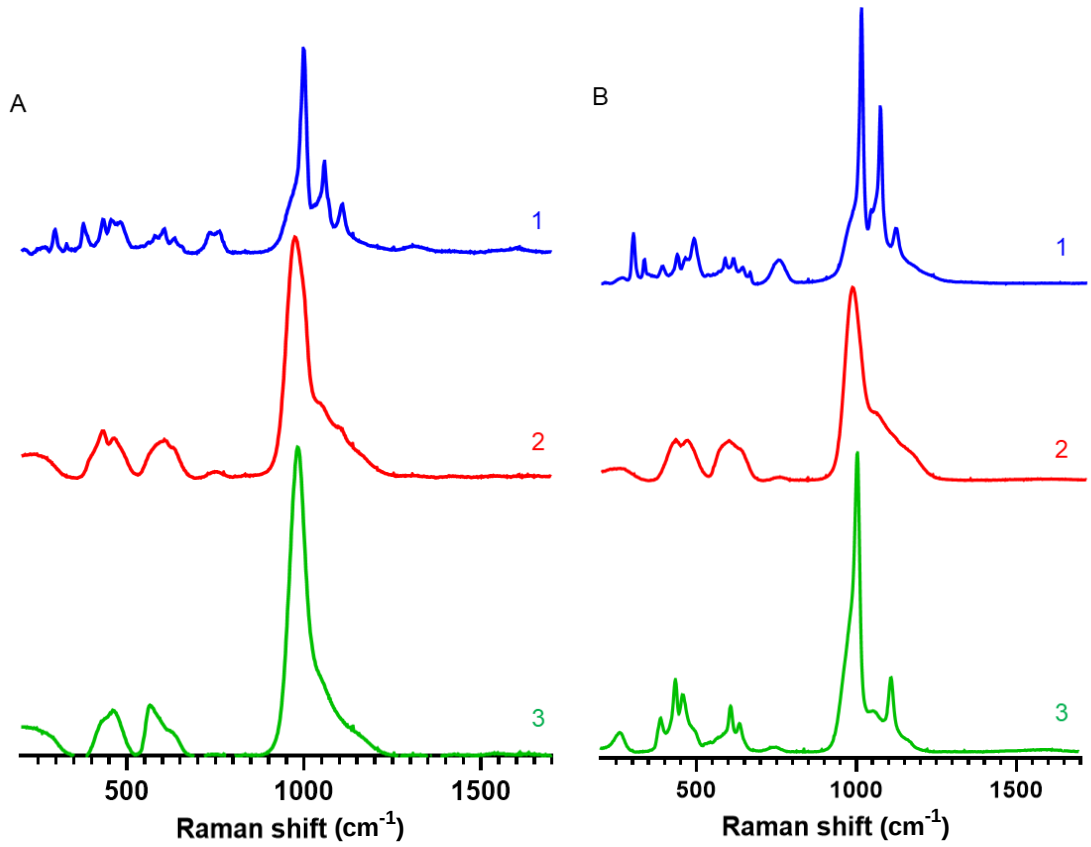

Figure 5.19 (A) The Raman spectra for three 30Y microsphere at 660nm excitation. (B) The Raman spectra for three 30Y microsphere at 532nm excitation.

5.2.10 Theoretical O/P calculations

The O/P ratio was calculated for P40, 30Y and 50Y solid microspheres based on the EDX values obtained. Equation 5.1 was used to calculate the ratio as follows:

$$O/P = \frac{[P_2O_5]x\,5+[CaO]+[MgO]+[NaO]+[Y_2O_3]x\,3}{[P_2O_5]x\,2} \qquad \textit{Equation 5.1}$$

As seen in Table 4.5.1, as the yttrium content in the microspheres increased there was a corresponding increase in the O/P ratio.

Table 4.5.1 Theoretical O/P calculations for P40, 30Y and 50Y solid microspheres

Solid microsphere formulation	O/P ratio
P40	3.33
30Y	4.01
50Y	5.77

5.2.11 X-ray photoelectron spectroscopy (XPS)

XPS analysis was performed to provide information on the signature binding energy of the peaks from their different elements. For the P40, 30Y and 50Y solid microspheres the survey spectra peaks were assigned to the glass constituents P, O, Ca, Mg and Na. For the 30Y and 50Y spectra an additional peak at 156 – 162 eV was observed and identified as a Y 3d peak [225] (see Figure 5.20).

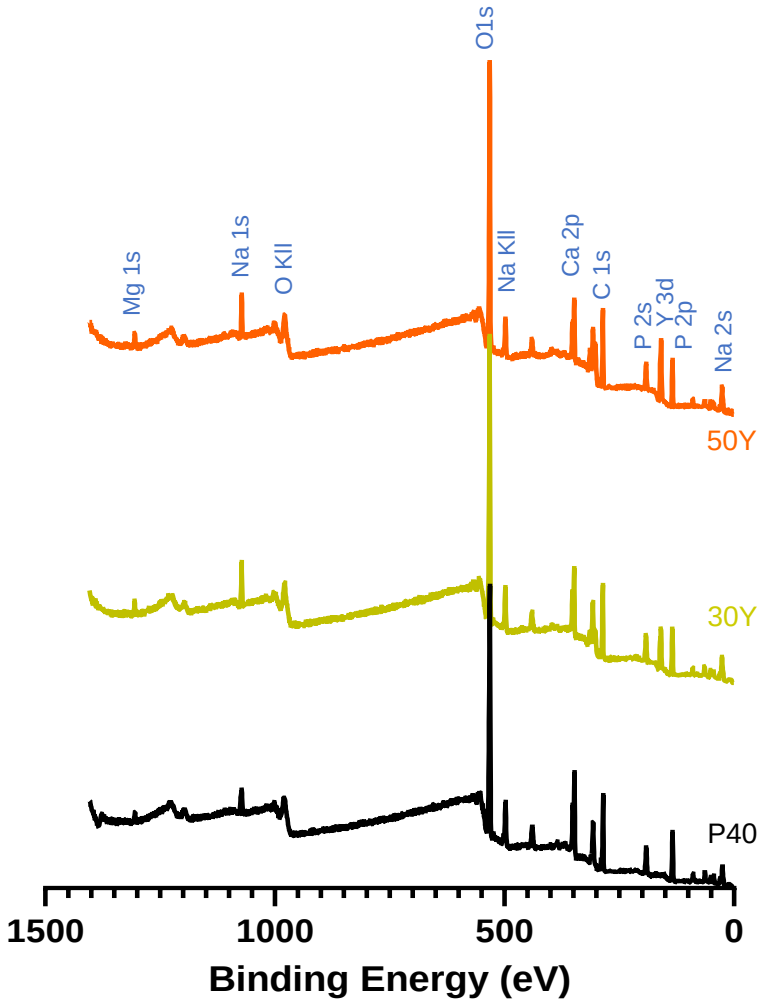

Figure 5.20 Survey X-ray photoelectron spectra for P40, 30Y and 50Y solid microspheres identifying all elemental photoelectron emissions.

High-resolution O 1s spectra were recorded for the P40, 30Y and 50Y solid microspheres. For the P40 SMS, the peaks were resolved into two components, with the highest binding energy peak at 533.1 eV (23.6%) corresponding to bridging oxygen (BO) within the glass structure, whilst the lowest binding energy peak at 531.4 eV (76.4%) was associated with non-bridging oxygens (NBO) (see Figure 5.21A). These binding energies were consistent with other XPS studies on phosphate-based glasses [226, 227].

In the 30Y microspheres there was an increase in the number of O peak components. A peak at 531.3 eV (78.0%; shift by 0.1 eV) for the NBO peak was seen. A peak at 532.4 eV (15.3%) was present and identified as Y-O-P bonding. This had a binding energy of 0.7 eV lower than the peak for BO (P-O-P) bond seen within the P40 solid glass microspheres and was likely due to the asymmetric bonding due to the difference in electronegativity between Y and P. Additional peaks at 533.6 eV (6.3%) were present and ascribed to Y-O-Y bonding as well as 528.9 eV (0.5%) that corresponded to Y-O bonding within Y_2O_3 (see Figure 5.21A and Table 4.5.2).

In the 50Y microspheres, the area for the peak at 531.2 eV (66.1%), which corresponded to NBO decreased, whilst the area of the peak at 529.0 eV (2.2%) for Y-O bonding within Y_2O_3 increased. Increases in the area for the peak at 532.7 eV (22.3%) for Y-O-P bonding and at 533.8 eV which corresponded to Y-O-Y (9.4%) were also oberved (see Figure 5.21A and Table 4.5.2).

Table 4.5.2 High-resolution O 1s spectra from XPS analysis of P40, 30Y and 50Y SMS.

Sample Code	Elements	Binding Energy (eV)	Corresponding Bonds	Area (%)
P40	O 1s	531.4	NBO	76.4
		533.1	BO	23.6
		534.2	Na KLL Auger	
30Y	O 1s	528.9	Y-O in Y_2O_3	0.5
		531.3	NBO (P-O-Mg/Ca/Na)	78.0
		532.4	Y-O-P	15.3
		533.6	Y-O-Y	6.3
		536.1	Na KLL	
50Y	O 1s	529.0	Y-O in Y_2O_3	2.2
		531.2	NBO (P-O-Mg/Ca/Na)	66.1
		532.7	Y-O-P	22.3
		533.8	Y-O-Y	9.4
		535.9	Na KLL	

High-resolution Y 3d spectra for 30Y was resolved into 2 components (see Figure 5.21B). The component at 158.1 eV (93.0%; 3d 5/2) was attributed to Y-P bonding [228]. The component at position 156.6 (7.0%) corresponded to Y-O bonding. For the 50Y SMS, there was an increase in the number of Y peak components. There was a slight decrease in the area of the peak at 158.0 (78.5%) for Y-P bonding, whereas the area of the peak at 156.7 (11.3%) associated with Y-O bonding increased. The additional peak observed at the highest binding energy of 159.6 eV (10.1%) most likely corresponded to Y-O-Y bonding within the structure (see Figure 5.21A B and Table 5.3).

Table 5.3 High-resolution Y 3d spectra from XPS analysis of P40, 30Y and 50Y SMS

Sample Code	Elements	Binding Energy (eV)	Corresponding Bonds	Area (%)
30Y	Y 3d	156.6	Y-O in Y_2O_3	7.0
		158.1	Y-P	93.0
50Y	Y 3d	156.6	Y-O in Y_2O_3	2.2
		158.0	Y-P	66.1
		159.0	Y-O-Y	22.3

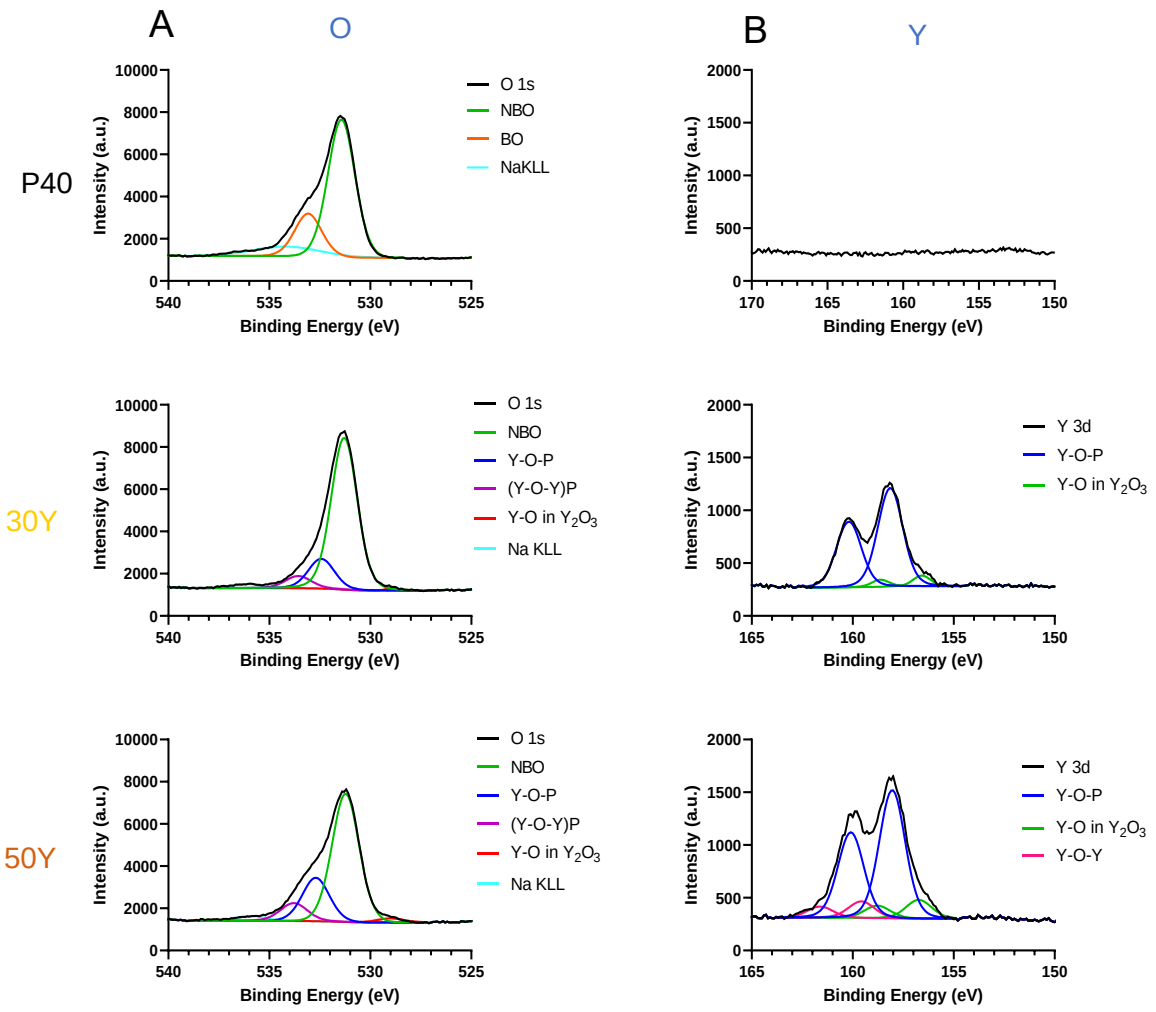

Figure 5.21(A) High-resolution spectra of O 1s peaks with overlapping Na KLL Auger emission and (B) High-resolution spectra of Y 3d peaks for P40, 30Y and 50Y solid microspheres.

5.2.12 Ion release studies

Figure 5.22 shows the cumulative ion release profiles for P40, 30Y and 50Y solid microspheres calculated from measurements obtained via ICP analysis over 28 days and the calculated ion release rates. The ions released from each microsphere formulation exhibited a linear relationship with time and were released consistently (apart from yttrium which was not released from P40 microspheres) (see Figure 5.22A– E). P40 solid microspheres released all the glass forming ions at a statistically significant higher rate in comparison to the yttrium-containing microspheres (Na and P: $p < 0.0001$; Mg and Ca*: vs* 30Y $p < 0.01$*, vs 50Y* $p < 0.001$*)* (see Figure 5.22F). As the yttrium content in the microspheres increased, there was a decrease in the release rate of the glass forming ions. P40 microspheres released Na^+ (3.47 ppm/day), Mg^{2+} (2.00 ppm/day), and P (8.35 ppm/day) at a rate around 3.5 times greater than that of the 30Y microspheres and around 10 times the rate compared to 50Y microspheres. P was the only ion that was released at a statistically significant higher release rate (2.18 ppm/day) by 30Y microspheres in comparison to 50Y microspheres (0.61 ppm/day) ($p < 0.01$). The yttrium containing microspheres released a very small amount of yttrium ions in comparison to all the other elements. 30Y microspheres had the highest release rate of Y^{3+} ions (0.39 ppm/day), whereas the 50Y microspheres, which contained a greater amount of yttrium, only released 0.10 ppm/day.

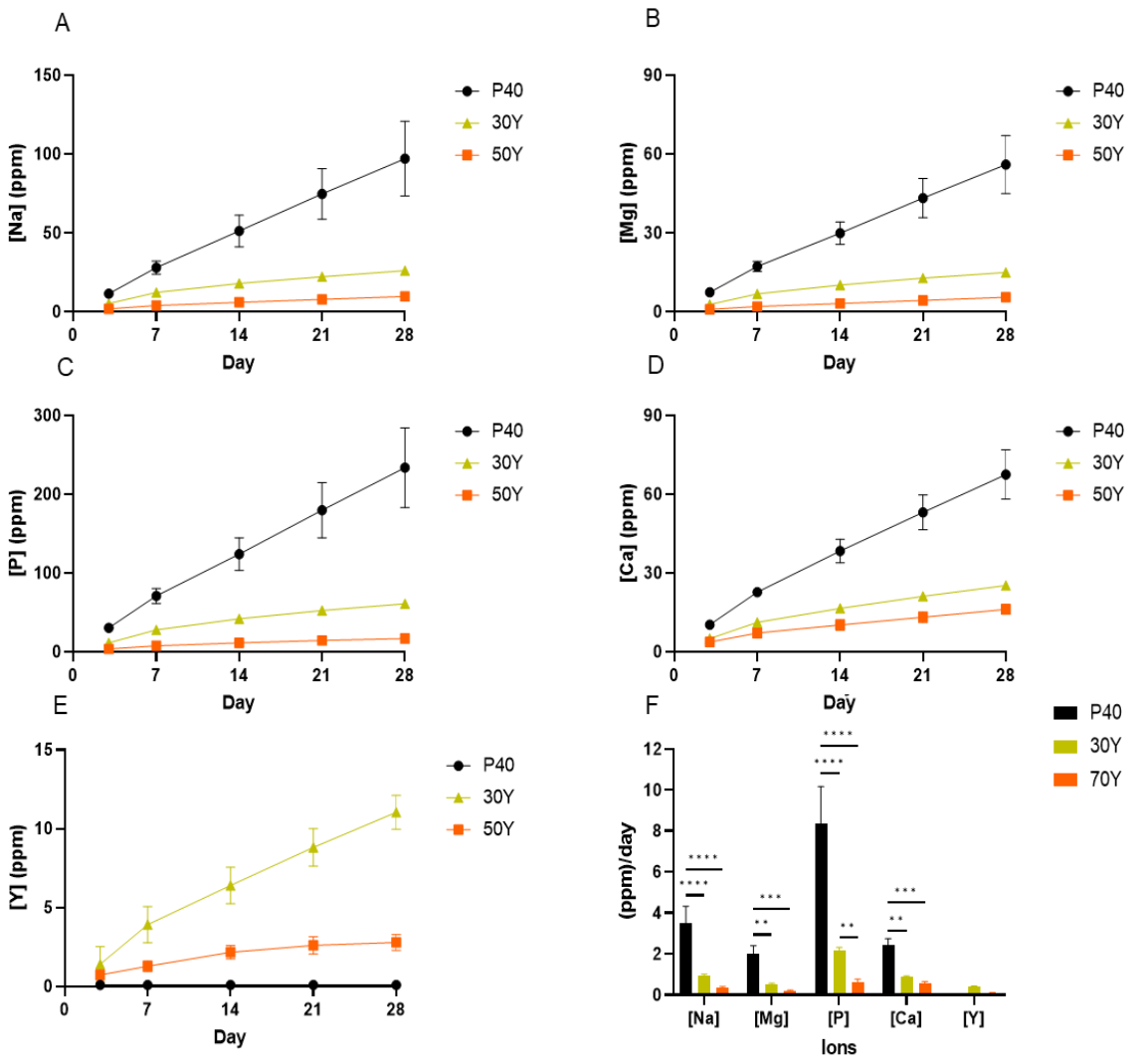

Figure 5.22 Cumulative ion release profile of (A) [Na], (B) [Mg], (C) [P], (D) [Ca] and (E) [Y] measured via ICP-MS PMS of solid P40, 30Y and 50Y microspheres immersed in milli-Q water over a 28 day period. (F) Ion release rates (ppm per day) of P40, 30Y and 50Y solid microspheres calculated from the linear cumulative ion release profiles (observed in A – E). (Error bars are also included in the data above).

Figure 5.23 shows the pH of the milli-Q water in which the microspheres were immersed over the 28-day period. For the solution containing P40 solid microspheres, there was a decrease in pH from ~7.2 at day 3 to ~7.0 at day 7, where it remained constant over the duration of the study. 30Y solution had a comparable value to the P40 sample at both day 3 and day 28 albeit with a slight decrease in pH which occurred more gradually. A pH of ~ 6.9 for 50Y was observed at day 3 which then increased to ~ 7.4 by the end of the 28-day period.

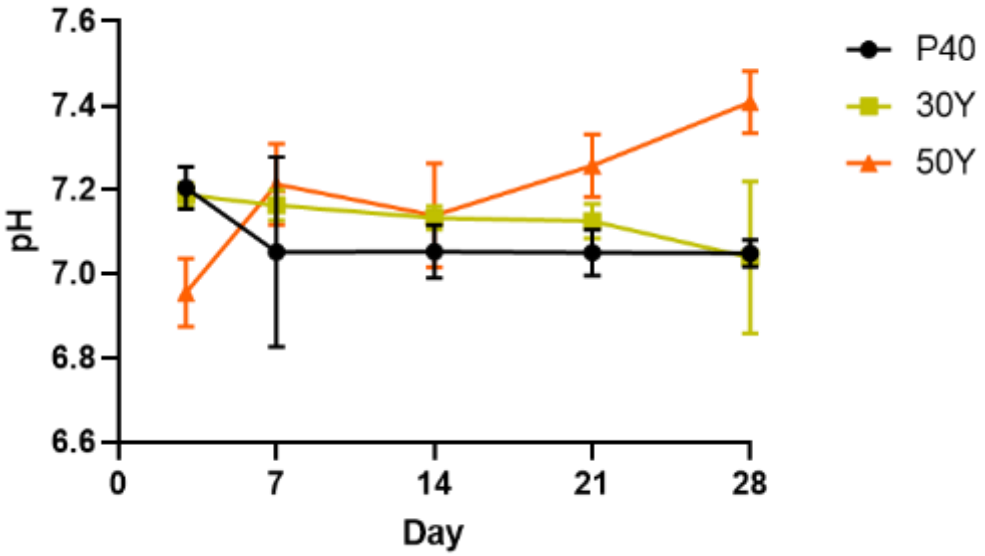

Figure 5.23 pH of milli-Q water during 28 days of P40, 30Y and 50Y solid microspheres immersion within the solution. (Error bars are also included in the data above).

SEM images of the P40, 30Y and 50Y microspheres following the period of immersion in milli-Q water are shown below in Figure 5.24. The P40 microspheres displayed evidence of cracking on their surface with the outer most layer appearing to flake and peel away from the surface of the microspheres after 28 days. These features were not observed on the surface of either 30Y or 50Y microspheres. The lack of structural and morphological changes to the yttrium containing microspheres correlated with the reduced ion release observed following 28 days immersion in milli-Q water. This was further evidence that yttrium incorporation into the microspheres had increased their durability when in an aqueous environment.

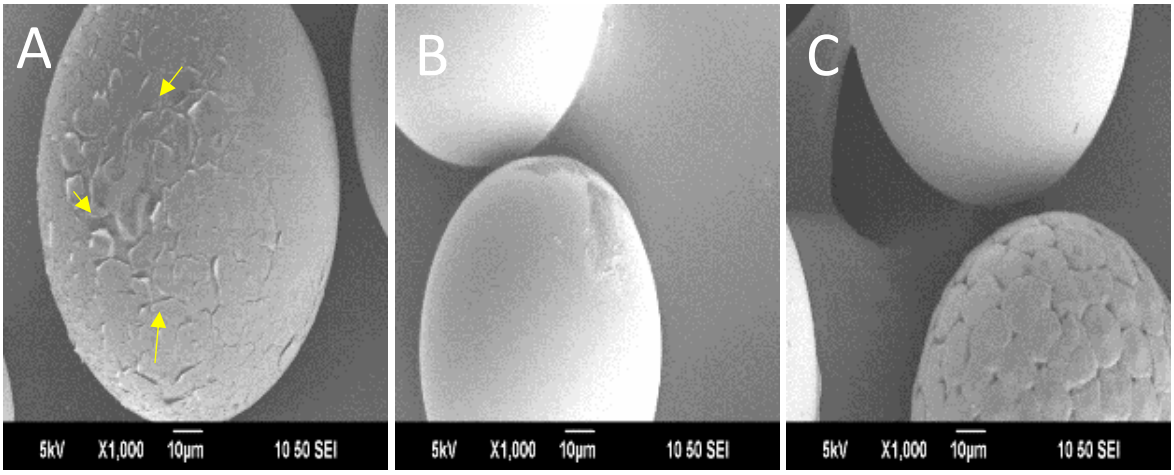

Figure 5.24 SEM images of (A) P40 (B) 30Y and (C) 50Y SMS after 28 days immersion in milli-Q water. Yellow arrows indicate regions of degradation on the microspheres surface.

5.2.13 Bioactivity studies in SBF: EDX Analysis

EDX analysis was performed on the P40, 30Y and 50Y microspheres prior to and after 28 days immersion in SBF. The Ca:P ratio (wt%) for each composition was calculated from the EDX values acquired (see Figure 5.25). Microspheres from each of the three formulations had a slight (but not significant) increase in the Ca:P ratio following 28 days immersion. The most pronounced increase was seen for the P40 microspheres with almost no discernible increase in the ratio for both yttrium-containing microspheres.

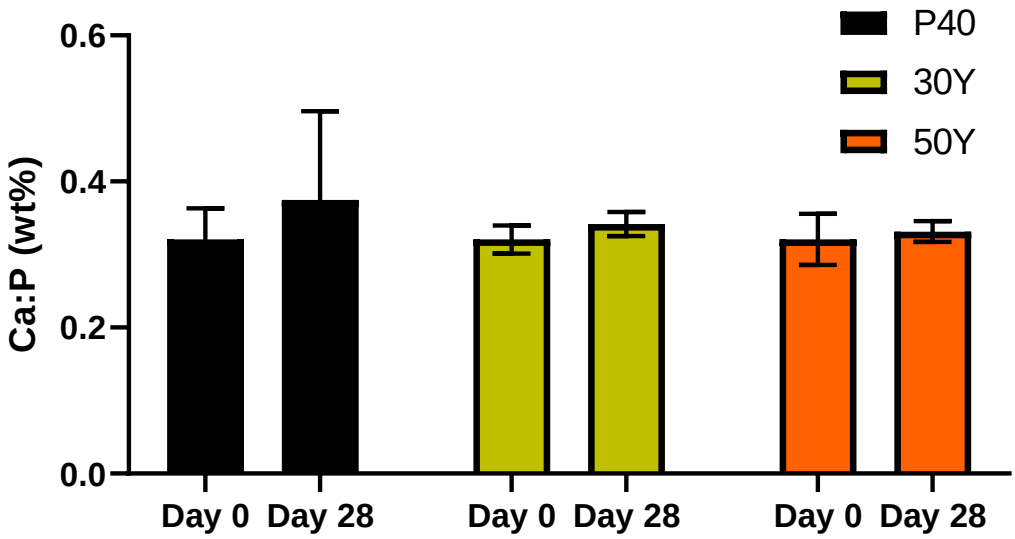

Figure 5.25 Ca:P ratio (wt%), determined by EDX, for P40, 30Y and 50Y solid microspheres prior to SBF immersion and after 28 days immersion.

5.2.14 Bioactivity studies in SBF: XRD Analysis

XRD profiles of P40, 30Y and 50Y solid microspheres and 45S5 (which was used as a positive control), following 28 days immersion in SBF are shown in Figure 5.26. The XRD spectra for 45S5 were in good agreement with the results seen in other studies, with sharp peaks at 2θ values of 26° and 32° observed from day 7 onwards revealing HCA (ICSD 01-084-1998) formation [136]. A single broad halo peak at 2θ values of ~–30-32° was observed for the P40 solid microspheres at both day 0 and day 28. The absence of any detectable crystalline peaks confirmed the amorphous nature of the microspheres prior to and following SBF immersion. In the 30Y microspheres, there was no additional peaks or change in the XRD spectra from day 0 to day 28 after immersion in SBF. The 50Y microspheres also exhibited no discernible additional peaks at day 28 to those that were present prior to SBF immersion. The lack of new crystalline phases suggested that no HA or alternative calcium phosphate phases had formed on the surface of the microsphere during 28 days immersion in SBF (see Figure 5.26).

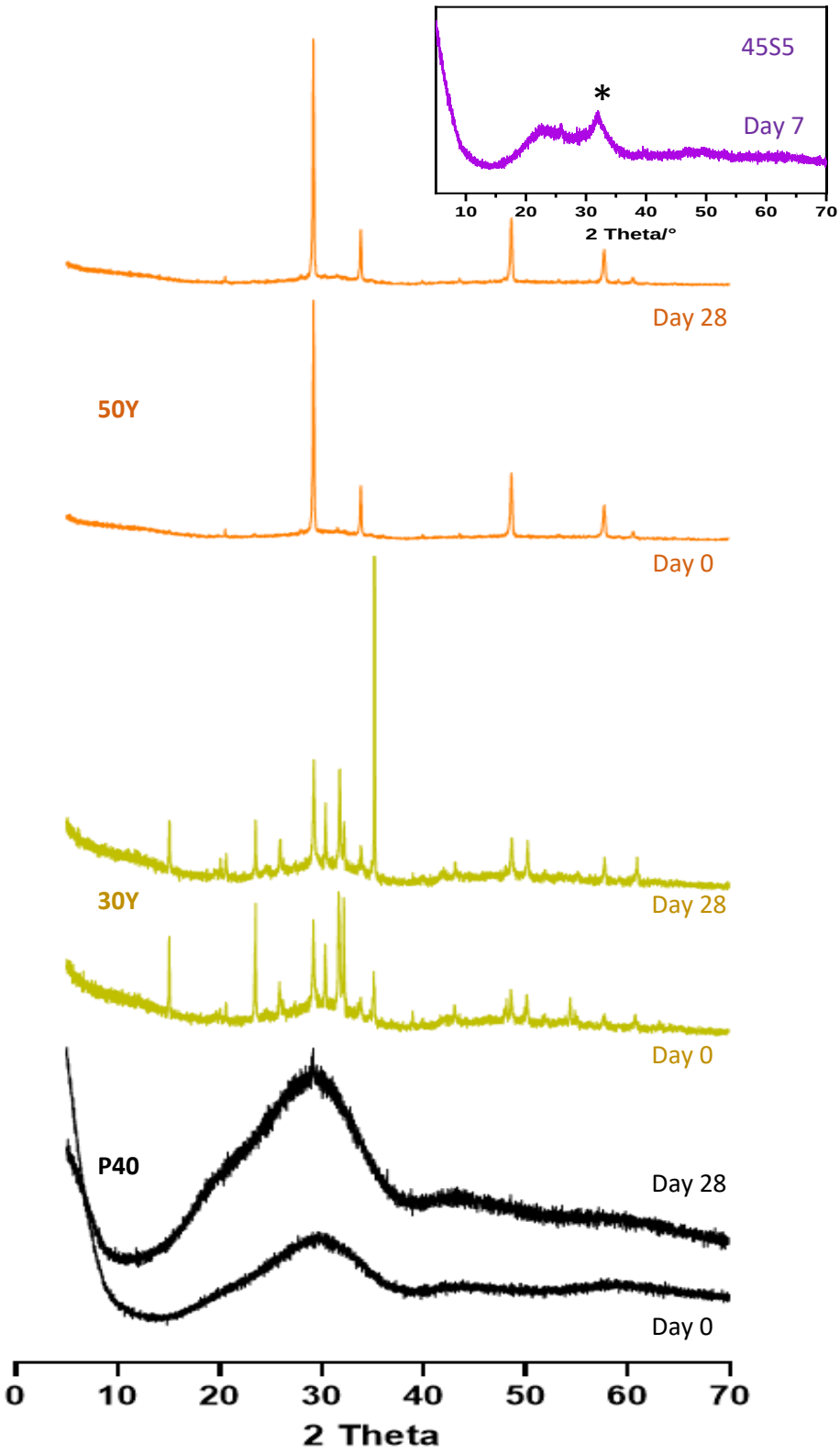

*Figure 5.26 XRD patterns for P40 (black), 30Y (gold) and 50Y (orange) solid microspheres prior to and after 28 days immersion in SBF. Inset is the XRD trace for 45S5 after 7 days immersion for SBF validation. * HCA (ICSD 01-084-1998).*

5.2.15 *In vitro* indirect cell culture method

To determine the cytocompatibility of the microspheres produced, an indirect cell culture method was performed which involved feeding microsphere-conditioned media to osteoblast-like cells (MG63s) to evaluate their biological response to the dissolution products released over time. Standard medium (SM) and SM containing 5% DMSO were included as positive and negative controls, respectively. Analysis of metabolic activity via the Alamar Blue assay showed a significant increase in cell response when both 30Y and 50Y microsphere conditioned media was added between day 2 to day 7 (D2 vs D7: $p < 0.0001$). This increase in metabolic activity was also seen for cells treated with SM but cells where SM + 5% DMSO was applied had no increase in metabolic activity from day 2 to day 7 (D2 vs D7: $p < 0.0001$). At day 2, cells treated with P40, 30Y and 50Y conditioned media had a significantly greater metabolic response compared to those treated with SM and SM + 5% DMSO ($p < 0.0001$). There was no statistically significant difference detected between cells treated with 30Y and 50Y conditioned media ($p > 0.05$). There was also no statistically significant difference between the cells treated with 30Y and 50Y conditioned media at day 7 ($p > 0.05$). At day 7, cells treated with P40 and SM media revealed a statistically significant increased metabolic response compared to the yttrium-formulations ($p < 0.001$), however no statistically significant differences were detected between P40 and SM ($p > 0.05$) (see Figure 5.27A).

Brightfield images of the MG63 cells after 2 days of culture within microsphere conditioned media confirmed the formation of homogenous cell monolayers in the presence of P40, 30Y and 50Y conditioned media. The confluency and morphology of the cells was comparable to that of the MG63s grown in SM. Conversely, cells grown in SM +5% DMSO were small and circular in morphology and sparsely distributed as expected (see Figure 5.27B).

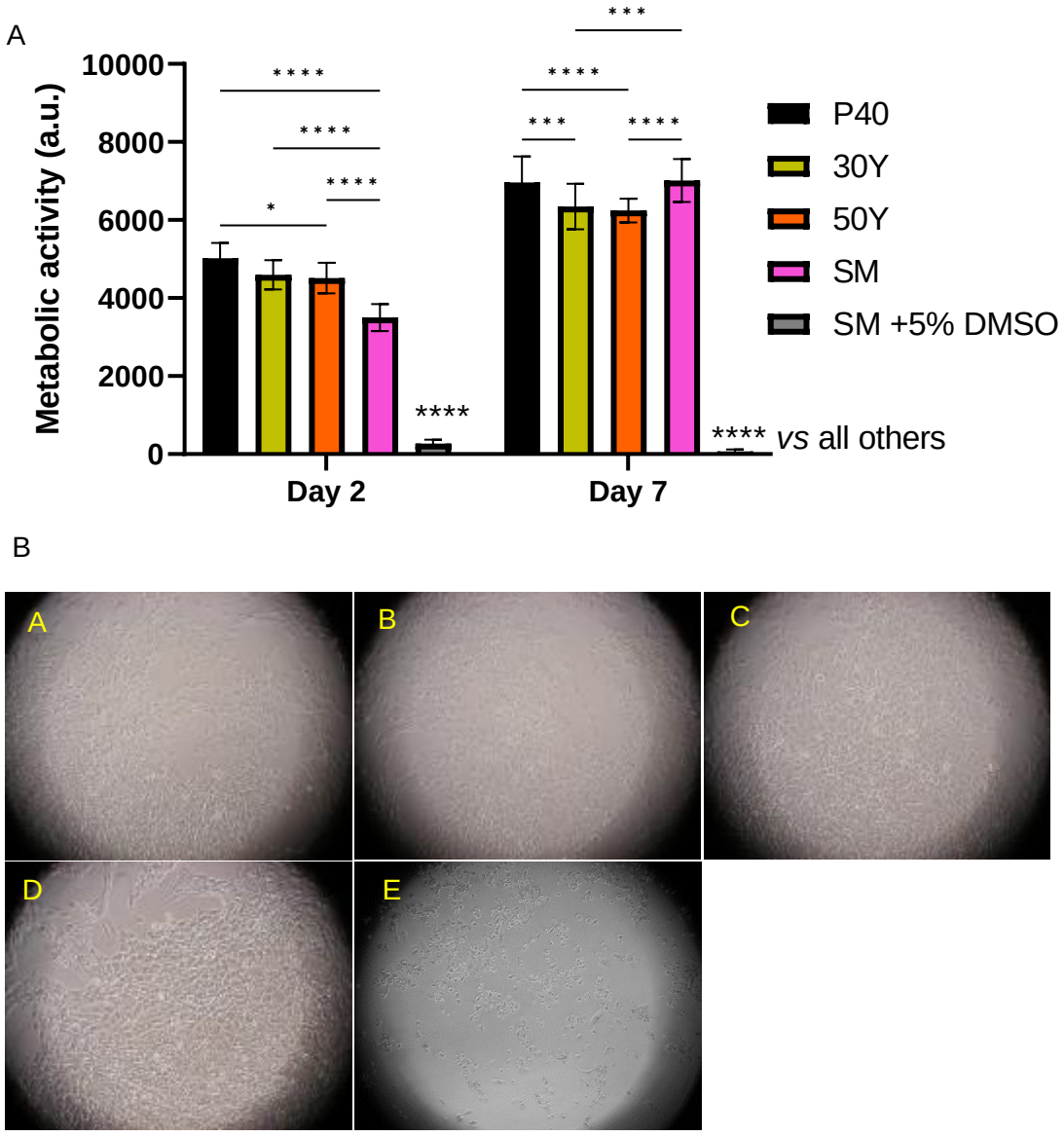

*Figure 5.27(A) Evaluation of cell metabolic activity in indirect culture of P40, 30Y and 50Y solid microspheres at day 2 and day 7. ****p < 0.0001, *** p < 0.001, * p < 0.05. (B) Cell appearance at day 2 of indirect culture; (A) P40, (B) 30Y, (C) 50Y, (D) SM and (E) SM + 5% DMSO.*

Alkaline phosphatase (ALP) activity was also measured as an early marker of osteogenic differentiation in MG63 cells after 7 days of indirect culture from P40, 30Y and 50Y microsphere formulations and SM. The ALP activity was normalised to the DNA content of the cells under investigation. At day 7, there was no statistically significant difference in ALP activity between cells grown in SM and both 30Y and 50Y conditioned media ($p > 0.05$). Cells grown in P40 media had statistically significantly higher ALP activity compared to cells to grown in the two yttrium-containing microsphere media (*vs* 30Y and 50Y: $p < 0.001$) (see Figure 5.28).

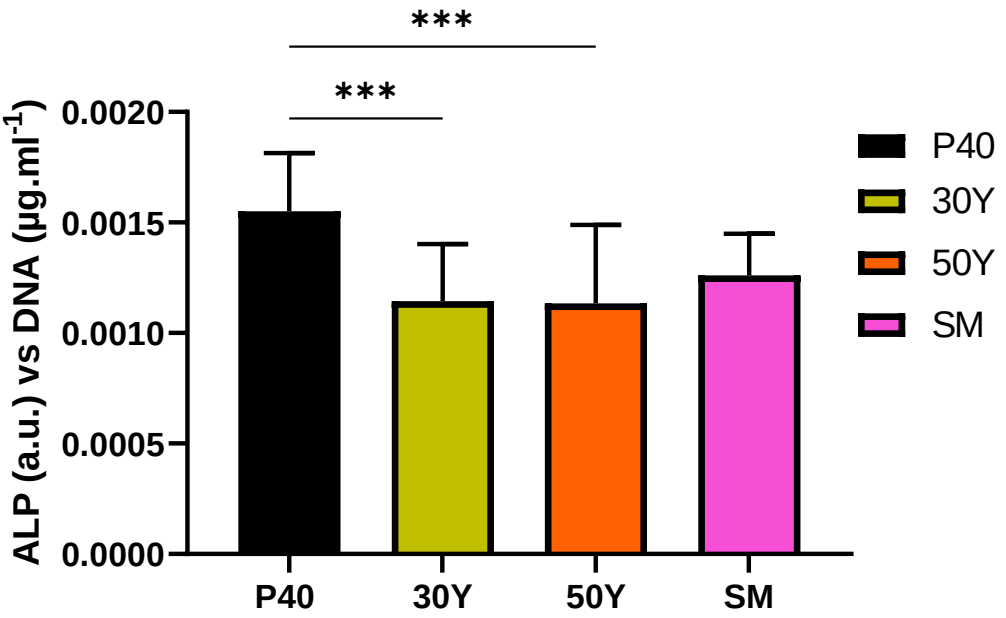

*Figure 5.28 Evaluation of ALP activity in indirect culture of P40, 30Y and 50Y solid microspheres at day 7. *** $p < 0.001$.*

5.2.16 Proteomic profiling by LC-MS/MS

Due to 30Y microspheres releasing a greater amount of yttrium ions and comparable cellular responses to indirect culture between 30Y and 50Y, the 30Y formulation was chosen to investigate how the release products from 30Y microspheres impacted protein expression within the cells. This was achieved using the indirect culture method and LC-MS/MS to compare cells treated with P40 conditioned media. LC-MS/MS analysis detected a total of 986 proteins from the samples measured (from a minimum of two peptide sequences with a protein threshold of 99.9% and a false positive discovery rate of 4.5%). 935 proteins were detected from the cells cultured in either P40 or 30Y conditioned media. 37 proteins were present from cells treated with P40 media that were not in the 30Y cells. The number of proteins unique to cells treated with 30Y microsphere media was found to be 14 (see Figure 5.29). Detection of proteins using LC-MS/MS is simply a broad indication of protein quantity. Failure to detect a protein indicates the absence of the protein or its presence in quantities below the detection limit.

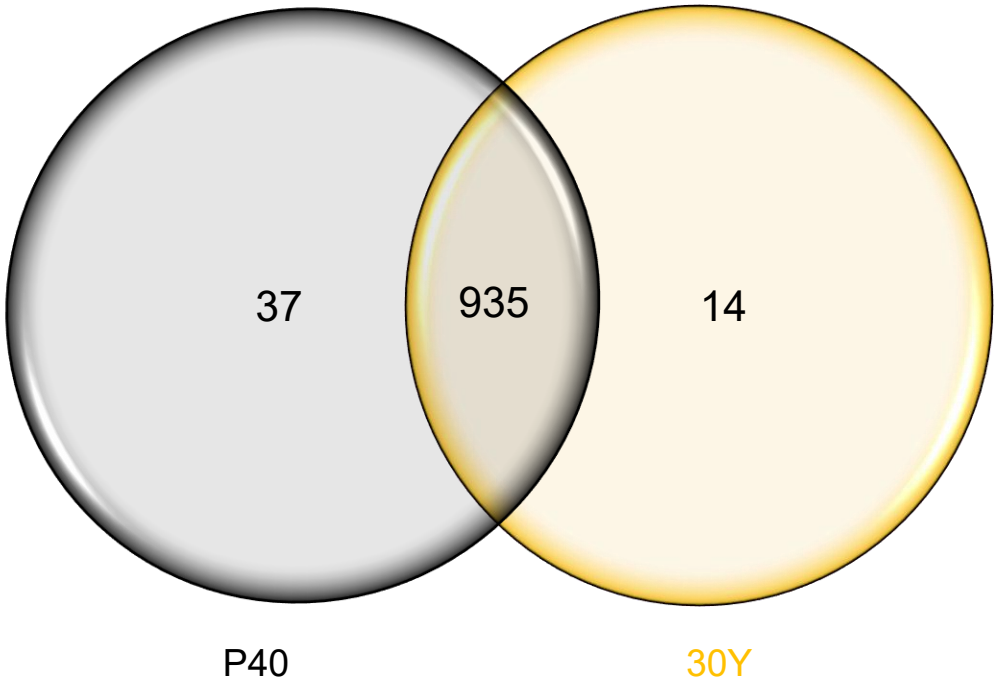

Figure 5.29 Venn diagram showing the number of proteins detected via LC-MS/MS and whether they were present in cells cultured in P40 and 30Y conditioned media or were exclusive to one condition.

A limitation of the experiment was that only one sample for each cultured condition underwent analysis. This meant that quantitative analysis tests could not be performed to assess whether there were statistically significant differences in the protein's quantitative values between the different samples. Only proteins that were present in one sample but not in another were considered significant. Studying the normalised total spectrum counts (semi-quantitative indicator of protein abundance generated within Scaffold software) of proteins unique to the 30Y sample revealed Beta-actin-like protein 2 (ACTBL2) (accession number Q562R1) to be present in the greatest amount (12.5 a.u.). This was followed by Transforming Growth Factor-Beta-Induced Protein (TGFBI) (accession number H0Y8L3) (3 a.u.). Table 5.4 displays the proteins unique to the 30Y samples and their normalised total spectrum counts

Table 5.4 LC-MS/MS analyses of MG63 protein expression which were only detected in cells cultured in 30Y conditioned-media.

Gene name	Identified proteins	Accession number	P40 (counts)	30Y (counts)
ACTBL2	Beta-actin-like protein 2 OS=Homo sapiens PE*=1 SV**=2	Q562R1	0	12.5
TGFBI	Transforming growth factor-beta-induced protein ig-h3 (Fragment) OS=Homo sapiens PE=1 SV=1	H0Y8L3	0	3.0
KRT7	Keratin, type II cytoskeletal 7 OS=Homo sapiens PE=1 SV=5	P08729	0	1.5
KRT14	Keratin, type I cytoskeletal 14 OS=Homo sapiens PE=1 SV=4	P02533	0	1.5
SLC5A3	Sodium/myo-inositol cotransporter OS=Homo sapiens PE=1 SV=2	P53794	0	1.5
IKBIP	Isoform 4 of Inhibitor of nuclear factor kappa-B kinase-interacting protein OS=Homo sapiens	Q70UQ0-4	0	1.5
HIST1H1C	Histone H1.2 OS=Homo sapiens PE=1 SV=2	P16403	0	1.5
PRPF6	Pre-mRNA-processing factor 6 OS=Homo sapiens PE=1 SV=1	O94906	0	1.5
THBS1	Thrombospondin-1 OS=Homo sapiens PE=1 SV=2	P07996	0	1.5

FKBP1A	Peptidyl-prolyl cis-trans isomerase FKBP1A OS=Homo sapiens PE=1 SV=2	P62942	0	1.5
GSTM2	Glutathione S-transferase OS=Homo sapiens PE=1 SV=1	E9PHN6	0	0.8
SUMF2	Sulfatase-modifying factor 2 OS=Homo sapiens PE=1 SV=1	C9J660	0	0.8
ALDH7A1	Alpha-aminoadipic semialdehyde dehydrogenase (Fragment) OS=Homo sapiens PE=1 SV=1	A0A1B0GVU0	0	0.8

*PE = p*rotein existence*, a numerical value describing the evidence for the existence of the protein (1 – 5; 1 being very high, 5 being very low).

**SE = Sequence Version, a version number of the sequence.

5.2.17 *In vitro* direct cell culture studies

MG63 cells were also directly seeded onto P40, 30Y and 50Y solid microspheres to assess the effect of direct physical contact on cellular responses and the microspheres' ability to provide a suitable surface to facilitate cell growth and proliferation. Analysis of metabolic activity at day 2, revealed that there was no statistically significant difference in metabolic activity between cells grown on P40 microspheres and the two yttrium-containing microsphere formulations ($p > 0.05$). Cells cultured on 30Y microspheres revealed higher metabolic activity at day 2 compared to those grown on 50Y ($p < 0.05$). Cells grown on any of the three microsphere formulations displayed statistically significantly lower metabolic activity compared to TCP control ($p < 0.0001$) (see Figure 5.30).

A statistically significantly higher metabolic activity was seen in cells cultured on each of the three microsphere formulations and TCP at day 7 in comparison to day 2 ($p < 0.0001$). At day 7, there was no statistically significant difference in metabolic activity between the cells cultured on 30Y and 50Y microspheres ($p > 0.05$), however it was statistically significantly

lower than those cultured on P40 microspheres (*vs 30Y*: $p < 0.01$; *vs 50Y*: $p < 0.001$) (see Figure 5.30).

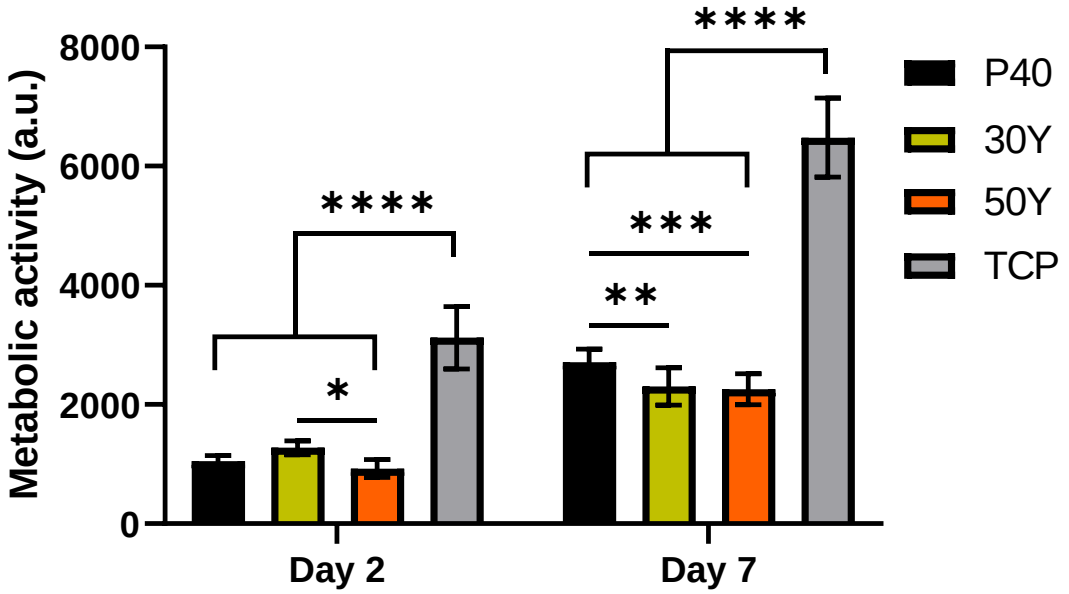

*Figure 5.30 Evaluation of cell metabolic activity in direct culture of P40, 30Y and 50Y solid microspheres at day 2 and day 7. **** p < 0.0001, *** p < 0.001, ** p < 0.01, * p < 0.5.*

The ALP activity after 7 days of MG63s grown directly on the microspheres and TCP was determined and normalised to the DNA concentration. Statistically significantly higher ALP activity was recorded in cells grown on P40, 30Y and 50Y microspheres in comparison to those grown on the TCP control ($p < 0.0001$). There was no statistically significant difference in ALP activity detected between cells grown on P40 and the two yttrium-containing microsphere formulations ($p > 0.05$) (see Figure 5.31).

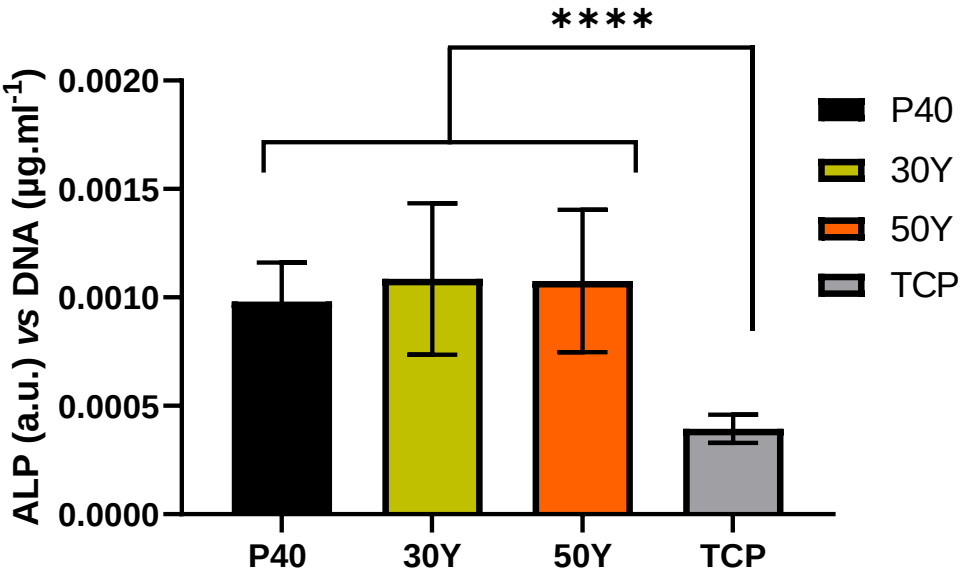

*Figure 5.31 Evaluation of ALP activity in direct culture of P40, 30Y and 50Y solid microspheres at day 7. *** $p < 0.001$.*

MG63 cells directly cultured onto the microspheres were visualised using ESEM at day 7. Cells were shown to adhere onto P40, 30Y and 50Y microspheres and appeared to be displaying lamellipodia and filopodia projections that were bridging adjacent neighbouring microspheres and spreading over the microsphere surfaces (see Figure 5.32).

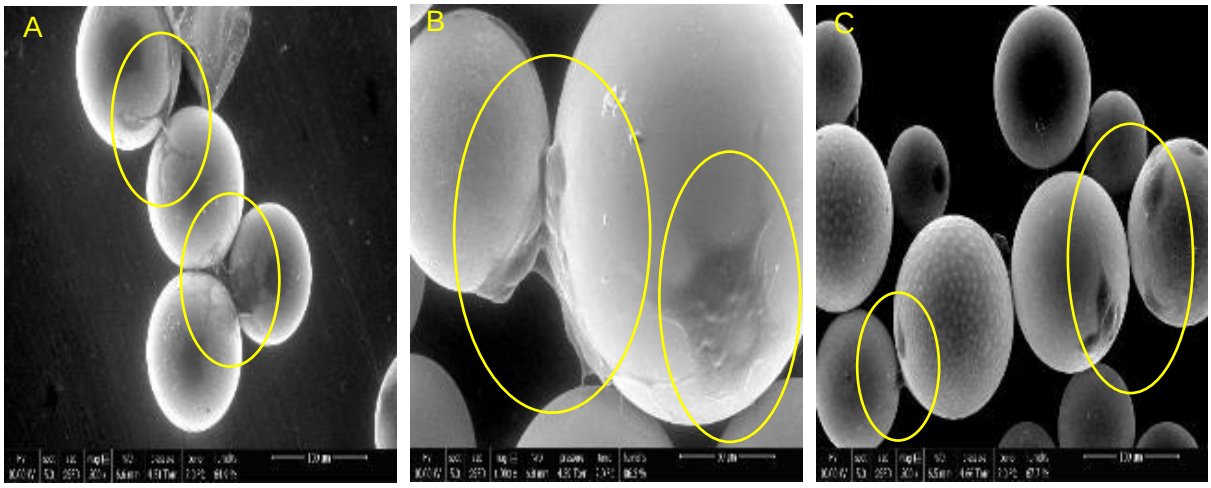

Figure 5.32 SEM images of (A) P40 (B) 30Y and (C) 50Y solid microspheres after 7 days direct culture with MG63 cells. Yellow circles indicate regions of cells attachment and the formation of colonies on the microspheres surface.

5.2.18 Manufacturing porous yttrium P40 microspheres

Similar to the previous chapter, attempts were also made to produce porous yttrium-containing microspheres using P40 glass particles. As seen in Table 4.5.5, a range of processing parameters were explored. Initially the same process that had been effectively employed to produce high yields of porous phosphate glass microspheres was used. The glass particles, Y_2O_3 and $CaCO_3$ (at different size ranges) were combine at various ratios and mixed using a benchtop vortex prior to flame spheroidisation. At first, the 30Y composition (30:70 ratio of yttrium oxide: glass) was used with the intention to try and increase yttrium content once a suitable processing procedure had been established. Evidence of porous microspheres was observed however the yield was very low. The failure of this method to produce a consistently high yield of porous yttrium-containing microspheres led to changes in the way in which the components were mixed prior to spheroidisation. Polyvinyl alcohol (PVA) was used as a binder for the particles, as was a ball milling machine prior to spheroidisation. Regardless of the parameters used, no significant added benefit on the yield of yttrium-containing porous microspheres within resulting particles was evident following flame spheroidisation.

Table 4.5.5 Processing parameters used prior to flame spheroidisation in attempting porous yttrium microsphere production.

Glass particle size (μM)	Yttrium:glass	Porogen size (μM)	Porogen ratio	Vortex mixing	Ball milling	PVA addition
45 - 63	30:70	45-63	1:1	X		
45 - 63	30:70	45-63	1:2	X		
45 - 63	30:70	45-63	1:3	X		
45 - 63	30:70	45-63	1:1		X	X
45 - 63	30:70	45-63	1:2		X	X
45 - 63	30:70	45-63	1:3		X	X
45 - 63	30:70	< 5	1:0.5	X		
45 - 63	30:70	< 5	1:1	X		
45 - 63	30:70	< 5	1:2	X		
45 - 63	30:70	< 5	1:0.5		X	X
45 - 63	30:70	< 5	1:1		X	X
45 - 63	30:70	< 5	1:2		X	X
45 - 63	50:50	< 5	1:0.5	X		
45 - 63	50:50	< 5	1:1	X		
45 - 63	50:50	< 5	1:2	X		
45 - 63	50:50	< 5	1:0.5		X	X
45 - 63	50:50	< 5	1:1		X	X
45 - 63	50:50	< 5	1:2		X	X

SEM analysis revealed that the resulting particles were largely agglomerated with a small proportion of solid microspheres and a very low yield of porous microspheres (see Figure 5.33). EDX analysis of the microspheres showed that the SMS contained yttrium but at a much lower level than when produced in the absence of $CaCO_3$. Elemental analysis of the microspheres that most closely resembled the desired porous morphology showed that these particles contained no yttrium or extremely low levels (<3 mol%). The porous microspheres also lacked the complete spherical geometry that was seen when porous phosphate glass microspheres of the P40, P35, P32.5 and P30 formulations were produced. The addition of a greater amount of $CaCO_3$ did not result in increased levels of porosity. When a greater amount of Y_2O_3 powder was added this also did not result in an increase in the yttrium content of the porous particles. These results demonstrated that this method of processing was not suitable for producing the desired final porous microsphere products.

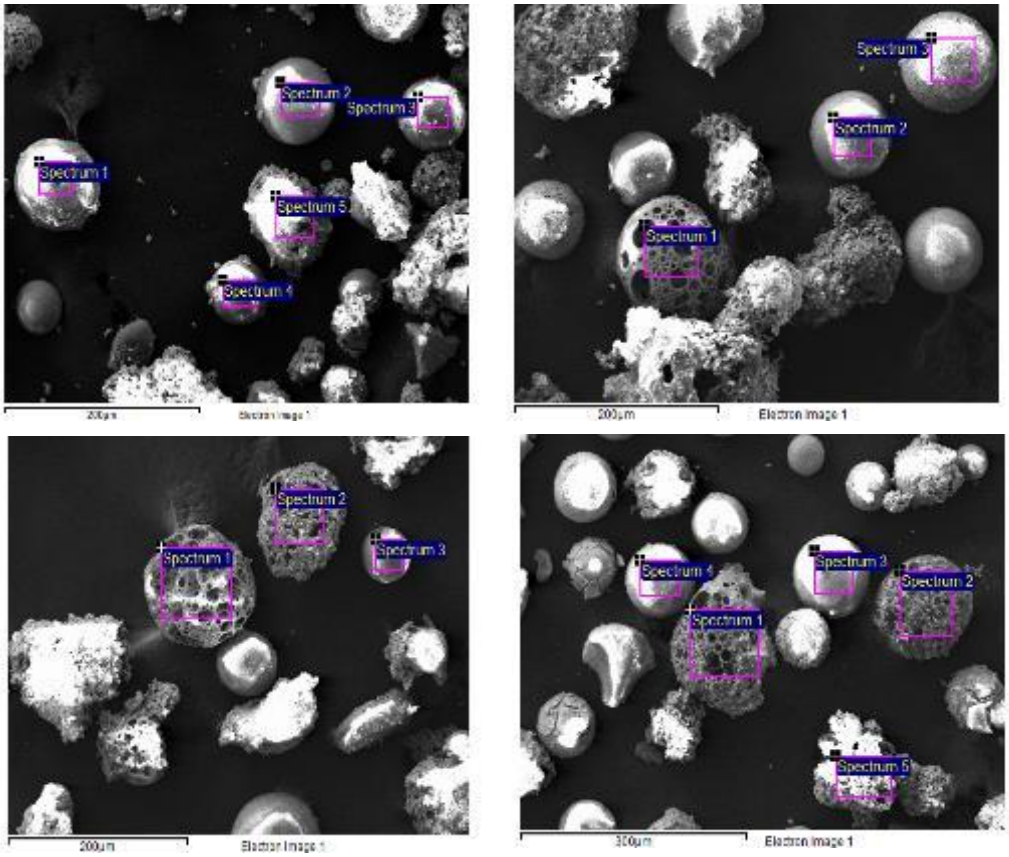

Figure 5.33 SEM images of attempts to form porous yttrium-containing microspheres using P40 glass particles and Y_2O_3.

In the studies above, a gravitational funnel feeding system to introduce particles into the flame and a vibratory motor was used to maintain a constant feed rate and prevent accumulation of particles within the feeder. To try and optimise the entry and trajectory of the particles, a pneumatic sand blasting gun (Neilsen CT5267, UK) was used to inject the particles into the flame. The particles were directed into the inner cone region of the flame from a slightly elevated angle and downstream along the same path of the flame (see Figure 5.34).

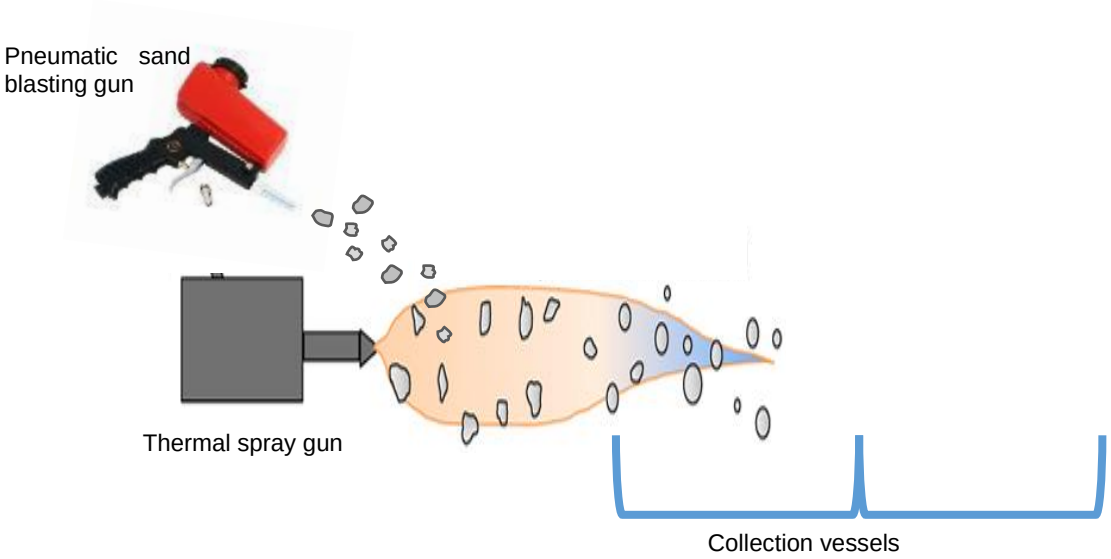

Figure 5.34 Schematic diagram of the modified flame spheroidisation technique using a pneumatic sand blasting gun to feed the particles into the flame.

The P40 glass and Y_2O_3 were mixed at a 70:30 ratio and then at a 1:1, 1:0.75 and 1:0.5 ratio with $CaCO_3$ prior to being fed into the flame using a pneumatic sand blasting gun. Due to the smaller starting glass particle size (45 – 63 µm), $CaCO_3$ porogen less than 5 *µ*m in size was chosen when optimising the process as it was hypothesised that this would allow the porogen to coat the outer surface of the glass particles and provide higher coverage.

SEM analysis revealed that this method of forcibly feeding particles into the flame resulted in the formation of a much higher yield of highly porous microspheres at each of the three ratios (see Figure 5.35A, B and C). The high yield of PMS with the desired shape and morphology was not seen when the particles were fed using the gravitational feeder. Despite the promising effect on morphology, EDX analysis revealed that again only low levels of yttrium were incorporated into the microspheres (Figure 5.35D). The lowest porogen ratio appeared to produce microspheres with the greatest Y_2O_3 content (~5%) and this decreased as the porogen content increased. The P_2O_5 content remained constant throughout the samples at around 36-37%.

As previously seen, simply increasing the amount of yttrium oxide mixed with the glass particles did not cause a significant increase in yttrium content of the porous microspheres. Although the results were promising with regards to the porosity, the low levels of yttrium incorporation meant that further optimisation of the process was required to produce porous microspheres with sufficient yttrium content.

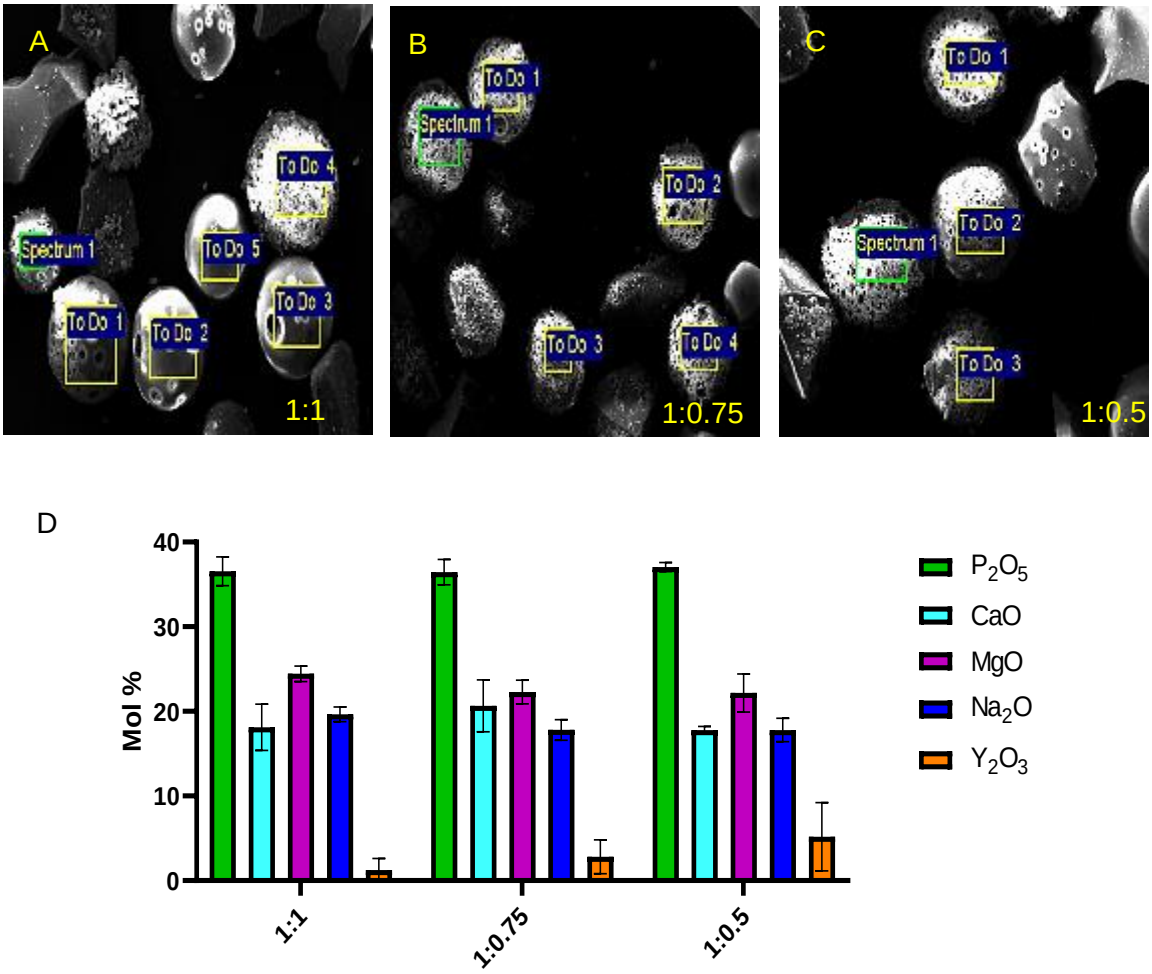

Figure 5.35 (A) SEM image of the porous yttrium-containing microspheres produced using 1:1 microsphere to porogen ratio and the regions analysed using EDX. (B) SEM image of the porous yttrium-containing microspheres produced using 1:0.75 microsphere to porogen ratio and the regions analysed using EDX (C) SEM image of the porous yttrium-containing microspheres produced using 1:0.5 microsphere to porogen ratio and the regions analysed using EDX and (D) EDX values for the microspheres produced at each porogen ratio.

An alternative approach to form porous microspheres was to first process solid yttrium-containing microspheres, crush the solid microspheres using a pestle and mortar and to then mix these with porogen. The hypothesis for processing the particles in this way was that delivering the particles into the flame using pneumatic sand blasting gun appeared to be effective at inducing porosity in the microspheres. This may be due to enhanced particle residence time or penetration within the flame. It was hypothesised that solid microspheres containing a confirmed amount of radionuclide incorporated within their structure would hopefully guarantee a higher yttrium content than was seen using previous methodology. Using the 30Y composition, a proportion of the microspheres produced displayed evidence of

surface porosity (see Figure 5.36A). EDX analysis of these microspheres revealed that they contained yttrium within their structure and at levels that were comparable to 30Y solid microspheres subjected to only a single round of flame spheroidisation. Elemental analysis showed that compositional heterogeneity existed between the microspheres particularly with respect to the yttrium content (see Figure 5.36B). However, the yield of porous microspheres remained low with less than 50% of the microspheres displaying apparent porosity. When 50Y solid microspheres were processed in the same manner, no porosity was seen in the resulting microspheres.

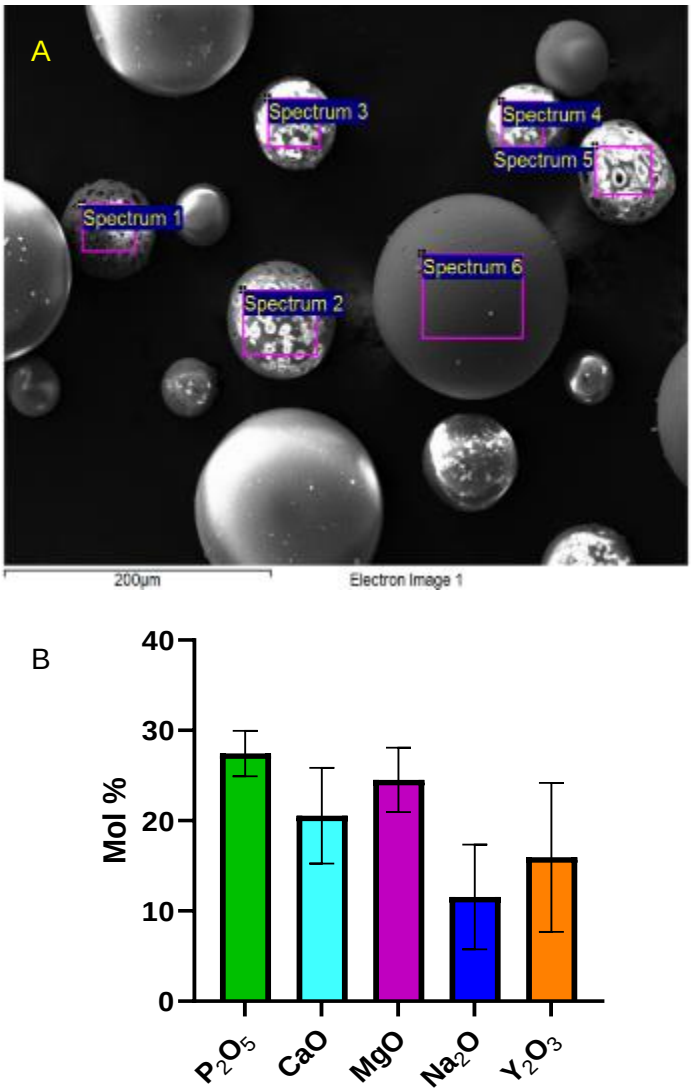

Figure 5.36 (A) SEM image of the 30Y porous yttrium-containing microspheres produced using 1:1 microsphere to porogen ratio and the regions analysed using EDX. (B) EDX values for the 30Y porous microspheres produced.

The major limitation of this processing method was the small quantity of the final product collected and the large quantity of particles lost during processing. The current method also introduced greater variability into the system due to inherent differences in the angle and position in which the particles were fed into the flame between batches. However, these studies were proof of concept that porous yttrium containing microspheres could be formed. Further optimisation would be required to increase the yield of porous microspheres to allow for further characterisation. Additional alterations to the processing procedure may also be necessary for the cost-effective production of high yttrium containing porous microspheres.

5.3 Discussion

In this work a novel processing method was established to combine Y_2O_3 with phosphate glass particles prior to spheroidisation using a thermal spray gun, facilitating the production of uniform solid microspheres containing high yttrium levels. This method allowed the yttrium content to be tailored, by varying the Y_2O_3 to glass ratio, which resulted in the formation of microspheres that had either equivalent or superior yttrium content in comparison to clinically available aluminosilicate glass microspheres used for internal radiotherapy applications (Therasphere^{TM}). 30Y microspheres were chosen for further characterisation and study due to their yttrium content (15.0 mol% ±1.8) being comparable to that of Therasphere^{TM} and containing a P_2O_5 content of ~30 mol%. Previous work in Chapter 3 had shown that glass microspheres with this phosphate content primarily contained ortho and pyrophosphate species that were beneficial for facilitating bone repair. 50Y microsphere were also used as these had the highest yttrium content (39.1 mol% ±3.3) and it was postulated they may retain some of the beneficial features from their parent P40 glass, such as release of therapeutic ions. In addition to this, microspheres have improved delivery properties, in comparison to irregular-shaped particles, and the ability to be administered by minimally invasive surgical injections. This is important when using the microspheres for internal radiotherapy, where the ability to administer them easily and accurately would be vital in order to maximise their therapeutic efficacy.

EDX analysis showed that in a similar way as to when $CaCO_3$ was mixed with phosphate glass particles to induce porosity, the addition of Y_2O_3 resulted in the formation of microspheres that had reduced content of all glass forming elements after processing. With increasing Y_2O_3 addition proportional decreases in these elements were observed (Figure 5.2). It is proposed that a high yttrium content is desirable for radiotherapy applications as it could enable more radiation to be delivered per dose of microspheres, leading to the use of fewer microspheres [229]. A higher yttrium content could also result in shorter neutron activation times and aid with logistical issues involving the time and transportation of the microspheres from the nuclear activation facility to the clinic. Nuclear decay occurs during this period and the greater the amount of radioactivity, the longer the transit time available in order for the patient to still receive an efficacious radiation dose [230].

The quantity of yttrium varied between microspheres produced from the same batch and was observed quantitatively and qualitatively by EDX and EDX mapping respectively (Figure 5.3, Figure 5.4, Figure 5.5). Preliminary studies involving P40 glass particles in the 63 – 125 µm size range, that had been used to produce porous phosphate glass microspheres in chapter

3, found that there was a much larger deviation in the yttrium content between microspheres. The size range of 45 – 63 µm was subsequently used which reduced the discrepancy between the size of the glass and the yttrium oxide particles resulting in more uniform yttrium content within the microspheres.

SEM analysis revealed that topographically distinct microspheres existed at the 30Y composition, and that the topography appeared indicative of the yttrium content. Most microspheres had a uniform shape and size and a smooth surface topography. A small proportion had rough surfaces and grain-like structures on their surface. This set of microspheres were found to have a yttrium content typically around 10 mol% or lower (Figure 5.3).

However, a significant proportion of the 50Y microspheres presented with an array of distinctive and topographically unique surface features (Figure 5.5). These were broadly categorised into three groups based on their topography using SEM and FEG-SEM analysis. FEG-SEM uses a high brightness electron beam and has a higher spatial resolution compared to SEM, which uses thermionic tungsten filaments, and was therefore more suitable for imaging the small surface features on the microspheres in greater detail [231]. The first subset of microspheres exhibited prominent, highly ordered structures and were visible on the surface of the majority of 50Y microspheres. The size of these structures varied between 3 – 10 µm in diameter and a trend was established in which the larger and more highly ordered the structures, the greater the yttrium content (as detected via EDX). EDX analysis also revealed that these structures contained localised regions of yttrium content. Yttrium was found to be concentrated at the central region of the structure with more of the elements from the parent glass in the region between each unit (Figure 5.6). This highlighted the potential to tailor the surface topography of the microspheres in addition to the yttrium content by altering the yttrium oxide to glass ratio prior to spheroidisation.

These surface structures were initial evidence that the addition of Y_2O_3 resulted in the formation of microspheres that were glass-ceramics [222]. Glass-ceramics are defined as polycrystalline materials, which are usually obtained by controlled crystallization of glass through heat-treatment. Typically, glass-ceramics are produced by quenching a glass, nucleating at an elevated temperature followed by crystal growth at a higher temperature (see Figure 5.37). Separate nucleation and crystal growth steps allow for greater control over the crystallisation process and final product. It is also possible to have substantial overlap in the temperature at which the nucleation and crystallisation occurs [232]. In the case of the 50Y microspheres with the unique topographies, it appears that a yttrium rich nucleus had formed and then crystal growth occurred, resulting in orientated glass-ceramic microstructures. The

appearance and size of the glass-ceramic microstructures appears to be related to the yttrium content of the microspheres, with larger, more prominent structures occurring with elevated yttrium content.

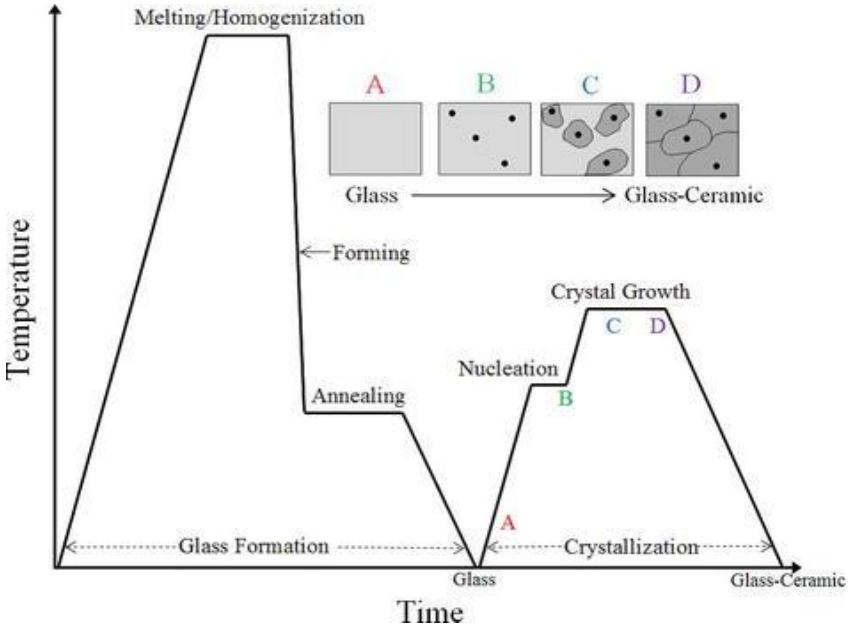

Figure 5.37 Schematic of glass processing in the formation of a glass ceramic. [4]

FIB-SEM analysis revealed that in the 50Y microspheres the formation of crystalline phases occurred within the body of the microspheres and was not limited to the surface. In Figure 5.8 and Figure 5.11, the crystalline structures appeared to be concentrated or culminated at regions where the prominent surface features were observed. In Figure 5.10, for 50Y microspheres that displayed a smooth surface topography, small spherical phases were visible which were distinct from a glassy matrix phase. The FIB-SEM analysis of the microspheres suggested that bulk crystallisation was occurring and it may be that the Y_2O_3 was not completely miscible within the phosphate glass and therefore forming microscopic clusters that are evenly dispersed throughout the microsphere [233]. EDX analysis of the crystalline regions within the 50Y microspheres revealed that these were yttrium-rich in comparison to the regions around them.

From the FIB-SEM analysis, it appeared that phase separation had occurred as seen by the physically and chemically distinct regions within the microspheres. During flame spheroidisation, phase separation into a “yttrium-rich” phase and a “glass-rich” phase has occurred, with both phases containing different proportions of the network forming ions [234].

The yttrium-rich phase is not vitrifiable, so upon cooling of the molten microsphere this phase crystallises, thereby forming the glass-ceramic microspheres. Interestingly, the phases present within different 50Y microspheres were morphologically discrete to one another. As seen in Figure 5.10, droplet-like phases were present and are formed via classical nucleation and growth (see Figure 5.38A). Similar phase separation with the characteristic droplet-like phases was seen in a study by Luo *et al.* where spherical Y^{3+} phases were dispersed within an yttrium silicate glass matrix upon heat treatment [235]. In some microspheres, as seen in Figure 5.8 and Figure 5.11, the yttrium-rich phases are different in appearance and may have formed via spinodal decomposition leading to the formation of intertwined tendril-like phases (see Figure 5.38B). Spinodal decomposition is a continuous phase transformation mechanism occurring throughout a solid resulting in spontaneous formation of distinct phases that are chemically and physical discrete from one another [236].

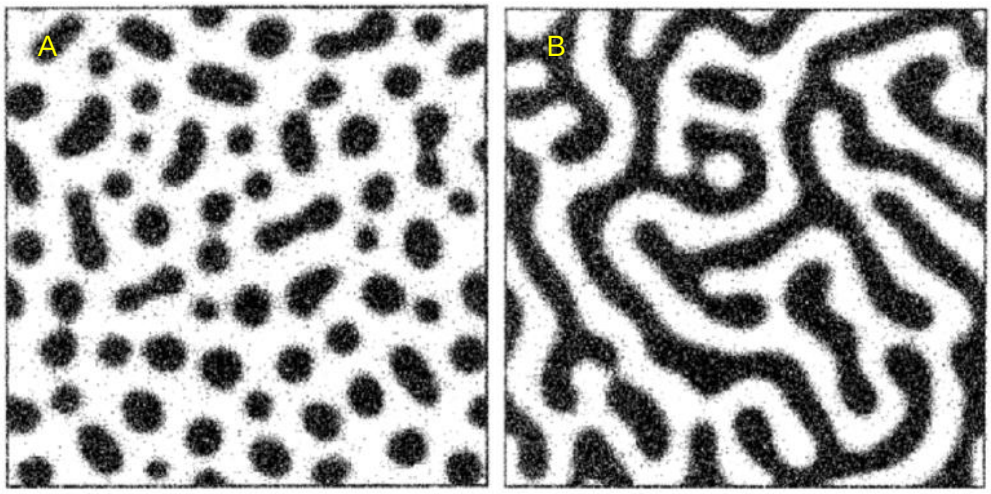

Figure 5.38 (A) Schematic of the classical droplet-like phases produced from nucleation and (B) "Tendril" patterns produced by spinodal decomposition. Reproduced from [10].

The XRD spectra of the microspheres studied was further evidence that the yttrium containing formulations were glass ceramics containing crystalline phases within an amorphous base glass (see Figure 5.12). 30Y microspheres had peaks that corresponded to both the cubic (ICDD 01-079-1257) and hexagonal phase (ICDD 01-076-7397) of Y_2O_3 as well as for $Y(PO_4)$ (ICDD 01-084-0335). The 50Y microspheres containing higher yttrium content, showed only peaks that correspond to the cubic phase of Y_2O_3 (ICDD 01-079-1257). Similar results were seen in a study by Kawashita *et al.* where ceramic microspheres were formed from solely Y_2O_3 or YPO_4 powder using a high-frequency induction thermal plasma melting technique [217].

Only peaks that corresponded to cubic Y_2O_3 were detected in the Y_2O_3 microspheres, whereas weak diffraction peaks that corresponded to both cubic and monoclinic Y_2O_3 were identified in addition to YPO_4 peaks in the YPO_4 derived microspheres. For the YPO_4 microspheres, it was found that the intensity of the YPO_4 peaks decreased whilst the Y_2O_3 peaks increased with increasing plasma flame power. This was attributed to the loss of P_2O_5 due to volatilisation. Similarly, the decreased P_2O_5 content within 50Y microspheres compared to 30Y may prevent the formation of a YPO_4 phase.

The 1D ^{31}P MAS-NMR spectra revealed that the P40 solid microspheres contained primarily Q^1 and Q^2 species but may have also contained a small proportion of orthophosphate Q^0 species within their amorphous structure (Figure 5.13). Due to the presence of only one peak within the 50Y and 30Y spectra it was not possible to definitively determine which Q^n species were present in these microspheres using this technique. Although not conclusive, the solitary peak could be interpreted to imply that both 30Y and 50Y microspheres were composed entirely of Q^0 species or that they were almost entirely composed of Q^1 and the Y components had shifted the peak to a higher chemical shift. The spectra for 30Y detected the presence of crystalline regions within the microsphere structure that had ^{31}P resonance. XRD analysis has confirmed that 30Y microspheres were not amorphous and contained crystalline phases that include $Y(PO_4)$ (ICDD 01-084-0335). Only cubic Y_2O_3 was detected in 50Y microspheres via XRD analysis confirming that these microspheres were also not amorphous like their parent P40 glass but glass-ceramics containing crystalline regions. Y_2O_3 has no ^{31}P resonance and meant that no crystalline regions were detected using 1D ^{31}P MAS-NMR within the 50Y microspheres.

Raman analysis was performed to gain additional structural information and to ascertain which phosphate species were present in the microspheres. Yttrium addition to phosphate glasses is known to result in depolymerisation of the glass network [237]. The depolymerisation is attributed to the greater proportion of non-bridging oxygen's that are required to charge balance the additional cations introduced into the glass network. This subsequently results in a reduction of bridging oxygen that are able to covalently bond with adjacent phosphate tetrahedra [141]. The microsphere in this study were now glass ceramics and had significantly higher yttrium content than has been achieved before in traditional phosphate glasses. Mapping experiments were performed in which a hot colour palette was used to generate images that plotted the intensity ratio (as peak area) of peaks associated with the cubic phase of Y_2O_3 (377 cm^{-1}, 345-410 cm^{-1}, Raman-active A_g mode) relative to the Raman-active PO_2 symmetric stretching mode of non-bridging oxygen's in Q^0 units within phosphate glass (965 cm^{-1}, 910-1020 cm^{-1}) [133]. Expressing the intensity as a peak ratio provided a measure of

internal normalisation and the ability to visually display the amount of cubic-Y_2O_3 relative to phosphate glass, rather than as an absolute quantity. This allowed for more viable cross-comparison within and between microspheres (Figure 5.17).

The Raman spectra for both the 30Y and 50Y microspheres revealed that the microspheres appeared to predominantly contain orthophosphate species. This correlated with the ^{31}P MAS-NMR spectra suggesting that only orthophosphate species were present. In the 50Y microspheres, XRD spectra had established that crystalline cubic Y_2O_3 was present, and this was confirmed via Raman analysis. The composition of the microspheres was found to be relatively uniform and, as was the case with EDX mapping experiments, the Raman mapping also showed that there were regions of localised yttrium content on the microspheres.

Although cubic Y_2O_3 was detected via XRD in the 30Y microspheres, this appeared not to be present or at very low levels in the Raman spectra. Additional Raman peaks at ~1100 – 1200 cm^{-1} in the spectra collected from one of the microspheres (Figure 5.19A) were present and were potentially associated with a different phase of the oxide. Husson *et al.* studied phase transitions in yttrium oxide and saw deviation from the most stable cubic phase to a monoclinic phase with increasing pressure and this resulted in alterations in the corresponding Raman spectrum [238]. XRD had shown hexagonal Y_2O_3 was an additional crystalline phase in these microspheres and may be responsible for the peaks seen. Since similar peaks were seen in both the 532 nm and 660 nm Raman spectra of 30Y microspheres, this confirmed their origin as Raman scattering as there was no wavelength dependence, as would be seen with emission spectra.

A study by Li *et al*. found that below 10 mol% the progressive addition of Y_2O_3 in the glass xY_2O_3–(100−)(12CaO–20Fe_2O3–68P_2O_5), x = 0 - 12 mol%, resulted in the formation of amorphous glasses but once 12 mol% Y_2O_3 was added a crystalline YPO_4 phase was detected. They stated that excessive Y_2O_3 was acting as a nucleating agent and its addition increased the O/P ratio causing depolymerisation of the glass network and reducing the glass-forming range [239]. A similar situation appeared to be happening within the 30Y microspheres in this study, where the Y_2O_3 content was ~15 mol% and a YPO_4 phase was detected using XRD (Figure 5.12). Interestingly, with progressive Y_2O_3 addition (when processing 50Y microspheres) a YPO_4 phase was no longer present and only a crystalline Y_2O_3 phase was detected via XRD. The crystal structure of YPO_4 consists of a YO_8 decahedron (coordination number 8) and PO_4 tetrahedra linked together by an edge (see Figure 5.39A), whereas Y_2O_3 has an octahedral coordination geometry of (coordination number 6) (see Figure 5.39B) [240]. A study by Cole *et al.* used Extended X-ray Absorption Fine Structure (EXAFS) analysis, which indicated that Y^{3+} cations were coordinated by 6–8 oxygen ions in phosphate glass structures

and further studies found that the coordination numbers of Y^{3+} cations in meta- and ultraphosphate glasses were ~6.5 and ~8.0, respectively [241, 242]. Christie *et al*. found that the addition of 6 mol% in their classical molecular dynamics simulations of yttrium-containing metaphosphate phosphate glasses had coordination number of 6.3 ± 0.2 suggesting they were bound in an octahedral structure (YO_6). The progressive addition of Y_2O_3 when forming the microspheres appeared to be changing the binding interactions of the Y^{3+} cations, which may have resulted in lower coordination number. This may also explain why YPO_4 is seen in 30Y microspheres but with progressive Y_2O_3 addition to achieve the 50Y formulation resulted in only crystalline Y_2O_3 detection.

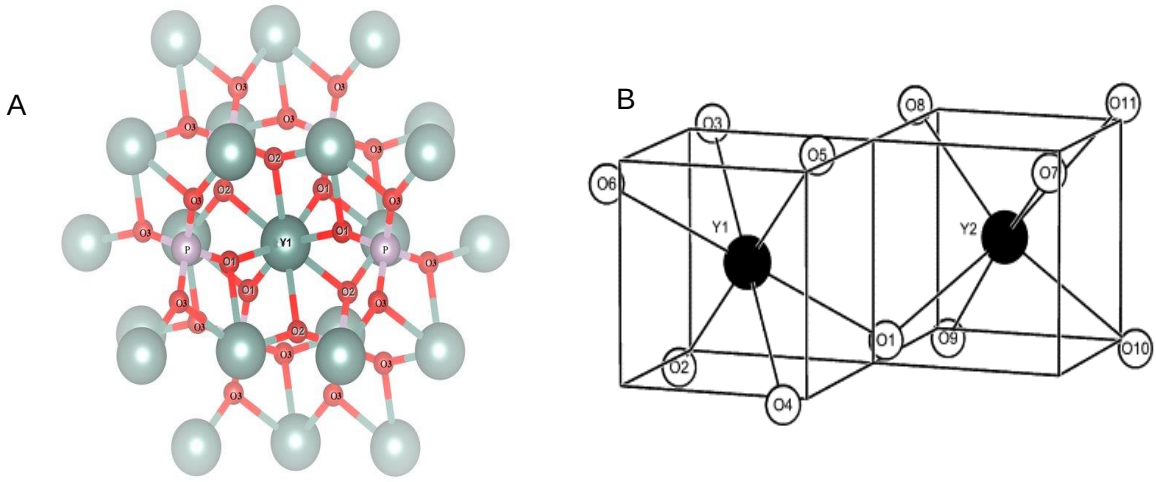

Figure 5.39 (A) YPO_4 cluster model. The central yttrium atom (grey) is shaded and represents a YO_8 decahedron with coordination number 8. O1 represent an oxygen atom (red) that belong to one orthophosphate (phosphorous; pink) group visible in the main cluster area, while O2 atoms belong to two adjacent orthophosphate groups. Reproduced from [6]. (B) Schematic of a fragment of a Y_2O_3 crystal. The central yttrium (black) atom is bound to 6 oxygen atoms (white) and has an octahedral coordination geometry of due to its coordination number of 6. Reproduced from [16].

During processing, the addition of Y_2O_3 into the microsphere structure and the resulting decrease in phosphate content altered the O/P ratio of the microspheres. In Chapter 3, theoretical calculations for O/P ratio with the glass compositions showed that an increase from 3.25 for P40 glass to 3.66 in P30 glass occurred across the glass series. The change in O/P ratio resulted in significant depolymerisation of the glass network and the formation of Q^0 species at the expense of Q^2 species. This increase in O/P ratio was also evident when additional CaO is introduced into the microspheres structure due to the use of $CaCO_3$ as a porogen for porous microsphere production. The addition of Y_2O_3 when processing 30Y microspheres caused a significant increase to the theoretically calculated O/P ratio to 4.01, in comparison to P40 SMS which is 3.33. This would suggest that each P atom would be bound

to 4 O atoms and therefore there would be no BO present within the structure. This hypothesis correlated with the Raman and NMR data indicating that the microspheres contained primarily orthophosphate species.

XPS analysis was performed to investigate the binding energy of the constituent elements within the microspheres. In the O1s components of phosphate-based glasses typically a higher binding energy contribution due to the presence of BO atoms and a lower binding energy associated with the NBO [243]. The components at 533.1 eV and 531.4 eV for the P40 solid microspheres were ascribed accordingly and were consistent with other studies [244]. O1s components in the solid yttrium microspheres may have arisen from oxygen atoms existing in some or all the following structural bonds: P–O–P (BO), P–O–Y, Y–O–Y and P–O–Mg/Ca/Na (NBO). ^{31}P MAS-NMR data showed that both 30Y and 50Y microspheres appeared to be formed exclusively of orthophosphates meaning that no P-O-P (BO) bonds should have formed. This meant that the component with the highest binding energy of 533.6 and 533.8 eV, in 30Y and 50Y microspheres respectively, was likely to be due to Y-O-Y bonds that had formed. Incremental Y_2O_3 addition has been shown to result in depolymerisation of phosphate glasses and disrupts phosphate chains via the formation of Y-O-P bonds [237]. Y^{3+} ions act as network modifiers to charge balance the negative charge of $[PO4]^{3-}$ tetrahedrons and can bond with $[PO4]^{3-}$ tetrahedrons via edge or corner sharing connectivity's (see Figure 5.40). In edge-sharing, one Y^{3+} bonds with two O^{2-} of a single $[PO_4]^{3-}$ tetrahedron, resulting in the subsequent formation of two P–O–Y bonds. As seen in Figure 5.40A, edge-sharing also results in the formation of Y-O-Y bonding, which was detected via XPS analysis. The edge-sharing bonding may lead to the formation of clusters of YO_n polyhedral through the formation of covalent bonds between the phosphate chains [245]. It could be that increased Y_2O_3 addition to the glass microsphere formulations created an increased clustering of yttrium ions resulting in the formation of the unique topographical features observed for the high yttrium-containing 50Y microspheres. Elemental analysis of these topographical features revealed a yttrium-rich core that appeared to be acting as a nucleus for crystallisation. In contrast, corner-sharing is when a single oxygen of the $[PO4]^{3-}$ tetrahedron is participating in the connectivity with the yttrium ion meaning less oxygens of the tetrahedra are occupied per bond with yttrium and can potentially form additional bonds with other elements (see Figure 5.40B).

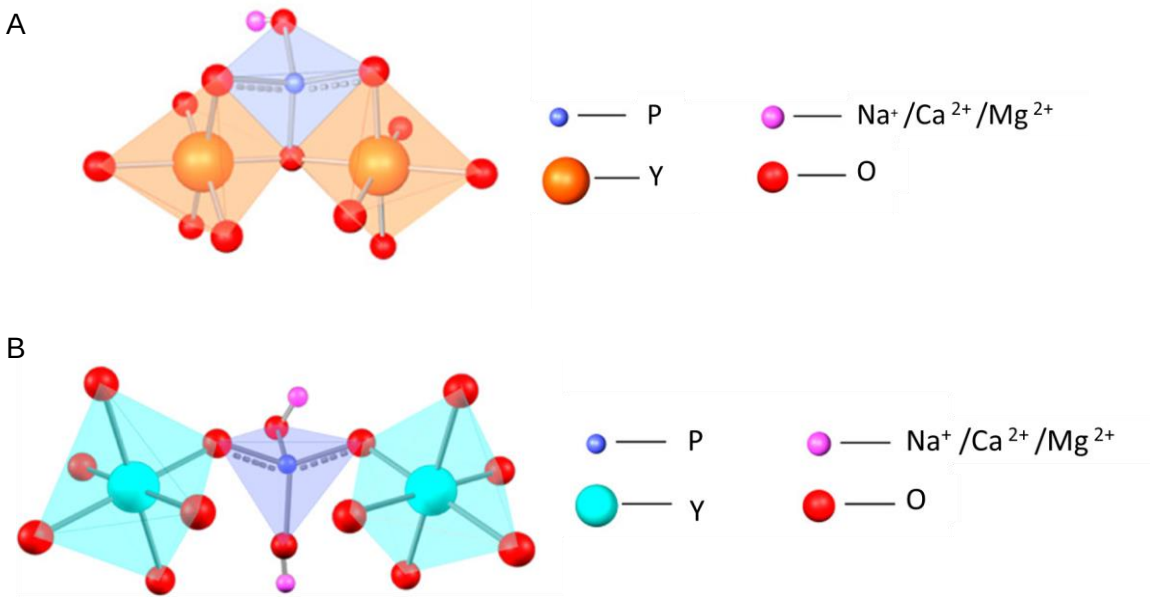

Figure 5.40 Structure depictions of yttrium ions bonding to a $[PO4]^{3-}$ tetrahedron via (A) edge-sharing and (B) corner sharing connectivities. Adapted from [245].

NBO bonds between P–O–Mg/Ca/Na were present and revealed a slight 0.2 and 0.1 eV shift for 30Y and 50Y microspheres compared to P40 SMS. The decrease in the area for NBO between 30Y and 50Y, at 531.1 – 531.2 eV, could be due to the decrease in concentration of P within the microsphere formulations and an increase in O/P ratio due to Y_2O_3 addition. There was subsequently less P available for binding relative to the other elements. An additional component at 532.4 and 532.7 eV was observed for 30Y and 50Y but not for P40 microspheres which had a binding energy intermediate to BO and NBO. A similar peak was observed in a study by Majjane *et al.* when using XPS to study vanadium barium phosphate glasses and they ascribed this peak to P-O-V bonding [243]. In the current work it is postulated that the peak here is due to Y-O-P bonding occurring in the microsphere structure and correlates with the XPS fitting for YPO_4 [228]. The Y-O-P bonding can lead to the formation of cross links between PO_4 tetrahedra via P-O· · · Y· · ·O-P bonds. The peak with the lowest binding energy in both the 30Y and 50Y samples was ascribed to Y-O bonding within Y_2O_3 and was consistent with the literature and not seen for the P40 SMS [246]. The increase in the component area for Y-O bonding within Y_2O_3 from 30Y and 50Y correlated with the XRD data where peaks associated with cubic- Y_2O_3 were seen at a greater intensity for the 50Y microspheres (Figure 5.12).

The Y3d components agree with the working hypothesis that edge-sharing connectivity's appear to be increasing with Y_2O_3 addition within the 50Y microsphere formulation. A decrease in area at 159.0 eV associated with Y-P bonding was seen in 50Y compared to 30Y

microspheres. There was an additional component in the 50Y microspheres attributed to Y-O-Y bonds and the increased amount of yttrium ions involved in this bonding meant fewer were able to participate in Y-P bonding. Studies have found that in crystallised cubic Y_2O_3, Y^{3+} is bound to six equivalent O^{2-} atoms and forms a mixture of distorted edge and corner-sharing YO_6 octahedra [247]. YPO_4 is bound to 8 instead of 6 equivalent O^{2-} atoms to form distorted YO_8 hexagonal bipyramids that share corners with four equivalent PO_4 tetrahedra, edges with four equivalent YO_8 hexagonal bipyramids, and edges with two equivalent PO_4 tetrahedra [248]. This demonstrates that the yttrium complexes detected in the 30Y and 50Y microspheres via XRD both exhibited edge-sharing and corner-sharing connectivity's. Increasing the amount of Y_2O_3 into the formulations altered the type and frequency of bonding occurring and dictated the structures that formed. Due to the microspheres being glass-ceramics and not fully crystalline materials with completely geometrically ordered structures it was only possible to postulate what binding was occurring within the microspheres based on the data available. The novel processing technique used and the high yttrium content (which has not previously been achieved before) with phosphate-based glasses meant that there was a lack a comparable literature to compare the XPS results with. Further structural characterisation, using techniques such as neutron diffraction, high energy XRD (HE-XRD) and X-ray absorption near edge structure (XANES) would be needed to establish the bonding and structures occurring within the microspheres at the atomic level.

The addition of yttrium to phosphate glass microspheres not only facilitated their potential use as a vector for radiotherapy delivery but could also be used to improve the durability of phosphate glasses [89]. Other transition oxides such as TiO_2, Al_2O_3 and Fe_2O_3 have been incorporated into phosphate glasses and have been shown to improve some of the physical properties, such as their rapid degradation within aqueous media that can limit their clinical applications [249-251]. The addition of certain transition oxides have been shown to decrease degradation rates by up to 3 to 4 orders of magnitude [252]. The role of yttrium oxide within silicate glass systems has been explored and it has been discovered that yttrium oxide can act as either a network former or a network modifier depending on the amount of yttrium oxide present. Classical molecular dynamics simulations have been conducted on the structure of yttrium doped phosphate-based glasses which found that yttrium oxide up to 6 mol% acted as a network modifier and resulted in depolymerisation of the phosphate network within quaternary phosphate glasses [253]. Structural analysis by Martin *et al*. revealed that yttrium acted as a network modifier within the studied alumino-phosphate glasses and that Y^{3+} cations preferentially bonded to the terminal oxygen atoms of PO_4 tetrahedra [211].

A study by Arafat *et al.* investigated the role of yttrium in phosphate-based glasses in the system $45(P_2O_5)–25(CaO)–(30\text{-}x)(Na_2O)–x(Y_2O_3)$ mol% ($0 \leq x \leq 5$) prepared via melt quenching [210]. As with silicate glasses, depolymerisation of the glass network was seen with increasing yttrium oxide addition. ^{31}P NMR analysis showed an increase of Q^1 species, from 23 to 42%, which was accompanied by a corresponding decrease of Q^2 species from 77 to 58% as Y_2O_3 addition increased from 0 to 5%. The increasing Y_2O_3 content also resulted in a decrease in the phosphate chain length (from 8.69 to 4.88), which was further evidence of depolymerisation and the dissociation of metaphosphate chains. As a network modifier, Y^{3+} occupy the interstitial space between PO_4 tetrahedra and bond with phosphate glass terminal oxygen's causing a decrease in BO and an increase in NBO. Previous studies have concluded that yttrium perturbs the glass network strongly, by stabilizing the formation of negatively charged species such as non-bridging oxygen atoms [254]. Due to it being a high field strength trivalent cation, yttrium forms strong cross-linking Y-O-P bonds between phosphate chains. Yttrium's field strength (~0.60 *e* $Å^{-2}$) is significantly higher than that of magnesium(~0.46 *e* $Å^{-2}$), calcium's (~0.33 *e* $Å^{-2}$) and sodium's (~0.19 *e* $Å^{-2}$) and this leads to the formation of stronger bonds within the phosphate glass network and is why an increase is chemical durability is seen with increasing Y_2O_3 content [212, 255]. Classical molecular dynamics simulations have revealed that in phosphate glasses, when there was multiple modifier atoms present, they compete for their preferred bonding environments, which leads to different amounts of NBOs and BOs. A study by Fu and Christie revealed that yttrium was found to bond almost completely exclusively to NBOs within their glass system [253].

Previous studies have found that the increase in cross-linking of the phosphate network with the addition of Y_2O_3 causes a decrease in the degradation of the glasses, since Y-O-P bonds are more resistant to hydration attack than P-O-P bonds [256]. Classical molecular dynamics simulations have shown that when yttrium is incorporated into a ternary phosphate glass series it bonds to a greater number of phosphate chains (4.2 – 4.3) in comparison to both calcium (3.8) and sodium (3.1-3.2) [253]. This indicated that yttrium cations bond to more chains in the glass network and strengthen the glass against dissolution. Decreased degradation results in a lower ion release profile which would be beneficial when developing glasses for radiotherapy applications [257]. The glass needs to be durable whilst the yttrium is radioactive to avoid leaching of the radionuclide and irradiating the patient away from the target site. In the aforementioned studies on yttrium incorporation within phosphate-based glasses, the Y_2O_3 content remained relatively low, less than 6%, due to crystallisation of the glass at higher Y_2O_3 content.

The yttrium content within 50Y microspheres of 39.1% is significantly higher than anything obtained and studied previously in phosphate glasses. For both 30Y aand 50Y microspheres, extensive depolymerisation of the network has occurred and crystalline phases were present throughout the bulk of the microspheres. Ion release studies demonstrated that increased yttrium content resulted in a reduction in the release of all ions from the microspheres. Despite 50Y microspheres containing more than twice the yttrium content on 30Y microspheres, 30Y microspheres released over three times the amount of yttrium ions over 28 days immersion (Figure 5.22). Considerably less yttrium was released from both microspheres in comparison to the glass forming elements. Further evidence of the increased durability of the yttrium-containing microspheres was apparent from the lack of surface deformation and degradation following the period of immersion within mill-Q water in comparison to the P40 solid microspheres (Figure 5.24). The yttrium-containing microspheres must have high chemical durability and resistance to degradation within bodily fluids to be used for internal radiotherapy delivery. The half-life of ^{90}Y means that radioactivity decays to a negligible level within 21 days after neutron bombardment, as such stability and minimal leaching of active radioisotopes during this period is essential [205].

30Y and 50Y microspheres were shown to retain their geometry and morphology following heat treatment up to 941°C during a thermal XRD experiment. This demonstrated the high durability of the microspheres and is further evidence of their suitability as devices to deliver internal radiotherapy. The high neutron fluxes during neutron activation required to produce ^{90}Y can result in high temperatures, which the microspheres must be able to withstand in order for the radioactive product to have the desired geometry and characteristics [258]. To empirically establish whether the microspheres are able to withstand such conditions, neutron activation experiments are required.

P40, 30Y and 70Y microspheres were immersed in SBF for 28 days to investigate their bioactivity. The EDX values (Figure 5.25) and XRD traces (Figure 5.26) indicated that no apatite formation had occurred during the duration of the study. The P40 solid microspheres did not appear to have intrinsic bioactivity during the 28 days immersion and similar results had been seen in section 4.4.11 with P40 porous microspheres. The yttrium containing microspheres released significantly less ions in comparison to P40 microspheres and also showed no evidence for HA formation whilst immersed in SBF. Decreased bioactivity with increasing yttrium content has also been seen in a study by Cacaina *et al.* in which the influence of Y_2O_3 on the bioactivity of glasses in the system SiO_2-Na_2O-P_2O_5-CaO-B_2O_3-K_2O-MgO was investigated. They found the tendency of the glasses to form a calcium phosphate layer was reduced with the progressive addition of Y_2O_3 to the parent glass formulation. They

suggested that the formation of thinner calcium phosphate layers on the glasses due to increased Y_2O_3 content had lower bioactivity and exhibited slower dissolution compared to the glass formulations that displayed a thick layer. The slower dissolution was accompanied with lower weight loss in the high Y_2O_3 containing glasses, signifying the increased structural stability that yttrium was imparting due to the high field strength of the Y^+ ion [200]. It has been suggested that the nanoscale clustering and aggregation ions can act as an inhibitor of bioactivity in bioactive glasses since clustering of modifiers can affect ionic transport [259]. The clustering of yttrium ions that may be occurring due to the proposed edge-sharing connectivity's may therefore be suppressing bioactivity.

Glass-ceramics are generally considered to have superior mechanical properties to that of their parent glass but lower bioactivity due to the increased stability of the crystalline phases [260]. The increased durability, reduced degradation and ion release from the yttrium-containing glass-ceramic microspheres was attributed to reducing the likelihood of HA formation in SBF. Although they have been empirically shown to be useful to establish the bioactivity of glass and glass-ceramics, *in vitro* studies involving SBF are not definitive since highly resorbable ceramics such as β-TCP and calcite ($CaCO_3$) do not demonstrate apatite formation in SBF but can bond to bone *in vivo* [97]. In addition to the physico-chemical processes, such as dissolution and precipitation, that cause bioactivity and resorption of glass and glass-ceramic biomaterials, cellular processes are also known to have direct effects. Cell-mediated resorption occurs on implanted materials due to inflammatory multinucleated cells that degrade materials through phagocytosis and by osteoclasts when the material is implanted adjacent to or within bone tissue [261]. The responses are also governed by the size and geometry of the glass/glass-ceramic material implanted *in vivo*. It is therefore important to look at the *in vitro* and *in vivo* cellular responses to yttrium containing microspheres.

Cytocompatibility results showed that MG63 cells cultured with P40 SMS conditioned media demonstrated the greatest levels of metabolic activity after 7 days and were comparable to that of cells cultured in SM. Cells cultured in both 30Y and 50Y media had significantly lower metabolic activity ($p < 0.001$) than those cultured in SM and P40 media at day 7 but their relatively high activity and the significant increase in metabolic activity seen from day 2 to day 7 demonstrated their cytocompatibility. Previous *in vitro* studies of porous glass microspheres of the P40 formulation ($40P_2O_5{\cdot}16CaO{\cdot}24MgO{\cdot}20Na_2O$ mol%) have shown that they were biocompatible according to the standard ISO 10993-5. *Hossain et al.* showed that the proliferation rate of hMSCs grown using an indirect culture method was shown to be greater than 70% of the cells grown in the SM when using an MTT assay [1].

As seen in Figure 5.22, P40 solid microspheres were faster degrading than both the 30Y and 50Y microspheres and released a significantly greater amount of all glass forming ions. The simultaneous exposure and quantity of ions released from the different microsphere formulations to the cells resulted in the differences in cell response. Phosphate, calcium, magnesium and sodium ions have all been shown to play vital roles within bone metabolism and homeostasis [105]. Extracellular Ca^{2+} plays an key role in the regulation of osteoblastic proliferation and differentiation by influencing the expression of specific Ca^{2+}-channel isoforms on osteoblasts [262]. The increased exposure of cells to ions from P40 SMS is therefore likely responsible for the increase metabolic activity seen at day 2 and 7 when compared to 30Y and 50Y formulations.

ALP is constitutively active at low levels in all cells, but during the early stages of osteogenic differentiation its activity significantly increases [161]. It is therefore used as a marker for the detection of early osteogenic differentiation. Cells exposed to P40 release products had significantly greater ALP activity compared to 30Y and 50Y formulations. The similar ALP activity within cells exposed to 30Y and 50Y correlated with the ion release data in that the levels were comparable between the two formulations and resulted in no significant difference between them.

Liquid chromatography coupled with mass spectrometry (LC-MS) has been widely employed for profiling protein expression levels. This approach to proteomics involves subjecting the proteins to enzymatic cleavage and separating the resulting peptide products based on chemical or physical properties [263]. Differences in hydrophobicity and polarity causes each peptide to elute from the LC column at a distinct retention time [264]. The eluted peptide products are then analysed using mass spectroscopy. Tandem mass spectrometry (MS//MS) is a technique involving two or more mass analysers. Samples are ionised and separated by their mass-to-charge (m/z) ratio in the first spectrometer. The ions are then split into smaller fragment ions and separated again by their m/z-ratio, thereby allowing the separation and identification of discrete ions with very similar m/z-ratios [265]. Computational approaches and software have been developed for automated assignment of peptide sequences to MS/MS spectra from available protein sequence databases.

Quantitative analysis using LC-MS/MS revealed that 935 proteins were detected in cells cultured using P40 or 30Y conditioned media and that 37 were unique to cells cultured in P40 media and 14 to those using 30Y media. The high proportion of shared proteins suggested that the proteome of the cells using the different culture conditions remain stable. Beta-actin-like protein 2 (ACTBL2) was only detected in MG63 cells cultured in 30Y conditioned media. Actins are highly conserved proteins ubiquitously expressed in all eukaryotic cells and are

involved in cell motility, structure and integrity [266]. Although there is limited published data concerning ACTBL2, it has been shown to be expressed at very low levels in several melanoma cell lines whilst other melanoma cells exhibited high *ACTBL2* expression [267]. Further studies are required to understanding the signalling pathways involved in ACTBL2 expression in health and disease and whether exposure to yttrium ions is influential. One protein of interest which was exclusively detected in MG63 cells cultured in 30Y conditioned media was transforming growth factor-beta-induced protein ig-h3 (TGFBI) (see Table 5.4). TGFBI is an extracellular matrix protein that has been reported to function as a tumour suppressor [268]. Loss of TGFBI expression has been associated with several types of malignant cancer cells, whilst ectopic expression of TGFBI significantly suppressed tumorigenesis in human bronchial epithelial cells [269]. The 30Y culture conditions appeared to cause an upregulation in TBFI expression which may repress tumorigenesis of malignant cells in comparison to cells cultured using P40 conditioned media.

ADP-ribosylation factor 5 (ARF5) was a protein detected exclusively in cells grown in P40 conditioned media and was present in the greatest amount (5 a.u.). ARF5 is a GTP-binding (guanosine triphosphate) protein that regulate protein and membrane trafficking events [270]. Dysfunction of ADP-ribosylation has been associated with several types of cancer [271]. Another protein, ribose-phosphate pyrophosphokinase 3 (PRPSL) was also only detected in cells cultured in P40 conditioned media. PRPSL function is to catalyse the synthesis of phosphoribosylpyrophosphate (PRPP) which is essential for nucleotide synthesis [272]. PRPSL is activated by magnesium and inorganic phosphate and the elevated release of these ions from P40 microspheres compared to 30Y is likely responsible for the upregulation of this protein. Synthesis of DNA and RNA is essential for transcription and translation to facilitate protein synthesis for cell growth and proliferation [273]. Upregulation of proteins involved in these biochemical pathways, such as PRPSL, may account for an increase in metabolic activity of cells cultured in P40 conditioned media compared to those using 30Y or 50Y - conditioned media (Figure 5.27). Compositional development of PBGs could lead to materials which can heavily influence cells via the activation and upregulation of certain proteins. Further studies are required to investigate how the culture conditions created by the microspheres affect cell phenotype and which proteins and biochemical pathways are responsible.

When cells were seeded directly on to the microspheres, both the 30Y, 50Y and parent P40 glass microspheres promoted cell growth, as seen by an increase in metabolic activity from day 2 to day 7. Cells cultured on 30Y microspheres showed initially higher cell metabolic activity at day 2 but there was no significant difference in metabolic activity observed after 7 days of culture on the two yttrium formulations. Surface roughness has been shown to play a

conductive role in the initial cellular adhesion and may explain the difference in metabolic activity at day 2 [274]. The durable nature of the yttrium-containing microspheres means that minimal changes to the materials surface integrity and a stable pH of the local microenvironment, evident from Figure 5.23 and Figure 5.24, facilitated a suitable environment for cell adhesion. The addition of ions, such a titanium and iron, is commonly employed to increase the durability of phosphate based glasses to increase cell adhesion and provide a more stable surface to support cell proliferation and differentiation [275]. Whilst the material surface is vital for cell adhesion and colony establishment it is not the sole determinant of subsequent biological processes, as the degradation products have the potential to influence the proliferation and differentiation of the cells [107].

Cells grown on P40, 30Y and 50Y microspheres all had increased ALP activity in comparison to TCP after 7 days of culture. The increased ALP activity of cells cultured on the microspheres suggested that the microspheres were a more favourable surface for influencing osteoblast cell differentiation than TCP. It is likely that the phosphate, calcium, magnesium and sodium ions released from the microspheres were stimulating an early osteogenic response. Studies have established that Ca^{2+} ions are required to promote osteocalcin expression and matrix mineralisation, whilst certain concentrations of phosphate and Mg^{2+} added to cells in culture can further induce mineralisation [276]. Cells grown on TCP were not exposed to these additional ions and is likely why there was significantly lower ALP activity in these cells. The surface topography of biomaterials has also been shown to directly influence cellular responses including adhesion, proliferation and osteogenic differentiation [277]. The rough surface of native bones mineralised ECM has been identified as an important feature that promotes adhesion and differentiation of osteoprogenitor cells to an osteogenic lineage [278]. A rough topography therefore can effectively mimic the mineralised ECM interface that cells adhere to *in vivo* when participating in bone remodelling and regeneration. The increased ALP activity seen in cells grown on the 30Y and 50Y microspheres, in comparison to the P40 microspheres, may be due to the surface roughness and topographies seen on many of the microspheres.

Yttrium has been added to calcium phosphate ceramics, in the form of yttrium phosphate, to increase the machinability of the ceramics to potentiate more applicable materials and geometries to be used as bone graft substitutes and in hard tissue engineering applications [216]. Up to 50 weight % yttrium phosphate has been incorporated into both hydroxyapatite (HA) and beta tricalcium phosphate (β-TCP) composites [216, 279]. MTT assays revealed that there was no significant difference in viability of MG63 cells cultured on the yttrium containing composites in comparison to both HA and β-TCP alone. Similarly, yttrium has also been added

to other ceramic materials such as zirconia and alumina to be used in orthopaedics and restorative dentistry. In a recent study, commercially available 8 mol% yttria-stabilised zirconia plates exhibited excellent cell attachment, proliferation, and cell differentiation of mouse L929 and mouse bone-marrow derived MSCs, indicating their promise as restorative materials [280]. These studies and the current study highlight the potential of yttrium containing calcium phosphate ceramics as materials to facilitate bone repair. The ability to neutron activate the yttrium-containing microspheres in this study highlights the potential applications beyond bone regeneration and may be used to deliver localised radiotherapy at the site of delivery. The novel microsphere formulations satisfy the necessary requirements for internal radiotherapy applications in that they; (i) contain high levels of radionuclide within their structure capable of delivering therapeutic radiation, (ii) are chemically durable and resistant to physiological fluids to prevent substantially radionuclide release during period of radioactivity. Additionally, the yttrium-containing microspheres were biocompatible and supported osteoblast-like cell growth and proliferation.

Although solid yttrium-containing microspheres of varying content were successfully produced, the conventional processing method that resulted in formation of highly porous phosphate glass microspheres (in Chapter 3) could not be applied to produce high yields of porous yttrium-containing microspheres. Alterations to the processing procedure prior to spheroidisation were investigated to try and achieve homogenous mixing of the glass, Y_2O_3 and $CaCO_3$. Irrespective of the mixing procedures used, significant agglomeration of the particles occurred resulting in the formation of a high proportion of large, irregular shaped particles. The particles that were porous contained no detectable or very low levels of yttrium content.

Hossain *et al.* proposed mechanism for porous microsphere formulation via flame spheroidisation involves the decomposition of the porogen and engulfing of the gas evolved within the molten glass particles. The entrapped gas subsequently escapes from within the molten glass to form pores as the material is cooled upon ejection from the flame. The spherical shape is formed due to the influence of surface tension [1]. The melting temperatures (T_m) of the phosphate glasses used in Chapter 3 range between 645 and 854°C, whereas the T_m for Y_2O_3 is much higher at 2,425°C [209]. This was very close to the maximum temperature of the flame that could be produced by the thermal spray gun (MK74, Metallisation Ltd, UK) which was reportedly around 3,000°C, although the actual flame temperature could not be verified with the equipment available. The flame spheroidisation method was able to form high yields of completely spherical yttrium-containing microspheres despite the high T_m of Y_2O_3. It appeared that when Y_2O_3 became embedded and dispersed within the P40 glass matrix that

the physico-chemical properties of the particles within the flame no longer facilitated the facile formation of porous microspheres. It was postulated that the temperatures achieved, or the particle residence times whilst in the flame may not have been sufficient for the majority of particles to become fully molten or to achieve levels of melt viscosity for CO_2 entrapment and release.

Changes in the physico-chemical properties to the yttrium-containing particles within the flame that may negatively affect porosity formation are likely further compounded by the addition of $CaCO_3$. The decomposition of $CaCO_3$ porogen ($CaCO_3 \rightarrow CaO + CO_2$), that is responsible for CO_2 production and release to impart porosity, has been shown to increase CaO content within particles post flame spheroidisation (Figure 4.9). Previous studies of ternary PBG in the P_2O_5-CaO-Na_2O glass system reported that increasing Ca content in place of Na increased the cross-linking between the phosphates chains and led to increased chemical durability [281]. It is postulated that the viscosity of the yttrium-rich particles may not be conducive to allow CO_2 to pass through them.

It was therefore suggested that higher temperatures and increase particle residence time are required for the glass, Y_2O_3 and $CaCO_3$ particles to coalesce within the flame and to achieve the required combination of physical and chemical parameters for porosity formation. In addition to this, the particles need to be in close proximity to one another and delivered into the flame simultaneously. The conventional method of producing porous phosphate glass microspheres appeared to be unable to fulfil this set of criteria when Y_2O_3 and $CaCO_3$ was simultaneously added and consequently meant optimisation of the process was necessary.

Studies have shown that it is the time-temperature combination to which the particles are subjected that determines successful microsphere formation via flame spheroidisation [282]. Incomplete spheroidisation can occur when particles travel a small trajectory within the flame or within regions that are not hot enough for the heat exchange kinetics required for the particles to become sufficiently molten. This can result in the particles not forming completely spherical shapes, which is often seen in large sized particles where agglomeration has occurred [283]. Smaller particles are also affected by higher initial acceleration when they enter the flame which can affect particle residence time. In addition to this, smaller and less dense particles can suffer from a “surfing effect”, in which they are unable to penetrate into the centre of the flame and are subsequently ejected along trajectories on the flame edge away from the primary flame direction. These regions are less hot and decrease the likelihood of the particles reaching the necessary temperature [29].

The greatest success seen in producing porous yttrium containing microsphere was achieved using ground particles of solid yttrium microspheres produced via a first round of flame spheroidisation that were then subjected to a second round using a pneumatic sand blasting gun and porogen. The rationale for this was to try and minimise the agglomeration of particles during the feeding stage, which can occur when using small particles. Additionally, Venturi *et al.* had shown that downstream injection, as opposed to perpendicular or upstream injection, of graphene nanoplatelets (GNPs) resulted in approximately 200°C increase in particulate temperature when investigating feedstock injection parameters using suspension high velocity oxy-fuel (SHVOF) thermal spray [284]. Increased flow rate of fed particles resulted in increased penetration within the flame but may result in reduced residence time due to the increased initial velocity of the particles. Although this study used a suspension feedstock it was postulated that the small particles used within the flame spheroidisation process would behave in a similar manner.

The modified feeding system did result in decreased agglomeration and furthermore, also appeared to increase porosity. Despite this, the yield of porous compared to solid microspheres remained comparatively low and did not allow for further characterisation. The greatest limitation to this processing method was the small quantity of particles collected at the end of processing. The high flow rate generated to eject the particles out of the pneumatic sand blasting gun contributed significantly to the scattering of particles when entering the flame and their subsequent loss to the surroundings. The increased porosity seen within the 30Y formulations in comparison to the 50Y may be due to the increased proportion of glass within each microsphere. The lower melting temperature of the glass in comparison to yttrium oxide would mean a greater likelihood of the particles becoming molten and allowing for CO_2 to become engulfed and released to impart porosity. The high cost associated with using Y_2O_3 meant that this is not a feasible process and significant quantities would be required to make sufficient amount of particles.

To produce microspheres for therapeutic applications it is vital that there is consistency and reliability in the final product. Whilst this can be achieved with yttrium-containing solid microspheres further optimisation is require for porous yttrium microsphere production. The setting and control of the process input parameters such as gas flow rates, particle size and feeding conditions, will reduce batch to batch variability and should assure the production of a high yield of quality microspheres with the desired characteristics.

Porosity within biomaterials facilitates enhanced gaseous and nutrient exchange and has been shown to result in favourable cell responses, especially for bone repair and regeneration. Interconnected pores allow for cellular and vasculature infiltration to promote new tissue

formation and matrix deposition [165]. The added potential of being able to load porous microspheres with therapeutic cargo was the rationale for developing a process for porous yttrium-containing microsphere production. Microspheres that are capable of delivering radiotherapy and chemotherapy simultaneously could have a synergistic effect if radiosensitisation of the target tissue could be achieved whilst sparing neighbouring healthy tissue [14]. A suitable methodology would have to be developed depending on whether the microspheres were loaded prior to neutron activation or after. Any cargo that would be loaded within the microsphere would have to be able to withstand the conditions of neutron activation and not form any undesirable radionuclides [285]. If they were to be loaded post-neutron activation the process becomes time sensitive as this would decrease the therapeutic dose received by the patient and may also expose clinicians to harmful doses of radiation.

6 Holmium-doped phosphate-based microspheres for internal radiotherapy delivery

6.1 Introduction

The favourable nuclear properties of ^{90}Y have led to the development and use of two commercially available microsphere products containing ^{90}Y for Selective Internal Radiation Therapy (SIRT) to treat unresectable hepatocellular carcinomas. Prior to microsphere administration during SIRT, a diagnostic angiography is conducted to assess the vasculature of the liver and tumour [286]. Technetium-99m macroaggregated albumin (^{99m}Tc-MAA) particles, that are comparable in size to the ^{90}Y microspheres, are injected as a scout dose and their distribution within the liver is studied. Due to ^{99m}Tc emitting readily detectable gamma (γ) rays, single-photon emission computer tomography (SPECT) can be used to estimate the dose to the tumour and surrounding parenchyma and evaluate the potential of pulmonary and extrahepatic shunting [287]. Although ^{99m}Tc-MAA SPECT dosimetry is considered accurate for SIRT, alternate methods are being developed that can combine therapeutic radiotherapy with the ability to simultaneously achieve diagnostic information at the tumour site.

Alternative radionuclides that not only emit high energy, tumoricidal β-radiation but can simultaneously emit gamma-radiation (γ) or possess inherent properties that can allow for visualisation through clinical imaging techniques are therefore highly desirable [288]. The incorporation of such a radionuclide within a biomaterial could facilitate a theranostic approach by providing real time diagnostic information on the biodistribution of radiotherapeutic agents within a tumour. This could help determine the optimal dose and monitor the response to treatment concurrently to and potentially following the delivery of delivering ionising radiation [288].

The radionuclide holmium-166 (^{166}Ho) possesses these decidedly beneficial properties as it emits high energy β-radiation as well as γ-radiation [289]. Due to ^{165}Ho having a natural abundance of 100% and a cross section of 64 b, it can be neutron activated in a relatively short neutron activation time resulting in ^{166}Ho with a high purity of the isotope [290]. The only by-product is metastable ^{166}Ho meaning that no costly chemical purification steps are required for production of nuclear reactor derived ^{166}Ho [291]. ^{166}Ho is comparable to ^{90}Y in that it emits β-radiation, but it has a significantly reduced half-life of 26.8 hours [292]. The maximum tissue range of β-radiation from ^{166}Ho is similar to ^{90}Y at 8.7 mm in soft tissue, with an average range of 2.2 mm and 90% of the total radiation dose is delivered in the first 2.1mm. However, the

resultant dose-rate is relatively high if the same cumulative dose was given in comparison to other radionuclides used for cancer therapy such as ^{90}Y, ^{131}I and ^{186}Re which have larger half-lives [293].

One of the primary advantages of using ^{166}Ho is that it is a γ-emitter, meaning that it can be detected using Single Photon Emission Computer Tomography (SPECT). Additionally, ^{165}Ho has paramagnetic properties allowing for visualisation using Magnetic Resonance Imaging (MRI) and also by Computer Tomography (CT) techniques because of its density [294]. These clinical imaging techniques can facilitate real time visualisation of holmium-doped biomaterials during and post-treatment and could be used to quantitatively measure ^{166}Ho distribution *in vivo [295]*.

Several compounds or materials have been investigated that are either labelled with or have incorporated within them ^{166}Ho for applications in interventional oncology. ^{166}Ho-labelled chitosan complexes have been investigated for intratumoral treatment of tumours located in the brain, prostate and liver [296-298]. Bone marrow transplantation is a possible curative treatment for several hematologic malignancies but requires high doses of local radiation to destroy old bone prior to transplantation. In order to achieve bone-seeking agents, phosphonate chelates have been combined with ^{166}Ho to form stable complexes to deliver high levels of radiation to bone and bone marrow [299]. ^{166}Ho has also been conjugated to various bone-seeking agents, such as EDTMP (ethylenediamine- tetramethylene phosphonic acid) and PAM (pamidronate), to generate high local radiation doses for bone marrow ablation and limit damage to healthy tissues and organs that may occur using external beam radiotherapy [300, 301].

Radiovertebroplasty is a further treatment method that has been developed to treat bone malignancies. This form of internal radiotherapy involves the incorporation of radionuclides, such as ^{166}Ho, within commonly used bone cement materials, such as Polymethylmethacrylate (PMMA), to treat spinal metastases [292]. These materials can be administered via minimally invasive percutaneous procedures and provide structural and mechanical support to the effected regions, whilst simultaneously irradiating malignant cells in the immediate area [302]. Donanzam *et al.* formed composite PMMA with multiphasic calcium phosphates that incorporated holmium as novel biomaterial to treat spinal metastases. Upon neutron activation, ^{166}Ho was produced with an activity calculated to be 32.5 MBq/mg, which was considered to be clinically suitable for site specific radiotherapy [303].

Microspheres that have holmium incorporated within them have also been developed for SIRT and the treatment of liver malignancies. Currently, the only commercially available and

clinically used microspheres for SIRT that utilise radioactive holmium is the ^{166}Ho-loaded poly(L-lactic acid) (PLLA) microspheres (^{166}Ho-PLLA) (QuiremSpheres®, Quirem Medical B.V., The Netherlands), which have been developed as an alternative to glass microspheres [304, 305]. The use of ^{166}Ho-PLLA has the potential to eliminate the need of a scout dose, such ^{99m}Tc-MAA, followed by a therapeutic dose since the ^{166}Ho-PLLA microspheres can perform both roles concurrently. The diagnostic feature of ^{166}Ho-PLLA could enable monitoring of the intrahepatic behaviour of the microspheres during and post treatment [289]. Knowledge of the quantity of microspheres that reach the cancerous and normal liver tissue of each patient allows clinicians to adjust the treatment plan accordingly and identify tumours that may be receiving an inadequate dose [306]. Polymers susceptibility to degradation due to the use of high neutron fluxes during neutron activation and the difficulty in achieving a high enough activity to produce a therapeutic effect must be circumvented when developing microspheres for SIRT [307]. The microspheres are not limited to just the treatment of liver malignancies but have been investigated for the treatment of tumours within the kidney and head-and-neck, amongst others [308, 309].

This chapter discusses processing and structural characterisation of holmium-containing phosphate-based microspheres that could be used to deliver radiotherapy for the treatment of bone cancers. *In vitro* bioactivity and cytocompatability studies have been performed to assess the microspheres' ability to support cell growth and proliferation and to facilitate bone repair and regeneration to damaged bone tissue following devastation due to bone cancer and it associated treatments.

6.2 Results

6.2.1 Morphological and elemental analysis

SEM analysis following processing and sieving confirmed that a high yield of spherical microspheres were produced via the flame spheroidisation method. As seen in Figure 6.1, a lack of aggregation and a narrow size distribution was achieved using this manufacturing process. This was apparent at each holmium oxide to glass ratio that was used prior to spheroidisation.

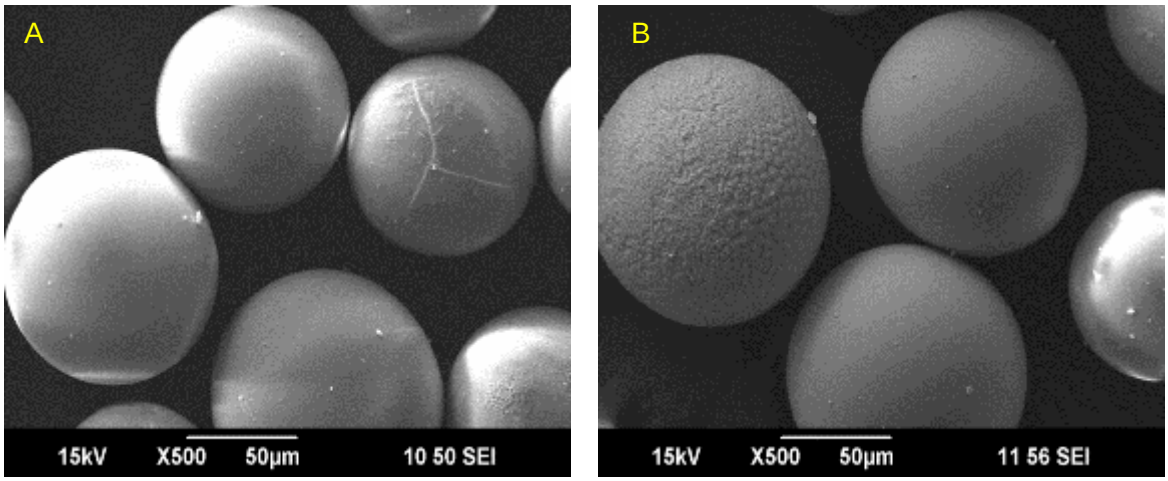

Figure 6.1 SEM images of the morphology of the holmium-containing microspheres produced. (a) Microspheres processed using a 30:70 holmium oxide to P40 glass ratio (30H) and (b) microspheres processed using a 50:50 holmium oxide to P40 glass ratio (50H).

*E*DX analysis was also performed to confirm composition of the microspheres manufactured at each holmium oxide to glass ratio. As seen with the yttrium microspheres in the previous chapter, as the amount of holmium oxide mixed with the glass increased so did the content of holmium in the microspheres formed. As holmium content increased, there was a proportional decrease in all the glass elements within the microspheres produced (see Figure 6.2).

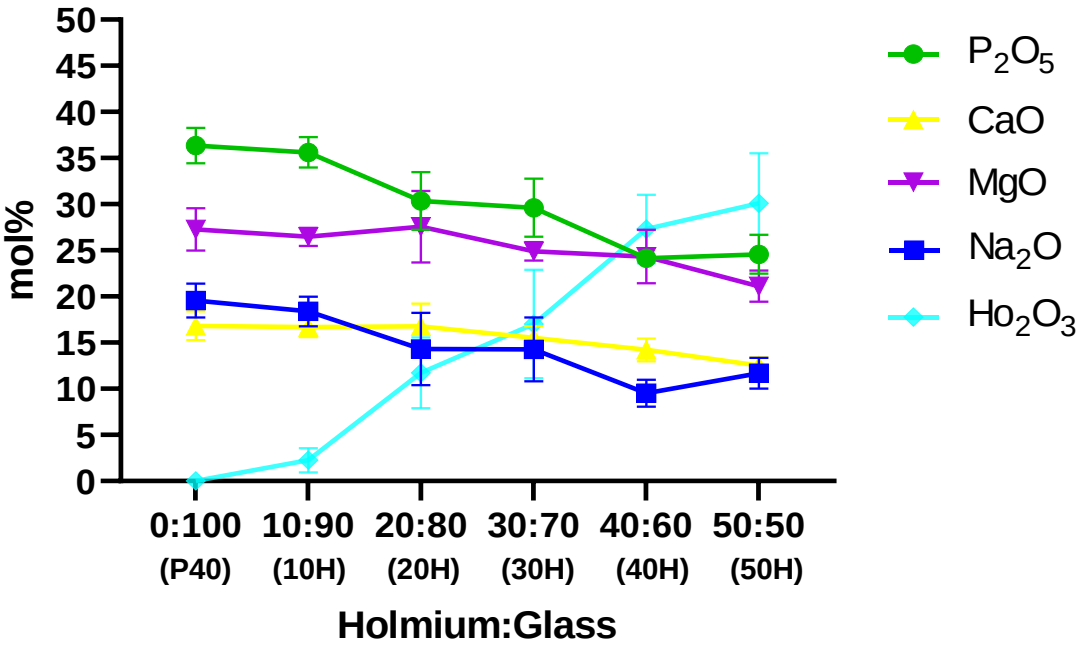

Figure 6.2 Elemental composition determined via EDX of the holmium containing microspheres produced via flame spheroidisation.

Throughout this work, the following naming convention is used to refer to the samples i.e 50H, where 50 refers to the ratio of holmium oxide mixed with P40 glass prior to spheroidisation and H the radionuclide of interest (holmium). As was done with yttrium containing microspheres, 30H microspheres were chosen for further characterisation and study due to their holmium content (17.2% ±5.8) which was comparable to that of the yttrium content of commercial Therasphere™ and a P_2O_5 content of ~30 mol%. 50H microspheres were also investigated as these had the highest holmium content (30.1% ±5.4) (see Figure 6.2).

6.2.2 30H Surface topography and elemental analysis

Figure 6.3 shows SEM images acquired of 30H microspheres which revealed the presence of two topographically distinct sets of microspheres, like those seen for the 30Y microspheres in Chapter 4. Most microspheres had a smooth surface with little to no discernible surface features (topography 1) (see Figure 6.3B). A second distinct group of microspheres possessing a rough surface containing randomly orientated grain-like structures over most of the microspheres surface were also seen (topography 2) (see Figure 6.3C).

EDX analysis of the two subsets of microsphere topographies revealed that the elemental composition of the microspheres was very similar. Slight deviations in exact quantity of each element, particularly holmium, was evident in microspheres produced in the same batch. A holmium content of approximately 15 mol% was detected in both sets of microspheres (see Figure 6.3D).

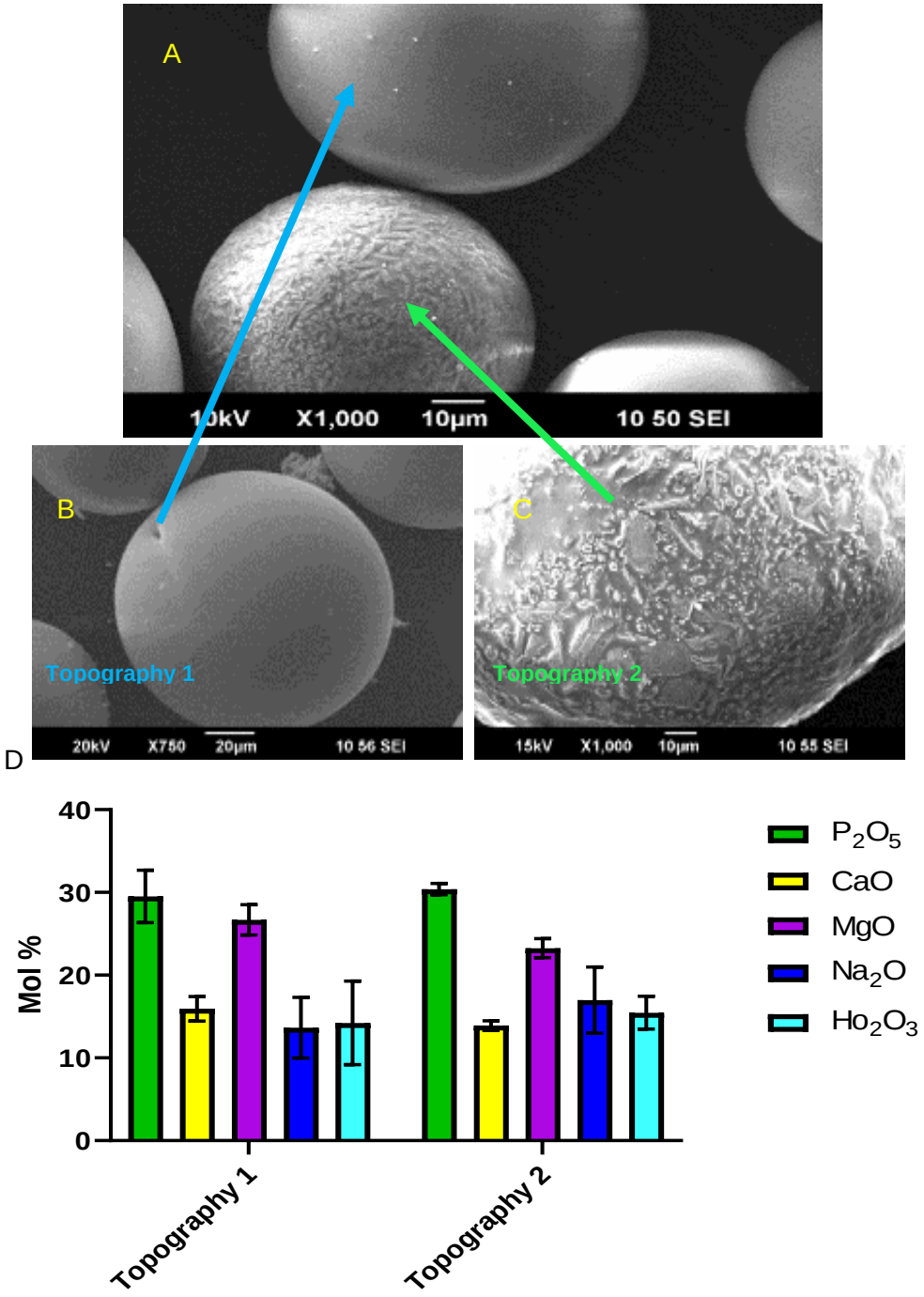

Figure 6.3 (A) SEM image of multiple 30H microspheres (B) SEM image at increased magnification showing example 30H microsphere with a smooth topography. (C) SEM image at increased magnification showing example 30H microsphere with a rough topography and grain-like structures on its surface. (D) Elemental composition determined EDX of 30Y microspheres with the two different topographies (n=10).

EDX mapping of resin embedded 30H microspheres was performed to establish whether any of the elements were concentrated at regions within the microspheres. The mapping showed that holmium and all the elements were homogenously distributed throughout the whole of the 30H microspheres and did not appear to be concentrated at the surface (see Figure 6.4).

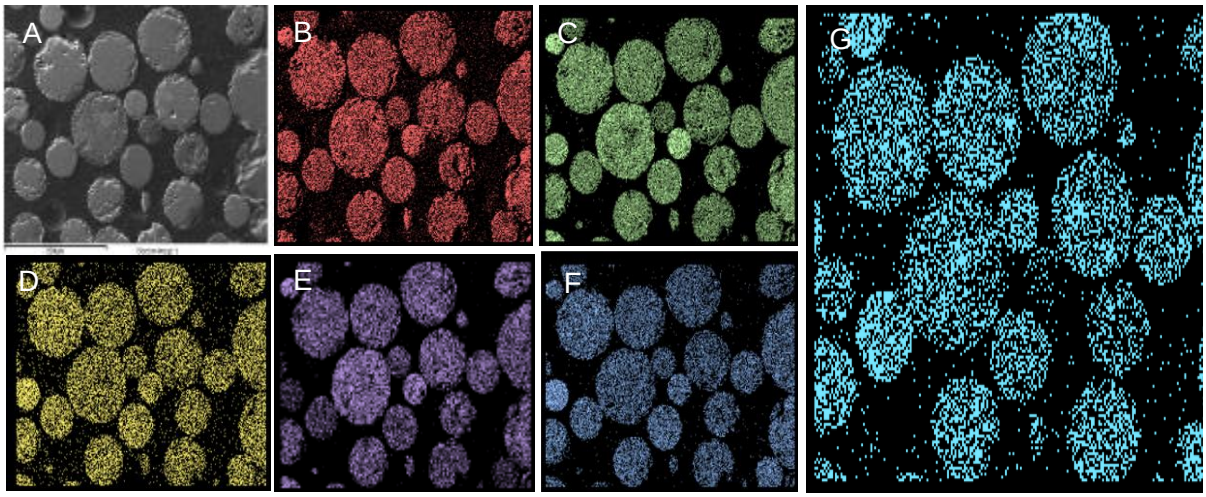

Figure 6.4 EDX mapping of resin embedded 30H microspheres showing the homogenous distribution of all the elements throughout the microspheres produced via flame spheroidisation. (a) SEM image (b) Oxygen (c) Phosphorous (d) Calcium (e) Magnesium (f) Sodium and (g) Holmium.

6.2.3 50H Surface topography and elemental analysis

In a similar manner to the 50Y microspheres in Chapter 4, SEM analysis revealed that a high yield of spherical particles was produced at the 45 – 125 µm size range, although topographically distinct 50H microspheres existed. A small proportion of the microspheres had a rough morphology with repeating units of irregular shape on their surface that were very similar to those seen on the 50Y microspheres. These highly ordered structures varied in size on the microspheres surface as well as between different microspheres (topography 1) (see Figure 6.5A and B). Most of the microspheres appeared to have a smooth surface, with some displaying evidence of submicron units on the surface at increased magnification (topography 2) (see Figure 6.5A and C).

EDX analysis of 50H microspheres revealed that the distinctive, highly ordered structures on the microspheres surface were indicative of holmium content. Microspheres that displayed highly ordered structures on their surface had the largest holmium content of 54.1 mol% (± 8.1). Like the 50Y microspheres, the larger, more prominent these features the greater the holmium content detected. Microspheres that appeared almost completely smooth or that had

much smaller features on their surface at increased magnification, had a slightly reduced holmium content of 28.3 mol% (± 9.2). Greater heterogeneity of holmium content was detected within this subset of microspheres (see Figure 6.5D).

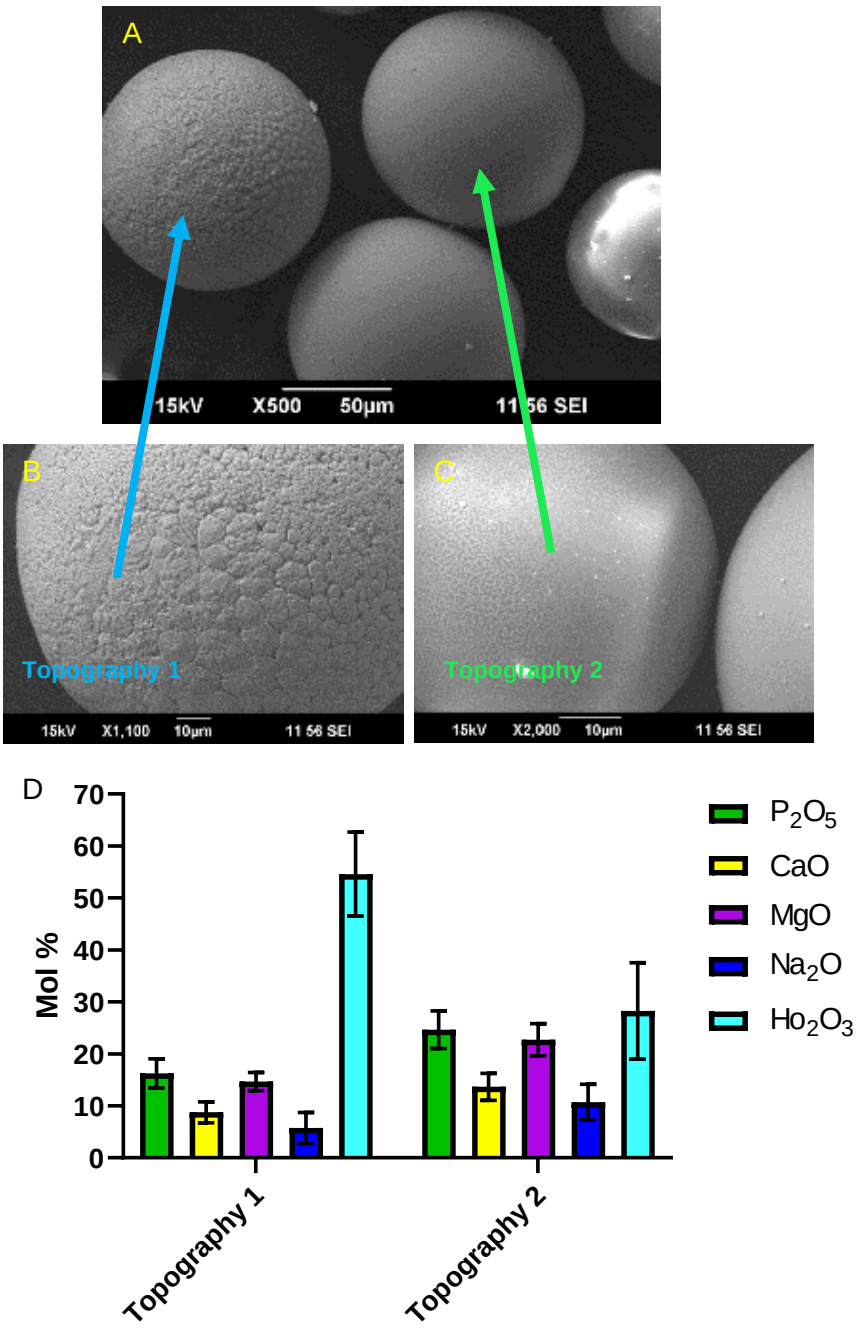

Figure 6.5: (A) SEM image of multiple 50H microspheres (B) SEM image at increased magnification showing example 50H microsphere with a smooth topography. (C) SEM image at increased magnification showing example 50H microsphere with a rough topography and grain-like structures on its surface. (D) Elemental composition determined EDX of 30Y microspheres with the two different topographies (n=10).

At increased magnification, EDX analysis of the surface features belonging to 50H microspheres with topography 1 revealed that the individual units on the surface displayed localised regions of holmium content. Analogous to the 50Y microspheres, the centre of the structures on the surface of 50H microspheres were shown to contain the greatest holmium content. The holmium content reduced slightly away from the central point of the units with increased levels of the glass forming elements found in the regions between the holmium-rich units (see Figure 6.6).

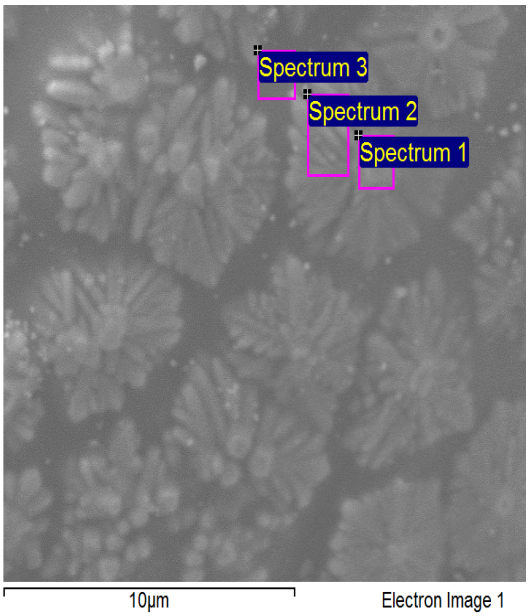

	Spectrum 1	Spectrum 2	Spectrum 3
P_2O_5	7.3	12.2	12.3
CaO	3.2	5.8	14.4
MgO	4.9	8.7	10.6
Na_2O	3.2	5.4	4.5
Ho_2O_3	81.4	67.8	58.6

Figure 6.6 (A) SEM image of the 50H microsphere surface and regions analysed. (B) Elemental values obtained via EDX of the different regions on the surface.

Despite the presence of localised regions of holmium content, EDX mapping of resin embedded 50H microspheres showed that all the elements were distributed throughout the microspheres. Holmium was detected and appeared homogenously distributed throughout the body of the microspheres (see Figure 6.7).

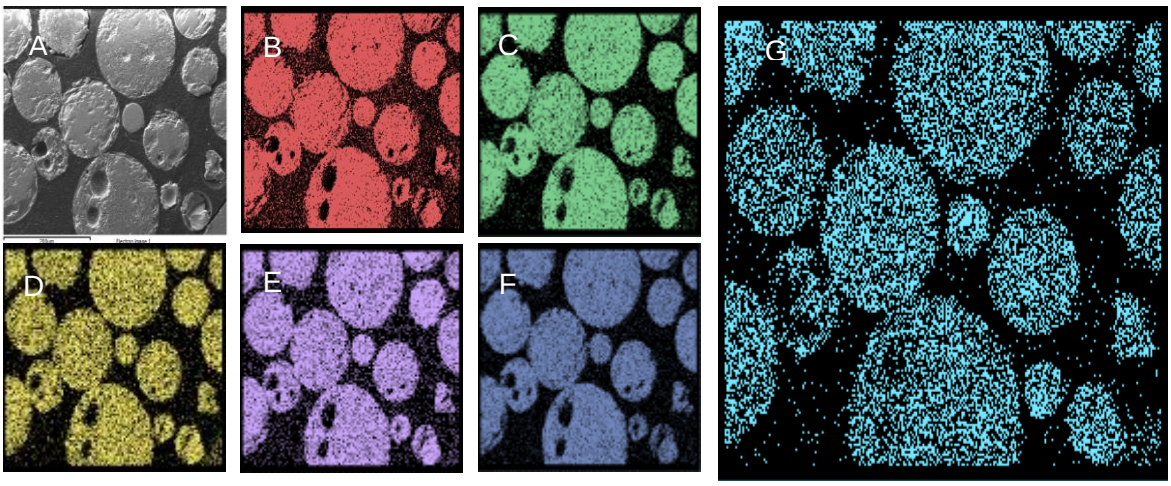

Figure 6.7 EDX mapping of resin embedded 50H microspheres showing the homogenous distribution of all the elements throughout the microspheres produced via flame spheroidisation. (a) SEM image (b) Oxygen (c) Phosphorous (d) Calcium (e) Magnesium (f) Sodium and (g) Holmium.

6.2.4 FIB-SEM

Focused Ion Beam Scanning Electron Microscopy (FIB-SEM) was employed to ablate away a section of the microspheres surface from 50H microspheres to perform high resolution observational analysis below the microsphere surface. As seen in Figure 6.8A, some 50H microspheres did not possess the smooth topography that most of the microspheres exhibited. Ablating away a section from one of these distinguishing microspheres revealed distinctive regions present within the bulk of the microspheres (see Figure 6.8B). The different regions were not homogenously organised and appeared randomly orientated through the bulk of the microsphere. The same technique was performed on a microsphere that exhibited the characteristic smooth morphology and revealed that there appeared to be an absence of discernible features within the body of the microsphere (see Figure 6.8C and D). In the absence of EDX analysis it was not possible to comment on the elemental composition of the distinct regions.

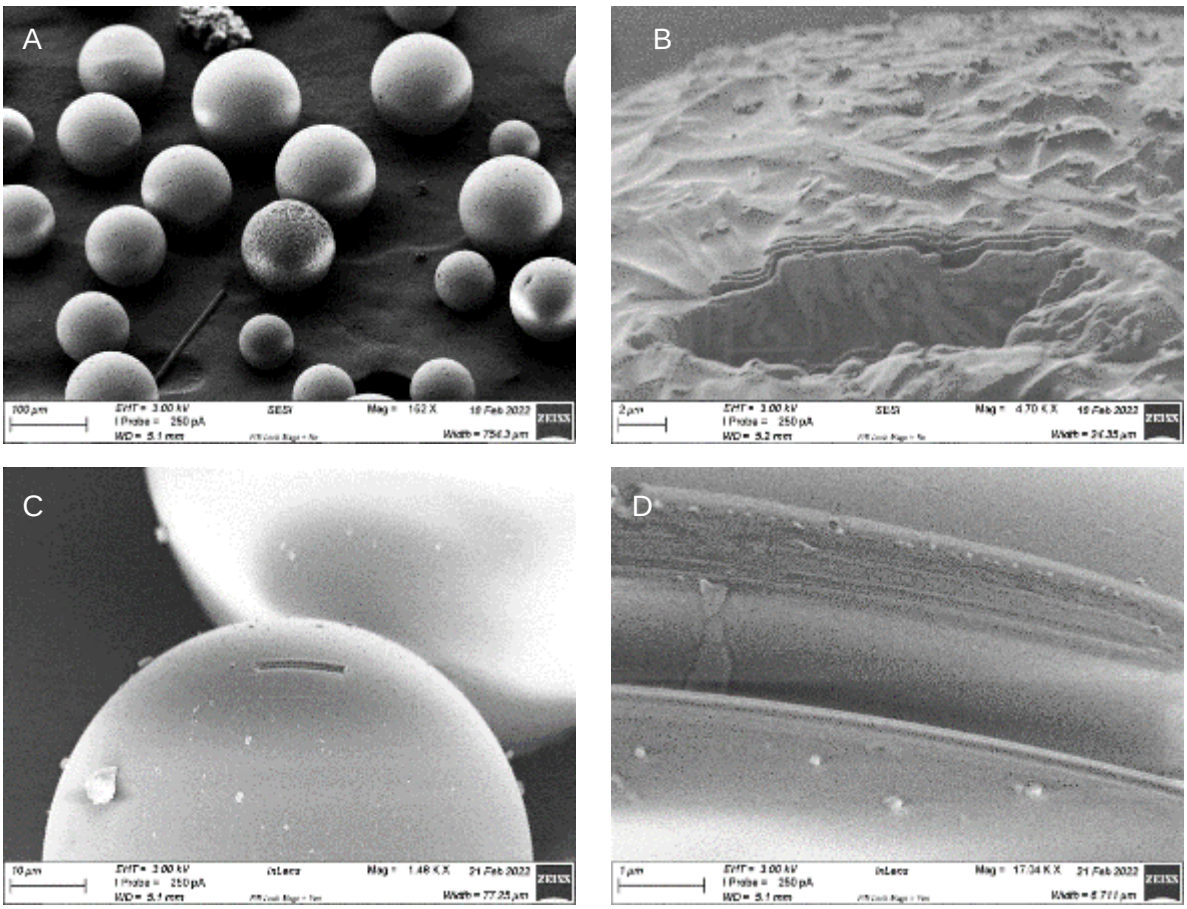

Figure 6.8 (A) An image acquired using FIB-SEM of 50H microspheres. (B) FIB-SEM image showing the inner section of a 50H microspheres with topography 1 once the FIB had milled through the surface. (C) FIB-SEM image showing 50H microsphere with smooth topography. (D) FIB-SEM image at increased magnification showing the inner section of a smooth 50H microsphere.

6.2.5 XRD Analysis

The XRD profiles for P40, 30H and 50H solid microspheres are shown in Figure 6.9. A single broad halo peak at 2θ values of ~–30-32° was observed for the P40 microspheres and the absence of any detectable crystalline peaks confirmed the amorphous nature of the solid glass microspheres (see Figure 6.9). In the spectra for 30H microspheres, the presence of crystalline peaks indicated that processing into solid holmium-containing microspheres via flame spheroidisation resulted in the production of glass-ceramic microspheres. Sharp peaks at ~ 29°, 34°, 49°, 58° and 61° 2θ values were observed, which were matched to cubic Ho_2O_3 according to powder diffraction file 00-043-1018 (ICDD database) (see Figure 6.9). An additional peak was also detected at ~32°, which was matched to hexagonal Ho_2O_3 according to powder diffraction file 01-076-7407 (ICDD database). Further peaks in the 30H spectra at

~20°, 26°, 35° and 52° were also detected and corresponded to $HoPO_4$ (ICDD 01-076-1533). In the 50H microspheres spectra, only peaks at ~ 29°, 34°, 49°, 58° and 61° 2θ values which corresponded to cubic Ho_2O_3 were observed (00-043-1018 ICDD database) (see Figure 6.9).

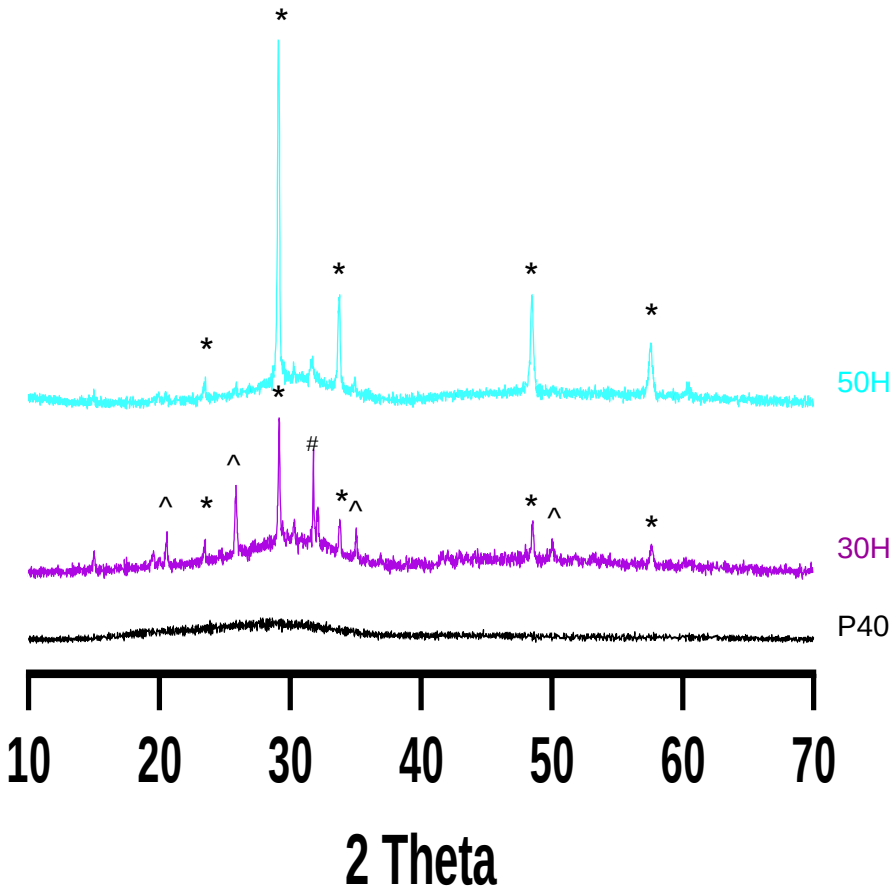

Figure 6.9 XRD spectra of P40 SMS (black), 30H (purple) and 50H (cyan) solid microspheres. The crystalline peaks matched for cubic Ho_2O_3 (*) (00-043-1018), hexagonal Ho_2O_3 (#) (01-076-7407) and $HoPO_4$ (^) (01-076-1533).

6.2.6 NMR

Quantitative 1D ^{31}P MAS-NMR spectroscopy was attempted to ascertain the distribution of Q^n species of the holmium-containing microspheres. Unfortunately, attempts to analyse 30H and 50H microspheres resulted in MAS rotors shattering immediately on loading into the probe. This meant that no further studies were performed and no results could be obtained.

6.2.7 Thermal analysis

The Differential scanning calorimetry (DSC) trace of the parent P40 glass showed the presence of a solitary crystallisation temperature of 573 °C. The initial crystallisation temperature increased for both the holmium-containing samples. In 30H microspheres, an initial crystallisation temperature of 605 °C was recorded and was higher still for the 50H sample at 686 °C. 30H microspheres exhibited additional crystallisation temperatures at 710 °C and 962 °C, whilst 50Y had additional crystallisation temperatures at 862 °C and 1005 °C. These peaks were broader and less defined than those seen in P40 sample. P40 displayed two melting temperatures at 645 °C and 765 °C. In the 30H microspheres the melting temperatures were higher at 830 °C and 994 °C and were at 660 °C, 830 °C and 923 °C for the 50H microspheres (see Figure 6.10).

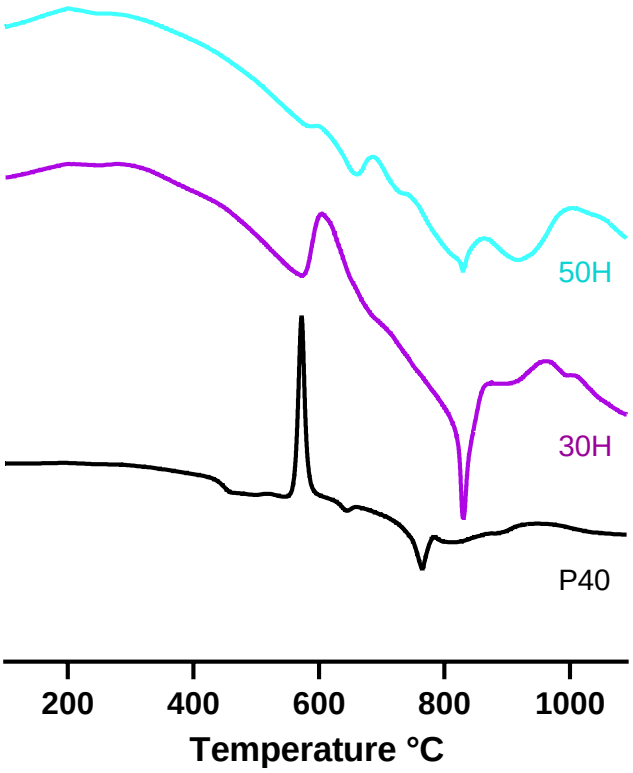

Sample	T_g		T_c			T_m		
	Onset	Mid	1	2	3	1	2	3
P40	434	463	573			645	765	
30H		572	605	710	962	830	994	
50H		588	686	862	1005	660	830	923

Figure 6.10 DSC thermal analysis profiles and corresponding Tg, Tm and Tc values for P40, 30H and 50H solid microspheres.

6.2.8 Raman Spectroscopy

Raman spectroscopy was performed to ascertain structural information about the holmium-containing microspheres and to try and identify which phosphate species were present in the microspheres. Initially, Raman spectra for Ho_2O_3 was obtained and compared to the Raman spectrum of Y_2O_3. At 660 nm excitation, the spectrum of Y_2O_3 was consistent with the Raman spectrum of the cubic phase of Y_2O_3 as reported previously using 633 nm excitation [310, 311]. The 660 nm spectrum of Ho_2O_3 was believed to be showing emission rather than Raman scattering due to the difference between the Ho_2O_3 and the Y_2O_3 660 nm Raman spectrum, as these oxides should be structurally related to one another and therefore have similar Raman spectra (see Figure 6.11A). At 532 nm excitation, Raman spectra of Y_2O_3 was

consistent with previous studies at 413 nm excitation and is most likely related to emission, rather than Raman scattering. The similarity of the 532 nm Raman spectra for Ho_2O_3 compared to the Y_2O_3 suggested that this could also be related to emission rather than Raman scattering.

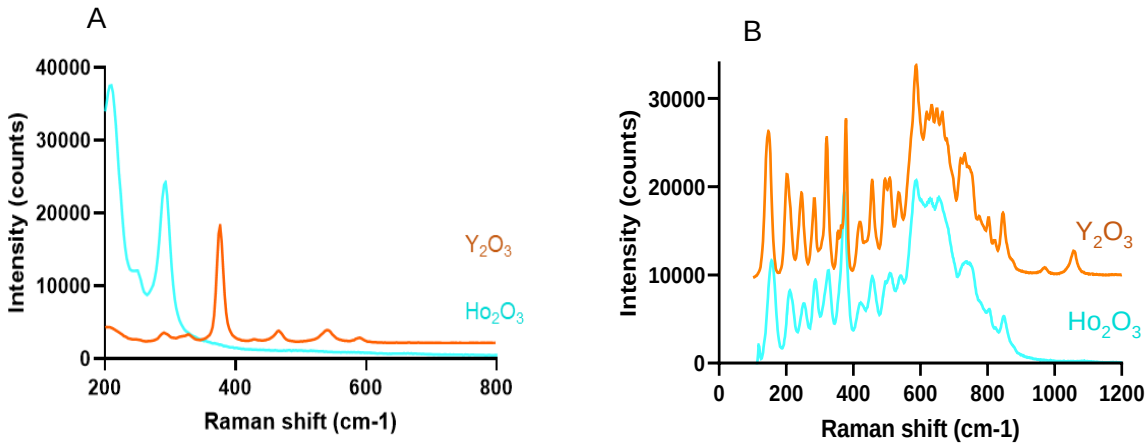

Figure 6.11(A) Raman spectra for Y_2O_3 (orange) and Ho_2O_3 (cyan) at 660 nm excitation. (B) Raman spectra for Y_2O_3 (orange) and Ho_2O_3 (cyan) at 532 nm excitation.

Images were generated by plotting the intensity (as peak area) of the peak associated with Ho_2O_3 (293 cm^{-1}, 270-320 cm^{-1}, unassigned emission) and were scaled to the minimum and maximum values and false coloured using the hot colour palette (see Figure 6.12). As only the peaks associated with Ho_2O_3 emission were observed and no Raman peaks from the phosphate species were seen, it was not possible to display the images using peak ratio as was done for the yttrium-containing microspheres in section 5.2.9. Therefore, a high intensity meant high Ho_2O_3 content, and a low intensity meant low Ho_2O_3 content, but further information on possible Q speciation of the microspheres was not able to be obtained.

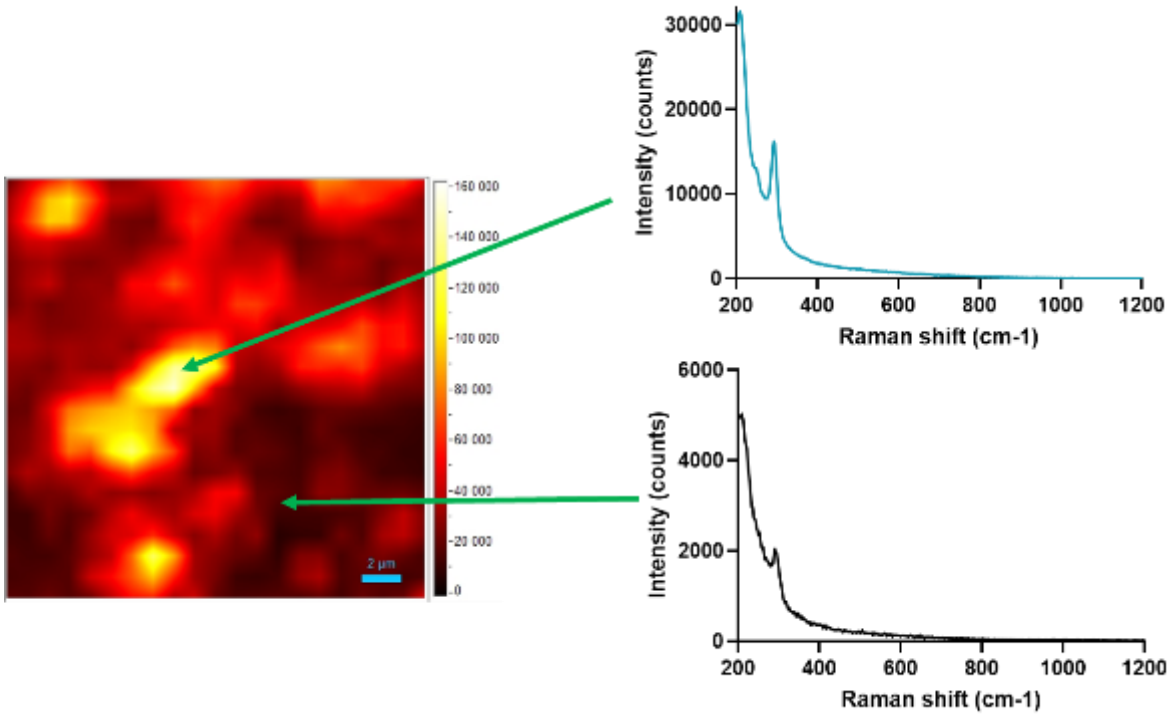

Figure 6.12 Raman mapping experiment in which hot colour palette image created by using peak associated with Ho_2O_3 (293 cm^{-1}) scaled to the minimum and maximum values and the corresponding spectra for a Ho_2O_3 –rich and Ho_2O_3 –poor region of a 50H microsphere.

The hot palette images and the mean spectrum extracted from each mapping experiment from three different 30H microspheres, using a 660 nm laser, are shown in Figure 6.13. From the images generated non-uniform coverage of Ho_2O_3 across the microspheres surface was observed (see Figure 6.13A, B and C). The mean spectrum extracted from each mapping experiment were near identical, indicating a high degree of composition uniformity and dominated by emission from Ho_2O_3. There was no direct evidence for phosphate glass in any of the maps, therefore it was not possible to comment on Q^n speciation within the microspheres.

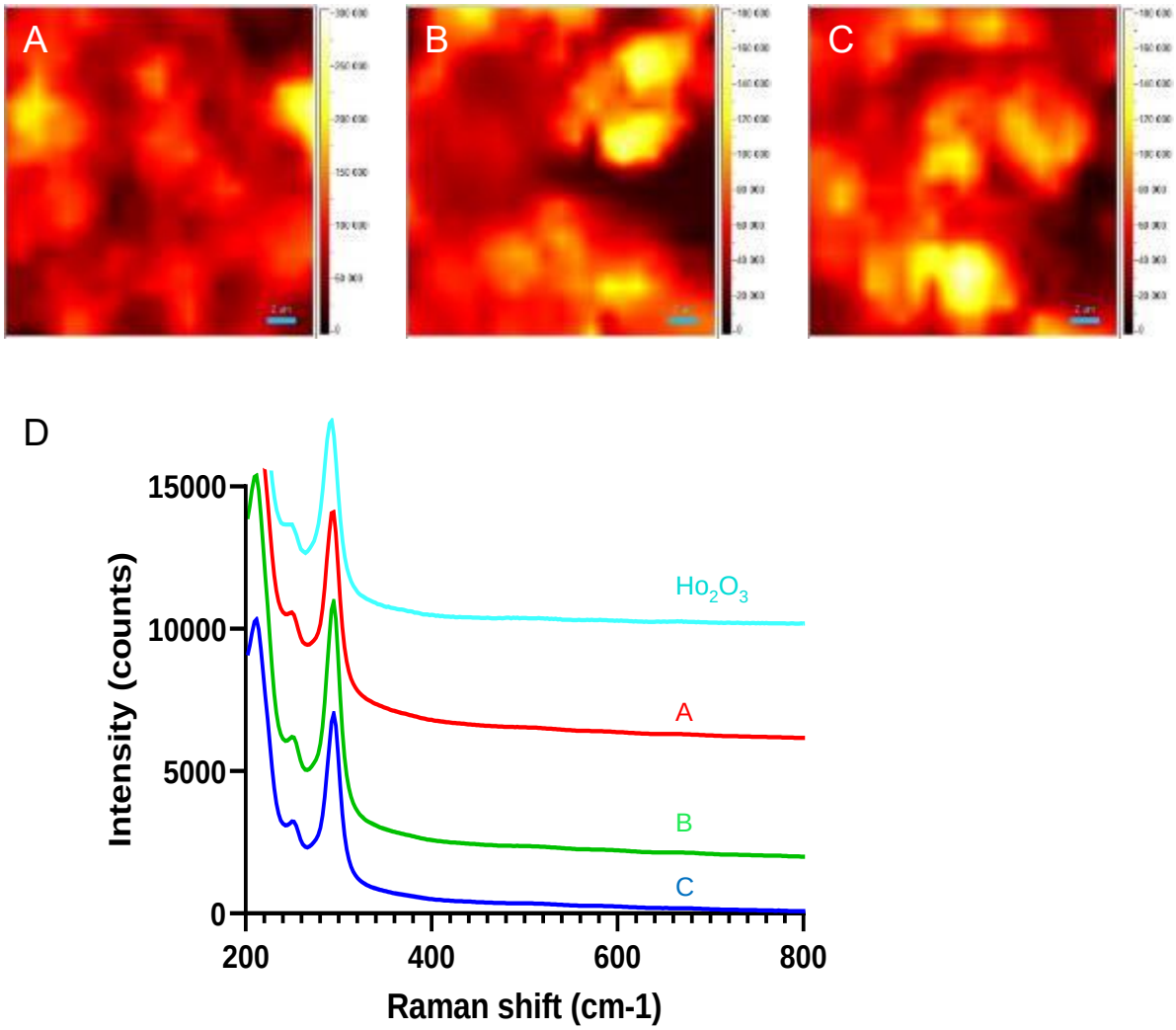

Figure 6.13 Raman mapping experiment using 660 nm laser in which hot colour palette image created by using peak associated with Ho_2O_3 (293 cm^{-1}) scaled to the minimum and maximum values for three separate 30H microspheres (A), (B) and (C). (D) The Raman spectra for 30H microsphere (A) red, microsphere (B) green and microsphere (C) blue.

The same process was performed at 532 nm excitation and images were generated by plotting the intensity (as peak area) of the peak associated with Ho_2O_3 (481 cm^{-1}, 355-580 cm^{-1}, unassigned emission) and were scaled to the minimum and maximum values and false coloured using the hot colour palette (see Figure 6.14). As was seen at 660 nm, the images showed reasonable compositional uniformity. The mean spectrum for microsphere A displayed weak evidence for Ho_2O_3 based on the match seen in the spectrum of the Ho_2O_3 in Figure 6.11B and for the other two microspheres that were mapped. There were a series of high intensity emissions below 700 cm^{-1} that do not correspond with the expected cubic phase of Ho_2O_3 but may represent different phases and/or forms of Ho_2O_3.

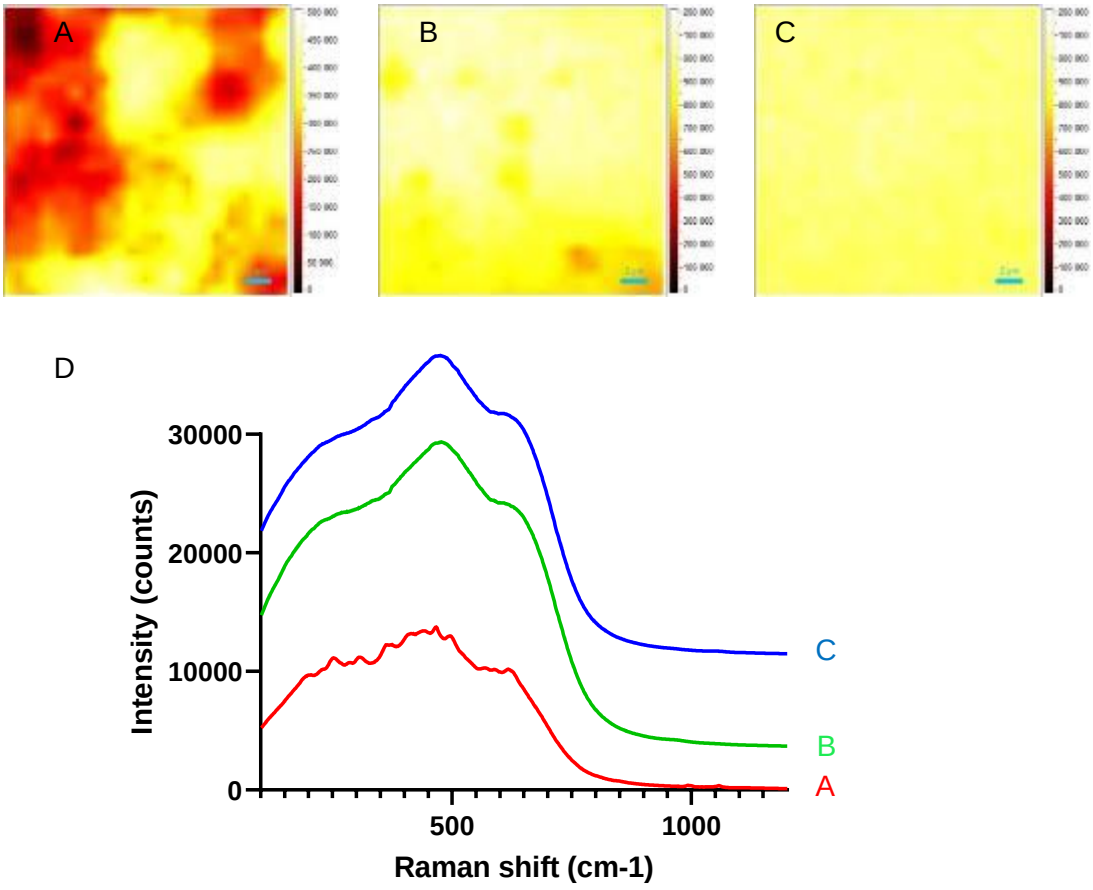

Figure 6.14 Raman mapping experiment using 532 nm laser in which hot colour palette image created by using peak associated with Ho_2O_3 (293 cm^{-1}) scaled to the minimum and maximum values for three separate 30H microspheres (A), (B) and (C). (D) The Raman spectra for 50H microsphere (A) red, microsphere (B) green and microsphere (C) blue.

The same experimental process at 660 nm excitation was performed for 50H microspheres. As was seen in high yttrium content 50Y microspheres, it was observed that the 50H microspheres displayed non-uniform Ho_2O_3 coverage (see Figure 6.15A, B and C). The spectra from each of the three microspheres are very similar, indicating generally homogenous composition between the microspheres and dominated by emission from Ho_2O_3 (Figure 6.15D). Again, there was no direct evidence for phosphate glass in any of the maps.

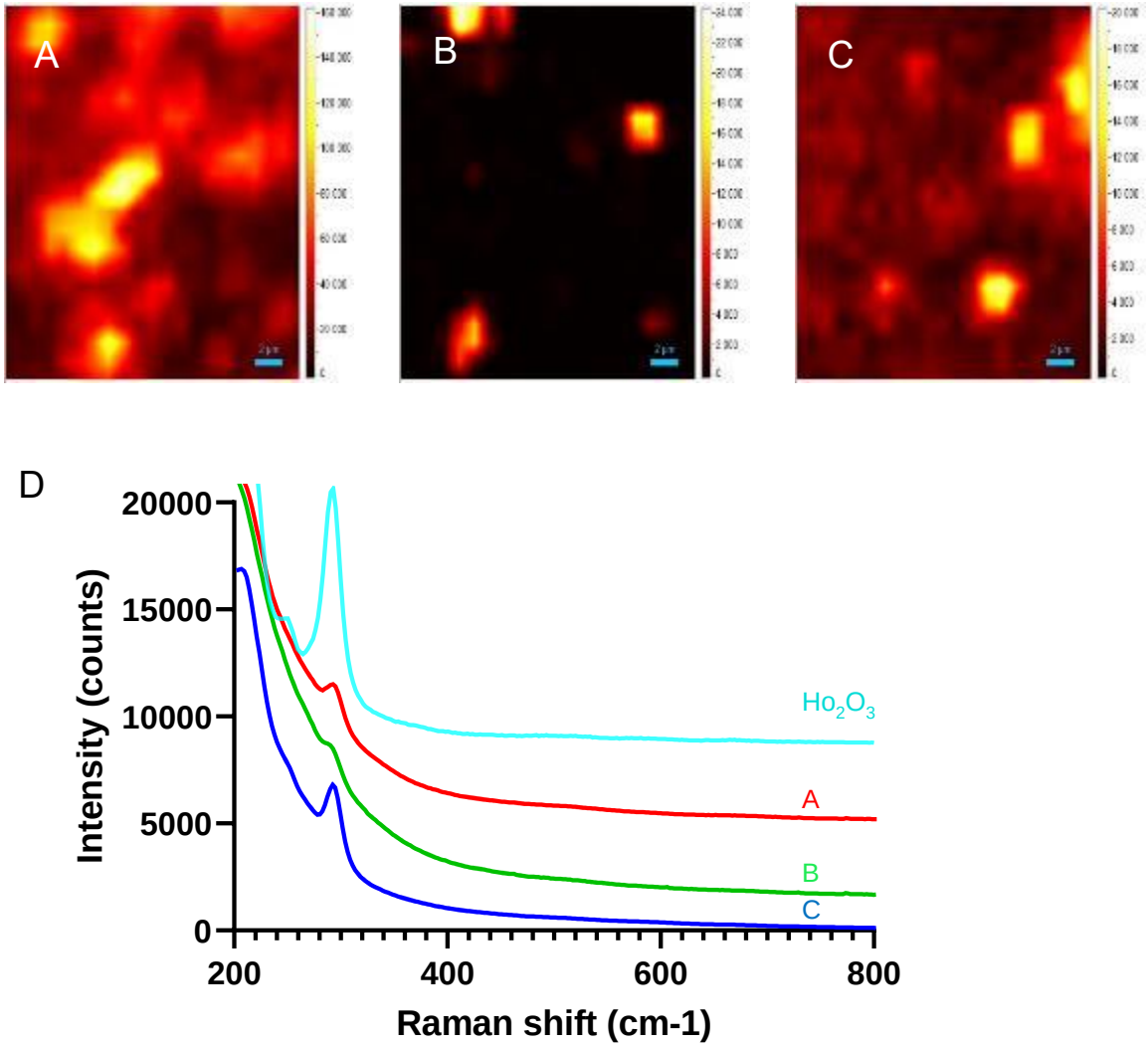

Figure 6.15 Raman mapping experiment using 660 nm laser in which hot colour palette image created by using peak associated with Ho_2O_3 (293 cm^{-1}) scaled to the minimum and maximum values for three separate 50H microspheres (A), (B) and (C). (D) The Raman spectra for 50H microsphere (A) blue, microsphere (B) red and microsphere (C) green.

For the 50H microspheres at 532 nm excitation, similar results were seen compared to those obtained at 660 nm in that the images generated and the spectrum from each mapping experiment were very similar, indicating a high degree of compositional uniformity and no direct evidence for phosphate glass (see Figure 6.16).

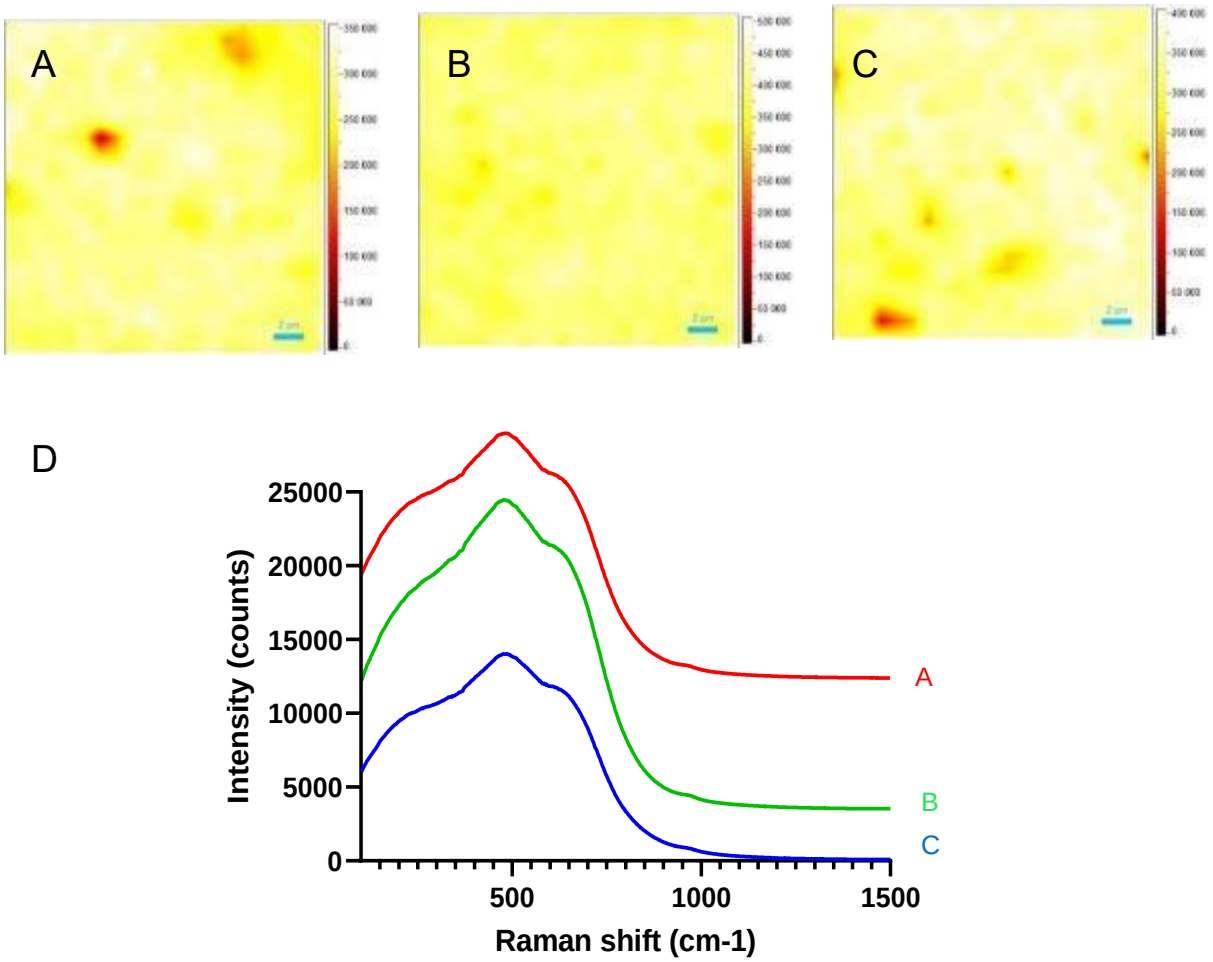

Figure 6.16 Raman mapping experiment using 532 nm laser in which hot colour palette image created by using peak associated with Ho_2O_3 (293 cm^{-1}) scaled to the minimum and maximum values for three separate 50H microspheres (A), (B) and (C). (D) The Raman spectra for 50H microsphere (A) blue, microsphere (B) red and microsphere (C) green.

6.2.9 Theoretical O/P calculations

The O/P ratios were calculated for P40, 30H and 50H solid microspheres based on the EDX values obtained. Equation 6.1 was used to calculate the ratio as follows:

Equation 6.1

$$\mathrm{O/P} = \frac{[P_2O_5]\mathrm{x}\,5 + [\mathrm{CaO}] + [MgO] + [NaO] + [Ho_2O_3]\mathrm{x}\,3}{[P_2O_5]\mathrm{x}\,2}$$

As seen in Table 5.6.1, as the holmium content in the microspheres increased there was a corresponding increase in the O/P ratio.

Table 5.6.1 Theoretical O/P calculations for P40, 30H and 50H solid microspheres.

Solid microsphere formulation	O/P ratio
P40	3.33
30H	4.28
50H	5.26

6.2.10 XPS Analysis

High-resolution O 1s spectra were recorded for the P40 SMS, as well as the 30Y and 50Y SMS samples. For the P40 SMS, the peaks were resolved into two components, with the highest binding energy peak at 533.1 eV (23.6%) corresponding to bridging oxygen (BO) within the glass structure, whilst the lowest binding energy peak at 531.4 eV (76.4%) was associated with non-bridging oxygen (NBO) (see Figure 6.17A).

In the 30H microspheres there was an increase in the number of O peak components. A peak at 531.4 eV (45.5%) was observed and attributed to NBO. It was postulated that no BO would be present in 30H microspheres based on the characterisation of 30Y microspheres and the theoretically calculated O/P ratio for 30H obtained in section 6.2.9. This meant the peak at 533.1 eV (29.8%) was assigned as Ho-O-P bonding. The peak with the highest binding energy at 534.6 eV (24.7%) was ascribed to Ho-O-Ho bonding (see Figure 6.17 and Table 6.2).

In the 50H microspheres, the area for the peak at 531.2 eV (53.7%), which corresponded to NBO increased. There was a slight decrease in the area for the peak at 532.4 eV (28.8%) for Ho-O-P bonding and a decrease at 533.5 eV that corresponded to Ho-O-Ho (16.1%) was seen. An additional component with a peak at 529.1 eV (1.5%) was present and was attributed to Ho-O bonding within Ho_2O_3 (see Figure 6.17 and Table 6.2).

Table 6.2 High-resolution O 1s spectra from XPS analysis of P40, 30H and 50H solid microspheres

Sample Code	Elements	Binding Energy (eV)	Corresponding Bonds	Area (%)
P40	O 1s	531.4	NBO	76.4
		533.1	BO	23.6
		534.2	Na KLL Auger	
30H	O 1s		Ho-O in Ho2O3	
		531.4	NBO (P-O-Mg/Ca/Na)	45.5
		533.1	Ho-O-P	29.8
		534.6	Ho-O-Ho in glass	24.7
		535.9	Na KLL	
50H	O 1s	529.2	Ho-O in Ho2O3	1.47
		531.2	NBO (P-O-Mg/Ca/Na)	53.6
		532.4	Ho-O-P	28.8
		533.5	Ho-O-Ho in glass	16.1
		534.1	Na KLL	

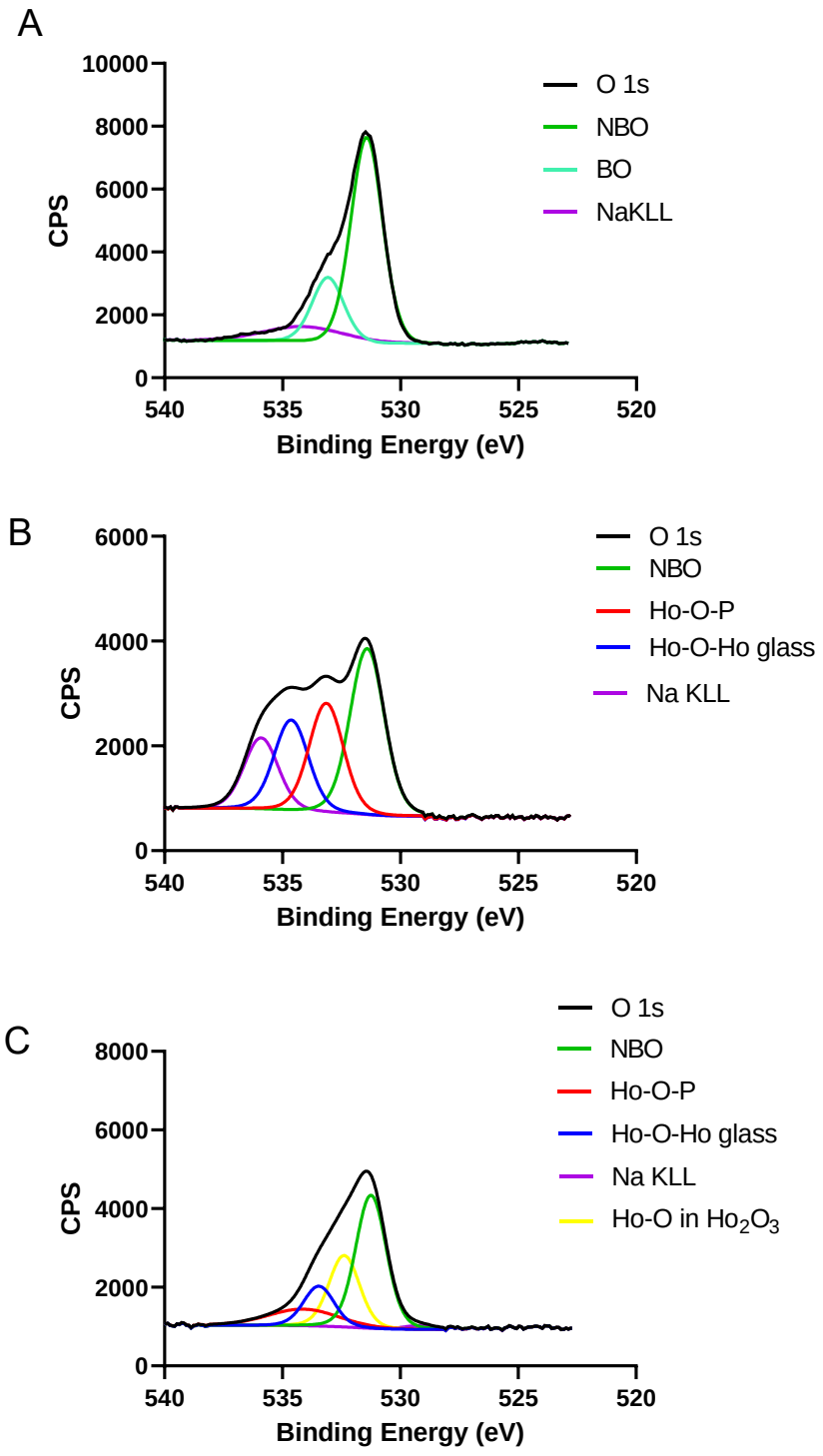

Figure 6.17 High-resolution spectra of O 1s peaks with overlapping Na KLL Auger emission for (A) P40, (B) 30H and (C) 50H solid microspheres.

6.2.11 Ion release studies

Figure 6.18 shows the cumulative ion release profiles for P40, 30H and 50H microspheres calculated from measurements obtained via ICP analysis over 28 days immersion in milli-Q water and the calculated ion release rates. The ions released from each microsphere formulation exhibited a linear relationship with time and were released consistently (apart from holmium which was not released from P40 microspheres).

P40 solid microspheres released all the glass forming ions at a statistically significant higher rate in comparison to the holmium-containing microspheres (Na and P: $p < 0.0001$; Mg and Ca*: vs* 30H $p < 0.05$*, vs 50Y* $p < 0.01$*)* (see Figure 6.18F). As the holmium content in the microspheres increased, there was a decrease in the release rate of the glass forming ions. P40 microspheres released Na^+ (3.5 ppm/day), Mg^{2+} (2.0 ppm/day), and P (8.4 ppm/day) at a rate around 3.5 times greater than that of the 30H microspheres and around 10 times the rate compared to 50H microspheres. The holmium containing microspheres released a very small amount of holmium ions in comparison to all the other elements. 30H microspheres releases Ho^{3+} ions at a rate of 0.4 ppm/day, which was twice the rate at which 50H microspheres released Ho^{3+} (0.2 ppm/day) despite the 30H microspheres having a lower holmium content.

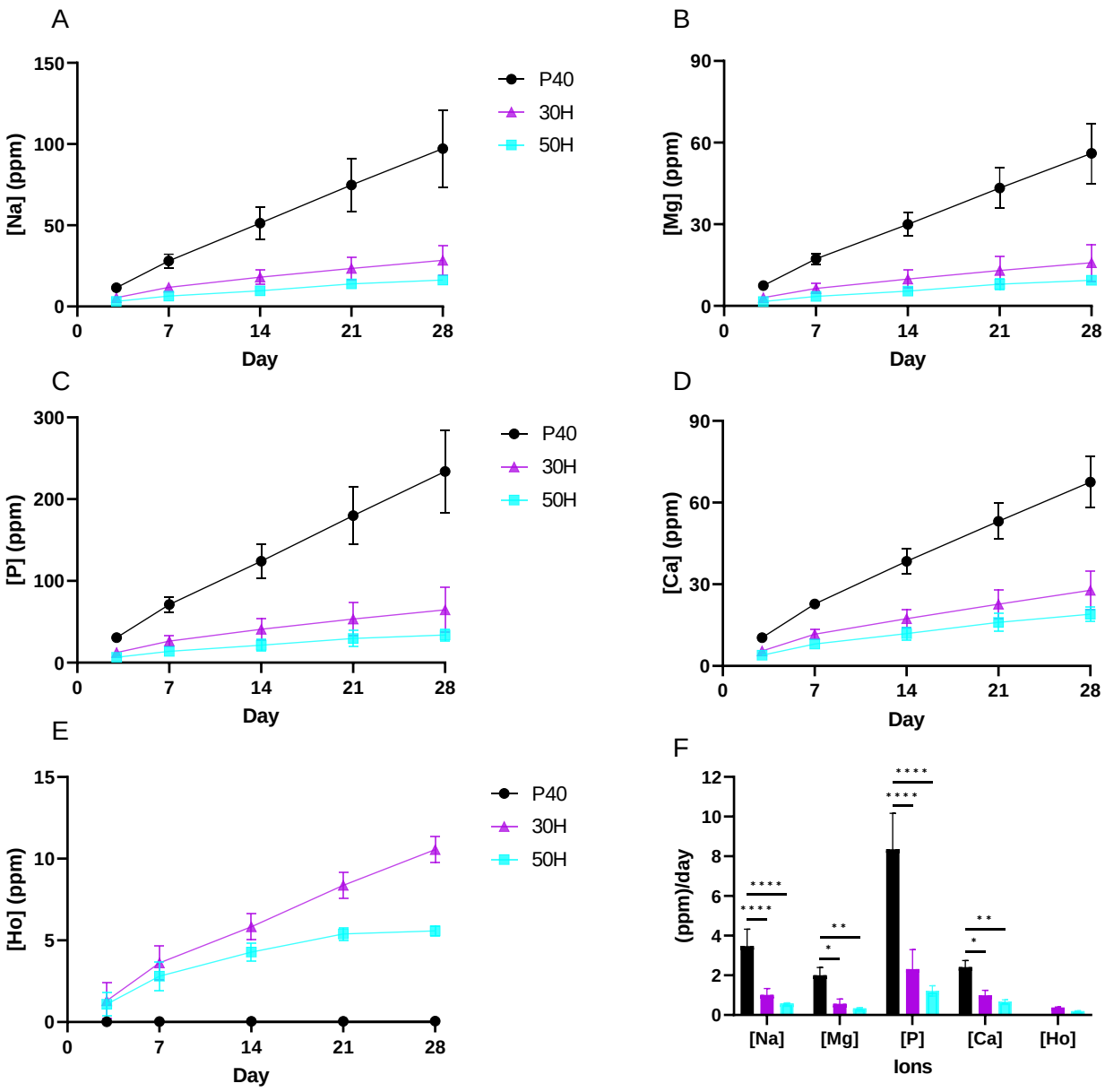

Figure 6.18 Cumulative ion release profile of (A) [Na], (B) [Mg], (C) [P], (D) [Ca] and (E) [Ho] measured via ICP-MS PMS of solid P40, 30H and 50H microspheres immersed in milli-Q water over a 28-day period. (Error bars are also included in the data above).

Figure 6.19 shows the pH of the milli-Q water that the microspheres were degraded in over a 28-day period. For the solution containing P40 solid microspheres, there was a decrease in pH from ~7.2 at day 3 to ~7.0 at day 7, where it remained constant over the duration of the study. The 30H solution had a comparable value to the P40 solution at both day 3 and day 28 but was slightly higher in the period between at around 7.2 pH as opposed to ~7. A pH of ~ 7.3 for 50H solution was observed at day 3 which then gradually decrease to ~ 6.9 by the end of the 28-day period.

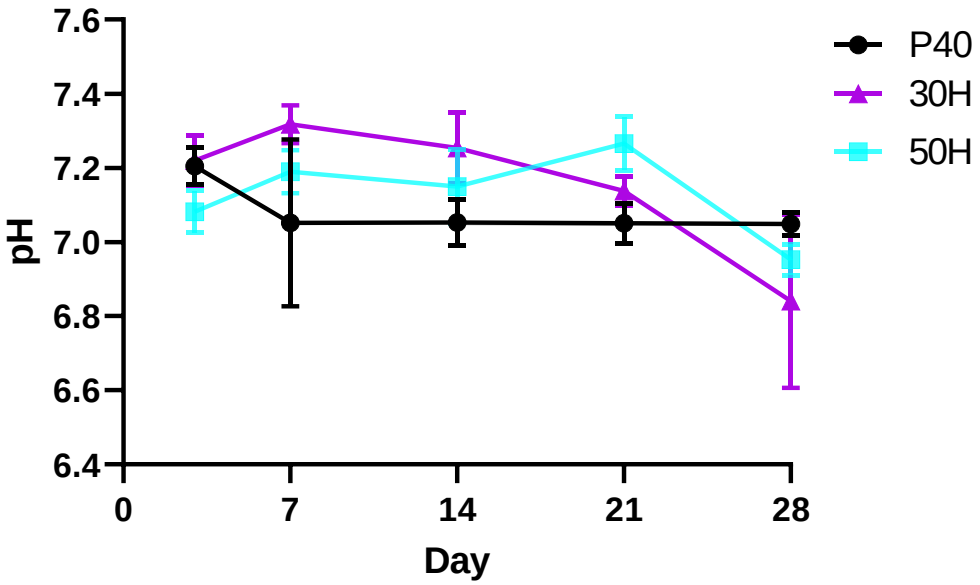

Figure 6.19 pH of milli-Q water during 28 days of P40, 30H and 50H solid microspheres immersion within the solution. (Error bars are also included in the data above).

SEM images of the P40 solid microspheres as well as both the 30H and 50H microspheres following the period of immersion in milli-Q water are shown in Figure 6.20. At day 28, P40 microspheres displayed evidence of cracking on their surface with the outer most layer appearing to flake and degrade from the core of the structure. These features did not occur on the surface of either 30H or 50H microspheres. The lack of structural and morphological changes to the holmium containing microspheres correlated with the reduced ion release observed following 28 days immersion in milli-Q water. This was further evidence that holmium incorporation into the microspheres had significantly increased their durability when in an aqueous environment.

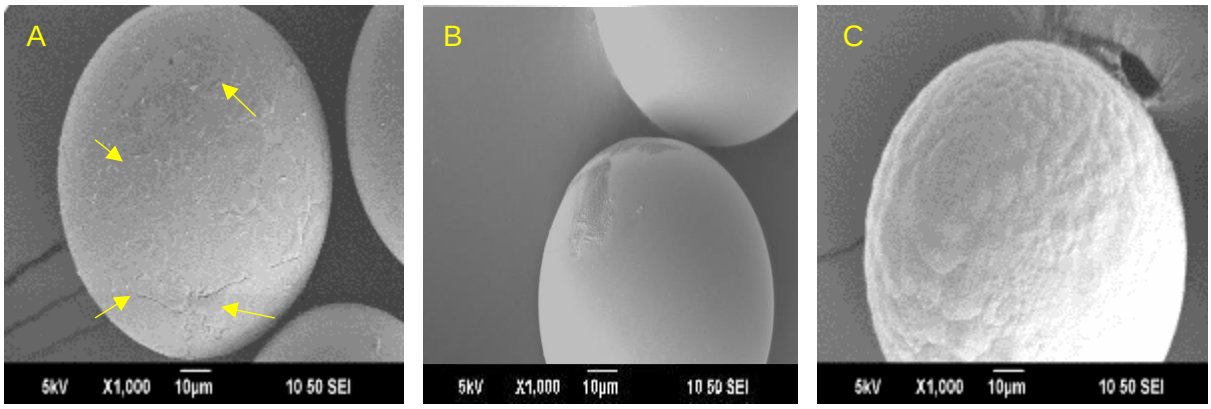

Figure 6.20 SEM images of (A) P40 (B) 30H and (C) 50H solid microspheres after 28 days immersion in milli-Q water. Yellow arrows indicate regions of degradation on the microspheres surface.

6.2.12 Bioactivity studies via SBF: EDX Analysis

EDX analysis was performed on P40 solid microspheres and both 30H and 50H microspheres prior to and after 28 days immersion in SBF. The Ca:P ratio (wt%) for each composition was calculated from the EDX values acquired. Microspheres from each of the three formulations had a slight but not significant increase in the Ca:P ratio following 28 days immersion (see Figure 6.21). This was most pronounced for the P40 microspheres, with almost no discernible increase in the ratio for both holmium-containing microspheres.

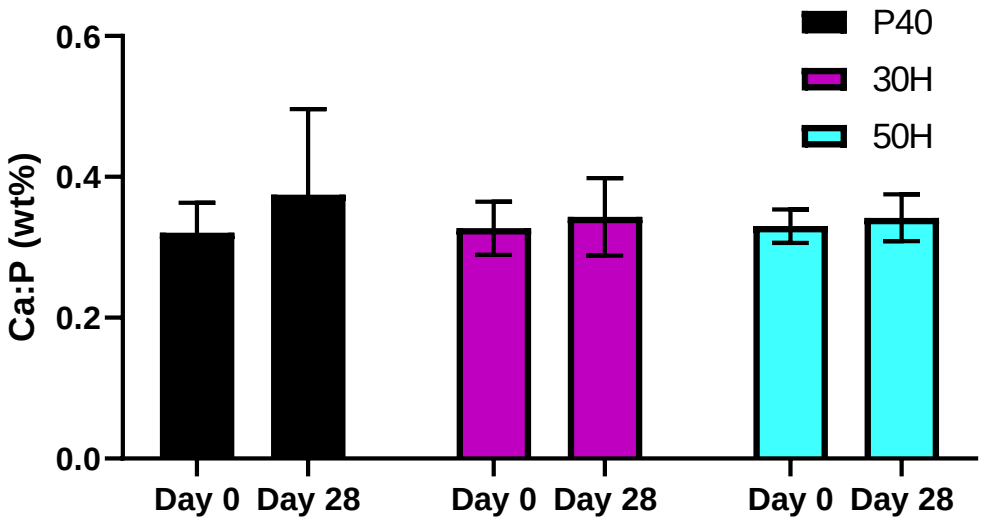

Figure 6.21 Ca:P ratio, determined by EDX, for P40, 30H and 50H solid microspheres prior to SBF immersion and after 28 days immersion.

6.2.13 Bioactivity studies via SBF: XRD Analysis

XRD profiles of P40, 30H and 50H solid microspheres and silicate-based 45S5 Bioglass (which was used as a positive control) following 28 days immersion in SBF are shown in Figure 6.22. The XRD profile for 45S5 were in good agreement with the results seen in other studies, with sharp peaks at 2θ values of 26° and 32° from day 7 onwards revealing HCA (ICSD 01-084-1998) formation [136]. A single broad halo peak at 2θ values of ~30-32° was observed for the P40 solid microspheres at both day 0 and day 28. The absence of any detectable crystalline peaks confirmed the amorphous nature of the microspheres prior to and following SBF immersion. For the 30H microspheres, there were no additional peaks or change in the XRD spectra from day 0 to day 28 after immersion in SBF. The 50H microspheres also exhibited no additional detectable peaks at day 28 to those that were present prior to SBF immersion. The lack of new crystalline phases suggested that no HA or alternative orthophosphate precursors had formed on the surface of the microsphere during 28 days immersion in SBF (see Figure 6.22).

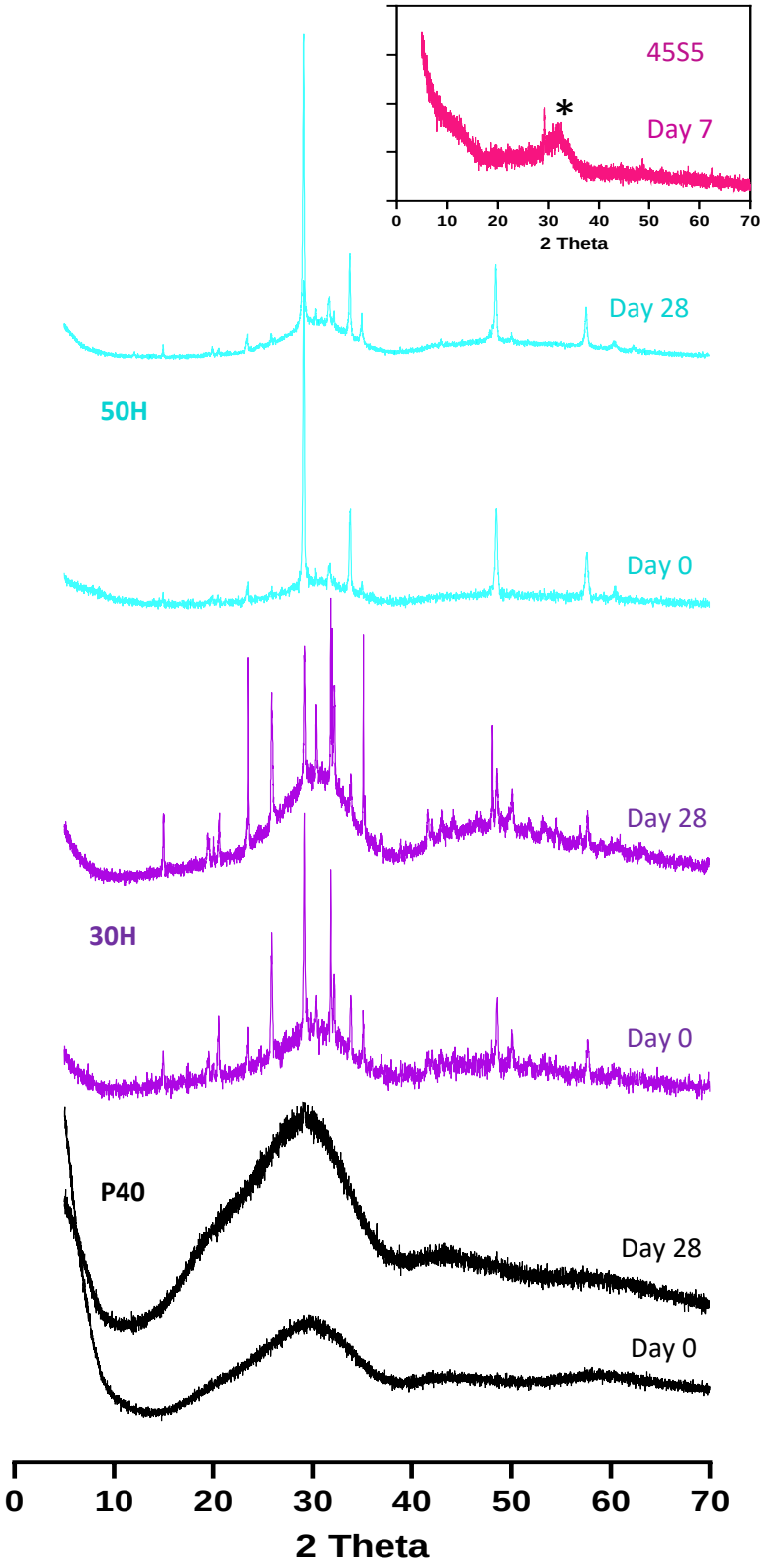

*Figure 6.22 XRD patterns for P40 (black), 30H (purple) and 50H (cyan) solid microspheres prior to and after 28 days immersion in SBF. Inset is the XRD trace for 45S5 after 7 days immersion for SBF validation. * HCA (ICSD 01-084-1998).*

6.2.14 *In vitro* indirect cell culture studies

The same indirect culture method utilised to determine the cytocompatibility of the yttrium-containing microspheres was also used to evaluate the biological response to the dissolution products from the holmium-containing microspheres. Analysis of metabolic activity via the Alamar Blue assay showed that after 2 days of culture, cells treated with P40 conditioned media had significantly higher cell response when compared to cells treated with the other media (*vs* 30H and 50H: $p < 0.01$; *vs* SM and SM + 5% DMSO: $p < 0.0001$) (see Figure 6.23A). There was no significant difference in metabolic activity seen with cells treated with either 30H or 50H conditioned media ($p > 0.05$) and the cellular response was significantly greater than for cells treated with SM ($p < 0.0001$). Cell treated with SM + 5% DMSO (negative control) had significantly lower metabolic activity at both day 2 and day 7 compared to cells treated with microsphere-conditioned media or SM ($p < 0.0001$). At day 7, cells treated with P40, 30H, 50H and SM all had significantly greater metabolic activity when compared to cells at day 2 ($p < 0.0001$). After 7 days of culture there was no significant difference detected in the metabolic activity of the MG63s cells when cultured using SM or P40, 30H and 50H conditioned media ($p > 0.05$) (see Figure 6.23A).

Brightfield images at day 2 of the MG63 cells confirmed the formation of homogenous cell monolayers in the presence of conditioned media from P40, 30H and 50H microsphere formulations. The confluency and morphology of the cells was analogous to that of the MG63s grown in SM. Conversely, cells grown in SM +5% DMSO were small and circular in morphology and sparsely distributed (see Figure 6.23B).

A

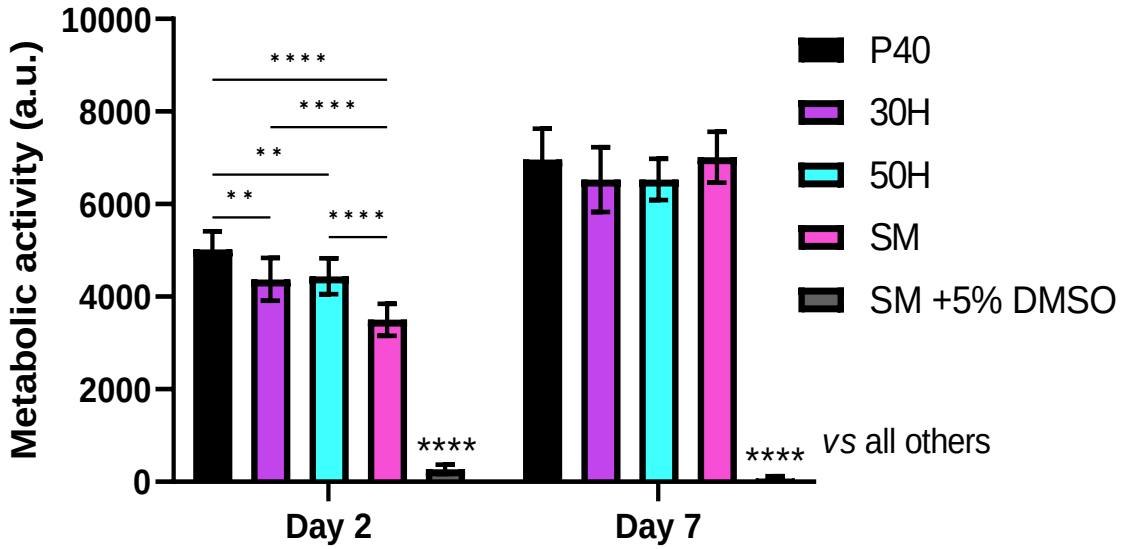

B

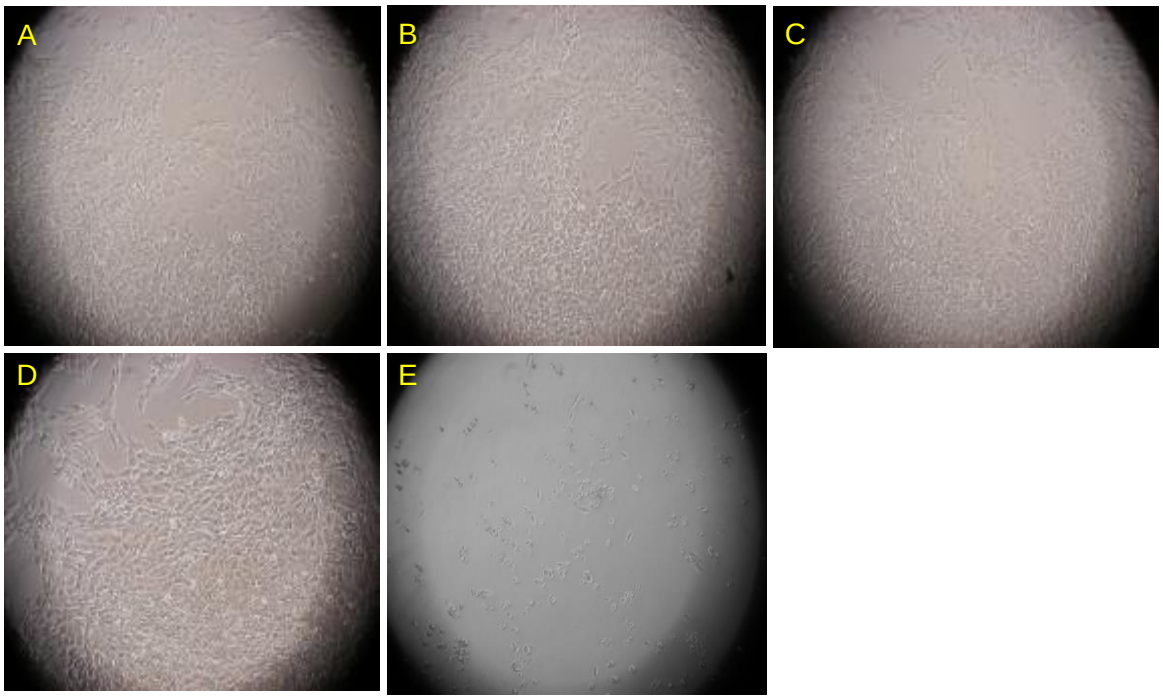

Figure 6.23 *(A) Evaluation of cell metabolic activity in indirect culture of P40, 30H and 50H solid microspheres at day 2 and day 7. ****p < 0.0001, *** p < 0.001, ** p < 0.01. (B) Cell appearance at day 2 of indirect culture; (A) P40, (B) 30H, (C) 50H, (D) SM and (E) SM + 5% DMSO*

Alkaline phosphatase (ALP) activity was measured as an early marker of osteogenic differentiation in MG63 cells after 7 days of indirect culture using P40, 30H and 50H conditioned media. The ALP activity was normalised to the DNA content of the cells under investigation. Cells grown in P40 conditioned media had significantly higher ALP activity compared to cells grown in 30H and 50H conditioned media (*vs* 30H: $p < 0.01$; *vs* 50H: $p < 0.001$). There was no significant difference in the ALP activity of cells cultured using P40-conditioned media and SM and between SM and both the 30H and 50H conditioned media ($p > 0.05$) (see Figure 6.24).

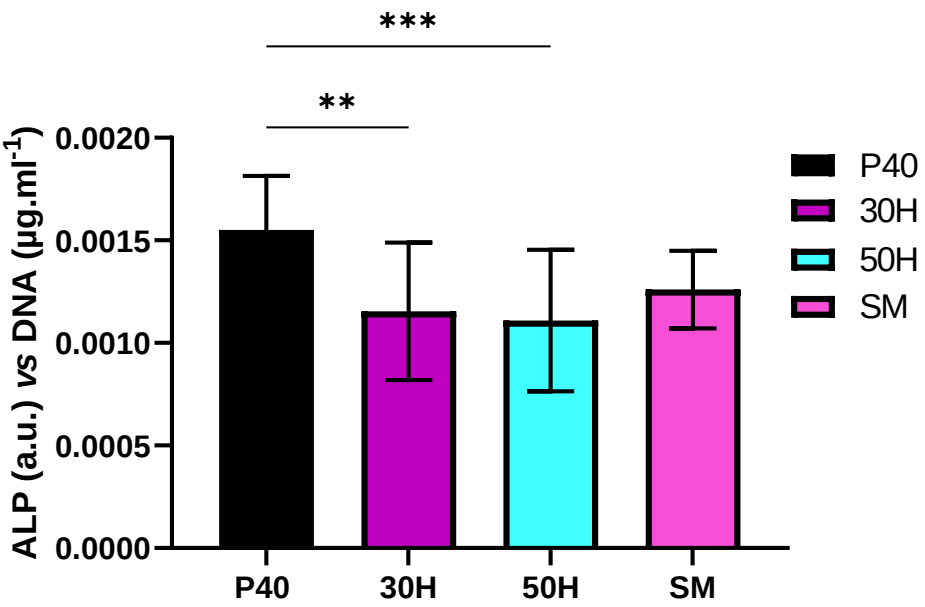

*Figure 6.24 Evaluation of ALP activity in indirect culture of P40, 30H and 50H solid microspheres at day 7. *** p < 0.001, ** p < 0.01.*

6.2.15 Proteomic profiling using LC-MS/MS

Due to 30H microspheres releasing a greater amount of holmium ions and the comparable cellular responses to both indirect and direct culture between 30H and 50H, the 30H formulation was selected to investigate how the release products from microspheres impacted protein expression within the cells. Protein expression from cells cultured in 30H, 30Y and P40 conditioned media were compared to one another. LC-MS/MS analysis detected a total of 992 proteins from the samples measured (from a minimum of two peptide sequences with a protein threshold of 99.9% and a false positive discovery rate of 4.5%). 905 proteins were detected from cells cultured in either P40, 30Y or 30H conditioned media. 30 proteins were present in cells treated with P40 media and 30H media but not 30Y media and a further 30 were found

to be present in cells from P40 and 30Y media that were not in the 30H treated cells. 7 proteins were found to be unique to cells treated with P40 media, 8 to cells treated with 30Y and 6 with 30H-conditioned media (see Figure 6.25).

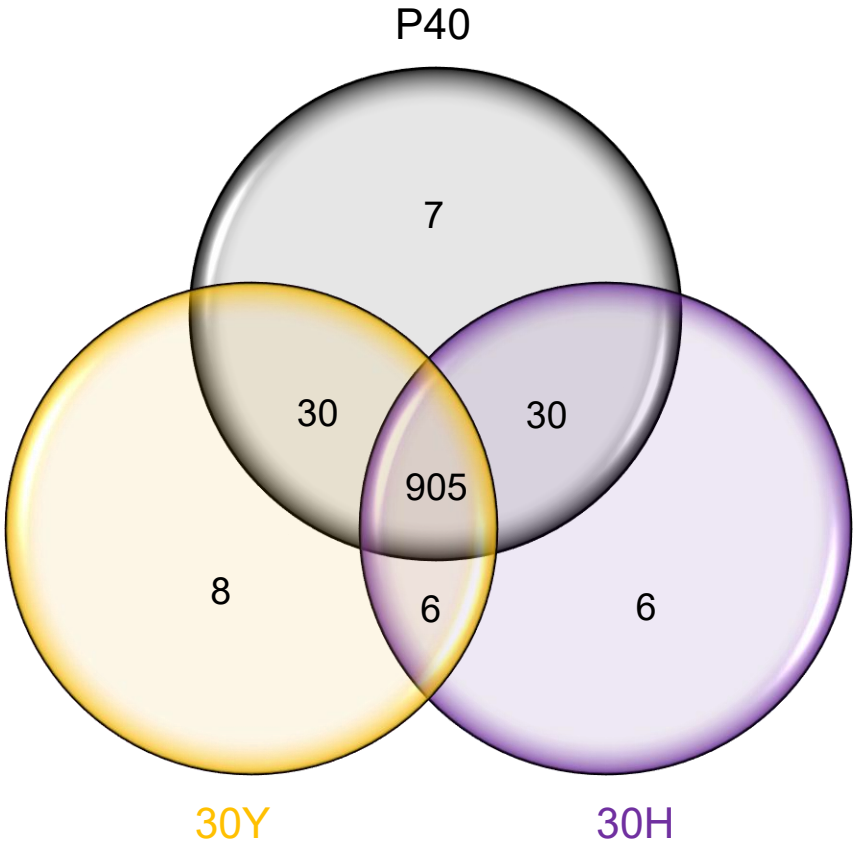

Figure 6.25 Venn diagram showing the number of proteins detected via LC-MS/MS and whether there present in cells cultured in P40, 30H and 30Y conditioned media or were exclusive to one condition.

Studying the normalised total spectrum counts (semi-quantitative indicator of protein abundance generated within Scaffold software) of proteins unique to the 30H sample revealed Tubulin alpha chain-like 3 (TUBAL3) (accession number A6NHL2) to be present in the greatest amount (4 a.u.). Of the proteins unique to cells cultured using P40-conditioned media, all were found to have a normalised total spectra value of 1.3, except for nuclear autoantigen Sp-100 (0.8) (see Table 6.3). Table 6.4 and Table 6.5 highlight the proteins that were exclusively detected in cells cultured in 30H and 30Y-conditioned media.

Table 6.3 LC-MS/MS analyses of MG63 protein expression which were only detected in cells cultured in P40 conditioned-media.

Gene name	Identified proteins	Accession number	Normalised total spectra counts (a.u.)
MT1H	Metallothionein-1H OS=Homo sapiens PE=1 SV=1	P80294	1.3
TFG	Protein TFG (Fragment) OS=Homo sapiens PE=1 SV=1	C9JJP5	1.3
SMC2	Structural maintenance of chromosomes protein 2 OS=Homo sapiens PE=1 SV=2	O95347	1.3
DDR2	Discoidin domain-containing receptor 2 OS=Homo sapiens PE=1 SV=2	Q16832	1.3
RPL35	60S ribosomal protein L35 OS=Homo sapiens PE=1 SV=1	F2Z388	1.3
SLC38A1	Sodium-coupled neutral amino acid transporter 1 OS=Homo sapiens PE=1 SV=1	F8VX04	1.3
SP100	Nuclear autoantigen Sp-100 OS=Homo sapiens PE=1 SV=3	P23497	0.8

Table 6.4 LC-MS/MS analyses of MG63 protein expression which were only detected in cells cultured in 30H conditioned-media.

Gene name	Identified proteins	Accession number	Normalised total spectra counts (a.u.)
TUBAL3	Tubulin alpha chain-like 3 OS=Homo sapiens PE=1 SV=2	A6NHL2	4
NEFM	Neurofilament medium polypeptide OS=Homo sapiens PE=1 SV=1	E7EMV2	1.5
MAP2K2	Dual specificity mitogen-activated protein kinase kinase 2 OS=Homo sapiens PE=1 SV=1	P36507	1.5
RAB5A	Ras-related protein Rab-5A OS=Homo sapiens PE=1 SV=2	P20339	1.5
ALDH1A2	Retinal dehydrogenase 2 OS=Homo sapiens PE=1 SV=1	HOYMG7	1.5
CDK5	Cyclin-dependent-like kinase 5 OS=Homo sapiens PE=1 SV=3	Q00535	0.8

Table 6.5 LC-MS/MS analyses of MG63 protein expression which were only detected in cells cultured in 30Y conditioned-media.

Gene name	Identified proteins	Accession number	Normalised total spectra counts (a.u.)
ACTBL2	Beta-actin-like protein 2 OS=Homo sapiens PE=1 SV=2	Q562R1	12.5
KRT7	Keratin, type II cytoskeletal 7 OS=Homo sapiens PE=1 SV=5	P08729	1.5
KRT14	Keratin, type I cytoskeletal 14 OS=Homo sapiens PE=1 SV=4	P02533	1.5
PRPF6	Pre-mRNA-processing factor 6 OS=Homo sapiens PE=1 SV=1	O94906	1.5
THBS1	Thrombospondin-1 OS=Homo sapiens PE=1 SV=2	P07996	1.5
FKBP1A	Peptidyl-prolyl cis-trans isomerase FKBP1A OS=Homo sapiens PE=1 SV=2	P62942	1.5
GSTM2	Glutathione S-transferase OS=Homo sapiens PE=1 SV=1	E9PHN6	0.8
ALDH7A1	Alpha-aminoadipic semialdehyde dehydrogenase (Fragment) OS=Homo sapiens PE=1 SV=1	A0A1B0GVU0	0.8

6.2.16 *In vitro* direct cell culture studies

Seeding of MG63 cells directly onto P40, 30H and 50H microspheres was also performed to evaluate cellular response in direct contact with these microsphere formulations and assess their ability to facilitate cell attachment and proliferation. Analysis of metabolic activity at day 2, revealed there was no statistically significant difference in metabolic activity between cells grown on P40 microspheres and 30H and 50H solid microspheres ($p > 0.05$). Cells grown on TCP (positive control) had significantly greater metabolic activity compared to cells grown on the solid microspheres, regardless of their formulation (*vs* P40, 30H and 50H: $p < 0.0001$) at day 2 and at day 7 (see Figure 6.26). Significantly higher metabolic activity was seen in cells cultured on P40, 30H and 50H microsphere formulations and TCP at day 7 in comparison to day 2 ($p < 0.0001$). After 7 days of direct culture, cells grown on P40 microspheres had significantly greater metabolic activity in comparison to both 30H and 50H microspheres ($p < 0.0001$). There was no significant difference in the metabolic activity of the MG63s when cultured on 30H and 50H microspheres ($p > 0.05$) (see Figure 6.26).

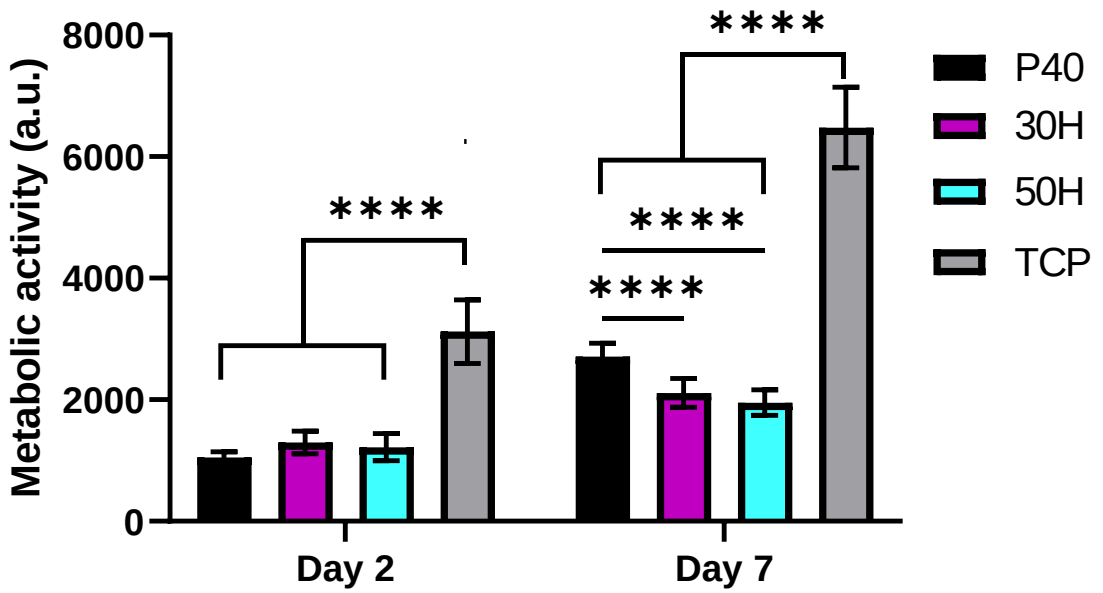

*Figure 6.26 Evaluation of cell metabolic activity in direct culture of P40, 30H and 50H solid microspheres at day 2 and day 7. **** $p < 0.0001$.*

The ALP activity after 7 days of MG63s grown directly on the microspheres and TCP was determined and normalised to the DNA concentration. Significantly higher ALP activity was recorded in cells grown on P40, 30H and 50H microspheres in comparison to those grown on the TCP control ($p < 0.0001$). No significant difference in ALP activity was detected between cells grown on P40 and the two holmium-containing microspheres ($p > 0.05$) (see Figure 6.27).

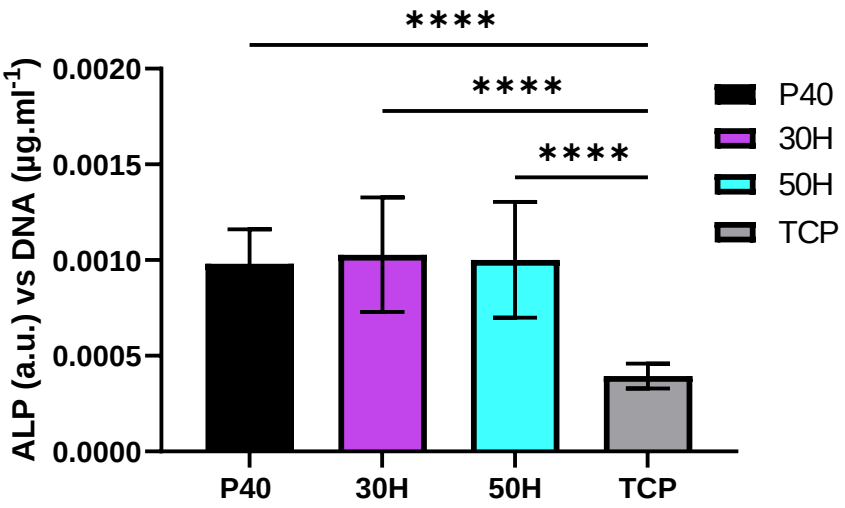

*Figure 6.27 Evaluation of ALP activity in direct culture of P40, 30H and 50H solid microspheres at day 7. **** p < 0.0001.*

MG63 cells directly cultured on microspheres were visualised using ESEM at day 7. Cells were shown to adhere onto P40, 30H and 50H microspheres and appeared to be displaying lamellipodia and filopodia projections bridging adjacent neighbouring microspheres and spreading over the microsphere surface (see Figure 6.28)

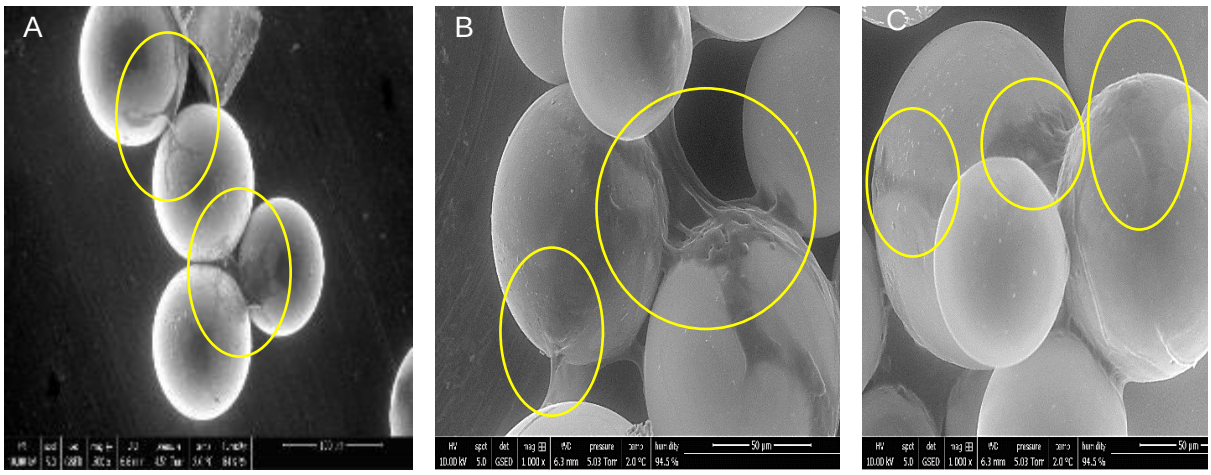

Figure 6.28 ESEM images of (A) P40 (B) 30H and (C) 50H solid microspheres after 7 days direct culture with MG63 cells. Yellow circles indicate regions of cells attachment and the formation of colonies on the microspheres surface.

6.2.17 Porous holmium P40 microspheres

Attempts were also made to produce porous holmium-containing microspheres using the flame spheroidisation process. The preceding studies involving the production of porous yttrium-containing microspheres had demonstrated the need for alterations to the conventional processing set-up and determine the methods employed when processing porous holmium-containing microspheres. A two-stage process was employed in which solid 30H microspheres were initially formed via flame spheroidisation. These microspheres (containing high Ho content) were sieved to collect microspheres in the 45 – 125 µm size range and subsequently broken down into irregular shaped particles using a pestle and mortar, mixed with 5 µm $CaCO_3$ (1:1 Ratio) and fed into the flame using a pneumatic sand blasting gun for a second round of flame spheroidisation. As seen in Figure 6.29A, a low yield of porous particles was produced at the 30H composition, with most particles appearing to be solid microspheres. EDX analysis microspheres revealed successful holmium incorporation within the porous microspheres, although there was considerable deviation in the holmium content between the porous microspheres (10.3 mol% ± 7.7) (see Figure 6.29B).

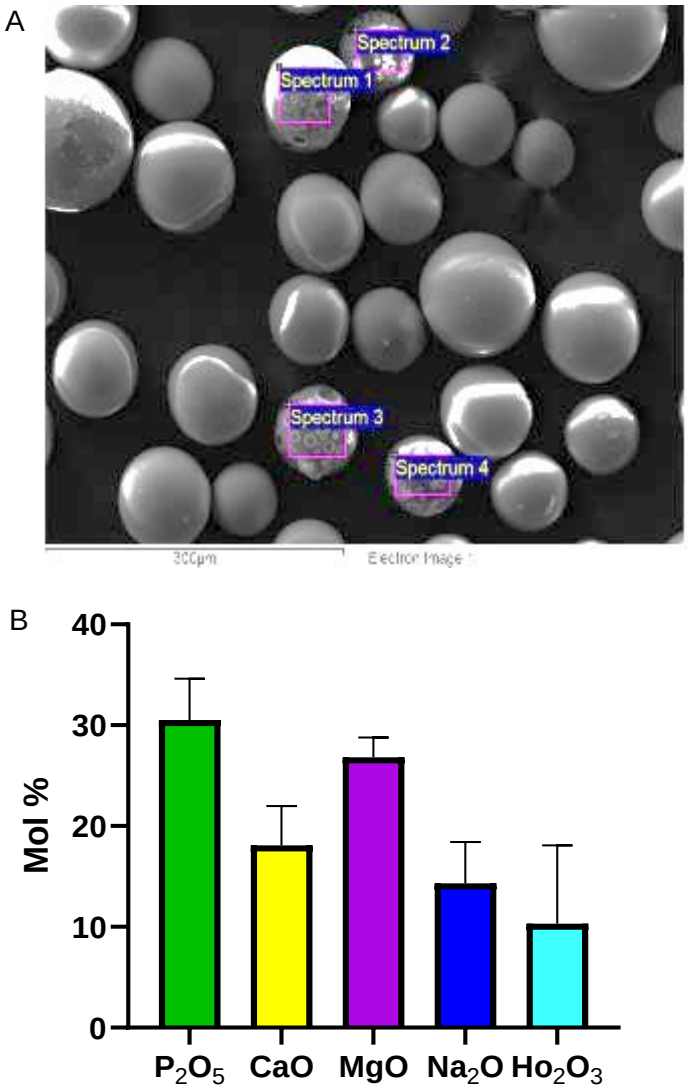

Figure 6.29 (A) SEM image of the porous 30H microspheres produced using 1:1 microsphere to $CaCO_3$ ratio and the regions analysed using EDX. (B) EDX values for the porous microspheres produced.

The same processing procedure was performed using solid microspheres of the 50H composition to investigate porous microsphere production at elevated holmium content. As seen in Figure 6.30, following the second round of flame spheroidisation with porogen addition the resulting microspheres had elevated Ho_2O_3 content (comparable to solid 50H produced via single-stage flame spheroidisation) but lacked desired porosity. These results mirrored those seen involving yttrium, where significantly increasing the holmium/yttrium resulted in the inability to produce porous microspheres using this method.

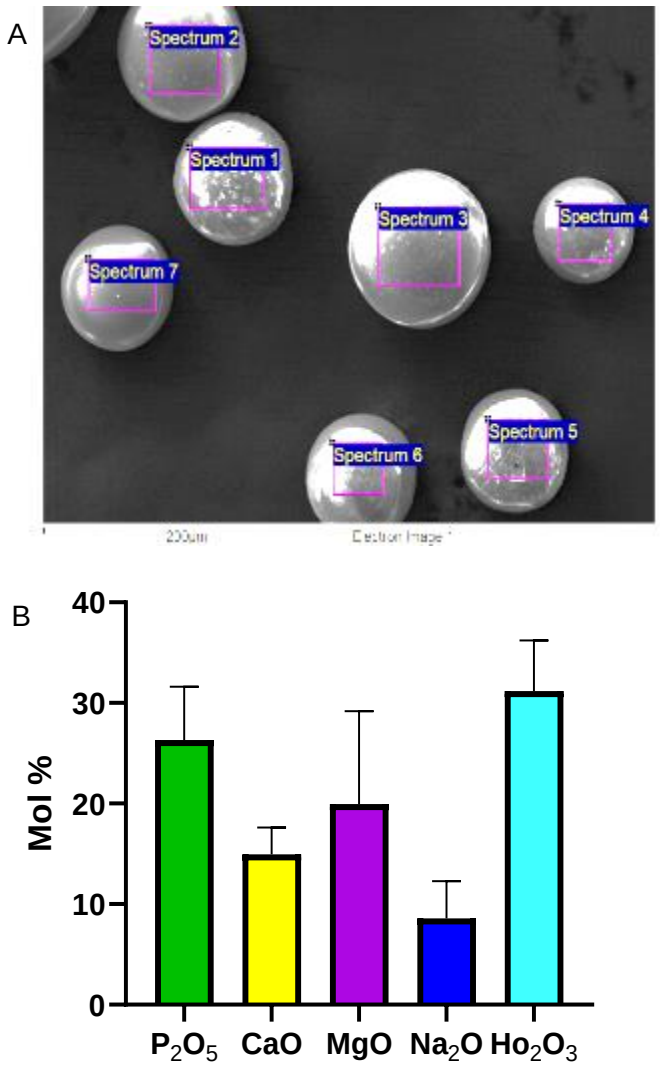

Figure 6.30 (A) SEM image of the attempted 50H porous microspheres produced using 1:1 microsphere to $CaCO_3$ ratio and the regions analysed using EDX. (B) EDX values for the microspheres analysed.

In an attempt to increase the yield of porous microspheres produced, Na_2CO_3 was used as an alternative porogen to $CaCO_3$. The same two-stage processing method was employed using the 30H composition, at a 1:1 microsphere to porogen ratio and the use of the pneumatic sand blasting gun. As seen in Figure 6.31, porous microspheres were successfully produced using Na_2CO_3 but similar to when using $CaCO_3$ the yield remained low. EDX analysis revealed holmium content within these microspheres to be 10.7 mol% ± 3.5 (see Figure 6.31B). EDX mapping of a porous 30H microsphere showed that holmium and all other elements were homogenously distributed throughout the whole of the microsphere (Figure 6.31C). These studies proved the feasibility of producing porous holmium-containing microspheres and the

suitability of Na_2CO_3 as an appropriate porogen for porous microsphere production. As was the case with porous yttrium-containing microspheres, the low amount of the final microsphere product and the low yield of porous microspheres produced meant that further characterisation was not possible.

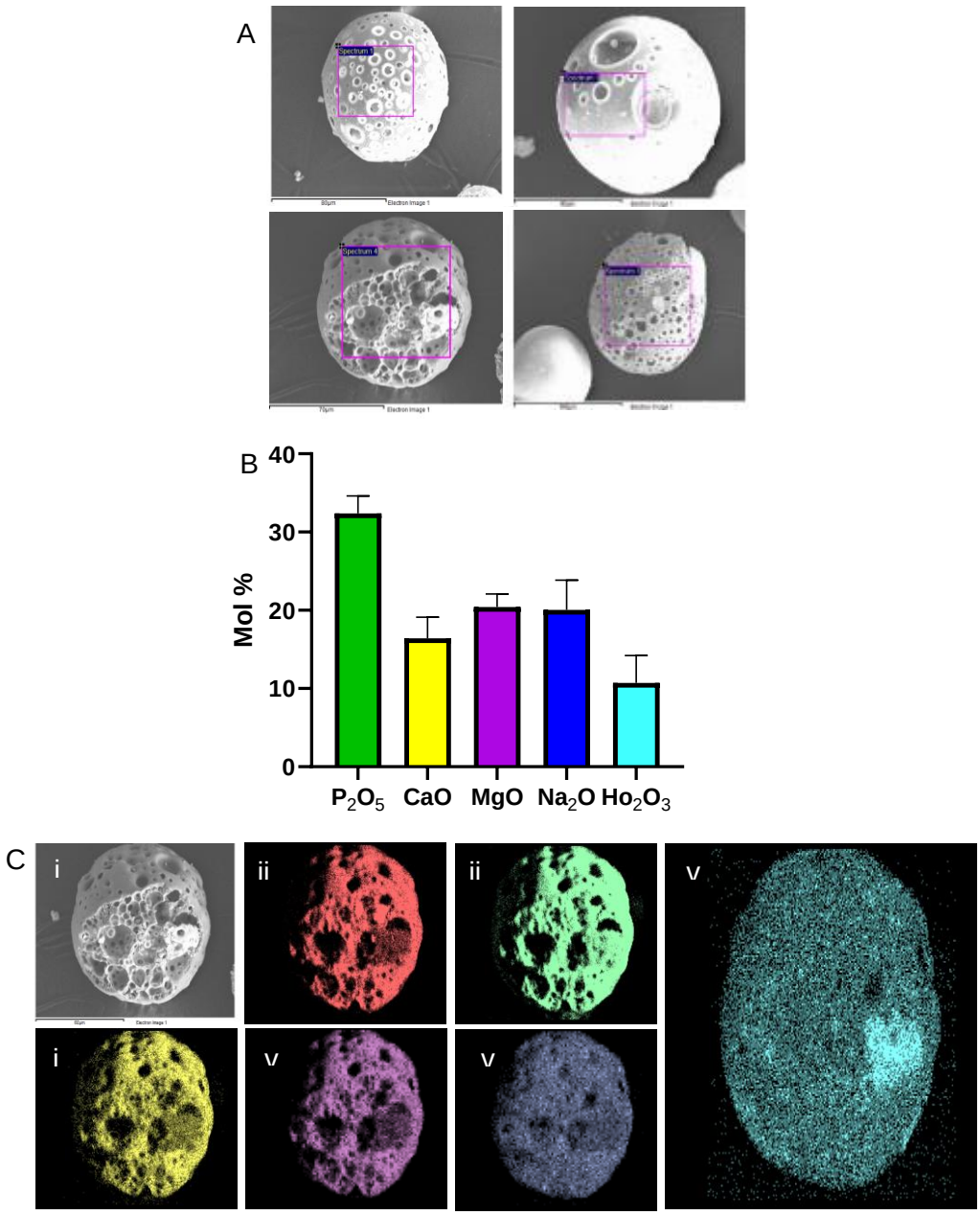

Figure 6.31 (A) SEM images of porous 30H microspheres produced using 1:1 microsphere to Na_2CO_3 ratio and the regions analysed using EDX. (B) EDX values for the porous microspheres produced. (C) EDX mapping of all elements within the microsphere. *(i) SEM image (ii) oxygen (iii) phosphorous (iv) calcium (v) magnesium (vi) sodium (vii) holmium and (viii) yttrium.*

6.2.18 Holmium and yttrium containing microspheres

The combination of holmium and yttrium oxide mixed with particles of P40 glass prior to spheroidisation was performed to incorporate both holmium and yttrium content into microspheres. Microspheres were initially processed using a 15:15:70 ratio of Ho_2O_3:Y_2O_3:glass to form microspheres with the 30HY formulation. SEM analysis confirmed that following processing and sieving a high yield of spherical microspheres were produced via the flame spheroidisation method (see Figure 6.32A). The microspheres produced displayed a smooth surface topography. EDX analysis was performed to confirm the composition of the microspheres produced. As seen in Figure 6.32B, both yttrium and holmium were successfully incorporated within the microspheres produced and in comparative amounts. The P_2O_5 content of the microspheres produced was 30.2 ± 1.7 mol%, which was comparable with the P_2O_5 content of the microspheres produced of the 30Y and 30H formulation.

EDX mapping of resin embedded 30HY microspheres was performed to establish whether any of the elements were concentrated at regions within the microspheres. The mapping showed that all the elements were homogenously distributed throughout the whole of the 30HY microspheres and did not appear to be concentrated at the surface (see Figure 6.32C).

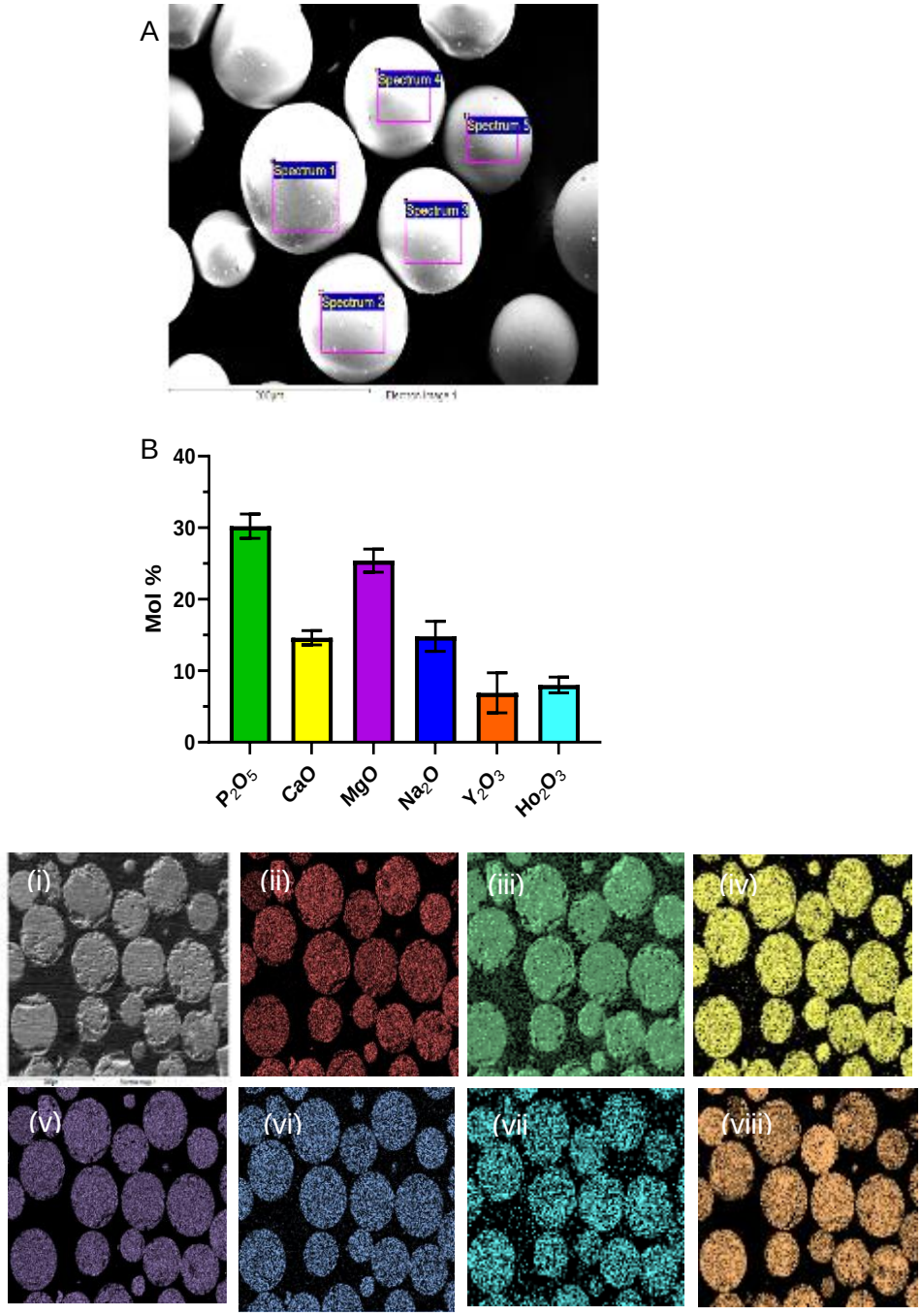

Figure 6.32 (A) SEM images of solid 30HY microspheres produced via flame spheroidisation and the regions analysed using EDX. (B) EDX values for the 30HY microspheres. (C) EDX mapping of all elements within the microsphere. *(i) SEM image (ii) oxygen (iii) phosphorous (iv) calcium (v) magnesium (vi) sodium (vii) holmium and (viii) yttrium.*

6.3 Discussion

In this chapter holmium was successfully incorporated at varying and increasing levels into phosphate-based microspheres at levels that have never been previously achieved using a novel flame spheroidisation process. As seen in Chapter 4 when using Y_2O_3, this method allowed the holmium content to be tailored, by varying the Ho_2O_3 to glass ratio prior to spheroidisation, and resulted in the formation of solid microspheres that had both equivalent and superior holmium content in comparison to the yttrium content of Therasphere™ (which was regarded as our benchmark). Regardless of the Ho_2O_3 to glass ratio used within this study, a high yield of solid microspheres with the desired morphology were able to be reproducibly processed in the 45 – 125 µm size range. When developing a material for therapeutic applications, especially when implantation *in vivo* is required, it is vital that there is consistency and reproducibility in the final product to reduce potential variability in the therapeutic efficacy.

EDX analysis revealed that progressive Ho_2O_3 addition prior to spheroidisation resulted in the formation of microspheres with increasing holmium content and a reduction in the content of all glass forming elements after processing. Increasing the holmium content within the microspheres was highly desirable for internal radiotherapy applications as this could result in a higher specific activity per microsphere. This could also facilitate the delivery of fewer microspheres to achieve the required therapeutic response and may provide more personalised treatments adjusted in activity through the number of microspheres administered [230]. Arranja *et al.* produced holmium acetylacetonate microspheres (HoAcAc-MS) via an emulsification and solvent evaporation method with substantially higher holmium content (46 wt%) in comparison to the commercially available formulation of ^{166}Ho loaded microspheres (QuiremSpheres®) (19 wt%). An activity of 47 GBq was produced following 6 hours of neutron bombardment (thermal flux 4.97×10^{16} n m^{-2} s^{-1}) of 600 mg of HoAcAc-MS, which was significantly greater than the 19 GBq achieved using equivalent QuiremSpheres [312]. The increased holmium content of the HoAcAc-MS resulted in a 2.5-fold higher radioactivity per mg of microspheres in comparison to QuiremSpheres, demonstrating the clinical benefits of increasing holmium content within microspheres. A labour intensive and time-consuming multi-step method, lasting over 7 days, was required to produce the HoAcAc-MS, whereas glass melt-quenching and holmium-microsphere production via flame spheroidisation can be performed in a single day.

The higher specific activity per microsphere can not only maximise the dose delivered to a tumour but due to holmium's inherent properties could also promote higher visibility in imaging

modalities such as SPECT, MRI and CT [313]. Bult *et al.* homogeneously dispersed high holmium content HoAcAc microspheres (45% w/w) within an agarose gel matrix and investigated the multimodality imaging characteristics in comparison to HoPLLA microspheres with a holmium content of 17% (w/w) [314]. MRI studies revealed the r2* relaxivity of the HoAcAc microspheres to be 264 ± 5.7 s^{-1} mg^{-1} ml, which was substantially higher than the r2* value for the HoPLLA microspheres of 92 ± 3.2 s^{-1} mg^{-1} ml [315]. The increased holmium content per sphere enhanced the sensitivity to MRI and allowed for the detection of 1 µg of HoAcAc microspheres in the gel. Similar results were seen with quantitative CT analysis of the microspheres within the agarose gel, with the HoAcAc microspheres having increased CT sensitivity. The increased holmium content of the HoAcAc microspheres meant that only 50 µg of microspheres was required for detection using CT. Holmium microspheres that can be visualised directly could also enable live tracking of the microspheres following the decay of radioactive ^{166}Ho. Non-invasive techniques, such as MRI and CT, can therefore be used to establish the *in vivo* fate of the microspheres injected. High holmium content that allows for the detection of microgram amounts could enable MRI guided administration of microspheres, allowing for accurate administration to tumour sites, whilst minimising radiation damage to neighbouring healthy tissues.

As was observed with the yttrium-containing microspheres, heterogeneity within holmium-containing microspheres was seen with respect to their topography. At the reduced holmium content of ~17.2% ±5.8 in the 30H microspheres, most of the microspheres were completely spherical and appeared to have a smooth topography under SEM analysis. A small proportion of the microspheres displayed a rough topography. The different topographies were very similar in appearance to those seen in the yttrium-containing 30Y microspheres in chapter 4. EDX analysis revealed that there was no significant difference in the elemental composition of the two topographically discrete 30H microspheres despite the altered appearance (see Figure 6.3).

More prominent surface features were evident on a greater proportion of the 50H microspheres. The highly ordered topographical features were almost identical to those observed on some of the 50Y microspheres. The features were not completely uniform and varied in appearance and size on the surface of individual microspheres and between microspheres (see Figure 6.5). EDX analysis revealed that microspheres with the unique topographical features (see Figure 6.5; topography 1) had a significantly increased holmium content compared to microspheres that appeared to have a smooth morphology. Analogous to the 50Y microspheres, the surface features on 50H microspheres were shown to be both indicative of holmium content within the microspheres and were shown to be localised regions

of holmium content. The central region of the highly ordered structures was found to contain the greatest amount of holmium. The grain-like surface structures, observed via SEM, which extended radially away from the central point had a slightly lower holmium content, which was still greater than the glass-rich regions between each feature (Figure 6.6). Both the appearance and composition of these features emulated those seen in the 50Y microspheres and demonstrated that both the holmium content and topography of the microspheres could be altered with progressive holmium addition. Akin to the 50Y microspheres, it appeared that holmium rich nuclei had formed followed by crystal growth, resulting in unique topographically orientated glass-ceramic microstructures. In a similar manner to the 50Y microspheres, most of the 50H microspheres appeared to display a smooth topography but at an increased magnification using SEM, submicron features became apparent (Figure 6.5).

Conventional production of glass-ceramics usually involves a two-stage heat treatment process to devitrify a glass. The first stage is a lower temperature treatment that induces a high nucleation rate (T_N), resulting in the formation of a high density of nuclei throughout the glass. This is followed by a second heat treatment at a higher temperature to promote growth of the crystals (T_G) (see Figure 6.33A) [316]. It is possible that extensive overlap of the nucleation and growth rate curves exist, and nucleation and growth could occur simultaneously during a rapid (milli-second) single-stage heat treatment/processing stage (T_{NG}) (see Figure 6.33B). These processes are sensitive to the glass composition and are temperature and time dependent [317]. The flame spheroidisation process used in this study subjected the particles to high temperatures but only for a very short period. The coalescence and subsequent chemical and physical alterations that occurred between the glass particles and the holmium oxide (or yttrium oxide) transpired over the millisecond or even nanosecond range. The point of entry and subsequent residence time of the particles was not entirely uniform resulting in heterogeneity in the final microsphere product. It may be that some particles are only exposed to temperatures that facilitate the formation of nuclei within them. The necessary temperature or time for abundant crystal growth is not achieved during the particle's trajectory and residence within the flame. This may explain why some microspheres only had small, submicron particles visible on their surface whereas large, orientated glass-ceramic microstructure were evident on a proportion of both the high content holmium and yttrium-containing microspheres.

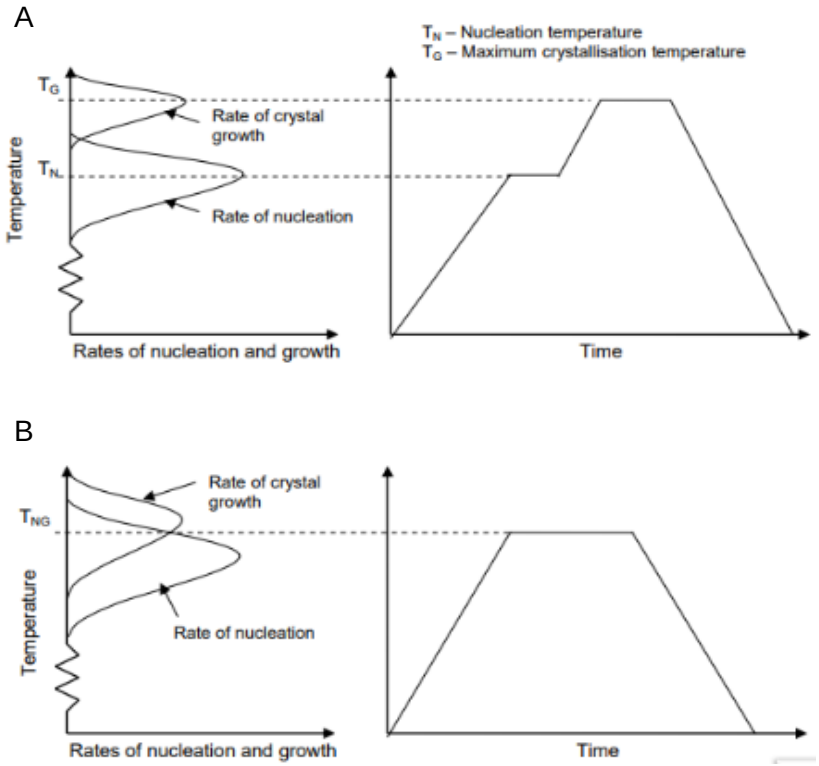

Figure 6.33 Crystallisation of a glass to form a glass-ceramic by (A) two-stage heat treatment. Negligible overlap of nucleation and growth rates. (B) A single-stage heat treatment. Temperature dependence of the nucleation and growth rates with significant overlap.

FIB-SEM analysis of 50H microspheres suggested further evidence of crystallisation with holmium addition. Distinct regions within the body of the microsphere were visible when a microsphere displaying the unique topographical features had a section of its surface ablated away using a gallium ion beam (Figure 6.8B). These regions were randomly orientated, as was seen with some of the 50Y microspheres, but no compositional information was obtained for these discrete regions. Ablation of a section of a 50H microsphere with a smooth topography revealed no distinguishable features present within the body of that specific microsphere (Figure 6.8D). Further analysis is required to establish whether there is any compositional difference between submicron features visible within the holmium-containing microspheres and how this differs at varying holmium content and between topographically distinct microspheres.

Although only a select few 50H microspheres underwent FIB-SEM analysis, there was still evidence that phase separation may be occurring within the microspheres. As seen in Figure

6.8B, physically distinct regions within a 50H microsphere were present and were similar in appearance to regions seen within certain 50Y microspheres. No elemental data was obtained from FIB-SEM analysis of the 50H microspheres, but it is hypothesised that these are likely to be holmium-rich regions embedded within the glassy matrix, like the yttrium-rich regions seen in the 50Y microspheres. The holmium-rich phase appears not to be vitrifiable and as a result crystallises following flame spheroidisation.

P40 solid microspheres were shown via XRD to retain the amorphous structure of the P40 glass particles following flame spheroidisation. The 30H composition resulted in the formation of glass-ceramic microspheres with crystalline phases detected using XRD. Crystalline phases that corresponded to both cubic Ho_2O_3 and hexagonal Ho_2O_3 were detected, as well as for $HoPO_4$ in the 30H microspheres. In the 50H microspheres, only cubic Ho_2O_3 was detected, and this mirrored the results seen in the yttrium-containing microspheres, where only cubic Y_2O_3 was detected in the 50Y microspheres. Similar crystalline structures formed at the comparable yttrium and holmium content within the solid microspheres were likely due to the fact that both Ho_2O_3 and Y_2O_3 are rare earth sesquioxides [318]. Both Ho^{3+} and Y^{3+} have identical effective ionic radius in six coordination of 0.90 Å and it is therefore unsurprising that similar crystalline structures formed upon microsphere formation [319]. A study by Wang *et al*. found that doping of yttria ceramics with Ho_2O_3 and the introduction of Ho^{3+} ions did not cause much deterioration of the thermal conductivity due to little disturbance of the lattice periodicity of Y_2O_3 due to similarity of the ions [318].

1D ^{31}P MAS-NMR spectra was unable to be obtained for the holmium-containing microspheres and provide structural information of the potential phosphate Q species present. Raman spectroscopy was performed on Ho_2O_3 and 30H and 50H microspheres to gain further structural information and to try and ascertain which phosphate species were present in the microspheres. At both 660 and 532 nm excitation the spectra were deemed to be dominated by emission rather than Raman scattering from Ho_2O_3. Since no Raman peaks from the holmium microspheres were detected, it was not possible to comment on the Q^n speciation within the microspheres, nor the specific phase of Ho_2O_3. Ho_2O_3 coverage was shown to be variable within and between microspheres at both the 30H and 50H composition. This trend was also seen for Y_2O_3 coverage within and between 30Y and 50Y microspheres. Interestingly, at both 660 and 532 nm excitation, the intensity of emissions was greater on average in 30H microspheres than in the higher holmium-containing 50H microspheres. As the feature at ~293 cm^{-1} was associated with emission rather than Raman scattering, it did not necessarily suggest that more of this unknown phase was present in the 30H microspheres, rather that the emission was quenched to a lesser extent.

In the absence of quantitative data regarding phosphate Q species present within the holmium-microspheres, it was postulated that progressive holmium addition resulted in increased depolymerisation of the glass network. The addition of modifying oxides are known to result in depolymerisation of the glass network due to the charge imbalance introduced by the additional cations and subsequent increase in NBOs [141]. Progressive Ho_2O_3 addition resulted in an increase in the theoretically calculated O/P ratio for the 30H (4.28) and 50H (5.26) compositions compared to a P40 solid microspheres (3.33). In a similar manner to the yttrium microspheres, the calculated O/P ratio suggests that each P atom within the holmium-containing microspheres would be bound to 4 O atoms, meaning that no BO shared between adjacent phosphate tetrahedra would exist. The structural similarities of Y^{3+} and Ho^{3+} ions in addition to the comparable surface features and XRD data obtained for the holmium and yttrium-containing microspheres, coupled with the low phosphate content (less than 30 mol%), resulted in the hypothesis that orthophosphate species would most likely dominate in both 30H and 50H microspheres.

Based on the assumption that orthophosphate species were likely to be exclusively present within the 30H and 50H microspheres, XPS analysis was performed to provide information on the binding energy of the constituent elements. Due to a lack of studies in the literature involving XPS and holmium, the binding energies from the high-resolution O 1s spectra from the yttrium studies in section 5.2.11 were used to help ascribe the likely bonding responsible. There was a significant decrease in the area for the peak assigned to NBO for 30H and 50H in comparison to P40 solid microspheres. Interestingly, as the holmium content increased from 30H to 50H an increase in area from 45.5% to 53.6% for NBO was observed, which was the opposite to what occurred in the 30Y to 50Y microspheres. The area associated with Ho-O-P bonding remained similar between the two holmium microsphere formulations but a decrease in the area for Ho-O-Ho bonding from 24.7% to 16.1% was observed between 30H and 50H, respectively. A possible explanation may be that preferential corner-sharing connectivity was occurring between Ho^{3+} ions and O^{2-} of $[PO_4]^{3-}$ tetrahedra. Reduced edge-sharing between Ho^{3+} ions and O^{2-} of $[PO_4]^{3-}$ could account for the decrease in peak areas associated with Ho-O-Ho bonding, since this was responsible for the formation of these bonds. In corner-sharing only one oxygen is occupied per bond with a holmium ion leaving an increased quantity of oxygen's available to participate in bonding with other elements i.e. NBO (see Figure 6.34). A study by Zhang *et al.* demonstrated that bismuth (Bi^{3+}) ions within Bi_2O_3–$NaPO_3$ glasses were involved in edge-sharing structures, whereas gallium (Ga^{3+}) ions within Ga_2O_3–$NaPO_3$ glasses participated in corner-sharing despite them both being trivalent ions. It may be that holmium and yttrium have preferential bonding connectivity's despite their physiochemical similarities. The additional peak at 529.2 eV for 50H microspheres was attributed to Ho-O bonding within

Ho_2O_3, due to similarity to Y_2O_3, and was consistent with other studies in the literature [320]. The detected Ho_2O_3 within the 50H microspheres correlated with the XRD results where an increased intensity in the detection of cubic- Ho_2O_3 was observed.

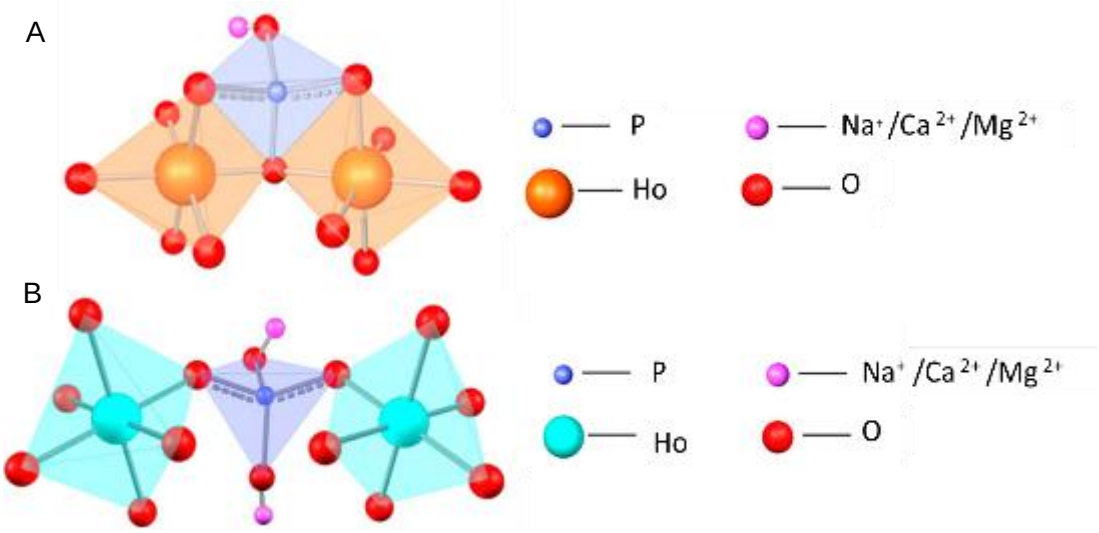

Figure 6.34 Structure depictions of holmium ions bonding to a $[PO4]^{3-}$ tetrahedron via (A) edge-sharing and (B) corner sharing connectivities. Adapted from [245].

Analogous to Y_2O_3, Ho^{3+} within crystallised cubic-Ho_2O_3 bonds with six equivalent O^{2-} atoms forming a mixture of distorted edge and corner-sharing HoO_6 octahedra [321]. In $HoPO_4$ it is bonded in an 8-coordinate geometry to eight equivalent O^{2-} atoms in the same manner to which Y^{3+} are in YPO_4 [322]. Progressive Ho_2O_3 within the microspheres in this study drastically altered the O/P ratio and increased O atoms alters the proportion and potential binding connectivity's and atomic structures that formed. Here additional studies would be required to ascertain structural information on the atomic scale and to determine the affect progressive holmium addition within the phosphate-based microspheres is having on the binding structures formed.

The ion release studies showed that P40 microspheres released all the glass forming ions at a statistically significant higher rate in comparison to holmium-containing microspheres. As was the case with yttrium content, the higher the holmium content within the microspheres the lower the release rate of all ions. It therefore may be possible to not only tailor the holmium-content for radiotherapy applications but its addition to the microspheres could be used to alter and determine the release rate of specific ions from the microspheres. This could be used to

influence cellular targets or stimulate cells to differentiate down a desired lineage [157]. 30H microspheres were shown to release holmium ions from the microspheres at a rate of 0.4 ppm/day, which was reduced to 0.2 ppm/day at the increased holmium content within 50H microspheres. The half-life of ^{166}Ho is 26.8 hours, meaning that over 90% of the radiation would be deposited within 4 days [291]. Although holmium was released at a very low rate for both microsphere compositions phosphorous ions can also be neutron activated into the β-emitter ^{32}P, which has a half-life 14.3 days [217]. Whilst ^{32}P could provide longer lasting localised radiotherapy after ^{166}Ho decay, it also increases the likelihood of irradiating non-target tissue due to increased release from the microspheres. It may be that the higher holmium containing 50H microspheres are more suitable for internal radiotherapy applications as not only do they contain more holmium, but they were also more durable and released fewer ions than the 30H microspheres. They could therefore increase the dose of radiotherapy received whilst minimising leaching of radionuclides that could irradiate non-target tissues and sites.

Bioactivity studies using SBF suggested that P40, 30H and 50H solid microspheres appeared to lack intrinsic bioactivity like that seen for 45S5 Bioglass during the period of immersion investigated. The lack of additional crystalline phases and the marginal increase in Ca:P (wt%) ratio, detected via XRD and EDX respectively, confirmed that that no apatite or alternative calcium phosphate phases had formed on the microspheres surface. Bioactivity occurs due to a specific set of surface reactions and it appears that the microspheres in this study did not release the specific ions at the required rates and provide the conditions necessary for the materials to be bioactive [323]. As seen in Figure 6.18F, holmium incorporation within the microspheres resulted in significantly reduced release rate of all the ions. A study by Delpino *et al.* investigating sol–gel-derived holmium-doped 58S bioactive glasses, with compositions $58SiO_2$–33CaO–9 P_2O_5–*x* Ho_2O_3 (*x* = 1.25, 2.5, and 5 wt.%), found that holmium addition significantly affected dissolution behaviour. The formation of Si-O-Ho covalent bonds reduced the dissolution rate but was found not to impede the bioactive behaviour of the glasses [324]. The encouraging bioactivity results from Delpino *et al.* and confirmation of cytocompatibility of the glasses via *in vitro* cell studies demonstrated the promising potential of holmium-containing glasses for brachytherapy applications. Although the 58S-holmium containing glasses in Delpino *et al.* study appeared promising, they were not processed into a practical geometry suitable for brachytherapy applications. The holmium content within the phosphate-based microspheres in this study was significantly greater than those achieved in the 58S glass composition, although they were formed from a parent glass that showed diminished bioactivity.

The indirect cell culture method confirmed the cytocompatibility of the release products from both the holmium-containing microsphere formulations. At day 2, cells treated with P40 conditioned media had a significantly greater metabolic activity compared to those treated with 30H and 50H media, whereas cells treated with SM had significantly lower metabolic activity than either of the three microsphere conditioned media. The MG63 cells treated with SM, P40, 30H and 50H conditioned media demonstrated a significant increase in metabolic activity from day 2 to day 7, which demonstrated the cytocompatibility of the conditioned media (see Figure 6.23). At day 7, apart from those cultured in SM + 5% DMSO, there was no statistically significant difference in the metabolic activity of cells cultured in the different media compositions ($p > 0.05$). Similar results were seen with the indirect studies involving 30Y and 50Y microspheres, where the dissolution products from the yttrium-containing microspheres did not have a negative effect on cell metabolic activity. The higher holmium or yttrium content within the microspheres did not reveal a statistically significant effect on the metabolic activity of the cells compared to the lower yttrium/holmium-containing microspheres after 7 days of culture. Positive cellular responses to holmium-doped bioactive glasses was also seen in a study by Zambanini *et al.* [325]. Indirect cell studies revealed that MC3T3-E1 cells exposed to conditioned media from glasses based on the 58S bioactive formulation containing 1.25 to 5 wt% Ho_2O_3 had enhanced proliferation compared to standard culture medium alone.

Analogous to the indirect yttrium studies, the ion release products from P40 solid microspheres resulted in cells with significantly increased ALP activity in comparison to both holmium-microsphere conditioned media compositions (see Figure 6.24). As seen in Figure 6.19, P40 microspheres released all ions at a significantly greater rate compared to 30H and 50H. Phosphate, calcium and magnesium ions are known to promote ALP activity in osteoblast cells and increased exposure as a result of decreased microsphere durability is likely responsible for the increased ALP response [326, 327]. The similarity between the indirect studies for the holmium and yttrium-containing microspheres is unsurprising given the comparable release rates of the ions from the microspheres with near equivalent yttrium and holmium content (see Table 6.6).

Table 6.6 Comparison of the ion release rates in milli-Q water from P40, 30Y, 50Y, 30H and 50H solid microspheres.

	P40 (ppm/day)	30Y (ppm/day)	50Y (ppm/day)	30H (ppm/day)	50H (ppm/day)
[Na]	3.47	0.93	0.35	1.02	0.58
[Mg]	2.00	0.54	0.20	0.57	0.34
[P]	8.35	2.18	0.61	2.31	1.21
[Ca]	2.41	0.90	0.58	0.99	0.68
[Y]	0.00	0.39	0.10	0.00	0.00
[Ho]	0.00	0.00	0.00	0.38	0.20

The indirect culture method revealed that cells grown in P40-conitioned media had a slightly greater (but not statistically significant) metabolic response after 7 days of culture and significantly greater ALP activity compared to cells grown in 30H or 50H-conditioned media. LC-MS/MS analyses was performed to attempt to elucidate whether changes in protein expression within the MG63 cells accounted for the detected phenotypes from the different culture conditions. For cells grown in P40-conditioned media, 60S ribosomal protein L35 (RPL35) was detected which was not expressed in cells grown in 30H or 30Y-conditioned media. RPL35 protein is a component of the large ribosomal subunit that forms the ribonucleoprotein complex responsible for the synthesis of proteins in the cell [328]. Increase in the production of proteins associated with growth and proliferation will increase metabolic activity. Conversely, dysregulation in the function or expression of proteins involved in protein synthesis is common in cancer [329]. Osteoblastic cells that can produce more proteins, such as ALP, that are associated with osteogenic differentiation and maturation could facilitate accelerated bone repair and regeneration [330].

During differentiation, osteoblasts increase their capacity for protein synthesis and secretion. Sodium-coupled neutral amino acid transporter 1 (SLC38A1) was exclusively detected in cells grown in P40-conditioned media and has a known role in the cotransport of glutamine and sodium ions [331]. A recent study found that a similar Neutral amino acid transporter B (0) (SLC1A5) was required for proficient protein synthesis in osteoblasts. SLC1A5 provided glutamine and asparagine for amino acid and protein synthesis, whilst also transporting glutamine to activate the mechanistic target of rapamycin complex 1 (mTORC1), an important regulator of both osteoblast proliferation and differentiation [332]. Additionally, multiple

myeloma cells responsible for osteolytic lesions have been found to metabolise very high amounts of glutamine and subsequent glutamine depletion has been shown to impair the differentiation of osteoprogenitor cells that form new bone tissue [333]. Increased expression of proteins, such as SLC1A5 and SLC38A1, which allow accumulation of glutamine into cells may stimulate increased osteogenic differentiation.

Another protein unique to cells cultured in P40-conditioned media was Discoidin domain-containing receptor 2 (DDR2). Studies have shown that DDR2 has an essential role in osteoblast differentiation by regulating the activity of Runx2, a master transcription factor involved in skeletal development [334]. The favourable culture conditions created by the ion release products from P40 solid microspheres appeared to increase the expression of proteins associated with osteogenic pathways in comparison to cells cultured in either 30H or 30Y-conditioned media.

Cyclin-dependent kinase 5 (CDK5) was detected exclusively in cells cultured in 30H-conditioned media. CDK5 has been identified as a suppressor of osteoblast differentiation in both murine and human osteoprogenitor cells. Conversely, downregulation of CDK5 expression has been shown to result in enhanced osteoblast-specific gene expression [335]. Holmium may have resulted in increased CDK5 expression and could be responsible for the diminished ALP activity of cells cultured in 30H and 50H conditioned media.

Future studies involving osteoprogenitor cells (i.e. mesenchymal stem cells), primary osteoblasts and osteoclasts are necessary to establish how the culture conditions induced by the microspheres affect cell phenotype since all are involved in bone remodelling and repair. The ion release products from the microspheres could stimulate the various cell types in different ways leading to up or down regulation of specific proteins. Proteomic profiling is a powerful tool to identify and quantify the altered levels of proteins within cells and can reveal detailed information about cells in healthy and diseased states. Identifying differentially expressed proteins, and their functions, interactions, and structural changes can provide detailed information on disease progression as well as treatment effects [336]. Identification of specific proteins that are indicated in certain disease states could also serve as therapeutic and diagnostic markers for bone cancers [337].

Direct cell culture studies demonstrated that 30H and 50H microspheres were able to facilitate cell attachment and proliferation over the period of study. A statistically significant increase in metabolic activity from day 2 to 7 was seen for cells cultured on P40, 30H and 50H microspheres. As was the case with the indirect studies, no significant difference was detected in metabolic activity levels at both days regardless of which holmium-microsphere formulation

the cells were exposed to. The highly durable nature of the holmium microspheres when in an aqueous environment meant that there were minimal changes to the integrity of the microspheres surface and a stable pH of the local microenvironment (see Figure 6.19 and Figure 6.20). This facilitated cell adhesion and subsequent proliferation during culture. ESEM images at day 7 (see Figure 6.28) confirmed that the MG63 cells had attached to the surface of P40, 30H and 50H microspheres and displayed cellular projections that bridged between adjacent microspheres. Although holmium-containing microspheres of various materials have been formulated for internal radiotherapy applications, based on literature searches the current study appears to be the first to demonstrate microspheres containing high levels of holmium content that can also facilitate direct cell growth and proliferation of human osteoblast-like cells. The microspheres are therefore promising biomaterials for both internal radiotherapy applications and for promoting bone repair and regeneration at damaged osseous tissue.

This work demonstrated the successful production of porous holmium-containing microspheres. This was achieved using a two-stage processing method with porosity induced using both $CaCO_3$ and Na_2CO_3 as a porogen. Further optimisation of the process is needed to increase the yield of porous microspheres produced to allow for further characterisation. It is hypothesised that a high holmium content may not be conducive for porous microsphere formation due to increased viscosity of the particles within the flame, thereby preventing gas entrapment and release. Porosity can enable the loading of the microspheres with therapeutic cargo to facilitate their use for orthobiological applications. Biological compounds released from the microspheres in a site specific manner could promote new and more rapid tissue growth at injured or diseased sites [338]. Additionally, pores present cells with a high surface area and a niche environment for growth and proliferation. Porous materials also more closely resemble the native 3D conformation of bone tissue which can increase osteogenic differentiation and influence cell fate [339]. Furthermore, a porous environment may favour the capture and utilisation of cell secreted factors which could further influence cell phenotype [340].

Currently, research has predominantly focused on biomaterials that contain only a single radioactive element that can be used to deliver *in situ* radiation to cancerous tissue. In this work, preliminary studies showed that the flame spheroidisation process can produce solid microspheres that contain multiple elements that can become radionuclides, following neutron activation, which would be capable of delivering therapeutic ionising radiation (see Figure 6.32). The various radionuclides could simultaneously irradiate the target tissue and the

differences in half-lives and emission energies could be utilised to optimise the radiation delivered to the tumour, dependent on it its size and location [207].

7 Conclusions and future work

7.1 Conclusions

The purpose of these studies was to develop and characterise phosphate-based glass microspheres tailored to form part of a treatment strategy for bone repair and regeneration to damaged tissue following devastation due to bone cancer and it's associated treatments. Initially, solid (SMS) and porous microspheres (PMS) were produced from four quaternary phosphate-based glasses (PBGs), in the series $xP_2O_5{\cdot}(56\text{-}x)CaO{\cdot}24MgO{\cdot}20Na_2O$ (mol%), where x is 40, 35, 32.5 or 30, via a flame spheroidisation process. PBGs were chosen for this study as they can be formulated to be compositionally similar to the inorganic component of bone and can be tailored to alter their degradation and release of therapeutic ions.

Microsphere porosity was desirable as it increased surface area which allowed for greater cell attachment, increased degradation, and release of therapeutic ions as well encapsulation of bioactive compounds. The facile production of high yields of highly porous microspheres with interconnected internal and superficial porosity was successfully achieved for each formulation. The use of $CaCO_3$ for PMS manufacture altered the chemical composition of the microspheres compared to the starting glass and increased network depolymerisation. Alterations to the microsphere formulations and geometry enabled the ability to tailor the ortho and pyrophosphate species content in the final product.

Tailoring the PMS formulation through increases in ortho and pyrophosphate species was shown to significantly reduce the ion release rates from the PMS. The P32.5 and P30 PMS containing a high proportion of ortho and pyrophosphate species demonstrated favourable bioactivity responses despite the reduced ion release rates. The localised release of cations and anionic ortho and pyrophosphate species from the PMS represent a promising resource and strategy for bone repair and regeneration. The *in vitro* cell culture studies confirmed the cytocompatibility of all four PMS formulations investigated and showed that they provided favourable surfaces to facilitate cell adhesion and proliferation. The P30 PMS containing ~65% pyro and ~35% ortho phosphate content is suggested to be highly suited for musculoskeletal repair, especially for orthobiologic applications owing to its highly porous morphology.

A frontline chemotherapeutic drug, Doxorubicin (DOX), was successfully loaded and released from P40 and P30 microspheres. The localised delivery of chemotherapeutics could improve their efficacy and reduce adverse effects associated with their systemic administration when used in bone cancer treatment. P40 PMS had a greater encapsulation efficiency than P30

which was attributed to increased porosity and improved electrostatic interactions with the positively charged amino group of DOX at physiological pH. P40 PMS also released a significantly greater amount of DOX over a 48-hour period. Both PMS formulations release more DOX at pH 5, which was representative of the tumour microenvironment, than at physiological pH of 7.4. A pH-responsive DOX release within tumour tissue could selectively kill cancer cells, whilst reducing DOX delivery to healthy cells within normal physiological pH environments.

Uniform, solid yttrium-containing phosphate-based microspheres were also produced to potentially deliver internal radiotherapy for the treatment of bone cancers. A novel processing method was established that allowed the yttrium content to be tailored, by varying the Y_2O_3 to glass ratio, which resulted in the formation of microspheres that had both equivalent and superior yttrium content in comparison to clinically available aluminosilicate glass microspheres (Therasphere^{TM}) used for internal radiotherapy applications. The glass-ceramic microspheres produced had unique topographical features that were indicative of yttrium-content and using elemental analysis were shown to be localised yttrium-rich regions. Structural analysis revealed that the progressive addition of yttrium within the microspheres caused depolymerisation of the glass network and the formation of orthophosphate species.

Indirect *in vitro* cell studies using osteoblast-like MG63 cells demonstrated that the release products from the 30Y (15 mol% Y_2O_3 content) and 50Y (39 mol% Y_2O_3 content) microsphere formulations were cytocompatible. No statistically significant difference was detected in the metabolic and ALP activity of the cells when cultured in the 30Y and 50Y-conditioned media after 7 days. Similar results were seen when the MG63 cells were seeded directly onto the 30Y and 50Y microspheres, with no statistically significant difference in metabolic and ALP activity detected between formulations. Cells cultured on the yttrium-containing microspheres had significantly increased ALP response compared to cells cultured on tissue culture plastic suggesting they were a more favourable surface for influencing osteoblast cell differentiation. ESEM images after 7 days of direct culture revealed that cellular projections were bridging adjacent neighbouring microspheres and spread over the microsphere surfaces.

Holmium was successfully incorporated at varying and increasing levels into phosphate-based microspheres at levels that have never previously been achieved using a novel flame spheroidisation process. The radionuclide holmium-166 (^{166}Ho) is comparable to the radionuclide yttrium-90 (^{90}Y) as it emits β-radiation and can be used to deliver tumoricidal doses of radiation over a similar tissue penetration range. However, a key benefit of ^{166}Ho is its inherent properties and ability to concurrently emit γ-radiation which could lead to visualisation using clinical imaging techniques (such as SPECT and MRI). The incorporation

of holmium within the microspheres could facilitate a theranostic approach by providing diagnostic information whilst simultaneously delivering a therapeutic dose of radiation. Increased holmium could also result in higher specific activity per microsphere that could maximise the dose delivered to a tumour whilst also promoting higher visibility in imaging modalities.

The glass-ceramic solid holmium-containing microspheres produced had comparable and elevated levels of holmium in comparison the yttrium content of Therasphere™. Holmium incorporation resulted in increased durability of the microspheres when in an aqueous environment and significantly reduced the release of all ions. The process employed to produce the holmium microspheres therefore allows the holmium content and the release rate of specific ions from the microspheres to be tailored to optimise their therapeutic potential.

In vitro cell culture studies revealed the microspheres to be cytocompatible with no significant difference in cell metabolic and ALP activity between formulations in both indirect and direct studies after 7 days. The current study appears to be the first to demonstrate microspheres containing high levels of holmium content that can also facilitate direct cell growth and proliferation of human osteoblast-like cells. The microspheres are therefore promising biomaterials for both internal radiotherapy applications and for promoting bone repair and regeneration at damaged sites.

7.2 Future work

Proposals for future work to build on the knowledge gained within this study and to address the various challenges encountered and are discussed below.

Increasing the holmium and yttrium content incorporated within the phosphate-based microspheres warrants further investigation. In the current studies, a 50:50 ratio of P40 glass particles to Y_2O_3/Ho_2Ho_3 was used to produce microspheres with the greatest levels of yttrium/holmium. This was so the final microspheres contained a P_2O_5 content of ~30 mol%, which had been shown to have beneficial bioactivity and cellular responses when using phosphate glass microspheres, and that the microspheres may retain some of the beneficial features from their parent P40 glass, such as release of therapeutic ions. Varying yttrium/holmium content resulted in the formation of topographically distinct microspheres and the detection of different crystalline phases via XRD. Further increases may alter the proportion of certain microspheres produced and lead to the formation of new topographical features that would require further observational and elemental analysis (ideally utilising HE-XRD and Neutron Diffraction at ISIS or Diamond). Alterations to the topography of the

microspheres may also result in changes to measurable cellular responses, such as adhesion and differentiation, which could be detected in future cell studies.

Alternative glass formulations could be utilised to deliver specific ions and used to adjust the amount and rate of ions delivered from the microspheres following their degradation *in vivo.* When investigating for radiotherapy applications careful consideration to formulation development is necessary to produce microspheres with nuclear properties that deliver radiotherapy over a suitable timeframe.

Studies investigating mesenchymal stem cells that can undergo osteogenic differentiation are needed to determine whether the PBG and yttrium/holmium-doped microspheres are osteoinductive in addition to being osteoconductive. Microspheres that have osteoinductive properties could recruit and stimulate immature cells down the osteogenic lineage and improve the bone healing process at damage tissue. *In vitro* studies involving other cells involved in the remodelling process, such as osteoclasts, may also be of interest.

Future work may also look at incorporating different and multiple elements that can either be activated into radionuclides capable of delivering tumorical radiation or as a contrast agent to improve visualisation in clinical imaging. Elements, such as samarium and rhenium, which have radionuclides that are currently used in internal radiotherapy are encouraging candidates for further study. Elemental, structural and cell studies will be required to ascertain their suitable for the intended application.

Neutron activation analysis is required to empirically determine the amount of radiation the specific microsphere formulations could deliver. This information is vital to establish the dose able to be delivered from a known quantity of microspheres. In the case of holmium, studies involving imaging modalities, such as SPECT, MRI and CT, are needed to establish the visibility of the microsphere and how this may affect the administration and monitoring of the microspheres *in vivo*.

Further optimisation is required to develop an efficient, inexpensive and scalable process to produce yttrium and holmium-containing porous phosphate-based microspheres. The current study demonstrated the potential of both $CaCO_3$ and Na_2CO_3 as porogen's to induce porosity and alternative porogen compounds could be investigated further. An appropriate methodology would be needed to load the microspheres with therapeutic cargo for orthobiological applications or for improving bone cancer treatment.

9 References

1. Hossain, K.M.Z., U. Patel, A.R. Kennedy, L. Macri-Pellizzeri, V. Sottile, D.M. Grant, B.E. Scammell, and I. Ahmed, *Porous calcium phosphate glass microspheres for orthobiologic applications.* Acta Biomater, 2018. **72**: p. 396-406.
2. Ahmad, S.S., M.A. Reinius, H.M. Hatcher, and T.V. Ajithkumar, *Anticancer chemotherapy in teenagers and young adults: managing long term side effects.* BMJ, 2016. **354**: p. i4567.
3. UK, C.R., *Bone Sarcoma Incidence.* 2022.
4. Khalf, A., *Ferroelectric Glass-Ceramic Systems for Energy Storage Applications*. 2020.
5. Saunders, M. and S. Truesdell, *Bone remodeling platforms: Understanding the need for multicellular lab-on-a-chip systems and predictive agent-based models.* Mathematical biosciences and engineering: MBE, 2019. **17**: p. 1233-1252.
6. Lomachuk, Y., D. Maltsev, N. Mosyagin, L. Skripnikov, R. Bogdanov, and A. Titov, *Which oxidation state of uranium and thorium as point defects in xenotime is favorable?* 2019.
7. Milborne, B.A., Abul; Layfield, Rob; Thompson, Alexander; Ahmed, Ifty *The Use of Biomaterials in Internal Radiation Therapy.* Recent Progress in Materials, 2020. **2**(2).
8. Senes-Lopes, T., J. López, V. Amaral, J. Brandão-Neto, A. Rezende, J. Luz, Z. Guterres, and M. Almeida, *Genotoxicity of Turnera subulata and Spondias mombin × Spondias tuberosa Extracts from Brazilian Caatinga Biome.* Journal of Medicinal Food, 2018. **21**.
9. Jiang, Z.-H. and Q.-Y. Zhang, *The structure of glass: A phase equilibrium diagram approach.* Progress in Materials Science, 2014. **61**: p. 144-215.
10. Gebauer, D., M. Kellermeier, J.D. Gale, L. Bergström, and H. Cölfen, *Pre-nucleation clusters as solute precursors in crystallisation.* Chemical Society Reviews, 2014. **43**(7): p. 2348-2371.
11. Clezardin, P., *Mechanisms of action of bisphosphonates in oncology: a scientific concept evolving from antiresorptive to anticancer activities.* Bonekey Rep, 2013. **2**: p. 267.
12. Zimmermann, E.A., E. Schaible, B. Gludovatz, F.N. Schmidt, C. Riedel, M. Krause, E. Vettorazzi, C. Acevedo, M. Hahn, K. Püschel, S. Tang, M. Amling, R.O. Ritchie, and B. Busse, *Intrinsic mechanical behavior of femoral cortical bone in young, osteoporotic and bisphosphonate-treated individuals in low- and high energy fracture conditions.* Scientific Reports, 2016. **6**(1): p. 21072.
13. Islam, M.T., L. Macri-Pellizzeri, K.M.Z. Hossain, V. Sottile, and I. Ahmed, *Effect of varying the Mg with Ca content in highly porous phosphate-based glass microspheres.* Materials Science and Engineering: C, 2021. **120**: p. 111668.
14. Lawrence, T.S., A.W. Blackstock, and C. McGinn, *The mechanism of action of radiosensitization of conventional chemotherapeutic agents.* Semin Radiat Oncol, 2003. **13**(1): p. 13-21.
15. Gdowski, A.S., A. Ranjan, and J.K. Vishwanatha, *Current concepts in bone metastasis, contemporary therapeutic strategies and ongoing clinical trials.* J Exp Clin Cancer Res, 2017. **36**(1): p. 108.

16. Putilov, L.P., A.N. Varaksin, and V.I. Tsidilkovski, *Defect formation and water incorporation in Y2O3.* Journal of Physics and Chemistry of Solids, 2011. **72**(9): p. 1090-1095.
17. Eyre, R., R.G. Feltbower, P.W. James, K. Blakey, E. Mubwandarikwa, D. Forman, P.A. McKinney, M.S. Pearce, and R.J. McNally, *The epidemiology of bone cancer in 0 - 39 year olds in northern England, 1981 - 2002.* BMC Cancer, 2010. **10**: p. 357.
18. Kakhki, V.R., K. Anvari, R. Sadeghi, A.S. Mahmoudian, and M. Torabian-Kakhki, *Pattern and distribution of bone metastases in common malignant tumors.* Nucl Med Rev Cent East Eur, 2013. **16**(2): p. 66-9.
19. Habibovic, P. and J.E. Barralet, *Bioinorganics and biomaterials: Bone repair.* Acta Biomaterialia, 2011. **7**(8): p. 3013-3026.
20. Lu, J., H. Yu, and C. Chen, *Biological properties of calcium phosphate biomaterials for bone repair: a review.* RSC Advances, 2018. **8**(4): p. 2015-2033.
21. Hou, X., L. Zhang, Z. Zhou, X. Luo, T. Wang, X. Zhao, B. Lu, F. Chen, and L. Zheng, *Calcium Phosphate-Based Biomaterials for Bone Repair.* J Funct Biomater, 2022. **13**(4).
22. Tang, G., Z. Liu, Y. Liu, J. Yu, X. Wang, Z. Tan, and X. Ye, *Recent Trends in the Development of Bone Regenerative Biomaterials.* Frontiers in Cell and Developmental Biology, 2021. **9**.
23. Hasan, M.S., I. Ahmed, A.J. Parsons, G.S. Walker, and C.A. Scotchford, *Material characterisation and cytocompatibility assessment of quinternary phosphate glasses.* J Mater Sci Mater Med, 2012. **23**(10): p. 2531-41.
24. Brauer, D.S., *Phosphate Glasses*, in *Bio-Glasses*, J.R. Jones, Editor. 2012. p. 45-64.
25. Isakoff, M.S., S.S. Bielack, P. Meltzer, and R. Gorlick, *Osteosarcoma: Current Treatment and a Collaborative Pathway to Success.* J Clin Oncol, 2015. **33**(27): p. 3029-35.
26. Senapati, S., A.K. Mahanta, S. Kumar, and P. Maiti, *Controlled drug delivery vehicles for cancer treatment and their performance.* Signal Transduct Target Ther, 2018. **3**: p. 7.
27. Johnstone, C. and S.T. Lutz, *External beam radiotherapy and bone metastases.* Annals of Palliative Medicine, 2014. **3**(2): p. 114-122.
28. Shirato, H., Q.-T. Le, K. Kobashi, A. Prayongrat, S. Takao, S. Shimizu, A. Giaccia, L. Xing, and K. Umegaki, *Selection of external beam radiotherapy approaches for precise and accurate cancer treatment.* Journal of Radiation Research, 2018. **59**(suppl_1): p. i2-i10.
29. Nuzulia, N., T. Islam, A. Saputra, T. Sudiro, G. Timuda, T. Mart, Y. Sari, and I. Ahmed, *Developing Highly Porous Glass Microspheres via a Single-Stage Flame Spheroidisation Process.* Journal of Physics: Conference Series, 2022. **2243**: p. 012005.
30. Qi, F., J. Wu, H. Li, and G. Ma, *Recent research and development of PLGA/PLA microspheres/nanoparticles: A review in scientific and industrial aspects.* Frontiers of Chemical Science and Engineering, 2019. **13**(1): p. 14-27.
31. Robling, A.G., A.B. Castillo, and C.H. Turner, *Biomechanical and molecular regulation of bone remodeling.* Annu Rev Biomed Eng, 2006. **8**: p. 455-98.
32. Downey, P.A. and M.I. Siegel, *Bone Biology and the Clinical Implications for Osteoporosis.* Physical Therapy, 2006. **86**(1): p. 77-91.

33. Alford, A.I., K.M. Kozloff, and K.D. Hankenson, *Extracellular matrix networks in bone remodeling.* Int J Biochem Cell Biol, 2015. **65**: p. 20-31.
34. Hubmacher, D. and S.S. Apte, *The biology of the extracellular matrix: novel insights.* Curr Opin Rheumatol, 2013. **25**(1): p. 65-70.
35. Morgan, E.F., G.U. Unnikrisnan, and A.I. Hussein, *Bone Mechanical Properties in Healthy and Diseased States.* Annual Review of Biomedical Engineering, 2018. **20**(1): p. 119-143.
36. Durfee, R.A., M. Mohammed, and H.H. Luu, *Review of Osteosarcoma and Current Management.* Rheumatol Ther, 2016. **3**(2): p. 221-243.
37. Arndt, C.A., P.S. Rose, A.L. Folpe, and N.N. Laack, *Common musculoskeletal tumors of childhood and adolescence.* Mayo Clin Proc, 2012. **87**(5): p. 475-87.
38. Misaghi, A., A. Goldin, M. Awad, and A.A. Kulidjian, *Osteosarcoma: a comprehensive review.* SICOT J, 2018. **4**: p. 12.
39. Ozaki, T., *Diagnosis and treatment of Ewing sarcoma of the bone: a review article.* J Orthop Sci, 2015. **20**(2): p. 250-63.
40. Macedo, F., K. Ladeira, F. Pinho, N. Saraiva, N. Bonito, L. Pinto, and F. Goncalves, *Bone Metastases: An Overview.* Oncol Rev, 2017. **11**(1): p. 321.
41. Manabe, J., N. Kawaguchi, S. Matsumoto, and T. Tanizawa, *Surgical treatment of bone metastasis: indications and outcomes.* Int J Clin Oncol, 2005. **10**(2): p. 103-11.
42. Nayir, E., *Pathogenesis of bone metastasis.* Journal of Oncological Science, 2016. **1**: p. 13-16.
43. D'Oronzo, S., R. Coleman, J. Brown, and F. Silvestris, *Metastatic bone disease: Pathogenesis and therapeutic options: Up-date on bone metastasis management.* J Bone Oncol, 2019. **15**: p. 004-4.
44. Ribatti, D., G. Mangialardi, and A. Vacca, *Stephen Paget and the 'seed and soil' theory of metastatic dissemination.* Clin Exp Med, 2006. **6**(4): p. 145-9.
45. Demirkan, B., *The Roles of Epithelial-to-Mesenchymal Transition (EMT) and Mesenchymal-to-Epithelial Transition (MET) in Breast Cancer Bone Metastasis: Potential Targets for Prevention and Treatment.* J Clin Med, 2013. **2**(4): p. 264-82.
46. Ren, G., M. Esposito, and Y. Kang, *Bone metastasis and the metastatic niche.* J Mol Med (Berl), 2015. **93**(11): p. 1203-12.
47. Kan, C., G. Vargas, F.L. Pape, and P. Clezardin, *Cancer Cell Colonisation in the Bone Microenvironment.* Int J Mol Sci, 2016. **17**(10).
48. Ottewell, P.D., *The role of osteoblasts in bone metastasis.* J Bone Oncol, 2016. **5**(3): p. 124-127.
49. David Roodman, G. and R. Silbermann, *Mechanisms of osteolytic and osteoblastic skeletal lesions.* Bonekey Rep, 2015. **4**: p. 753.
50. Sousa, S. and P. Clezardin, *Bone-Targeted Therapies in Cancer-Induced Bone Disease.* Calcif Tissue Int, 2018. **102**(2): p. 227-250.
51. Saad, F., A. Lipton, R. Cook, Y.M. Chen, M. Smith, and R. Coleman, *Pathologic fractures correlate with reduced survival in patients with malignant bone disease.* Cancer, 2007. **110**(8): p. 1860-7.
52. Lin, S.C., Y.C. Lee, G. Yu, C.J. Cheng, X. Zhou, K. Chu, M. Murshed, N.T. Le, L. Baseler, J.I. Abe, K. Fujiwara, B. deCrombrugghe, C.J. Logothetis, G.E. Gallick, L.Y. Yu-Lee, S.N. Maity, and S.H. Lin, *Endothelial-to-Osteoblast Conversion Generates Osteoblastic Metastasis of Prostate Cancer.* Dev Cell, 2017. **41**(5): p. 467-480 e3.

53. Gutowski, C.J., A. Basu-Mallick, and J.A. Abraham, *Management of Bone Sarcoma.* Surg Clin North Am, 2016. **96**(5): p. 1077-106.
54. Chugh, R., *Experimental therapies and clinical trials in bone sarcoma.* J Natl Compr Canc Netw, 2010. **8**(6): p. 715-25.
55. Kundu, Z.S., V. Gupta, S.S. Sangwan, and P. Rana, *Curettage of benign bone tumors and tumor like lesions: A retrospective analysis.* Indian J Orthop, 2013. **47**(3): p. 295-301.
56. Wu, P.K., C.F. Chen, C.M. Chen, S.W. Tsai, Y.C. Cheng, M.C. Chang, and W.M. Chen, *Grafting for bone defects after curettage of benign bone tumor - Analysis of factors influencing the bone healing.* J Chin Med Assoc, 2018. **81**(7): p. 643-648.
57. Andreou, D., J. Hardes, G. Gosheger, M.P. Henrichs, M. Nottrott, and A. Streitburger, *[Interdisciplinary diagnostic and treatment of bone sarcomas of the extremities and trunk].* Handchir Mikrochir Plast Chir, 2015. **47**(2): p. 90-9.
58. Matsubara, H. and H. Tsuchiya, *Treatment of bone tumor using external fixator.* Journal of Orthopaedic Science, 2019. **24**(1): p. 1-8.
59. O'Kane, G.M., K.A. Cadoo, E.M. Walsh, R. Emerson, P. Dervan, C. O'Keane, B. Hurson, G. O'Toole, S. Dudeney, E. Kavanagh, S. Eustace, and D.N. Carney, *Perioperative chemotherapy in the treatment of osteosarcoma: a 26-year single institution review.* Clin Sarcoma Res, 2015. **5**: p. 17.
60. Ferrari, S. and M. Serra, *An update on chemotherapy for osteosarcoma.* Expert Opin Pharmacother, 2015. **16**(18): p. 2727-36.
61. Kirkinis, M.N., C.J. Lyne, M.D. Wilson, and P.F. Choong, *Metastatic bone disease: A review of survival, prognostic factors and outcomes following surgical treatment of the appendicular skeleton.* Eur J Surg Oncol, 2016. **42**(12): p. 1787-1797.
62. von Moos, R., L. Costa, C.I. Ripamonti, D. Niepel, and D. Santini, *Improving quality of life in patients with advanced cancer: Targeting metastatic bone pain.* Eur J Cancer, 2017. **71**: p. 80-94.
63. Soeharno, H., L. Povegliano, and P.F. Choong, *Multimodal Treatment of Bone Metastasis-A Surgical Perspective.* Front Endocrinol (Lausanne), 2018. **9**: p. 518.
64. Bigi, A. and E. Boanini, *Calcium Phosphates as Delivery Systems for Bisphosphonates.* J Funct Biomater, 2018. **9**(1).
65. Cole, L.E., T. Vargo-Gogola, and R.K. Roeder, *Targeted delivery to bone and mineral deposits using bisphosphonate ligands.* Adv Drug Deliv Rev, 2016. **99**(Pt A): p. 12-27.
66. Cattalini, J.P., A.R. Boccaccini, S. Lucangioli, and V. Mourino, *Bisphosphonate-based strategies for bone tissue engineering and orthopedic implants.* Tissue Eng Part B Rev, 2012. **18**(5): p. 323-40.
67. Ozben, H., L. Eralp, G. Baysal, A. Cort, N. Sarkalkan, and T. Ozben, *Cisplatin loaded PMMA: mechanical properties, surface analysis and effects on Saos-2 cell culture.* Acta Orthop Traumatol Turc, 2013. **47**(3): p. 184-92.
68. Hochdorffer, K., K. Abu Ajaj, C. Schafer-Obodozie, and F. Kratz, *Development of novel bisphosphonate prodrugs of doxorubicin for targeting bone metastases that are cleaved pH dependently or by cathepsin B: synthesis, cleavage properties, and binding properties to hydroxyapatite as well as bone matrix.* J Med Chem, 2012. **55**(17): p. 7502-15.

69. Schroeder, A., D.A. Heller, M.M. Winslow, J.E. Dahlman, G.W. Pratt, R. Langer, T. Jacks, and D.G. Anderson, *Treating metastatic cancer with nanotechnology.* Nat Rev Cancer, 2011. **12**(1): p. 39-50.
70. Atun, R., D.A. Jaffray, M.B. Barton, F. Bray, M. Baumann, B. Vikram, T.P. Hanna, F.M. Knaul, Y. Lievens, T.Y. Lui, M. Milosevic, B. O'Sullivan, D.L. Rodin, E. Rosenblatt, J. Van Dyk, M.L. Yap, E. Zubizarreta, and M. Gospodarowicz, *Expanding global access to radiotherapy.* Lancet Oncol, 2015. **16**(10): p. 1153-86.
71. Baskar, R., K.A. Lee, R. Yeo, and K.W. Yeoh, *Cancer and radiation therapy: current advances and future directions.* Int J Med Sci, 2012. **9**(3): p. 193-9.
72. Wang, J.-s., H.-j. Wang, and H.-l. Qian, *Biological effects of radiation on cancer cells.* Military Medical Research, 2018. **5**(1): p. 20.
73. Srinivas, U.S., B.W.Q. Tan, B.A. Vellayappan, and A.D. Jeyasekharan, *ROS and the DNA damage response in cancer.* Redox Biol, 2019. **25**: p. 101084.
74. Jackson, S.P. and J. Bartek, *The DNA-damage response in human biology and disease.* Nature, 2009. **461**(7267): p. 1071-8.
75. Joubert, A., G. Vogin, C. Devic, A. Granzotto, M. Viau, M. Maalouf, C. Thomas, C. Colin, and N. Foray, *[Radiation biology: major advances and perspectives for radiotherapy].* Cancer Radiother, 2011. **15**(5): p. 348-54.
76. Donahoe, L.L., B.J. Cho, and M. de Perrot, *Induction radiotherapy and mesothelioma surgery.* Shanghai Chest, 2018. **2**(8).
77. Baskar, R., J. Dai, N. Wenlong, R. Yeo, and K.W. Yeoh, *Biological response of cancer cells to radiation treatment.* Front Mol Biosci, 2014. **1**: p. 24.
78. Lutz, S. and E. Chow, *A review of recently published radiotherapy treatment guidelines for bone metastases: Contrasts or convergence?* J Bone Oncol, 2012. **1**(1): p. 18-23.
79. De Felice, F., A. Piccioli, D. Musio, and V. Tombolini, *The role of radiation therapy in bone metastases management.* Oncotarget, 2017. **8**(15): p. 25691-25699.
80. Chow, E., K. Harris, G. Fan, M. Tsao, and W.M. Sze, *Palliative radiotherapy trials for bone metastases: a systematic review.* J Clin Oncol, 2007. **25**(11): p. 1423-36.
81. McDonald, R., E. Chow, H. Lam, L. Rowbottom, and H. Soliman, *International patterns of practice in radiotherapy for bone metastases: A review of the literature.* J Bone Oncol, 2014. **3**(3-4): p. 96-102.
82. Shulman, R.M., J.E. Meyer, T. Li, and K.J. Howell, *External beam radiation therapy (EBRT) for asymptomatic bone metastases in patients with solid tumors reduces the risk of skeletal-related events (SREs).* Ann Palliat Med, 2019. **8**(2): p. 159-167.
83. Furubayashi, N., T. Negishi, S. Ura, Y. Hirai, and M. Nakamura, *Palliative effects and adverse events of strontium-89 for prostate cancer patients with bone metastasis.* Mol Clin Oncol, 2015. **3**(1): p. 257-263.
84. Das, T. and S. Banerjee, *Radiopharmaceuticals for metastatic bone pain palliation: available options in the clinical domain and their comparisons.* Clinical & Experimental Metastasis, 2017. **34**: p. 1-10.
85. Bedard, G. and E. Chow, *The failures and challenges of bone metastases research in radiation oncology.* J Bone Oncol, 2013. **2**(2): p. 84-8.
86. Harrison, M.R., T.Z. Wong, A.J. Armstrong, and D.J. George, *Radium-223 chloride: a potential new treatment for castration-resistant prostate cancer patients with metastatic bone disease.* Cancer Manag Res, 2013. **5**: p. 1-14.

87. Skowronek, J., *Current status of brachytherapy in cancer treatment - short overview.* J Contemp Brachytherapy, 2017. **9**(6): p. 581-589.
88. Edeline, J., M. Gilabert, E. Garin, E. Boucher, and J.L. Raoul, *Yttrium-90 microsphere radioembolization for hepatocellular carcinoma.* Liver Cancer, 2015. **4**(1): p. 16-25.
89. Christie, J.K., J. Malik, and A. Tilocca, *Bioactive glasses as potential radioisotope vectors for in situ cancer therapy: investigating the structural effects of yttrium.* Physical Chemistry Chemical Physics, 2011. **13**(39): p. 17749-17755.
90. Hench, L.L., R.J. Splinter, W.C. Allen, and T.K. Greenlee, *Bonding mechanisms at the interface of ceramic prosthetic materials.* Journal of Biomedical Materials Research, 1971. **5**(6): p. 117-141.
91. Ciraldo, F.E., E. Boccardi, V. Melli, F. Westhauser, and A.R. Boccaccini, *Tackling bioactive glass excessive in vitro bioreactivity: Preconditioning approaches for cell culture tests.* Acta Biomater, 2018. **75**: p. 3-10.
92. Jones, J.R., *Reprint of: Review of bioactive glass: From Hench to hybrids.* Acta Biomater, 2015. **23 Suppl**: p. S53-82.
93. Rabiee, S.M., N. Nazparvar, M. Azizian, D. Vashaee, and L. Tayebi, *Effect of ion substitution on properties of bioactive glasses: A review.* Ceramics International, 2015. **41**(6): p. 7241-7251.
94. Knowles, J.C., *Phosphate based glasses for biomedical applications.* Journal of Materials Chemistry, 2003. **13**(10): p. 2395-2401.
95. Fernandes, H.R., A. Gaddam, A. Rebelo, D. Brazete, G.E. Stan, and J.M.F. Ferreira, *Bioactive Glasses and Glass-Ceramics for Healthcare Applications in Bone Regeneration and Tissue Engineering.* Materials (Basel), 2018. **11**(12).
96. Mourino, V., J.P. Cattalini, and A.R. Boccaccini, *Metallic ions as therapeutic agents in tissue engineering scaffolds: an overview of their biological applications and strategies for new developments.* J R Soc Interface, 2012. **9**(68): p. 401-19.
97. Eliaz, N. and N. Metoki, *Calcium Phosphate Bioceramics: A Review of Their History, Structure, Properties, Coating Technologies and Biomedical Applications.* Materials (Basel), 2017. **10**(4).
98. Ahmed, I., H. Ren, and J. Booth, *Developing Unique Geometries of Phosphate-Based Glasses and their Prospective Biomedical Applications.* Johnson Matthey Technology Review, 2019. **63**(1): p. 34-42.
99. Ahmed, I., M. Lewis, I. Olsen, and J.C. Knowles, *Phosphate glasses for tissue engineering: Part 1. Processing and characterisation of a ternary-based P2O5-CaO-Na2O glass system.* Biomaterials, 2004. **25**(3): p. 491-9.
100. Patel, U., R.M. Moss, K.M.Z. Hossain, A.R. Kennedy, E.R. Barney, I. Ahmed, and A.C. Hannon, *Structural and physico-chemical analysis of calcium/strontium substituted, near-invert phosphate based glasses for biomedical applications.* Acta Biomater, 2017. **60**: p. 109-127.
101. Abou Neel, E.A., D.M. Pickup, S.P. Valappil, R.J. Newport, and J.C. Knowles, *Bioactive functional materials: a perspective on phosphate-based glasses.* Journal of Materials Chemistry, 2009. **19**(6): p. 690-701.
102. Maeno, S., Y. Niki, H. Matsumoto, H. Morioka, T. Yatabe, A. Funayama, Y. Toyama, T. Taguchi, and J. Tanaka, *The effect of calcium ion concentration on osteoblast viability, proliferation and differentiation in monolayer and 3D culture.* Biomaterials, 2005. **26**(23): p. 4847-55.

103. Rude, R.K., F.R. Singer, and H.E. Gruber, *Skeletal and hormonal effects of magnesium deficiency.* J Am Coll Nutr, 2009. **28**(2): p. 131-41.
104. Gentleman, E., Y.C. Fredholm, G. Jell, N. Lotfibakhshaiesh, M.D. O'Donnell, R.G. Hill, and M.M. Stevens, *The effects of strontium-substituted bioactive glasses on osteoblasts and osteoclasts in vitro.* Biomaterials, 2010. **31**(14): p. 3949-56.
105. Hoppe, A., V. Mouriño, and A.R. Boccaccini, *Therapeutic inorganic ions in bioactive glasses to enhance bone formation and beyond.* Biomaterials Science, 2013. **1**(3): p. 254-256.
106. Brauer, D.S., C. Rüssel, W. Li, and S. Habelitz, *Effect of degradation rates of resorbable phosphate invert glasses on in vitro osteoblast proliferation.* Journal of Biomedical Materials Research Part A, 2006. **77A**(2): p. 213-219.
107. De Melo, N., L. Murrell, M.T. Islam, J.J. Titman, L. Macri-Pellizzeri, I. Ahmed, and V. Sottile, *Tailoring Pyro- and Orthophosphate Species to Enhance Stem Cell Adhesion to Phosphate Glasses.* International Journal of Molecular Sciences, 2021. **22**(2): p. 837.
108. Pujari-Palmer, M., S. Pujari-Palmer, X. Lu, T. Lind, H. Melhus, T. Engstrand, M. Karlsson-Ott, and H. Engqvist, *Pyrophosphate Stimulates Differentiation, Matrix Gene Expression and Alkaline Phosphatase Activity in Osteoblasts.* PLoS One, 2016. **11**(10): p. e0163530.
109. Grover, L., A. Wright, U. Gbureck, A. Bolarinwa, J. Song, Y. Liu, D. Farrar, G. Howling, J. Rose, and J. Barralet, *The effect of amorphous pyrophosphate on calcium phosphate cement resorption and bone generation.* Biomaterials, 2013. **34**.
110. Jones, J.R., D.S. Brauer, L. Hupa, and D.C. Greenspan, *Bioglass and Bioactive Glasses and Their Impact on Healthcare.* International Journal of Applied Glass Science, 2016. **7**(4): p. 423-434.
111. Tesavibul, P., R. Felzmann, S. Gruber, R. Liska, I. Thompson, A.R. Boccaccini, and J. Stampfl, *Processing of 45S5 Bioglass® by lithography-based additive manufacturing.* Materials Letters, 2012. **74**: p. 81-84.
112. Colquhoun, R. and K.E. Tanner, *Mechanical behaviour of degradable phosphate glass fibres and composites-a review.* Biomed Mater, 2015. **11**(1): p. 014105.
113. Islam, M.T., R.M. Felfel, E.A. Abou Neel, D.M. Grant, I. Ahmed, and K.M.Z. Hossain, *Bioactive calcium phosphate-based glasses and ceramics and their biomedical applications: A review.* J Tissue Eng, 2017. **8**: p. 2041731417719170.
114. Ghosh Dastidar, D., S. Saha, and M. Chowdhury, *Porous microspheres: Synthesis, characterisation and applications in pharmaceutical & medical fields.* Int J Pharm, 2018. **548**(1): p. 34-48.
115. Cai, Y., Y. Chen, X. Hong, Z. Liu, and W. Yuan, *Porous microsphere and its applications.* Int J Nanomedicine, 2013. **8**: p. 1111-20.
116. Wu, D., F. Xu, B. Sun, R. Fu, H. He, and K. Matyjaszewski, *Design and preparation of porous polymers.* Chem Rev, 2012. **112**(7): p. 3959-4015.
117. Gupta, D., K.M.Z. Hossain, I. Ahmed, V. Sottile, and D.M. Grant, *Flame-Spheroidized Phosphate-Based Glass Particles with Improved Characteristics for Applications in Mesenchymal Stem Cell Culture Therapy and Tissue Engineering.* ACS Appl Mater Interfaces, 2018. **10**(31): p. 25972-25982.
118. Liang, J., Z. Zhang, H. Zhao, S. Wan, X. Zhai, J. Zhou, R. Liang, Q. Deng, Y. Wu, and G. Lin, *Simple and rapid monitoring of doxorubicin using streptavidin-*

modified microparticle-based time-resolved fluorescence immunoassay. RSC Advances, 2018. **8**: p. 15621-15631.
119. Bongio, M., J.J.J.P. van den Beucken, S.C.G. Leeuwenburgh, and J.A. Jansen, *Development of bone substitute materials: from 'biocompatible' to 'instructive'.* Journal of Materials Chemistry, 2010. **20**(40): p. 8747-8759.
120. Winkler, T., F.A. Sass, G.N. Duda, and K. Schmidt-Bleek, *A review of biomaterials in bone defect healing, remaining shortcomings and future opportunities for bone tissue engineering: The unsolved challenge.* Bone & joint research, 2018. **7**(3): p. 232-243.
121. Neves, M.I., M.E. Wechsler, M.E. Gomes, R.L. Reis, P.L. Granja, and N.A. Peppas, *Molecularly Imprinted Intelligent Scaffolds for Tissue Engineering Applications.* Tissue Eng Part B Rev, 2017. **23**(1): p. 27-43.
122. Gomes, M.E., M.T. Rodrigues, R.M.A. Domingues, and R.L. Reis, *Tissue Engineering and Regenerative Medicine: New Trends and Directions-A Year in Review.* Tissue Eng Part B Rev, 2017. **23**(3): p. 211-224.
123. Chen, Y., X. Liu, R. Liu, Y. Gong, M. Wang, Q. Huang, Q. Feng, and B. Yu, *Zero-order controlled release of BMP2-derived peptide P24 from the chitosan scaffold by chemical grafting modification technique for promotion of osteogenesis in vitro and enhancement of bone repair in vivo.* Theranostics, 2017. **7**(5): p. 1072-1087.
124. Chauhan, N., N. Lakhkar, and A. Chaudhari, *Development and physicochemical characterization of novel porous phosphate glass bone graft substitute and in vitro comparison with xenograft.* Journal of Materials Science: Materials in Medicine, 2021. **32**(6): p. 60.
125. Brow, R., *Review: The Structure of Simple Phosphate Glasses.* Journal of Non-Crystalline Solids, 2000. **263-264**: p. 1-28.
126. Brow, R.K., *Review: the structure of simple phosphate glasses.* Journal of Non-Crystalline Solids, 2000. **263-264**: p. 1-28.
127. Flambard, A., L. Montagne, L. Delevoye, G. Palavit, J.-P. Amoureux, and J.-J. Videau, *Solid-state NMR study of mixed network sodium–niobium phosphate glasses.* Journal of Non-Crystalline Solids, 2004. **345-346**: p. 75-79.
128. Yung, S.W., Y.S. Huang, Y.-M. Lee, and Y.S. Lai, *An NMR and Raman spectroscopy study of Li2O–SrO–Nb2O5–P2O5 glasses.* RSC Advances, 2013. **3**(43): p. 21025-21032.
129. Shih, P.Y., J.Y. Ding, and S.Y. Lee, *MAS-NMR and FTIR analyses on the structure of CuO-containing sodium poly- and meta-phosphate glasses.* Materials Chemistry and Physics, 2003. **80**(2): p. 391-396.
130. Lee, I.-H., S.-H. Shin, F. Foroutan, N.J. Lakhkar, M.-S. Gong, and J.C. Knowles, *Effects of magnesium content on the physical, chemical and degradation properties in a MgO−CaO−Na2O−P2O5 glass system.* Journal of Non-Crystalline Solids, 2013. **363**: p. 57-63.
131. Oueslati Omrani, R., A. Kaoutar, A. El Jazouli, S. Krimi, I. Khattech, M. Jemal, J.-J. Videau, and M. Couzi, *Structural and thermochemical properties of sodium magnesium phosphate glasses.* Journal of Alloys and Compounds, 2015. **632**: p. 766-771.
132. Lu, M., F. Wang, Q. Liao, K. Chen, J. Qin, and S. Pan, *FTIR spectra and thermal properties of TiO2-doped iron phosphate glasses.* Journal of Molecular Structure, 2015. **1081**: p. 187-192.
133. Yadav, A.K. and P. Singh, *A review of the structures of oxide glasses by Raman spectroscopy.* RSC Advances, 2015. **5**(83): p. 67583-67609.

134. Ahmed, I., M. Lewis, I. Olsen, and J.C. Knowles, *Phosphate glasses for tissue engineering: Part 1. Processing and characterisation of a ternary-based P2O5–CaO–Na2O glass system.* Biomaterials, 2004. **25**(3): p. 491-499.
135. Boccardi, E., A. Philippart, V. Melli, L. Altomare, L. De Nardo, G. Novajra, C. Vitale-Brovarone, T. Fey, and A.R. Boccaccini, *Bioactivity and Mechanical Stability of 45S5 Bioactive Glass Scaffolds Based on Natural Marine Sponges.* Ann Biomed Eng, 2016. **44**(6): p. 1881-93.
136. Macon, A.L., T.B. Kim, E.M. Valliant, K. Goetschius, R.K. Brow, D.E. Day, A. Hoppe, A.R. Boccaccini, I.Y. Kim, C. Ohtsuki, T. Kokubo, A. Osaka, M. Vallet-Regi, D. Arcos, L. Fraile, A.J. Salinas, A.V. Teixeira, Y. Vueva, R.M. Almeida, M. Miola, C. Vitale-Brovarone, E. Verne, W. Holand, and J.R. Jones, *A unified in vitro evaluation for apatite-forming ability of bioactive glasses and their variants.* J Mater Sci Mater Med, 2015. **26**(2): p. 115.
137. Wojcik-Pastuszka, D., J. Krzak, B. Macikowski, R. Berkowski, B. Osiński, and W. Musiał, *Evaluation of the Release Kinetics of a Pharmacologically Active Substance from Model Intra-Articular Implants Replacing the Cruciate Ligaments of the Knee.* Materials (Basel), 2019. **12**(8).
138. Abou Neel, E.A., W. Chrzanowski, D.M. Pickup, L.A. O'Dell, N.J. Mordan, R.J. Newport, M.E. Smith, and J.C. Knowles, *Structure and properties of strontium-doped phosphate-based glasses.* Journal of the Royal Society, Interface, 2009. **6**(34): p. 435-446.
139. Hasan, M.S., I. Ahmed, A.J. Parsons, G.S. Walker, and C.A. Scotchford, *Material characterisation and cytocompatibility assessment of quinternary phosphate glasses.* Journal of Materials Science: Materials in Medicine, 2012. **23**(10): p. 2531-2541.
140. Jeong, J., J.H. Kim, J.H. Shim, N.S. Hwang, and C.Y. Heo, *Bioactive calcium phosphate materials and applications in bone regeneration.* Biomater Res, 2019. **23**: p. 4.
141. Elgayar, I., A.E. Aliev, A.R. Boccaccini, and R.G. Hill, *Structural analysis of bioactive glasses.* Journal of Non-Crystalline Solids, 2005. **351**(2): p. 173-183.
142. Walter, G., J. Vogel, U. Hoppe, and P. Hartmann, *The structure of CaO–Na2O–MgO–P2O5 invert glass.* Journal of Non-Crystalline Solids, 2001. **296**(3): p. 212-223.
143. Edén, M., *NMR studies of oxide-based glasses.* Annual Reports Section "C" (Physical Chemistry), 2012. **108**(1): p. 177-221.
144. Jäger, C., P. Hartmann, R. Witter, and M. Braun, *New 2D NMR experiments for determining the structure of phosphate glasses: a review.* Journal of Non-Crystalline Solids, 2000. **263-264**: p. 61-72.
145. Kim, J., R.J. Narayan, X. Lu, and M. Jay, *Neutron-activatable needles for radionuclide therapy of solid tumors.* J Biomed Mater Res A, 2017. **105**(12): p. 3273-3280.
146. Habraken, W., P. Habibovic, M. Epple, and M. Bohner, *Calcium phosphates in biomedical applications: materials for the future?* Materials Today, 2016. **19**(2): p. 69-87.
147. Combes, C. and C. Rey, *Amorphous calcium phosphates: Synthesis, properties and uses in biomaterials.* Acta Biomaterialia, 2010. **6**(9): p. 3362-3378.
148. Eanes, E.D., *Amorphous Calcium Phosphate: Thermodynamic and Kinetic Considerations*, in *Calcium Phosphates in Biological and Industrial Systems*, Z. Amjad, Editor. 1998, Springer US: Boston, MA. p. 21-39.

149. Kasuga, T., Y. Hosoi, M. Nogami, and M. Niinomi, *BIOMIMETIC APATITE FORMATION ON CALCIUM PHOSPHATE INVERT GLASSES.* Phosphorus Research Bulletin, 2001. **12**: p. 39-44.
150. Kasuga, T., T. Fujimoto, Y. Hosoi, and M. Nogami, *Calcium Phosphate Invert Glasses and Glass-Ceramics with Apatite-Forming Ability.* Key Engineering Materials, 2002. **240-242**: p. 265-268.
151. Kim, H.D., H.L. Jang, H.Y. Ahn, H.K. Lee, J. Park, E.S. Lee, E.A. Lee, Y.H. Jeong, D.G. Kim, K.T. Nam, and N.S. Hwang, *Biomimetic whitlockite inorganic nanoparticles-mediated in situ remodeling and rapid bone regeneration.* Biomaterials, 2017. **112**: p. 31-43.
152. Cheng, H., R. Chabok, X. Guan, A. Chawla, Y. Li, A. Khademhosseini, and H.L. Jang, *Synergistic interplay between the two major bone minerals, hydroxyapatite and whitlockite nanoparticles, for osteogenic differentiation of mesenchymal stem cells.* Acta Biomater, 2018. **69**: p. 342-351.
153. Muñoz, F., J. Rocherullé, I. Ahmed, and L. Hu, *Phosphate Glasses*, in *Springer Handbook of Glass*, J.D. Musgraves, J. Hu, and L. Calvez, Editors. 2019, Springer International Publishing: Cham. p. 553-594.
154. Ahmed, I., M.P. Lewis, S.N. Nazhat, and J.C. Knowles, *Quantification of Anion and Cation Release from a Range of Ternary Phosphate-based Glasses with Fixed 45 mol% P2O5.* Journal of Biomaterials Applications, 2005. **20**(1): p. 65-80.
155. Islam, M.T., K.M.Z. Hossain, N. Sharmin, A.J. Parsons, and I. Ahmed, *Effect of magnesium content on bioactivity of near invert phosphate-based glasses.* International Journal of Applied Glass Science, 2017. **8**(4): p. 391-402.
156. Brauer, D.S., *Bioactive glasses—structure and properties.* Angew Chem Int Ed Engl, 2015. **54**(14): p. 4160-81.
157. Bosch-Rué, E., L. Diez-Tercero, B. Giordano-Kelhoffer, L.M. Delgado, B.M. Bosch, M. Hoyos-Nogués, M.A. Mateos-Timoneda, P.A. Tran, F.J. Gil, and R.A. Perez, *Biological Roles and Delivery Strategies for Ions to Promote Osteogenic Induction.* Frontiers in cell and developmental biology, 2021. **8**: p. 614545-614545.
158. Caplan, A.I., *Adult mesenchymal stem cells for tissue engineering versus regenerative medicine.* Journal of Cellular Physiology, 2007. **213**(2): p. 341-347.
159. Bunker, B.C., G.W. Arnold, and J.A. Wilder, *Phosphate glass dissolution in aqueous solutions.* Journal of Non-Crystalline Solids, 1984. **64**(3): p. 291-316.
160. Valerio, P., M.M. Pereira, A.M. Goes, and M.F. Leite, *Effects of extracellular calcium concentration on the glutamate release by bioactive glass (BG60S) preincubated osteoblasts.* Biomed Mater, 2009. **4**(4): p. 045011.
161. Patel, U., L. Macri-Pellizzeri, K.M. Zakir Hossain, B.E. Scammell, D.M. Grant, C.A. Scotchford, A.C. Hannon, A.R. Kennedy, E.R. Barney, I. Ahmed, and V. Sottile, *In vitro cellular testing of strontium/calcium substituted phosphate glass discs and microspheres shows potential for bone regeneration.* J Tissue Eng Regen Med, 2019. **13**(3): p. 396-405.
162. Skelton, K.L., J.V. Glenn, S.A. Clarke, G. Georgiou, S.P. Valappil, J.C. Knowles, S.N. Nazhat, and G.R. Jordan, *Effect of ternary phosphate-based glass compositions on osteoblast and osteoblast-like proliferation, differentiation and death in vitro.* Acta Biomater, 2007. **3**(4): p. 563-72.

163. Ciraldo, F.E., E. Boccardi, V. Melli, F. Westhauser, and A.R. Boccaccini, *Tackling bioactive glass excessive in vitro bioreactivity: Preconditioning approaches for cell culture tests.* Acta Biomaterialia, 2018. **75**: p. 3-10.
164. Lowe, B., M.P. Ottensmeyer, C. Xu, Y. He, Q. Ye, and M.J. Troulis, *The Regenerative Applicability of Bioactive Glass and Beta-Tricalcium Phosphate in Bone Tissue Engineering: A Transformation Perspective.* Journal of Functional Biomaterials, 2019. **10**(1): p. 16.
165. Khan, W.S., F. Rayan, B.S. Dhinsa, and D. Marsh, *An Osteoconductive, Osteoinductive, and Osteogenic Tissue-Engineered Product for Trauma and Orthopaedic Surgery: How Far Are We?* Stem Cells International, 2012. **2012**: p. 236231.
166. Youssif, E., H. Doweidar, and R. Ramadan, *Bioactivity of microporous borate glass-ceramics prepared from solution and derived glasses.* Journal of Non-Crystalline Solids, 2021. **557**: p. 120649.
167. Orriss, I.R., T.R. Arnett, and R.G.G. Russell, *Pyrophosphate: a key inhibitor of mineralisation.* Current Opinion in Pharmacology, 2016. **28**: p. 57-68.
168. Hughes, E.A.B., T.E. Robinson, D.B. Bassett, S.C. Cox, and L.M. Grover, *Critical and diverse roles of phosphates in human bone formation.* J Mater Chem B, 2019. **7**(47): p. 7460-7470.
169. Niu, X., Z. Liu, F. Tian, S. Chen, L. Lei, T. Jiang, Q. Feng, and Y. Fan, *Sustained delivery of calcium and orthophosphate ions from amorphous calcium phosphate and poly(L-lactic acid)-based electrospinning nanofibrous scaffold.* Scientific Reports, 2017. **7**(1): p. 45655.
170. Mao, J., P. Wei, Z. Yuan, W. Jing, J. Cao, G. Li, J. Guo, H. Wang, D. Chen, and Q. Cai, *Osteoconductive and osteoinductive biodegradable microspheres serving as injectable micro-scaffolds for bone regeneration.* J Biomater Sci Polym Ed, 2021. **32**(2): p. 229-247.
171. Kulchar, R.J., B.R. Denzer, B.M. Chavre, M. Takegami, and J. Patterson, *A Review of the Use of Microparticles for Cartilage Tissue Engineering.* Int J Mol Sci, 2021. **22**(19).
172. Wilkinson, A., R.N. Hewitt, L.E. McNamara, D. McCloy, R.M. Dominic Meek, and M.J. Dalby, *Biomimetic microtopography to enhance osteogenesis in vitro.* Acta Biomater, 2011. **7**(7): p. 2919-25.
173. Zhang, Q., S. Lin, T. Zhang, T. Tian, Q. Ma, X. Xie, C. Xue, Y. Lin, B. Zhu, and X. Cai, *Curved microstructures promote osteogenesis of mesenchymal stem cells via the RhoA/ROCK pathway.* Cell Prolif, 2017. **50**(4).
174. Boanini, E., P. Torricelli, M. Gazzano, E. Della Bella, M. Fini, and A. Bigi, *Combined effect of strontium and zoledronate on hydroxyapatite structure and bone cell responses.* Biomaterials, 2014. **35**(21): p. 5619-26.
175. Ripamonti, U., *Biomimetism, biomimetic matrices and the induction of bone formation.* J Cell Mol Med, 2009. **13**(9b): p. 2953-72.
176. McLaren, J.S., L. Macri-Pellizzeri, K.M.Z. Hossain, U. Patel, D.M. Grant, B.E. Scammell, I. Ahmed, and V. Sottile, *Porous Phosphate-Based Glass Microspheres Show Biocompatibility, Tissue Infiltration, and Osteogenic Onset in an Ovine Bone Defect Model.* ACS Appl Mater Interfaces, 2019. **11**(17): p. 15436-15446.
177. Hasan, A., R. Waters, B. Roula, R. Dana, S. Yara, T. Alexandre, and A. Paul, *Engineered Biomaterials to Enhance Stem Cell-Based Cardiac Tissue Engineering and Therapy.* Macromol Biosci, 2016. **16**(7): p. 958-77.

178. Burdick, J.A., R.L. Mauck, J.H. Gorman, 3rd, and R.C. Gorman, *Acellular biomaterials: an evolving alternative to cell-based therapies.* Science translational medicine, 2013. **5**(176): p. 176ps4-176ps4.
179. Wang, S.-Y., H.-Z. Hu, X.-C. Qing, Z.-C. Zhang, and Z.-W. Shao, *Recent advances of drug delivery nanocarriers in osteosarcoma treatment.* Journal of Cancer, 2020. **11**(1): p. 69-82.
180. Crenn, V., K. Biteau, J. Amiaud, C. Dumars, R. Guiho, L. Vidal, L.-R.L. Nail, D. Heymann, A. Moreau, F. Gouin, and F. Redini, *Bone microenvironment has an influence on the histological response of osteosarcoma to chemotherapy: retrospective analysis and preclinical modeling.* American journal of cancer research, 2017. **7**(11): p. 2333-2349.
181. Dong, H.M., Q. Wang, W.L. Wang, G. Wang, X.K. Li, G.D. Li, and J. Chen, *A clinical analysis of systemic chemotherapy combined with radiotherapy for advanced gastric cancer.* Medicine (Baltimore), 2018. **97**(23): p. e10786.
182. Dong, H.-M., Q. Wang, W.-L. Wang, G. Wang, X.-K. Li, G.-D. Li, and J. Chen, *A clinical analysis of systemic chemotherapy combined with radiotherapy for advanced gastric cancer.* Medicine, 2018. **97**(23): p. e10786-e10786.
183. Zhou, Z.-F., T.-W. Sun, F. Chen, D.-Q. Zuo, H.-S. Wang, Y.-Q. Hua, Z.-D. Cai, and J. Tan, *Calcium phosphate-phosphorylated adenosine hybrid microspheres for anti-osteosarcoma drug delivery and osteogenic differentiation.* Biomaterials, 2017. **121**: p. 1-14.
184. Thorn, C.F., C. Oshiro, S. Marsh, T. Hernandez-Boussard, H. McLeod, T.E. Klein, and R.B. Altman, *Doxorubicin pathways: pharmacodynamics and adverse effects.* Pharmacogenetics and genomics, 2011. **21**(7): p. 440-446.
185. Liu, X., K.A. Fundora, Z. Zhou, A.L. Miller, 2nd, and L. Lu, *Composite Hydrogel Embedded with Porous Microspheres for Long-Term pH-Sensitive Drug Delivery.* Tissue engineering. Part A, 2019. **25**(3-4): p. 172-182.
186. Hess, U., S. Shahabi, L. Treccani, P. Streckbein, C. Heiss, and K. Rezwan, *Co-delivery of cisplatin and doxorubicin from calcium phosphate beads/matrix scaffolds for osteosarcoma therapy.* Materials Science and Engineering: C, 2017. **77**: p. 427-435.
187. Tischendorf and B. Conrad, *Interactions between water and phosphate glasses.* 2005.
188. Lara-Ochoa, S., W. Ortega-Lara, and C.E. Guerrero-Beltran, *Hydroxyapatite Nanoparticles in Drug Delivery: Physicochemistry and Applications.* Pharmaceutics, 2021. **13**(10).
189. Di Pompo, G., M. Cortini, N. Baldini, and S. Avnet, *Acid Microenvironment in Bone Sarcomas.* Cancers, 2021. **13**(15): p. 3848.
190. Corre, I., F. Verrecchia, V. Crenn, F. Redini, and V. Trichet, *The Osteosarcoma Microenvironment: A Complex But Targetable Ecosystem.* Cells, 2020. **9**(4): p. 976.
191. Delahaye, F., L. Montagne, G. Palavit, J. Claude Touray, and P. Baillif, *Acid dissolution of sodium–calcium metaphosphate glasses.* Journal of Non-Crystalline Solids, 1998. **242**(1): p. 25-32.
192. Brauer, D.S., C. Rüssel, and J. Kraft, *Solubility of glasses in the system P2O5–CaO–MgO–Na2O–TiO2: Experimental and modeling using artificial neural networks.* Journal of Non-Crystalline Solids, 2007. **353**(3): p. 263-270.
193. Dash, S., P.N. Murthy, L. Nath, and P. Chowdhury, *Kinetic modeling on drug release from controlled drug delivery systems.* Acta Pol Pharm, 2010. **67**(3): p. 217-23.

194. Singhvi, G. and M. Singh, *Review: In vitro Drug Release Characterization Models.* International Journal of Pharmaceutical Studies and Research, 2011. **2**: p. 77-84.
195. Arora, G., K. Malik, and I. Singh, *Formulation and evaluation of mucoadhesive matrix tablets of taro gum: optimization using response surface methodology.* Polimery w medycynie, 2011. **41**: p. 23-34.
196. Neville-Webbe, H.L., M. Gnant, and R.E. Coleman, *Potential anticancer properties of bisphosphonates.* Semin Oncol, 2010. **37 Suppl 1**: p. S53-65.
197. Gnant, M. and P. Clezardin, *Direct and indirect anticancer activity of bisphosphonates: a brief review of published literature.* Cancer Treat Rev, 2012. **38**(5): p. 407-15.
198. Santini, D., A. Zoccoli, C. Gregorj, M. Di Cerbo, M. Iuliani, F. Pantano, R. Zamarchi, F. Sergi, G. Flammia, M. Buscarini, S. Rizzo, G. Cicero, A. Russo, B. Vincenzi, G. Avvisati, and G. Tonini, *Zoledronic acid induces a significant decrease of circulating endothelial cells and circulating endothelial precursor cells in the early prostate cancer neoadjuvant setting.* Oncology, 2013. **85**(6): p. 342-7.
199. Garibaldi, C., B.A. Jereczek-Fossa, G. Marvaso, S. Dicuonzo, D.P. Rojas, F. Cattani, A. Starzynska, D. Ciardo, A. Surgo, M.C. Leonardi, and R. Ricotti, *Recent advances in radiation oncology.* Ecancermedicalscience, 2017. **11**: p. 785.
200. Cacaina, D., H. Ylanen, M. Hupa, and S. Simon, *Study of yttrium containing bioactive glasses behaviour in simulated body fluid.* J Mater Sci Mater Med, 2006. **17**(8): p. 709-16.
201. Mosconi, C., A. Cappelli, C. Pettinato, and R. Golfieri, *Radioembolization with Yttrium-90 microspheres in hepatocellular carcinoma: Role and perspectives.* World J Hepatol, 2015. **7**(5): p. 738-52.
202. Baino, F., S. Hamzehlou, and S. Kargozar, *Bioactive Glasses: Where Are We and Where Are We Going?* Journal of Functional Biomaterials, 2018. **9**(1): p. 25.
203. Molvar, C. and R. Lewandowski, *Yttrium-90 Radioembolization of Hepatocellular Carcinoma-Performance, Technical Advances, and Future Concepts.* Semin Intervent Radiol, 2015. **32**(4): p. 388-97.
204. Westcott, M.A., D.M. Coldwell, D.M. Liu, and J.F. Zikria, *The development, commercialization, and clinical context of yttrium-90 radiolabeled resin and glass microspheres.* Adv Radiat Oncol, 2016. **1**(4): p. 351-364.
205. Cacaina, D., H. Ylanen, S. Simon, and M. Hupa, *The behaviour of selected yttrium containing bioactive glass microspheres in simulated body environments.* J Mater Sci Mater Med, 2008. **19**(3): p. 1225-33.
206. Kawashita, M., N. Matsui, Z. Li, T. Miyazaki, and H. Kanetaka, *Preparation, structure, and in vitro chemical durability of yttrium phosphate microspheres for intra-arterial radiotherapy.* J Biomed Mater Res B Appl Biomater, 2011. **99**(1): p. 45-50.
207. Day, D.E., *Glasses for radiotherapy*, in *Bio-Glasses*, R. Baskar and K.A. Lee, Editors. 2012, John Wiley & Sons: NJ, USA. p. 203–228.
208. Hoppe, A., N.S. Güldal, and A.R. Boccaccini, *A review of the biological response to ionic dissolution products from bioactive glasses and glass-ceramics.* Biomaterials, 2011. **32**(11): p. 2757-2774.
209. Sheindlin, A., M. Kenisarin, and V. Chekhovskoi, *Melting point of yttrium oxide.* 1974.

210. Arafat, A., S.A. Samad, M.D. Wadge, M.T. Islam, A.L. Lewis, E.R. Barney, and I. Ahmed, *Thermal and crystallization kinetics of yttrium-doped phosphate-based glasses.* International Journal of Applied Glass Science, 2020. **11**(1): p. 120-133.
211. Martin, R.A., P.S. Salmon, D.L. Carroll, M.E. Smith, and A.C. Hannon, *Structure and thermal properties of yttrium alumino-phosphate glasses.* J Phys Condens Matter, 2008. **20**(11): p. 115204.
212. Christie, J.K. and A. Tilocca, *Integrating biological activity into radioisotope vectors: molecular dynamics models of yttrium-doped bioactive glasses.* Journal of Materials Chemistry, 2012. **22**(24): p. 12023-12031.
213. Dorozhkin, S.V., *Bioceramics of calcium orthophosphates.* Biomaterials, 2010. **31**(7): p. 1465-85.
214. Kokubo, T., H.M. Kim, and M. Kawashita, *Novel bioactive materials with different mechanical properties.* Biomaterials, 2003. **24**(13): p. 2161-75.
215. Zhou, H. and S.B. Bhaduri, *Preparation of Yttrium Phosphate and Yttrium-Doped Calcium Phosphate Microspheres via Hydrated Ions Exchange.* International Journal of Applied Ceramic Technology, 2015. **12**(S2): p. E146-E151.
216. Ghosh, R., R. Sarkar, S. Paul, and S.K. Pal, *Biocompatibility and drilling performance of beta tricalcium phosphate: Yttrium phosphate bioceramic composite.* Ceramics International, 2016. **42**(7): p. 8263-8273.
217. Kawashita, M., R. Shineha, H.M. Kim, T. Kokubo, Y. Inoue, N. Araki, Y. Nagata, M. Hiraoka, and Y. Sawada, *Preparation of ceramic microspheres for in situ radiotherapy of deep-seated cancer.* Biomaterials, 2003. **24**(17): p. 2955-63.
218. Kawashita, M., F. Miyaji, T. Kokubo, G.H. Takaoka, I. Yamada, Y. Suzuki, and M. Inoue, *Surface structure and chemical durability of P+-implanted Y2O3–Al2O3–SiO2 glass for radiotherapy of cancer.* Journal of Non-Crystalline Solids, 1999. **255**(2): p. 140-148.
219. Höland, W., V. Rheinberger, and M. Schweiger, *Control of Nucleation in Glass Ceramics.* Philosophical Transactions of The Royal Society A: Mathematical, Physical and Engineering Sciences, 2003. **361**: p. 575-589.
220. Allix, M. and L. Cormier, *Crystallization and Glass-Ceramics*, in *Springer Handbook of Glass*, J.D. Musgraves, J. Hu, and L. Calvez, Editors. 2019, Springer International Publishing: Cham. p. 113-167.
221. Penttinen, R.P.K., *7 - Cell interaction with bioactive glasses and ceramics*, in *Bioactive Glasses (Second Edition)*, H. Ylänen, Editor. 2018, Woodhead Publishing. p. 145-180.
222. Rawlings, R.D., J.P. Wu, and A.R. Boccaccini, *Glass-ceramics: Their production from wastes—A Review.* Journal of Materials Science, 2006. **41**(3): p. 733-761.
223. Fernandes, J.S., P. Gentile, R.A. Pires, R.L. Reis, and P.V. Hatton, *Multifunctional bioactive glass and glass-ceramic biomaterials with antibacterial properties for repair and regeneration of bone tissue.* Acta Biomaterialia, 2017. **59**: p. 2-11.
224. Catauro, M. and F. Bollino, *Advanced Glass-Ceramic Materials for Biomedical Applications.* Journal of Bone Reports & Recommendations, 2017. **03**.
225. Mai, L., N. Boysen, E. Subasi, T. de los Arcos, D. Rogalla, G. Grundmeier, C. Bock, L. Hong, and A. Devi, *Water assisted atomic layer deposition of yttrium oxide using tris(N , N '-diisopropyl-2-dimethylamido-guanidinato) yttrium(iii):*

process development, film characterization and functional properties. RSC Advances, 2018. **8**: p. 4987-4994.
226. Massera, J., A. Mishra, S. Guastella, S. Ferraris, and E. Verné, *Surface functionalization of phosphate-based bioactive glasses with 3-aminopropyltriethoxysilane (APTS).* Biomedical glasses, 2016. **2**(1).
227. Sato, P.S., T. Watanabe, H. Maeda, A. Obata, and T. Kasuga, *Structural Analysis of 65ZnO–30P₂O₅–5Nb₂O₅ Invert Glass Using X-ray Photoelectron Spectroscopy.* MATERIALS TRANSACTIONS, 2019. **60**(8): p. 1707-1710.
228. Database, X., *XPS Database.* https://xpsdatabase.com/yttrium-spectra-ypo4/ 2022. **YPO4**.
229. d'Abadie, P., M. Hesse, A. Louppe, R. Lhommel, S. Walrand, and F. Jamar, *Microspheres Used in Liver Radioembolization: From Conception to Clinical Effects.* Molecules, 2021. **26**(13).
230. Arranja, A.G., W.E. Hennink, C. Chassagne, A.G. Denkova, and J.F.W. Nijsen, *Preparation and characterization of inorganic radioactive holmium-166 microspheres for internal radionuclide therapy.* Materials Science and Engineering: C, 2020. **106**: p. 110244.
231. Erdman, N., N. Kikuchi, A. Laudate, and V. Robertson, *Multispectral imaging in an FEG-SEM.* 2009. **167**: p. 28-31.
232. McCloy, J.S. and A. Goel, *Glass-ceramics for nuclear-waste immobilization.* MRS Bulletin, 2017. **42**(3): p. 233-240.
233. Karpukhina, N., R.G. Hill, and R.V. Law, *Crystallisation in oxide glasses – a tutorial review.* Chemical Society Reviews, 2014. **43**(7): p. 2174-2186.
234. Schuller, S., *Phase separation in glass*. 2018.
235. Luo, W., Y. Wang, F. Bao, and Y. Cheng, *Phase separation in yttrium silicate glass prepared by the sol–gel method.* Journal of Non-Crystalline Solids, 2005. **351**(37): p. 3114-3120.
236. Rudraraju, S., A. Van der Ven, and K. Garikipati, *Mechanochemical spinodal decomposition: a phenomenological theory of phase transformations in multi-component, crystalline solids.* npj Computational Materials, 2016. **2**(1): p. 16012.
237. Arafat, A., S.A. Samad, J.J. Titman, A.L. Lewis, E.R. Barney, and I. Ahmed, *Yttrium doped phosphate-based glasses: structural and degradation analyses.* Biomedical Glasses, 2020. **6**(1): p. 34-49.
238. Husson, E., C. Proust, P. Gillet, and J.P. Itié, *Phase transitions in yttrium oxide at high pressure studied by Raman spectroscopy.* Materials Research Bulletin, 1999. **34**(12): p. 2085-2092.
239. Li, H., H. Zou, Z. Sun, Y. Xu, C. Wang, X. Xie, J. Yi, and F. Zhao, *Spectroscopic and Surface Crystallization Characterizations of Yttrium-Doped Phosphate Glasses.* Crystals, 2022. **12**(1): p. 109.
240. Lai, H., H. Yang, C. Tao, and X. Yang, *Preparation, characterization and luminescence property of YPO4:Eu nanocrystals.* physica status solidi (a), 2007. **204**(4): p. 1178-1184.
241. Cole, J.M., E.R.H.v. Eck, G. Mountjoy, R. Anderson, T. Brennan, G. Bushnell-Wye, R.J. Newport, and G.A. Saunders, *An x-ray diffraction and³¹P MAS NMR study of rare-earth phosphate glasses, (R₂O₃)_x(P₂O₅)_{1-x},x= 0.175-0.263, R = La, Ce, Pr, Nd,*

Sm, Eu, Gd, Tb, Dy, Ho, Er. Journal of Physics: Condensed Matter, 2001. **13**(18): p. 4105-4122.
242. Hoppe, U., R.K. Brow, D. Ilieva, P. Jóvári, and A.C. Hannon, *Structure of rare-earth phosphate glasses by X-ray and neutron diffraction.* Journal of Non-Crystalline Solids, 2005. **351**(40): p. 3179-3190.
243. Majjane, A., A. Chahine, M. Et-tabirou, B. Echchahed, and P. Breen, *X-ray photoelectron spectroscopy (XPS) and FTIR studies of vanadium barium phosphate glasses.* Materials Chemistry and Physics, 2014. **143**: p. 779–787.
244. He, Q., P. Wang, M. Sun, M. Lu, and B. Peng, *Significant improvement of gamma radiation resistance in CeO_2 doped phosphate glass by co-doping with Sb_2O_3.* Optical Materials Express, 2017. **7**: p. 1113.
245. Zhang, R., J. Ren, X. Yuan, Y. Cui, L. Zhang, and L. Zhang, *Structural Studies of Bi2O3–NaPO3 Glasses by Solid State Nuclear Magnetic Resonance and X-ray Photoelectron Spectroscopy.* The Journal of Physical Chemistry C, 2017. **121**(18): p. 10087-10094.
246. Database, X., *XPS Database.* https://xpsdatabase.com/yttrium-spectra-y2o3/#Six-BE-Tables.
247. The Materials, P., *Materials Data on Y2O3 by Materials Project*. 2020: United States.
248. The Materials, P., *Materials Data on YPO4 by Materials Project*. 2020: United States.
249. Parsons, A.J., M. Evans, C.D. Rudd, and C.A. Scotchford, *Synthesis and degradation of sodium iron phosphate glasses and their in vitro cell response.* J Biomed Mater Res A, 2004. **71**(2): p. 283-91.
250. Yue, Y., Y. Wang, Y. Cao, S. Chen, Q. Zhou, W. Chen, and L. Hu, *Effect of Al2O3 on structure and properties of Al2O3-K2O-P2O5 glasses.* Optical Materials Express, 2018. **8**(2): p. 245-258.
251. Abou Neel, E.A., W. Chrzanowski, and J.C. Knowles, *Effect of increasing titanium dioxide content on bulk and surface properties of phosphate-based glasses.* Acta Biomater, 2008. **4**(3): p. 523-34.
252. Marino, A., S. Arrasmith, L. Gregg, S. Jacobs, G. Chen, and Y. Duc, *Durable phosphate glasses with lower transition temperatures.* Journal of Non-crystalline Solids - J NON-CRYST SOLIDS, 2001. **289**: p. 37-41.
253. Fu, Y. and J.K. Christie, *Atomic structure and dissolution properties of yttrium-containing phosphate glasses.* International Journal of Applied Glass Science, 2017. **8**(4): p. 412-417.
254. Schaller, T. and J.F. Stebbins, *The Structural Role of Lanthanum and Yttrium in Aluminosilicate Glasses: A 27Al and 17O MAS NMR Study.* The Journal of Physical Chemistry B, 1998. **102**(52): p. 10690-10697.
255. Sreenivasan, H., P. Kinnunen, E. Adesanya, M. Patanen, A.M. Kantola, V.-V. Telkki, M. Huttula, W. Cao, J.L. Provis, and M. Illikainen, *Field Strength of Network-Modifying Cation Dictates the Structure of (Na-Mg) Aluminosilicate Glasses.* Frontiers in Materials, 2020. **7**(267).
256. Malik, J. and A. Tilocca, *Hydration Effects on the Structural and Vibrational Properties of Yttrium Aluminosilicate Glasses for in Situ Radiotherapy.* The Journal of Physical Chemistry B, 2013. **117**(46): p. 14518-14528.
257. Baino, F., E. Fiume, S. Ciavattini, S. Kargozar, R. Borges, L.A. Genova, J. Marchi, and E. Verné, *Biomedical Radioactive Glasses for Brachytherapy.* Materials, 2021. **14**(5): p. 1131.

258. Shikama, T., *Study of Irradiation Effects in Materials with High Neutron-Flux Fission Reactors*. 2011: International Atomic Energy Agency (IAEA). p. 135-142.
259. Tilocca, A., *Structural Models of Bioactive Glasses from Molecular Dynamics Simulations.* Proceedings: Mathematical, Physical and Engineering Sciences, 2009. **465**(2104): p. 1003-1027.
260. Rahaman, M.N., W. Xiao, and W. Huang, *11 - Bioactive glass composites for bone and musculoskeletal tissue engineering*, in *Bioactive Glasses (Second Edition)*, H. Ylänen, Editor. 2018, Woodhead Publishing. p. 285-336.
261. Gremillard, L., J. Chevalier, S. Meille, J. Zhao, V. Fridrici, P. Kapsa, J. Geringer, and J. Uribe, *Degradation of Implant Materials, Chapter 9: Degradation of bioceramics*. 2012.
262. Maeno, S., Y. Niki, H. Matsumoto, H. Morioka, T. Yatabe, A. Funayama, Y. Toyama, T. Taguchi, and J. Tanaka, *The effect of calcium ion concentration on osteoblast viability, proliferation and differentiation in monolayer and 3D culture.* Biomaterials, 2005. **26**(23): p. 4847-4855.
263. Karpievitch, Y.V., A.D. Polpitiya, G.A. Anderson, R.D. Smith, and A.R. Dabney, *Liquid Chromatography Mass Spectrometry-Based Proteomics: Biological and Technological Aspects.* Ann Appl Stat, 2010. **4**(4): p. 1797-1823.
264. Tsai, T.H., M. Wang, and H.W. Ressom, *Preprocessing and Analysis of LC-MS-Based Proteomic Data.* Methods Mol Biol, 2016. **1362**: p. 63-76.
265. Nesvizhskii, A.I., *Protein identification by tandem mass spectrometry and sequence database searching.* Methods Mol Biol, 2007. **367**: p. 87-119.
266. Drazic, A., H. Aksnes, M. Marie, M. Boczkowska, S. Varland, E. Timmerman, H. Foyn, N. Glomnes, G. Rebowski, F. Impens, K. Gevaert, R. Dominguez, and T. Arnesen, *NAA80 is actin's N-terminal acetyltransferase and regulates cytoskeleton assembly and cell motility.* Proc Natl Acad Sci U S A, 2018. **115**(17): p. 4399-4404.
267. Malek, N., A. Michrowska, E. Mazurkiewicz, E. Mrówczyńska, P. Mackiewicz, and A.J. Mazur, *The origin of the expressed retrotransposed gene ACTBL2 and its influence on human melanoma cells' motility and focal adhesion formation.* Scientific Reports, 2021. **11**(1): p. 3329.
268. Wen, G., M. Hong, B. Li, W. Liao, S.K. Cheng, B. Hu, G.M. Calaf, P. Lu, M.A. Partridge, J. Tong, and T.K. Hei, *Transforming growth factor-β-induced protein (TGFBI) suppresses mesothelioma progression through the Akt/mTOR pathway.* Int J Oncol, 2011. **39**(4): p. 1001-9.
269. Zhao, Y.L., C.Q. Piao, and T.K. Hei, *Downregulation of Betaig-h3 gene is causally linked to tumorigenic phenotype in asbestos treated immortalized human bronchial epithelial cells.* Oncogene, 2002. **21**(49): p. 7471-7.
270. Randazzo, P.A., K. Miura, and T.R. Jackson, *37 - Assay and Purification of Phosphoinositide-Dependent ADP-Ribosylation Factor (ARF) GTPase Activating Proteins*, in *Methods in Enzymology*, W.E. Balch, C.J. Der, and A. Hall, Editors. 2001, Academic Press. p. 343-354.
271. Scarpa, E.S., G. Fabrizio, and M. Di Girolamo, *A role of intracellular mono-ADP-ribosylation in cancer biology.* The FEBS Journal, 2013. **280**(15): p. 3551-3562.
272. Bhagavan, N.V. and C.-E. Ha, *Chapter 25 - Nucleotide Metabolism*, in *Essentials of Medical Biochemistry (Second Edition)*, N.V. Bhagavan and C.-E. Ha, Editors. 2015, Academic Press: San Diego. p. 465-487.
273. Brown, W.A.C. and S. Clancy. *Translation: DNA to mRNA to Protein*. 2008.

274. Zareidoost, A., M. Yousefpour, B. Ghaseme, and A. Amanzadeh, *The relationship of surface roughness and cell response of chemical surface modification of titanium.* Journal of materials science. Materials in medicine, 2012. **23**(6): p. 1479-1488.
275. Lakhkar, N.J., J.H. Park, N.J. Mordan, V. Salih, I.B. Wall, H.W. Kim, S.P. King, J.V. Hanna, R.A. Martin, O. Addison, J.F. Mosselmans, and J.C. Knowles, *Titanium phosphate glass microspheres for bone tissue engineering.* Acta Biomater, 2012. **8**(11): p. 4181-90.
276. Yoshizawa, S., A. Brown, A. Barchowsky, and C. Sfeir, *Magnesium ion stimulation of bone marrow stromal cells enhances osteogenic activity, simulating the effect of magnesium alloy degradation.* Acta Biomaterialia, 2014. **10**(6): p. 2834-2842.
277. Zhang, J., M.T. Dalbay, X. Luo, E. Vrij, D. Barbieri, L. Moroni, J.D. de Bruijn, C.A. van Blitterswijk, J.P. Chapple, M.M. Knight, and H. Yuan, *Topography of calcium phosphate ceramics regulates primary cilia length and TGF receptor recruitment associated with osteogenesis.* Acta Biomaterialia, 2017. **57**: p. 487-497.
278. Du, Y., J.L. Guo, J. Wang, A.G. Mikos, and S. Zhang, *Hierarchically designed bone scaffolds: From internal cues to external stimuli.* Biomaterials, 2019. **218**: p. 119334-119334.
279. Ghosh, R., S. Pal, and R. Sarkar, *Study on the Development of Machinable Hydroxyapatite - Yttrium Phosphate Composite for Biomedical Applications.* Transactions of the Indian Ceramic Society, 2014. **73**(2): p. 121-125.
280. Kazi, G.A.S. and R. Yamagiwa, *Cytotoxicity and biocompatibility of high mol% yttria containing zirconia.* Restor Dent Endod, 2020. **45**(4): p. e52.
281. Ahmed, I., M. Lewis, I. Olsen, and J.C. Knowles, *Phosphate glasses for tissue engineering: Part 2. Processing and characterisation of a ternary-based P2O5–CaO–Na2O glass fibre system.* Biomaterials, 2004. **25**(3): p. 501-507.
282. Bortot, M., S. Prastalo, and M. Prado, *Production and Characterization of Glass Microspheres for Hepatic Cancer Treatment.* Procedia Materials Science, 2012. **1**: p. 358.
283. Hou, H., Z. Ji, Z. Xie, and H. Jin, *Spheroidizing mechanisms and simulation of spherical silica in Oxygen-Acetylene flame.* Advanced Powder Technology, 2018. **29**(3): p. 789-795.
284. Venturi, F. and T. Hussain, *Radial Injection in Suspension High Velocity Oxy-Fuel (S-HVOF) Thermal Spray of Graphene Nanoplatelets for Tribology.* Journal of Thermal Spray Technology, 2020. **29**(1): p. 255-269.
285. SQUAIR, P.L., *Neutron activation of microspheres containing sup(165)Ho: theoretical and experimental radionuclidic impurities study*, ed. L. Pozzo, et al. 2014.
286. Sancho, L., M. Rodriguez-Fraile, J.I. Bilbao, C. Beorlegui Arteta, M. Iñarrairaegui, V. Moran, and B. Sangro, *Is a Technetium-99m Macroaggregated Albumin Scan Essential in the Workup for Selective Internal Radiation Therapy with Yttrium-90? An Analysis of 532 Patients.* J Vasc Interv Radiol, 2017. **28**(11): p. 1536-1542.
287. Garin, E., Y. Rolland, S. Laffont, and J. Edeline, *Clinical impact of (99m)Tc-MAA SPECT/CT-based dosimetry in the radioembolization of liver malignancies with (90)Y-loaded microspheres.* Eur J Nucl Med Mol Imaging, 2016. **43**(3): p. 559-75.

288. Degrauwe, N., A. Hocquelet, A. Digklia, N. Schaefer, A. Denys, and R. Duran, *Theranostics in Interventional Oncology: Versatile Carriers for Diagnosis and Targeted Image-Guided Minimally Invasive Procedures.* Front Pharmacol, 2019. **10**: p. 450.
289. Smits, M.L., J.F. Nijsen, M.A. van den Bosch, M.G. Lam, M.A. Vente, J.E. Huijbregts, A.D. van het Schip, M. Elschot, W. Bult, H.W. de Jong, P.C. Meulenhoff, and B.A. Zonnenberg, *Holmium-166 radioembolization for the treatment of patients with liver metastases: design of the phase I HEPAR trial.* J Exp Clin Cancer Res, 2010. **29**: p. 70.
290. Nijsen, J.F.W., B.A. Zonnenberg, J.R.W. Woittiez, D.W. Rook, I.A. Swildens-van Woudenberg, P.P. van Rijk, and A.D. van het Schip, *Holmium-166 poly lactic acid microspheres applicable for intra-arterial radionuclide therapy of hepatic malignancies: effects of preparation and neutron activation techniques.* European Journal of Nuclear Medicine, 1999. **26**(7): p. 699-704.
291. Klaassen, N.J.M., M.J. Arntz, A. Gil Arranja, J. Roosen, and J.F.W. Nijsen, *The various therapeutic applications of the medical isotope holmium-166: a narrative review.* EJNMMI Radiopharmacy and Chemistry, 2019. **4**(1): p. 19.
292. Bult, W., S.G. Kroeze, M. Elschot, P.R. Seevinck, F.J. Beekman, H.W. de Jong, D.R. Uges, J.G. Kosterink, P.R. Luijten, W.E. Hennink, A.D. van het Schip, J.L. Bosch, J.F. Nijsen, and J.J. Jans, *Intratumoral administration of holmium-166 acetylacetonate microspheres: antitumor efficacy and feasibility of multimodality imaging in renal cancer.* PLoS One, 2013. **8**(1): p. e52178.
293. Johnson, L.S. and J.C. Yanch, *Absorbed dose profiles for radionuclides of frequent use in radiation synovectomy.* Arthritis Rheum, 1991. **34**(12): p. 1521-30.
294. Smits, M.L.J., J.F.W. Nijsen, M.A.A.J. van den Bosch, M.G.E.H. Lam, M.A.D. Vente, W.P.T.M. Mali, A.D. van het Schip, and B.A. Zonnenberg, *Holmium-166 radioembolisation in patients with unresectable, chemorefractory liver metastases (HEPAR trial): a phase 1, dose-escalation study.* The Lancet Oncology, 2012. **13**(10): p. 1025-1034.
295. Smits, M.L., M. Elschot, M.A. van den Bosch, G.H. van de Maat, A.D. van het Schip, B.A. Zonnenberg, P.R. Seevinck, H.M. Verkooijen, C.J. Bakker, H.W. de Jong, M.G. Lam, and J.F. Nijsen, *In vivo dosimetry based on SPECT and MR imaging of 166Ho-microspheres for treatment of liver malignancies.* J Nucl Med, 2013. **54**(12): p. 2093-100.
296. Ha, E.J., H.S. Gwak, C.H. Rhee, S.M. Youn, C.W. Choi, and G.J. Cheon, *Intracavitary radiation therapy for recurrent cystic brain tumors with holmium-166-chico : a pilot study.* J Korean Neurosurg Soc, 2013. **54**(3): p. 175-82.
297. Sohn, J.H., H.J. Choi, J.T. Lee, J.D. Lee, J.H. Kim, Y.M. Moon, K. Park, K.B. Park, E. Kim, and N.C. Yoo, *Phase II study of transarterial holmium-166-chitosan complex treatment in patients with a single, large hepatocellular carcinoma.* Oncology, 2009. **76**(1): p. 1-9.
298. Kwak, C., S.K. Hong, S.K. Seong, J.M. Ryu, M.S. Park, and S.E. Lee, *Effective local control of prostate cancer by intratumoral injection of (166)Ho-chitosan complex (DW-166HC) in rats.* Eur J Nucl Med Mol Imaging, 2005. **32**(12): p. 1400-5.
299. Bahrami-Samani, A., R. Bagheri, A.R. Jalilian, S. Shirvani-Arani, M. Ghannadi-Maragheh, and M. Shamsaee, *Production, quality control and pharmacokinetic studies of Ho-EDTMP for therapeutic applications.* Sci Pharm, 2010. **78**(3): p. 423-33.

300. Sohaib, M., M. Ahmad, M. Jehangir, and A. Perveen, *Ethylene diamine tetramethylene phosphonic acid labeled with various β(-)-emitting radiometals: labeling optimization and animal biodistribution.* Cancer Biother Radiopharm, 2011. **26**(2): p. 159-64.
301. Vaez-Tehrani, M., S. Zolghadri, H. Yousefnia, and H. Afarideh, *Estimation of human absorbed dose for 166Ho-PAM: comparison with 166Ho-DOTMP and 166Ho-TTHMP.* The British Journal of Radiology, 2016. **89**(1066): p. 20160153.
302. Hirsch, A.E., D.C. Medich, B.S. Rosenstein, C.B. Martel, and J.A. Hirsch, *Radioisotopes and vertebral augmentation: dosimetric analysis of a novel approach for the treatment of malignant compression fractures.* Radiother Oncol, 2008. **87**(1): p. 119-26.
303. Donanzam, B.A., T.P. Campos, I. Dalmazio, and E.S. Valente, *Synthesis and characterization of calcium phosphate loaded with Ho-166 and Sm-153: a novel biomaterial for treatment of spine metastases.* J Mater Sci Mater Med, 2013. **24**(12): p. 2873-80.
304. van Roekel, C., M.L.J. Smits, J.F. Prince, R.C.G. Bruijnen, M. van den Bosch, and M. Lam, *Quality of life in patients with liver tumors treated with holmium-166 radioembolization.* Clin Exp Metastasis, 2020. **37**(1): p. 95-105.
305. van de Maat, G.H., P.R. Seevinck, M. Elschot, M.L. Smits, H. de Leeuw, A.D. van Het Schip, M.A. Vente, B.A. Zonnenberg, H.W. de Jong, M.G. Lam, M.A. Viergever, M.A. van den Bosch, J.F. Nijsen, and C.J. Bakker, *MRI-based biodistribution assessment of holmium-166 poly(L-lactic acid) microspheres after radioembolisation.* Eur Radiol, 2013. **23**(3): p. 827-35.
306. Radosa, C.G., J.C. Radosa, S. Grosche-Schlee, K. Zophel, V. Plodeck, J.P. Kuhn, J. Kotzerke, and R.T. Hoffmann, *Holmium-166 Radioembolization in Hepatocellular Carcinoma: Feasibility and Safety of a New Treatment Option in Clinical Practice.* Cardiovasc Intervent Radiol, 2019. **42**(3): p. 405-412.
307. Hafeli, U.O., W.K. Roberts, G.J. Pauer, S.K. Kraeft, and R.M. Macklis, *Stability of biodegradable radioactive rhenium (Re-186 and Re-188) microspheres after neutron-activation.* Appl Radiat Isot, 2001. **54**(6): p. 869-79.
308. Bult, W., H. de Leeuw, O.M. Steinebach, M.J. van der Bom, H.T. Wolterbeek, R.M. Heeren, C.J. Bakker, A.D. van Het Schip, W.E. Hennink, and J.F. Nijsen, *Radioactive holmium acetylacetonate microspheres for interstitial microbrachytherapy: an in vitro and in vivo stability study.* Pharm Res, 2012. **29**(3): p. 827-36.
309. van Nimwegen, S.A., R.C. Bakker, J. Kirpensteijn, R.J.J. van Es, R. Koole, M. Lam, J.W. Hesselink, and J.F.W. Nijsen, *Intratumoral injection of radioactive holmium ((166) Ho) microspheres for treatment of oral squamous cell carcinoma in cats.* Vet Comp Oncol, 2018. **16**(1): p. 114-124.
310. Panitz, J.-C., *Characterization of ytterbium–yttrium mixed oxides using Raman spectroscopy and x-ray powder diffraction.* Journal of Raman Spectroscopy, 1999. **30**(11): p. 1035-1042.
311. Repelin, Y., C. Proust, E. Husson, and J.M. Beny, *Vibrational Spectroscopy of the C-Form of Yttrium Sesquioxide.* Journal of Solid State Chemistry, 1995. **118**(1): p. 163-169.
312. Arranja, A.G., W.E. Hennink, A.G. Denkova, R.W.A. Hendrikx, and J.F.W. Nijsen, *Radioactive holmium phosphate microspheres for cancer treatment.* International Journal of Pharmaceutics, 2018. **548**(1): p. 73-81.
313. Prince, J.F., M. van den Bosch, J.F.W. Nijsen, M.L.J. Smits, A.F. van den Hoven, S. Nikolakopoulos, F.J. Wessels, R.C.G. Bruijnen, M. Braat, B.A.

Zonnenberg, and M. Lam, *Efficacy of Radioembolization with (166)Ho-Microspheres in Salvage Patients with Liver Metastases: A Phase 2 Study.* J Nucl Med, 2018. **59**(4): p. 582-588.
314. Bult, W., P.R. Seevinck, G.C. Krijger, T. Visser, L.M. Kroon-Batenburg, C.J. Bakker, W.E. Hennink, A.D. van het Schip, and J.F. Nijsen, *Microspheres with ultrahigh holmium content for radioablation of malignancies.* Pharm Res, 2009. **26**(6): p. 1371-8.
315. Nijsen, J.F.W., J.-H. Seppenwoolde, T. Havenith, C. Bos, C.J.G. Bakker, and A.D.v.h. Schip, *Liver Tumors: MR Imaging of Radioactive Holmium Microspheres—Phantom and Rabbit Study.* Radiology, 2004. **231**(2): p. 491-499.
316. Höland, W. and G. Beall, *Principles of Designing Glass-Ceramic Formation*. 2012. p. 1-74.
317. Rawlings, R., J. Wu, and A. Boccaccini, *Glass-Ceramics: Their Production from Wastes—A Review.* Journal of Materials Science, 2006. **41**: p. 733-761.
318. Wang, J., Y. Zhao, D. Yin, P. Liu, J. Ma, Y. Wang, D. Shen, Z. Dong, L.B. Kong, and D. Tang, *Holmium doped yttria transparent ceramics for 2-μm solid state lasers.* Journal of the European Ceramic Society, 2018. **38**(4): p. 1986-1989.
319. Shannon, R.D., *Revised effective ionic radii and systematic studies of interatomic distances in halides and chalcogenides.* Acta Crystallographica Section A, 1976. **32**(5): p. 751-767.
320. Onik, T.A.M., H.F. Hawari, M.F.M. Sabri, and Y.H. Wong, *Formation and characterization of holmium oxide on germanium-based metal-oxide-semiconductor capacitor.* International Journal of Energy Research, 2021. **45**(10): p. 14761-14779.
321. The Materials, P., *Materials Data on Ho2O3 by Materials Project*. 2020: United States.
322. The Materials, P., *Materials Data on HoPO4 by Materials Project*. 2020: United States.
323. Islam, M.T. and I. Ahmed, *CHAPTER 12 Recent Advances in the Development and Applications of Phosphate and Borate Glass Microspheres*, in *Phosphate and Borate Bioactive Glasses*. 2022, The Royal Society of Chemistry. p. 227-247.
324. Delpino, G.P., R. Borges, T. Zambanini, J.F.S. Joca, I. Gaubeur, A.C.S. de Souza, and J. Marchi, *Sol-gel-derived 58S bioactive glass containing holmium aiming brachytherapy applications: A dissolution, bioactivity, and cytotoxicity study.* Mater Sci Eng C Mater Biol Appl, 2021. **119**: p. 111595.
325. Zambanini, T., R. Borges, A.C.S. de Souza, G.Z. Justo, J. Machado, Jr., D.R. de Araujo, and J. Marchi, *Holmium-Containing Bioactive Glasses Dispersed in Poloxamer 407 Hydrogel as a Theragenerative Composite for Bone Cancer Treatment.* Materials (Basel), 2021. **14**(6).
326. He, L.Y., X.M. Zhang, B. Liu, Y. Tian, and W.H. Ma, *Effect of magnesium ion on human osteoblast activity.* Braz J Med Biol Res, 2016. **49**(7).
327. Bosch-Rué, E., L. Diez-Tercero, B. Giordano-Kelhoffer, L.M. Delgado, B.M. Bosch, M. Hoyos-Nogués, M.A. Mateos-Timoneda, P.A. Tran, F.J. Gil, and R.A. Perez, *Biological Roles and Delivery Strategies for Ions to Promote Osteogenic Induction.* Frontiers in Cell and Developmental Biology, 2021. **8**.
328. Odintsova, T.I., E.C. Müller, A.V. Ivanov, T.A. Egorov, R. Bienert, S.N. Vladimirov, S. Kostka, A. Otto, B. Wittmann-Liebold, and G.G. Karpova, *Characterization and analysis of posttranslational modifications of the human*

large cytoplasmic ribosomal subunit proteins by mass spectrometry and Edman sequencing. J Protein Chem, 2003. **22**(3): p. 249-58.
329. Lindqvist, L.M., K. Tandoc, I. Topisirovic, and L. Furic, *Cross-talk between protein synthesis, energy metabolism and autophagy in cancer.* Curr Opin Genet Dev, 2018. **48**: p. 104-111.
330. MacDonell, R., M.W. Hamrick, and C.M. Isales, *Protein/amino-acid modulation of bone cell function.* Bonekey Rep, 2016. **5**: p. 827.
331. Wang, H., W. Huang, M. Sugawara, L.D. Devoe, F.H. Leibach, P.D. Prasad, and V. Ganapathy, *Cloning and functional expression of ATA1, a subtype of amino acid transporter A, from human placenta.* Biochem Biophys Res Commun, 2000. **273**(3): p. 1175-9.
332. Sharma, D., Y. Yu, L. Shen, G.-F. Zhang, and C.M. Karner, *SLC1A5 provides glutamine and asparagine necessary for bone development in mice.* eLife, 2021. **10**: p. e71595.
333. Chiu, M., D. Toscani, V. Marchica, G. Taurino, F. Costa, M.G. Bianchi, R. Andreoli, V. Franceschi, P. Storti, J. Burroughs-Garcia, R.A. Eufemiese, B. Dalla Palma, N. Campanini, E. Martella, C. Mancini, J. Shan, M.S. Kilberg, G. D'Amico, E. Dander, L. Agnelli, G. Pruneri, G. Donofrio, O. Bussolati, and N. Giuliani, *Myeloma Cells Deplete Bone Marrow Glutamine and Inhibit Osteoblast Differentiation Limiting Asparagine Availability.* Cancers (Basel), 2020. **12**(11).
334. Zhang, Y., J. Su, J. Yu, X. Bu, T. Ren, X. Liu, and L. Yao, *An essential role of discoidin domain receptor 2 (DDR2) in osteoblast differentiation and chondrocyte maturation via modulation of Runx2 activation.* J Bone Miner Res, 2011. **26**(3): p. 604-17.
335. Ahmad, M., B.T. Krüger, T. Kroll, S. Vettorazzi, A.-K. Dorn, F. Mengele, S. Lee, S. Nandi, D. Yilmaz, M. Stolz, N.K. Tangudu, D.C. Vázquez, J. Pachmayr, I.C. Cirstea, M.V. Spasic, A. Ploubidou, A. Ignatius, and J. Tuckermann, *Inhibition of Cdk5 increases osteoblast differentiation and bone mass and improves fracture healing.* Bone Research, 2022. **10**(1): p. 33.
336. Madda, R., C.-M. Chen, J.-Y. Wang, C.-F. Chen, K.-Y. Chao, Y.-M. Yang, H.-Y. Wu, W.-M. Chen, and P.-K. Wu, *Proteomic profiling and identification of significant markers from high-grade osteosarcoma after cryotherapy and irradiation.* Scientific Reports, 2020. **10**(1): p. 2105.
337. Di Meo, A., D. Sohaei, I. Batruch, P. Alexandrou, I. Prassas, and E.P. Diamandis, *Proteomic Profiling of the Human Tissue and Biological Fluid Proteome.* Journal of Proteome Research, 2021. **20**(1): p. 444-452.
338. Dhillon, M.S., P. Behera, S. Patel, and V. Shetty, *Orthobiologics and platelet rich plasma.* Indian J Orthop, 2014. **48**(1): p. 1-9.
339. Di Luca, A., A. Longoni, G. Criscenti, C. Mota, C. van Blitterswijk, and L. Moroni, *Toward mimicking the bone structure: design of novel hierarchical scaffolds with a tailored radial porosity gradient.* Biofabrication, 2016. **8**(4): p. 045007.
340. Murphy, W.L., T.C. McDevitt, and A.J. Engler, *Materials as stem cell regulators.* Nature Materials, 2014. **13**(6): p. 547-557.